PX # 353 BNL-79215-2007

Technical Design Report for a Nosecone Calorimeter (NCC) for the PHENIX Experiment

PHENIX Experiment, et al.

June 23, 2007

Physics Department/PO/2-182

Brookhaven National Laboratory
P.O. Box 5000
Upton, NY 11973-5000
www.bnl.gov

DISCLAIMER

Technical Design Report
for a Nosecone Calorimeter (NCC)
for the PHENIX Experiment

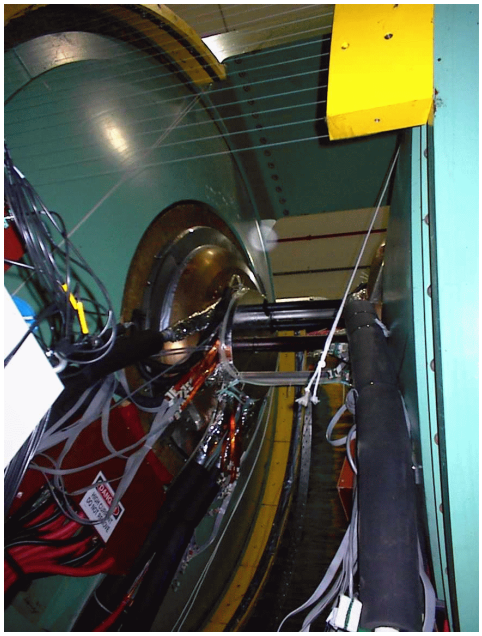

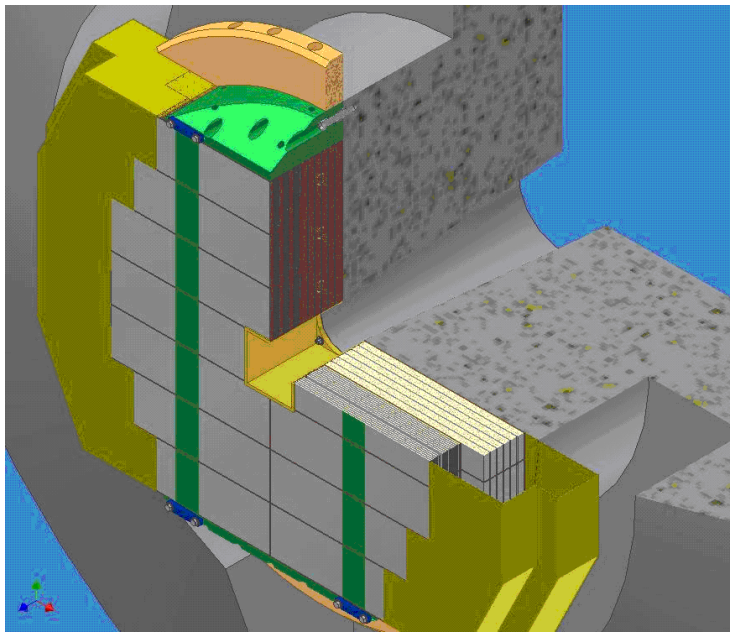

Relativistic Heavy Ion Collider
Brookhaven National Laboratory
June 23, 2007 TDR - version 4.1

PHENIX

PHENIX Nosecone Calorimeter

Participants

May, 2007

University of California, *Riverside, CA 92521, USA*
K. Barish, S. Bathe, O. Chvala, T. Hester, A. Kazantev, A. Moreale, S. Rolnick, Ken Sedgewick, R. Seto

Instrumentation Dept., Brookhaven National Laboratory, *Upton, NY 11973-5000, USA*
Z. Li, V. Radeka, S. Rescia

Physics Dept., Brookhaven National Laboratory, *Upton, NY 11973-5000, USA*
S. Boose, M. Chiu, B.M. Johnson, E.P. Kistenev, D. Lynch, R. Nouicer, R. Pak, R. Pisani, S.P. Stoll, A. Sukhanov, C.L. Woody

Charles University, *Ovocny trh 5, Praha 1, 116 36, Prague, Czech Republic*
Michael Finger, Miroslav Finger, M. Slunecka

Chonbuk University, *Chonju Chonbuk, 664-14, Korea*
J.B. Choi, E.J. Kim

University of Colorado, *Boulder, CO 80309, USA*
E. Kinney, J. Nagle

Columbia University and Nevis Laboratories, *Irvington, NY 10 533, USA*
C.Y. Chi

Czech Technical University, *Zikova 4, 166 36 Prague 6, Czech Republic*
M. Virius, T. Liska

Ewha Womans University, *Seoul 120-750, Korea*
I.S. Hahn, A. Kim, J. Lee, N.H. Lee, S.W. Nam, I.H. Park, J.S. Yoo

Florida State University, *Tallahassee, FL 32306, USA*
S. J. Edwards, A.D. Frawley

FNAL - Fermi National Accelerator Laboratory, *Batavia, IL 60510, USA*
W. E. Cooper, M. Demarteau, M. Hrycyk, K. Krempetz, H. Nguyen, Y. Orlov

University of Illinois Urbana-Champaign, *Urbana, IL 61801, USA*
M. Grosse-Perdekamp, J. Koster, J.C. Peng

Institute of Physics, Academy of Sciences of Czech Republic, *Na Slovance 2, 182 21 Prague 8, Czech Republic*
P. Mikes, J. Popule, P. Ruzicka, L. Tomasek, M. Tomasek, V. Vrba

Iowa State University, *Ames, IA 50011, USA*
J.C. Hill, J.L. Lajoie, F. Wei

Joint Institute for Nuclear Research- Dubna *Moscow Region, Russia*
S. Afanasiev, S. Bazylev, A. Baskakov, A. Bychkov, A. Cheremukhin, V. Elsha, N. Gorbunov, A. Isupov, N. Kotsev, A. Litvinenko, A. Malakhov, V. Peresedov, P. Rukoyatkin, V. Slepnev, I. Slepnev, N. Zamyatin, L. Zolin, E. Zubarev

University of Jyvaskyla/Helsinki Institute of Physics, *P.O.Box 35, FIN-40014, Jvyaskyla, Finland / P.O.Box 64 FIN-00014, Helsinki, Finland*
A. Kaskela, D.J. Kim, M. Oinonen, J. Rak, H. Steppänen

Korea University, *Seoul, 136-701, Korea*
B. Hong, H.H. Shim, K.S. Sim

Myongji University, *Yongin Kyonggido, 449-728, Korea*
K.S. Joo D.W. Kim, H.J. Moon

RIKEN, The Institute of Physical and Chemical Research, *Wako, Saitama 351-0198, Japan*
I. Nakagawa, A. Taketani

Skobeltsyn Institute of Nuclear Physics, Lomonosov Moscow State University, *Voro b'evy Gory, Moscow 119992, Russia*
G.A. Bogdanova, D. Karmanov, M. Merkin, V. Volkov, A. Voronin

Dept. of Physics and Astronomy, Stony Brook University, *SUNY, Stony Brook, NY 11794, USA*
A. Deshpande

Institute of Physics, University of Tsukuba, *Tsukuba, Ibaraki 305, Japan*
S. Esumi

Yonsei University, *Seoul 120-749, Korea*
J.H. Kang, Y. Kwon, S. Kim

Contents

Chapter 1

Introduction and Executive Summary

A remarkable result has emerged from the first several years of data taking at RHIC - the high temperature and density phase of QCD matter created in heavy ion collisions at RHIC is best described as a near perfect fluid - the strongly interacting Quark-Gluon-Plasma (sQGP). This state is characterized by a small viscosity to entropy ratio, and a high density of color charges which induces huge energy losses of partons transversing the medium. The task for the future is to understand the characteristics of the sQGP, and perhaps more importantly - to gain some insight into how and why such a medium is created. The PHENIX detector has been one of the primary experimental tools at RHIC; in particular the electromagnetic calorimeter has been a critical component of many of the measurements leading to this discovery. The coverage of the present PHENIX electromagnetic calorimeter is rather limited, covering half the azimuth and -0.35$< \eta <$0.35 Further progress requires larger coverage of electromagnetic calorimetry, both to increase the rate for low cross section phenomena, and to cover a broader range of pseudorapidity to study the rapidity dependence of the medium.

A pair of Nosecone Calorimeters (NCC) has been designed covering both positive and negative rapidity regions $1< |\eta| <3$ of the PHENIX detector. The NCC will make it possible to perform tomographic studies of the jet energy dependence of energy loss and medium response, by using direct photons as trigger particles over a large rapidity range. The technique of correlating trigger hadrons with low momentum hadrons has been powerfully exploited at RHIC to study the evolution of back to back jets [1, 2] and hence the response of the medium. The NCC will make it possible to do such studies using direct photons as the trigger particles. The direct photon in such "photon-jet" events tags the transverse momentum of outgoing parton which then fragments into lower energy particles. Together with the Forward Silicon Vertex detector (FVTX), the NCC will make PHENIX a large acceptance spectrometer, capable of detecting photons, electrons, muons, and hadrons. Our prime motivation is to provide precision measurements of direct photons, π^0s and dielectrons in A+A, p(d)+A, and polarized p+p collisions. The upgrade will provide access to physics observables that are not currently accessible to PHENIX or that are now available only indirectly with very limited accuracy.

The primary measurements addressed by the NCC are:

1. The Strongly Interacting Quark Gluon Plasma - Heavy Ion Collisions

   (a) The opacity of the sQGP via studies of correlated high energy hadron-jet and γ-jet events

   (b) The suppression of the quarkonium states due to screening via measurements of the χ_c state

   (c) The response of the medium via the study of jet-particle correlations.

2. The structure of very high energy density cold nuclear matter and the behavior of the gluon structure function over a large x-range as a possible precursor to the sQGP. These studies will be done in p(d)+A collisions via measurements of

   (a) The gluon distributions in cold nuclei via direct photons jets, and hadrons (particularly π^0s and ηs)

3. The spin structure of the nucleon in polarized p+p collisions

   (a) $\Delta G(x)$ particularly at low x_{BJ} through measurements of double spin asymmetries for inclusive π^0s, ηs, direct photons, jets and photon-jet events.

   (b) determination of quark transversity distribution functions of the proton from azimuthal hadron asymmetries in Collins fragmentation in jets. In addition the Sivers effect can be directly accessed through the observation of single spin asymmetries in inclusive jet production.

   (c) background rejection in measurements of quark and anti-quark spin distribution functions in W-production through isolations cuts.

The strengths of the NCC are as follows. First, by correctly identifying multi-photon showers in the high position resolution layers built into the calorimeters, the NCC enables measurements of π^0 yields at large rapidities, greatly extending the PHENIX sensitivity to jet quenching studies. Secondly, the NCC adds the capability of measuring direct photons at forward rapidity with large acceptance, making possible the study of correlated photon-jet production. These photon jet correlation measurements will be crucial to understanding major questions in all areas of the RHIC program. They can be used to measure cleanly the opacity of the sQGP to hard probes in heavy ion collisions, they can provide gluon distribution data down to $\approx 10^{-3}$ in cold nuclei via p(d)+A collisions for studying a possible CGC phase and establishing the initial state in heavy ion collisions, and they will also allow the determination of the gluon contribution to the nucleon spin at low x in polarized pp collisions. Such a measurement will be crucial before the total contribution from gluon spin to the proton spin can be understood. Historically, in the determination of the quark contribution to the spin of the nucleon, initial measurements at moderate x were consistent with the quark-parton model. It was not until low-x measurements at CERN indicated a deficit, that the so called "spin-crisis" was born [3, 4, 5]. Third, by providing energy measurements in a cone around leptons or photons, the NCC will improve background conditions for the identification of leptons from W and direct photons.

Finally, a key advantage for the NCC is the presence of the muon spectrometer in the forward (and backward) regions. The combination of the NCC and the muon spectrometer

will give PHENIX the capability to measure the χ_c charmonium state via its decay to J/ψ (measured in the muon spectrometer) and photon (measured in the NCC). This is probably the only case in which the χ_c can be measured in heavy ion collisions at high energies.

The NCC replaces the present copper nosecones in front of the muon spectrometer. It is a silicon-tungsten sandwich sampling calorimeter, which is longitudinally composed of 3 calorimeter sections read out by Si pads 1.5×1.5 cm^2. In addition there are two precision sections read out by strip pixels at 468 μm pitch. These are located at a depth of 2 and 9 radiation lengths and enable us to identify π^0s to high energy even when there is an overlap of showers in the pads. This also allows separation of direct photons and high energy π^0s.

To avoid cost intensive and time consuming R&D, we rely heavily on established technologies and expertise already available in collaborating laboratories. For the calorimeter we propose to use silicon sensors closely resembling those currently in use for prototyping future calorimeters for ILC and a number of cosmic ray experiments. For coordinate detectors we follow the lead of the PHENIX Silicon Vertex Tracker and use pixilated strips with 2-D sensitivity. As a backup to this latter solution we are working with the NUCLON experiment in Russia on implementing standard one-coordinate strip detectors with the identical strip width of 468 μm. We plan to use hybrid preamplifier chips developed at BNL for the ATLAS experiment at CERN as a base solution for signal conditioning in the calorimeter and the SVX4 readout chip developed at FNAL to read out the strip detectors.

Over 70 NCC participants from 20 institutions are cooperating to design, construct, install, and operate the NCC. Among these participants are many experts with extensive experience in calorimetry, in silicon detector technology, the design, fabrication and operation of modern readout electronics, mechanical and integration issues, software experts as well as physicists who are well versed in the different aspects of analysis necessary to extract physics from this detector. With the help of institutional contributions, PHENIX was able to maintain a small but well focused effort over the past two years to aid in the design of the detector, and to establish expertise in the relevant technologies.

We propose to construct our NCC detector over a period of three years, U.S. FY08, FY09, and FY10. To carry out this project we seek funding of a total of $4M through the DOE Office of Nuclear Physics. While the plan is to eventually construct an NCC for both the North and South arms of the PHENIX spectrometer, we propose to initially build only one NCC using funds from the DOE. Note that even with only one NCC installed the coverage of the electromagnetic calorimetry will be increased by more than a factor of 10. We are actively working to secure funding for a second NCC from our Japanese and European colleagues. In addition, we expect smaller contributions from the Czech Republic and Russia. A majority of the physics topics discussed in this proposal can be addressed using just one NCC. However, there are significant advantages to having two NCC detectors available. These include (a) in p+A collisions - the ability to simultaneously study the proton and the heavy ion side of the collision, (b) in p+p collisions - the ability to provide isolation cuts for W boson physics for the measurement of anti-quark spin, and (c) a factor of 2 in rate for rare processes such as high momentum direct photons and the χ_c with high statistics.

Chapter 2

Physics Overview

Over the first five years of data taking at RHIC, numerous critical measurements and discoveries have been made. In particular,the medium created in gold-gold reactions equilibrates very rapidly on times scales ≤ 1 fm/c as indicated by comparisons of the collective motion of created particles and hydrodynamic model calculations. In fact, these calculations indicate the medium after equilibration behaves like a nearly perfect liquid (low viscosity to entropy ratio), demanding that the system be strongly interacting. The initial energy densities are extremely high – perhaps 2 orders of magnitude greater than an ordinary nucleus. This state of matter has been given the name Strongly Interacting Quark Gluon Plasma (sQGP). In addition, the state of virtual saturated gluons in each of the nuclei before collision, referred to in some models as the colored glass condensate (CGC), is an important element to our understanding of the nuclear initial state from which the sQGP is formed.

These conclusions have come from several experimental observations using the initial suite of PHENIX detector subsystems [6, 7].

1. The suppression of high energy particles (jet quenching) in central heavy ion collisions at *midrapidity* together with the lack of suppression in deuteron nucleus collisions, indicates that energy densities of 10-20 GeV/fm^3 are reached in central Au+Au collisions-far above the critical energy density predicted by lattice calculations.

2. The large values of elliptic flow demonstrate that the initial system thermalizes rapidly and has nearly zero viscosity to entropy ratio.

3. The strong suppression and large values of elliptic flow of heavy quarks shows that heavy quarks themalize and loose large amounts of energy in traversing the medium. Such an observation requires that the interaction between constituents is extremely strong.

4. The large baryon to meson ratio at moderate values of momentum (several GeV). Together with the scaling behavior of the elliptic flow this observation indicates that the effective degrees of freedom at hadronization carry the quantum numbers of quarks.

5. The suppression of high energy particles at *forward rapidity* in deuteron nucleus collisions is consistent with gluon saturation.

In addition, the polarized p+p program has made initial steps in the measurement of the gluon contribution to the spin structure of the nucleon. It is important to note here that the measurements thus far have been at moderate x_{BJ}, and are consistent with the gluons carrying very little of the nucleon spin. Similar measurements at moderate x at SLAC in the late 1970's and early 1980's indicated that the quark contribution to the nucleon spin was consistent with the naive quark model [3]. It was not until measurements at low x from CERN became available that it was realized that the quarks could only account for a quarter of the nucleon [4, 5]. Since then an enormous amount of theoretical and experimental effort has been expended to understand the origin of the nucleon spin. Measurements of the low x behavior of the quark spin structure functions have been measured extensively at CERN, DESY, SLAC and JLAB. Measurements of the gluon structure function is now considered critical to solving this puzzle.

The observations made so far by the RHIC experiments are rather qualitative. Further understanding and discovery will require precision measurements. This will be made possible by an upgrade of the machine luminosity (RHIC II) and significant upgrades of the detectors. The demands of the program require that the unique capabilities of the PHENIX experiment at RHIC – that is the ability to make precision measurements of leptons and photons – be extended to larger rapidity coverage. The Nose-Cone Calorimeter provides this capability. The NCC increases the calorimetric coverage of the PHENIX detector to forward and backward rapidities $1< |\eta| <3$ increasing the rapidity coverage by more than an order of magnitude. This impacts the entire PHENIX physics program in A+A, p(d)+A, and polarized p+p collisions.

For the study of heavy-ion collisions, the essential questions revolve around our understanding of the sQGP state of matter. High p_T photons opposite a high energy parton can be used to calibrate the partons energy to directly measure its energy loss in the plasma. Measuring the energy loss dependence on parton identity, energy and angular distribution will address outstanding questions the energy loss mechanism. For example, is the interaction with the medium calculable with perturbative QCD or does it require a continuous medium using other, more complex, theoretical descriptions? An understanding of the energy loss depending on parton identity, initial parton momentum, and angular distribution will yield information to discriminate between various models of the medium; i.e., whether the medium can be understood using perturbative methods or whether is must be understood as a continuous medium using alternative methods of calculation. One recent idea is that the deposited energy excites a bulk response of the system yielding a shock wave in the form of a Mach Cone or Cerenkov emission, as might be expected from a continuous medium. It may turn out that various descriptions of the problem are identical in some limit, but theories must be constrained by precise data over a wide kinematic region

The yield of quarkonium states, particularly the χ_c, measured in conjunction with the muon spectrometer, will give information on what has traditionally been understood as the deconfinement temperature. The original idea proposed by Matsui and Satz [8] predicted that yields of quarkonium states would be suppressed in heavy ion collisions because of the Debye screening due to the deconfined quarks and gluons. As our understanding of the sQGP progresses the precise meaning of deconfinement is undergoing reevaluation. Theoretical cal-

culations done on the lattice have shown that heavy quark-antiquark pairs remain correlated even above the critical temperature for quark gluon plasma formation, and have yielded estimates of the temperature at which the quarkonium correlation functions disappear.

Finally, since the NCC can be used to find the reaction plane with great accuracy, all such signatures can be studied as a function of the geometry of the colliding system.

The wealth of new information from RHIC experiments reveals the time development of a heavy ion collision. The picture is as follows: the initial state of the nucleus at x values accessible at RHIC may be a state of saturated gluons known as Color Glass Condensate. This CGC state allows for a rapid thermalization of the colliding partons needed to explain the strength of the elliptic flow. Measurements in p(d)+A collisions at low x_{BJ} will give us access to the gluon distribution in cold nuclear matter thereby giving information on the initial state. Plasma instabilities developed at an early time may also provide an explanation of the rapid thermalization – or perhaps the answer will be a combination of the two phenomena.

The collision and subsequent equilibration of the partons gives rise to a near perfect fluid, namely a system with a very small viscosity to entropy ratio. This Strongly Interacting Quark Gluon Plasma (sQGP) is opaque to high momentum partons and has an energy density two orders of magnitude greater than that of normal nuclei. Pressure gradients build up very rapidly resulting in a large elliptic flow. These exciting results immediately lead to many questions which demand quantitative answers- among them: (a) What is the energy loss mechanism of partons as they traverse this matter? (b) Is the picture of energy loss by gluon radiation correct? (c) What is the importance of collisional energy loss? (d) Does the strength of the interaction demand a totally different picture? (e) What is the mechanism by which the CGC thermalizes so rapidly? (f) Can we explicitly observe the deconfinement of quarks and gluons, or must we revise our understanding of deconfinement in the sQGP? (g) What are the relevant degrees of freedom?

For the spin program direct photons, jets, and high momentum particles in polarized p+p collisions are an effective way to extend the reach of present measurements of the gluon spin contribution at RHIC to low x. In addition transversely polarized protons will give access to the transverse quark distribution functions of the nucleon. Finally the NCC will provide a method to impose isolation cuts for the rejection of backgrounds in W-production. The resulting improvement in the signal to background ratio for W production will increase the figure of merit for asymmetries observed in spin dependent W-production.

The electromagnetic calorimeter in the central region (EMC) has been a critical element in many of the most important measurements made by the PHENIX detector. The strongest and cleanest understanding of the suppression of high momentum hadrons – i.e., "jet quenching" comes from $\pi^0 s$ measured by the EMC. The unique capabilities of PHENIX to make precise measurements of leptons and photons must now be extended to larger coverage While a number of the physics processes we wish to study require luminosity of RHIC II to be fully addressed, many things can be done before the luminosity upgrade. Rates and plots will be shown for RHIC II, however, when appropriate rates for RHIC I will be mentioned. This is particularly true for the measurement of π^0s spectra, direct photon spectra and the χ_C where initial measurements can be made rather early. High momentum correlations and

multi-dimensional studies as a function of transverse momentum and centrality will require higher luminosities.

2.1 Heavy Ion Physics

As mentioned previously a remarkable result has emerged from the first several years of RHIC data taking in heavy ion collisions. It appears that a strongly interacting Quark-Gluon Plasma is produced, which can be understood as a near perfect fluid. It is imperative to understand the characteristics of this medium. One of the critical differences between the system created at RHIC and the traditional way of understanding high energy particle collisions is the fact that bulk properties of the medium affect the experimental observables. In fact pion rapidity distributions are Gaussian and fit and are more correctly described by Landau type initial conditions than a boost invariant Bjorken type of initial condition [9] and hence behaves not as an expanding cylinder, but rather as an expanding 3D fireball. Hence we must understand the spacial characteristics of a variety of quantities such and the energy density and temperature as a function of rapidity to get a tomographic picture of the "fireball".

- The NCC will measure direct photons with correlated high momentum particles. As photons do not lose energy as they traverse the medium, photons produced by QCD Compton scattering tag the initial transverse momentum of the opposing scattered parton. This allows tomographic study of energy loss in the medium. In addition, the NCC will extend the PHENIX rapidity coverage for neutral hadrons and allow study as a function of the reaction plane. Finally, the distributions of particles opposite direct photons or high momentum hadrons are sensitive to the response of the medium. Such measurements will show whether the medium responds collectively (e.g., by density or sound waves), or whether more conventional pQCD pictures are appropriate.

- The NCC will also make possible the measurement of the χ_C charmonium state. One of the important advantages of the NCC is its use in conjunction with the present muon-spectrometer. The χ_C can be detected via its decay to J/ψ detected in the muon spectrometer, and photon detected in the NCC. The measurement of the χ_C is a critical element in understanding the temperature at which deconfinement (or what we at present understand as "deconfinement" via the lattice) occurs. Of course, this was one of the primary objectives of the original heavy ion program.

2.1.1 Hard Scattering

Hard scattered partons are an important probe of the matter created in heavy-ion collisions. Because the hard scattering event occurs early in the evolution of the collisions ($\tau <$ 1 fm/c), the scattered partons can be affected by the evolution of the surrounding QCD matter, particularly if this matter passes through a deconfined phase. The scattered partons will be sensitive to the medium primarily through the mechanism of energy loss resulting in a reduction of the energy available to the parton when it fragments into hadrons. This

phenomenon was predicted to lead to a suppression of particles with large transverse momentum in heavy-ion collisions at RHIC and this suppression has been quantified by excellent measurements from the first RHIC runs [10, 11, 12, 13]. Measurements in d+Au collisions have demonstrated that the suppression is not due to initial state effects [14].

The four RHIC experiments have measured hadron spectra from Au+Au collisions at $\sqrt{s_{NN}}$ = 130 and 200 GeV, extending out to $p_T \sim 20$ GeV/c. All of these measurements show a suppression of high transverse momentum hadrons in central collisions when compared to data from p+p collisions (suitably scaled by the number of binary collisions). At RHIC the particle composition of the inclusive charged measurements change dramatically for transverse momenta between 2 and 5 GeV/c [15], further complicating the physics interpretation; in particular there is a large baryon excess in this region of intermediate p_T (which is of interest in itself) which complicates the interpretation. The present PHENIX detector is capable of reconstructing the decay of the π^0 meson to two photons using the electromagnetic calorimeter at mid-rapidity. Using the measured production of π^0 mesons in both p+p and Au+Au collisions, we can construct a ratio known as the nuclear modification factor R_{AA}:

$$R_{AA} = \frac{dN_{AA}}{< N_{coll} > \times dN_{pp}} \tag{2.1}$$

where dN_{AA} is the differential yield for a point-like process in an A+A collision, and dN_{pp} is the differential yield for the same process in nucleon-nucleon collisions. The number of binary collisions for a given centrality class N_{coll} is estimated using a Glauber model of the nuclear overlap. In the naive limit that a nucleus-nucleus collision can be thought of as a superposition of independent nucleon-nucleon collisions, R_{AA} at high p_T should be unity. Figure 2.1 shows R_{AA} for charged hadrons and neutral pions as measured by the PHENIX collaboration. There is a significant suppression of high transverse momentum hadrons observed in Au+Au collisions, consistent with substantial energy loss of the scattered partons.

The excess in the charged particle yields compared to π^0s at intermediate p_T comes about because of the change in composition of the inclusive charged measurements for transverse momenta between 2 and 5 GeV/c [15]. Neutral pions, do not have this complication and can be more easily understood. In addition, at high-p_T there are background processes that can result in a low p_T particle being mis-reconstructed as a high momentum particle. In contrast, the measurement of π^0 mesons becomes essentially background-free at high-p_T.

Models of energy loss that incorporate the expansion of the system indicate the energy loss in the matter created in heavy-ion collisions at RHIC may be as much as fifteen times larger than the energy loss of a comparable parton in ordinary nuclear matter [16]. The measurements can be used to fit the transport coefficient $\hat{q}$ in the BDMPS formalism, which uses perturbative methods to calculate the energy loss of partons traversing a dense medium [17, 18] (See Fig. 2.2). Other approaches that parametrize the energy loss in terms of quantities such as the gluon density can also be used as the basis for fits to the data [19]. Using such fits we find that the gluon density created in a heavy ion collision is more than an order of magnitude larger than in cold nuclei.

One of the first measurements to be done by the NCC will be to extend such measurements

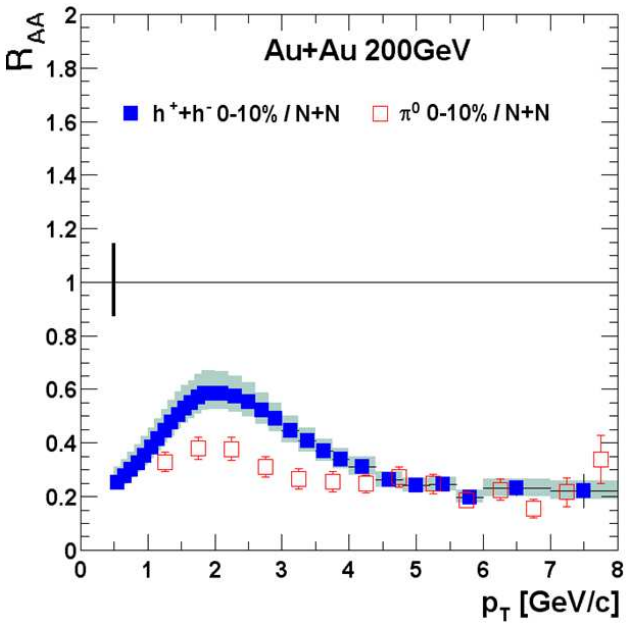

Figure 2.1: R_{AA} for π^0 mesons and inclusive charged particles from as measured by PHENIX. The difference in the observed suppression for charged hadrons and neutral pions between 1-4 GeV/c is due to the changing particle composition of the charged hadrons, highlighting the importance of the π^0 measurement.

to larger rapidity, thereby allowing PHENIX to measure the suppression of high momentum hadrons as a function of rapidity to obtain a rapidity dependent energy loss parameter, and energy density, which is the first step to making a tomographic map of the fireball. Tables A.4-A.7 summarize the rates of high p_T π^0 production expected in a 12 week run. Even during RHIC I, the rates are such that the NCC can easily make a measurement of π^0 out to a p_T of greater than 10 GeV/c. For RHIC II this range extends to 20 GeV/c.

Originally the mechanism of energy loss was thought to be primarily through medium-induced gluon radiation [21, 22, 23, 24, 25, 26, 27, 28], however recent PHENIX measurements of electrons from the decay of heavy quarks show similar suppression as for light quarks Figure 2.3 [29]. Gluon radiation should be significantly reduced for heavy quarks, and one would expect that the suppression should be much weaker. In order to explain the data, models of energy loss via gluon radiation must invoke parameters which are far in excess of reasonable values. This has led theorists to examine other mechanisms such as collisional energy loss.

The NCC will add the capacity to identify and measure electron energy at forward rapidity. One of the primary goals of the Forward Vertex Detector upgrade (FVTX) is to identify detached vertices in charm and bottom decays to muons in the forward region. The capability of measuring electron decays of bottom and charm NCC will give an additional channel complementing the muon measurements. At the moment it is not clear that we will be able to measure the sign of the electron, but given that the system is largely baryon free, whether the outgoing parton is charm or anti-charm, should not matter.

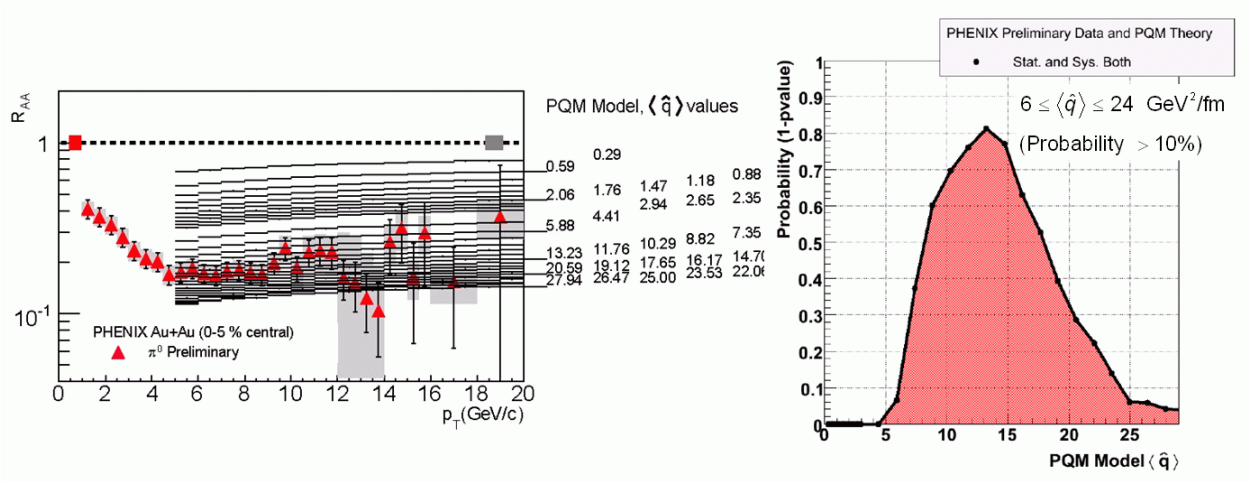

Figure 2.2: (Left) R_{AA} for π^0 mesons fit to the Parton Quenching Model (PQM model) which uses the BDMPS formalism together with the appropriate nuclear geometry in a monte-carlo implementation. (Right) A probability distribution extracted from fits to the data for $\hat{q}$. The increase in statistics from RHIC II will significantly improve such measurements so that $\hat{q}$ can be determined to better than 10%. [19, 20]

2.1.1.1 Photon-Tagged Jets

One of the primary motivations of the NCC is the detection of photon-tagged jets. The suppression of high-p_T hadrons seen at RHIC is a complicated interplay between the density and time evolution of the created matter, the collision geometry, and the transverse momentum of the probe. One way to clarify the picture is to use jets that are produced in coincidence with photons via a QCD-Compton process (see Figure 2.4). The photon escapes the colored medium essentially unmodified and without undergoing energy loss, and therefore provides a measure of the total energy of its partner jet. However, the cross-section for such a process is substantially smaller than the full dijet cross section. Precision measurement requires both the higher luminosity of RHIC II and the large acceptance of the NCC.

Direct photons at mid-rapidity in Au+Au collisions at $\sqrt{s_{NN}} = 200$ GeV have already been measured by the PHENIX collaboration, as shown in Figs. 2.5 and 2.6. These initial measurements demonstrate not only the feasibility of measuring direct photons in a heavy-ion environment but the observed scaling with the number of binary collisions indicates that the photons do indeed survive unmodified to the final state. Preliminary analyses of photon-jet correlations have shown that the direct photon triggered contribution can be separated statistically from decay photon triggers. Future studies with direct-photon tagged jets will allow a detailed, quantitative study of the energy loss suffered by the partner jet, further elucidating the nature of the matter created at RHIC.

Since the NCC dramatically increases the coverage for the detection of photons, the rates at high p_T become substantial. For a run of 12 weeks at RHIC I luminosities in Au+Au collisions, PHENIX will be able to observe about 10K photons above a transverse momentum of 10 GeV/c. At RHIC II the range is extended to almost 20 GeV/c. (See Tables A.5 and

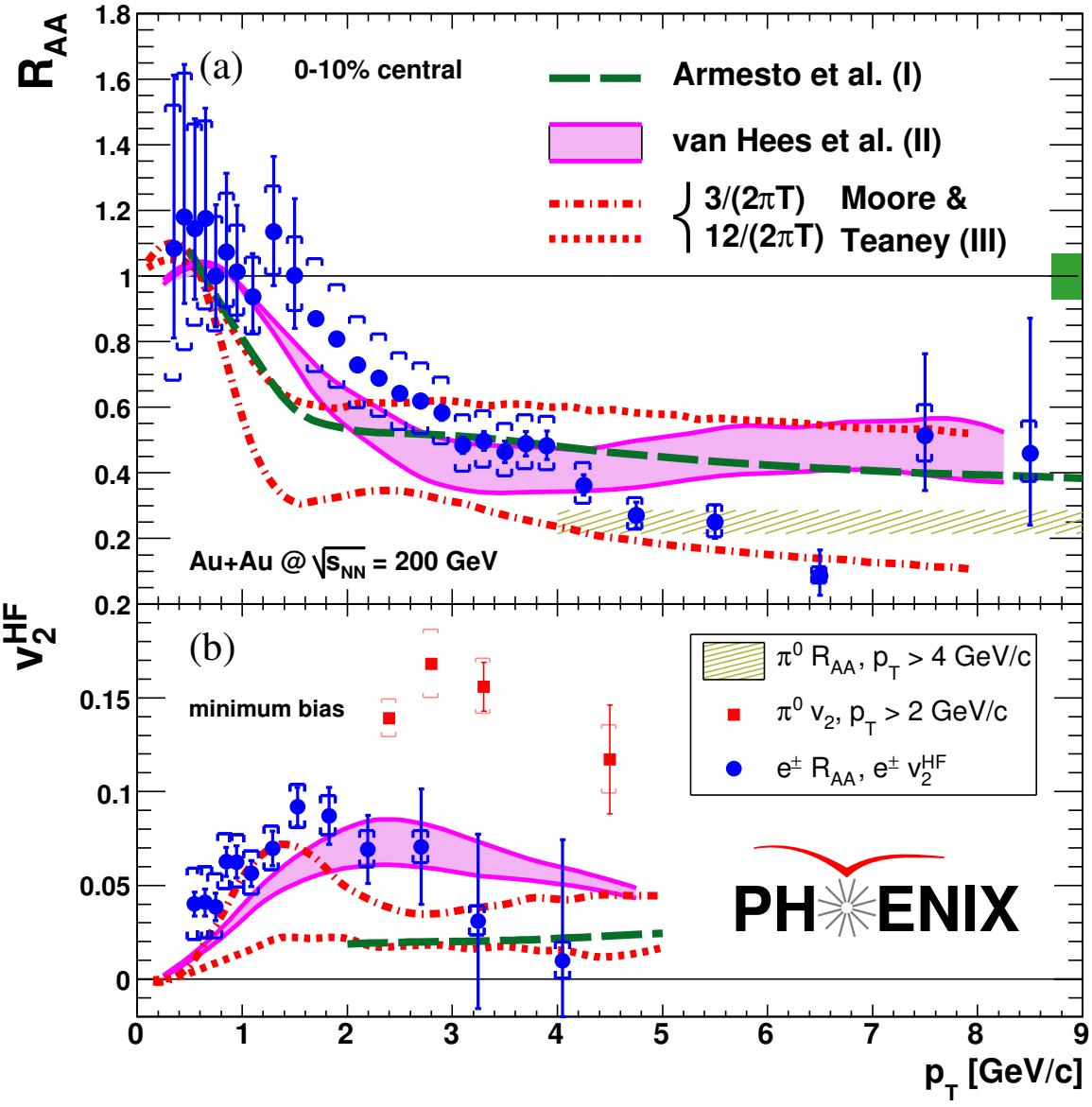

Figure 2.3: R_{AA} and v_2 from PHENIX showing electrons from charm and bottom decay [29] as compared to perturbative QCD calculations of Armesto et.al. [30]. Parameters far in excess of reasonable pQCD values are required to fit the data. In this case the transport coefficient $\hat{q}$=14 GeV^2/fm which implies a strongly coupled medium. Also shown are models of van Hees et al, and Moore and Teaney [31, 32] with a small relaxation time for heavy quarks, again implying a strongly interacting medium.

A.6)

In heavy-ion collisions at RHIC energies direct detection of jets is complicated by large backgrounds from particles in the underlying event. However, jets of hadrons can still be identified using two-particle correlation techniques, which take advantage of the fact that

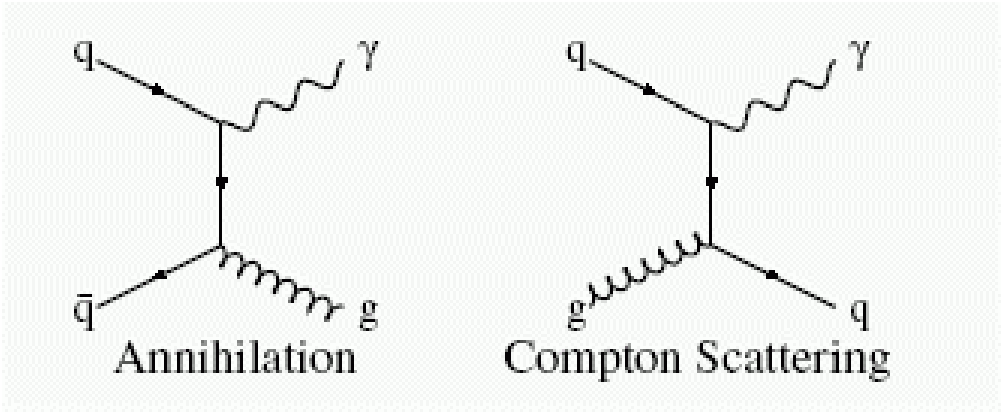

Figure 2.4: Tree level diagrams for the production of direct photons. The photon produced in the hard scattering only interacts electromagnetically and will escape the surrounding medium produced in nucleus-nucleus collisions without interacting. The jet produced by the partner parton in the interaction will, however, interact and suffer energy loss. Measuring both the photon and jet in the final state allows for a calibration of the energy loss. Pythia simulations show that the QCD-Compton diagram dominates over the annihilation diagram by a factor of 9 to 1, hence direct photons primarily tag an outgoing quark on the opposite side.

hadrons resulting from a parton cascade will be correlated in azimuthal angle and pseudorapidity. Such techniques make use of the "leading hadron" effect in jet fragmentation, where a single hadron often ends up with a large fraction of the parton momentum. Selecting high transverse momentum hadrons provides a good proxy for the jet direction and momentum. Particles are then correlated with this high p_T trigger particle and one can clearly see particles associated with both the original jet of the trigger particle, and the correlated "opposite" side jet. This is illustrated in the left panel of Fig. 2.7. In the case of p+p collisions (open points) one sees the expected correlations of the original jet with the trigger particle, and the opposite side jet at 180°. The behavior of from Au+Au collisions is more interesting and will be discussed in the next section. In any case, such correlation studies have proved to be an extremely powerful tool in observing the behavior of "jets" in an extremely high multiplicity environment, where low transverse momentum particles are of paramount importance. Such correlations will be used in the study of the recoil jet in photon-jet events.

2.1.1.2 Response of the Medium

Experiments have been able to study the response of the medium gaining understanding of the energy loss by selecting high momentum hadrons or direct photons and examining the recoil particles on the opposite side. One finds that the recoil particles show a behavior which may be indicative of a shock wave, such as a Mach cone as can be seen in Figure 2.7 [33, 34, 35], where one observes a "double hump" structure in the opposite side jet. Instead of treating energy loss in a pQCD framework, it may be more enlightening to think of the system as a continuous medium – a fluid – and to calculate and measure transport

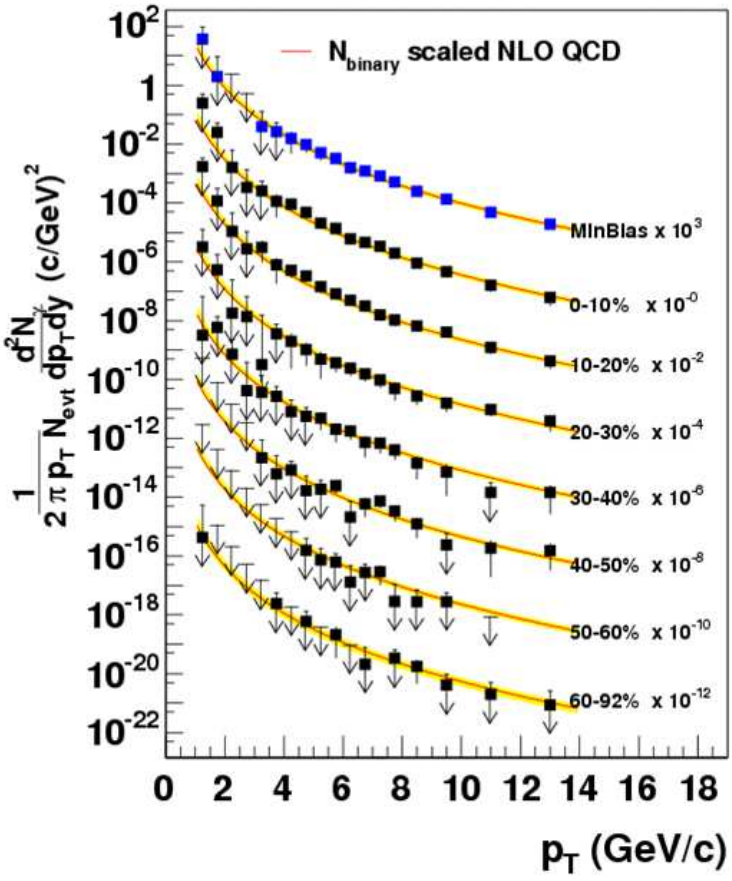

Figure 2.5: Measured direct photon invariant multiplicity at mid-rapidity as a function of centrality in Au+Au collisions.

coefficients such as the viscosity and diffusion coefficients and other quantities such as the speed of sound. Recently a powerful new theoretical technique has been used to calculate transport coefficients directly using AdS/CFT correspondence from string theory. While theory that is modeled is a super-symmetric conformal field theory – it has been shown to behave at high temperatures – particularly near the critical point, in a manner similar to QCD [36, 37]. This connection between a gravitational theory in 5 dimensional AdS space and RHIC physics is clearly exciting. One of the first of the papers to use this technique was published by Son and his collaborators, who found the viscosity to entropy ratio to be very small – presumably exactly what we are seeing at RHIC [38]. Gubser and his colleagues have calculated the response energy deposited by high momentum partons, and find that the medium responds by producing a "Mach Cone" [39, 40]. It has been suggested by Shuryak and Antroini that the angular opening of such a cone should be dependent on the mass of the outgoing parton [41, 35]. Whether or not one takes these ideas at face value, it is clear

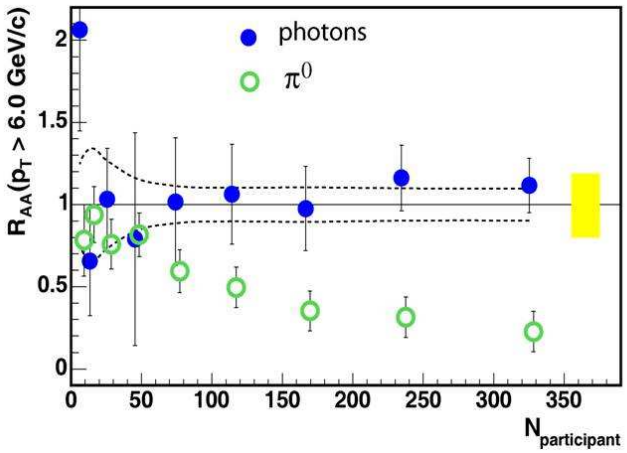

Figure 2.6: R_{AA} for direct photons as a function of transverse momentum as compared with that for $\pi^0 s$ showing that the direct photon suppression is consistent with zero.

that the characteristics of particles correlated with outgoing high momentum partons should be carefully measured as a function of energy or momentum, mass of the outgoing parton, rapidity, and centrality.

For the measurement of the "Mach Cone" mentioned above, trigger particles can be hadrons, heavy quarks, or direct photons. In the case of light hadrons, the primary partons are a mixture of gluons and light quarks. Since the QCD Compton diagram dominates over the annihilation diagram (See figure 2.4), direct photon events primarily tag the quark as the initial parton. Finally, the detection of a heavy quark would indicate that the heavy quark is both the primary parton and the parton on the opposite side. Heavy quarks can be identified by the FVTX and VTX detectors together with leptons measured in the EMCAL, Muon Arms, and NCC. Direct photons and hadrons (e.g., π^0s) can be identified and measured in the NCC to extend these capabilities to large rapidity. The NCC will then be able to detect particles correlated with these trigger particles (i.e., those particles forming the related "Mach Cone") over a large range of rapidity in the forward and directions. The radius of the cone, or more generally the response of the medium to energy loss, is expected to be dependent on the identity and momentum of the parton, and will serve as a powerful probe of the characteristics of the medium.

2.1.2 Heavy Quarkonia

Heavy quarkonia states are among the best probes created in heavy ion collisions for understanding modifications of the interactions amongst partons in the medium – a quark gluon plasma. The formation of charm-anti-charm $c\overline{c}$ and bottom-anti-bottom $b\overline{b}$ quark pairs occurs on very short time scales ($t \approx 0.1$ fm/c) proportional to the inverse mass. A small fraction of the time the pair evolves into a physical bound quarkonia state with a time scale determined by the relative momentum of the heavy quarks in the bound state ($t \approx 1$ fm/c). Charm and bottom quarks have a mass much larger than the expected temperature of the

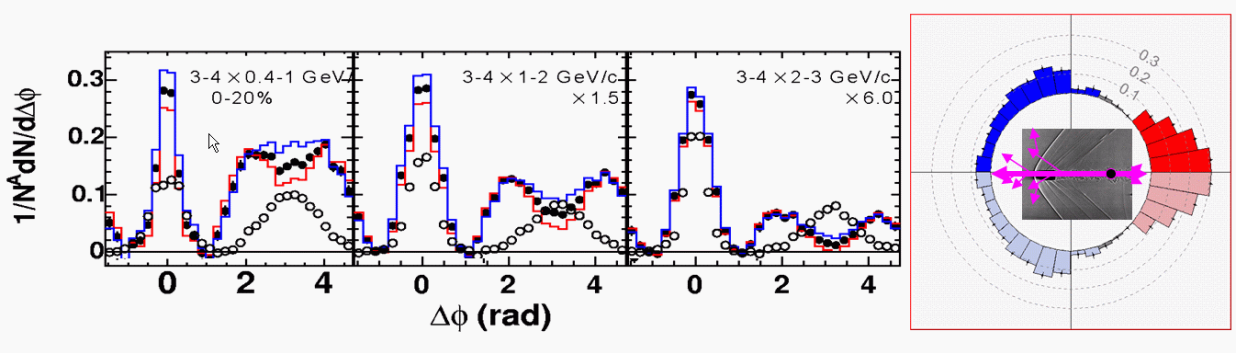

Figure 2.7: (left) Plots of correlated particles with a trigger particle of between 3 and 4 GeV for 0-20% central Au+Au events as a function of the azimuthal angle between the trigger particle and correlated particle. The three panels are for correlated particles of 0.4-1 GeV, 1-2 GeV and 2-3 GeV. Open circles indicate p+p collisions, and closed circles indicate Au+Au. (right) Polar plot of the leftmost panel.

medium and are only abundantly created in the earliest stage of the nuclear collision. Thus, we can ascribe the final yield of heavy quarkonia to how the quarks and antiquarks interact with the surrounding cold and hot nuclear medium between their creation time and the final freeze-out of the system ($t \approx 10$ fm/c).

The original suggestion [8] that color screening in a deconfined medium should lead to a suppression of heavy quarkonia states has evolved significantly over the past 20 years. New evidence from studies of lattice QCD reveal that some of the quarkonium states continue to exist, in modified form, inside the deconfined medium of a quark gluon plasma up to temperatures well beyond the expected 170 MeV transition value [42]. The current state of the art in lattice QCD yields a somewhat ambiguous picture where considerations of free energy give a different melting point for quarkonia than studies of the spectral functions [43, 44]. However, it is common amongst the pictures that the more weakly bound ψ' and χ_c should be modified and melt at a lower temperature compared with the J/ψ and Υ states. This is shown from two different calculations in Table 2.1 [45]. The sequential suppression expected as one increases the temperature of the medium is shown in Figure 2.8 [46].

Particular interest in the χ_c state, in addition to the J/ψ, is twofold. First, in the different lattice calculations it is likely that the χ_c and J/ψ states span the binding energy range where one of the states at least will have some color screening effects. Second, it is expected from hadron-hadron and hadron-nucleus measurements that of order 40% of the reconstructed J/ψ are from χ_c decay feeddown. Thus, the measurement of both states is likely necessary to disentangle various effects and extract the fundamental physics from this probe.

There are three P wave quarkonia states $(\chi_{c1}, \chi_{c2}, \chi_{c3})$ all of which can decay via $\chi_c \longrightarrow \gamma J/\psi$, though only the first two have appreciable branching fractions, 0.27 and 0.17 respectively. The PHENIX experiment currently measures the J/ψ away from mid-rapidity via reconstruction of the two decay muons, and needs to add the capability to measure the associated photon. The photon from the radiative decay of the χ_c has a small relative mo-

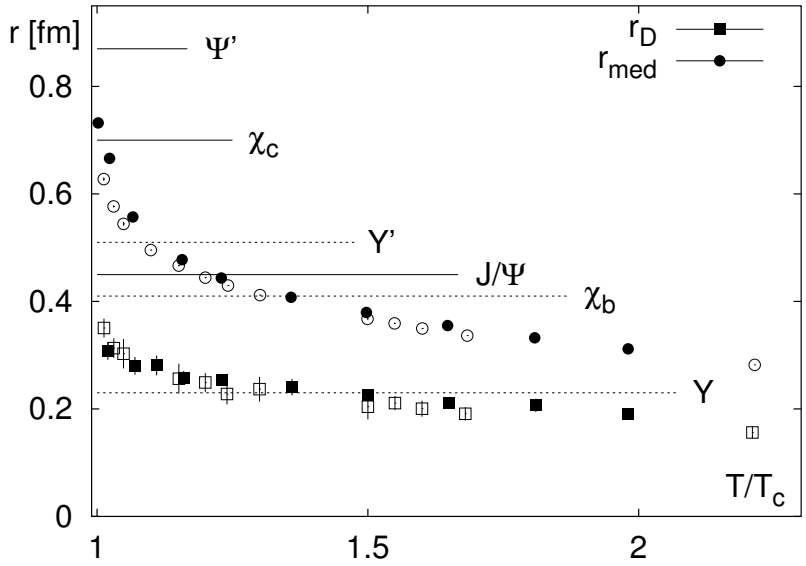

Figure 2.8: The scale r_{med} which gives an estimate for the distance beyond which the force between a static quark anti-quark pair is strongly modified by temperature effects and the Debye screening radius, $R_D = 1/m_D$. Open (closed) symbols correspond to SU(3) (2-flavor QCD) calculations. The horizontal lines give the mean squared charge radii of some charmonium and bottomonium states.

Table 2.1: Dissociation temperatures obtained from different analyses in quenched QCD.

Heavy Quarkonium	$U^{(1)}_{Q\bar{Q}}(\mathbf{r},T)$ Potential	$F_1(\mathbf{r},T)$ Potential	$U_1(\mathbf{r},T)$ Potential	Spectral Analysis
$J/\psi, \eta_c$	$1.62\,T_c$	$1.40\,T_c$	$2.60\,T_c$	$\sim 1.6\,T_c$
χ_c	unbound in QGP	unbound in QGP	$1.19\,T_c$	dissolved below $1.1\,T_c$
ψ', η_c'	unbound in QGP	unbound in QGP	$1.20\,T_c$	
Υ, η_b	$4.10\,T_c$	$3.50\,T_c$	$\sim 5.0\,T_c$	
χ_b	$1.18\,T_c$	$1.10\,T_c$	$1.73\,T_c$	
Υ', η_b'	$1.38\,T_c$	$1.19\,T_c$	$2.28\,T_c$	

mentum to that of its parent and therefore the NCC will have good acceptance (58%) for γ when the J/ψ is accepted into the existing PHENIX forward spectrometer. In addition, due to the forward rapidity of these χ_c, the photon is boosted and can have an appreciable momentum.

The first statistically significant results on heavy quarkonia in heavy ion collisions at

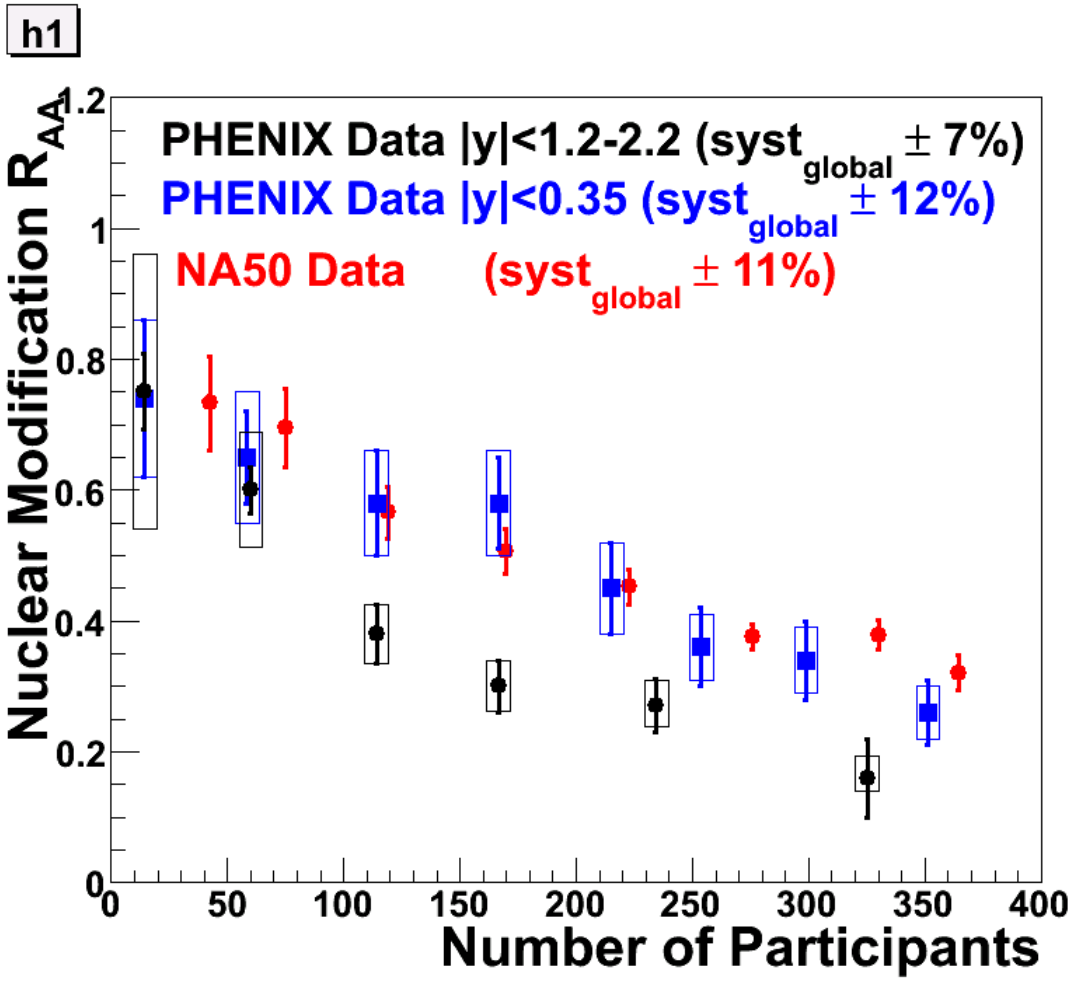

Figure 2.9: PHENIX R_{AA} for J/ψ in $Au + Au$ and 200 GeV reactions.

RHIC Fig. 2.9 come from the PHENIX experiment [47]. Surprisingly the nuclear suppression factor is quite similar at RHIC energies as the results at almost an order of magnitude lower in collision energy from the NA50 and NA60 experiments [48, 49] at the CERN-SPS. Most model calculations of expected J/ψ production, whether via color screening or co-mover absorption, predicted a substantially larger suppression at RHIC due to the higher energy density and also higher temperature. In fact, there were many predictions that the J/ψ might be so suppressed as to make any observation difficult, and thus turning the focus to the more tightly bound and thus less suppressed $\Upsilon(1s)$ state. A further observation shown in Fig. 2.9 is that the suppression at larger rapidities is stronger than at mid-rapidity, where it is believed that the energy density is the highest. Newer theoretical models include the possibility of J/ψ production by the recombination of charm pairs. In addition, suppression at forward rapidities due to the saturation of the gluon structure functions (a popular model for this is the Colored Glass Condensate, described in the next section) may also influence the

production of charmonium. This new experimental information drives us to make precision measurements not just of the more tightly bound states, but also the less tightly bound χ_c and ψ'.

In order to see the χ_c one reconstructs the $\mu^+\mu^-\gamma$ invariant mass and subtracts off the $\mu^+\mu^-$ invariant mass where the dimuon mass is required to be in the J/ψ peak. The χ_c should show up as a peak at the χ_c-J/ψ mass difference of about 400-500 MeV. PHENIX has made a proof of principle measurement of the χ_c in p+p collisions using the central arms, where we have electromagnetic coverage. See Fig. 2.10. While it will be difficult to obtain enough statistics in the central arms to make a measurement of χ_c suppression in heavy ion collisions, the substantially larger acceptance of the NCC together with the muon arms will make this measurement possible.

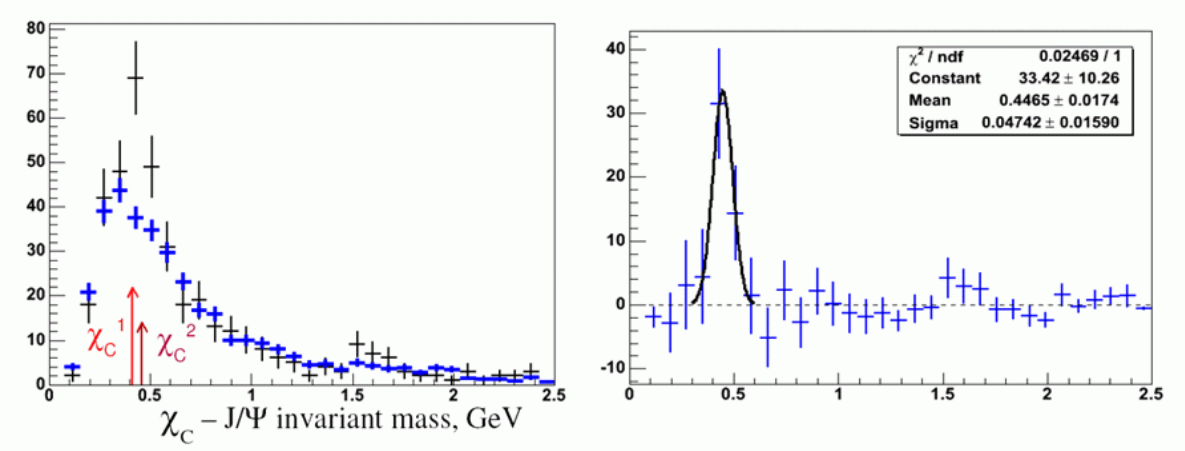

Figure 2.10:
$J\psi\gamma J\psi$ invariant mass spectrum showing the χ_c peak in p+p collisions as seen by the PHENIX central arm in run-5. We see about 50 χ_c. Background subtracted spectrum is shown on the right. The resolution of the peak is about 50MeV consistent with the resolution of the EMCAL.

The expected R_{AA} for the χ_C as measured by the NCC is shown in Fig. 2.11 where the J/ψ is detected via its dimuon decay in the muon spectrometer. The photon detected by the NCC is in the rapidity range $1<|\ y\ |<1.5$. This is compared to the R_{AA} of the J/ψ measured by PHENIX in Run-4. Error bars for RHIC I will be about a factor of 3-5 larger and will make for a reasonable first measurement. RHIC II statistics will allow an analysis with reasonably fine bins in both centrality and p_T. Errors for the χ_C are statistical only. It is assumed that the p+p measurement of the χ_C adds a negligible error to the ratio. The errors are of the order of 10% coming simply from the fact that about 10K χ_C's are detected over a background of 600K. Since this is a S/B of less than 2%, systematic errors on the background subtraction must be evaluated carefully.

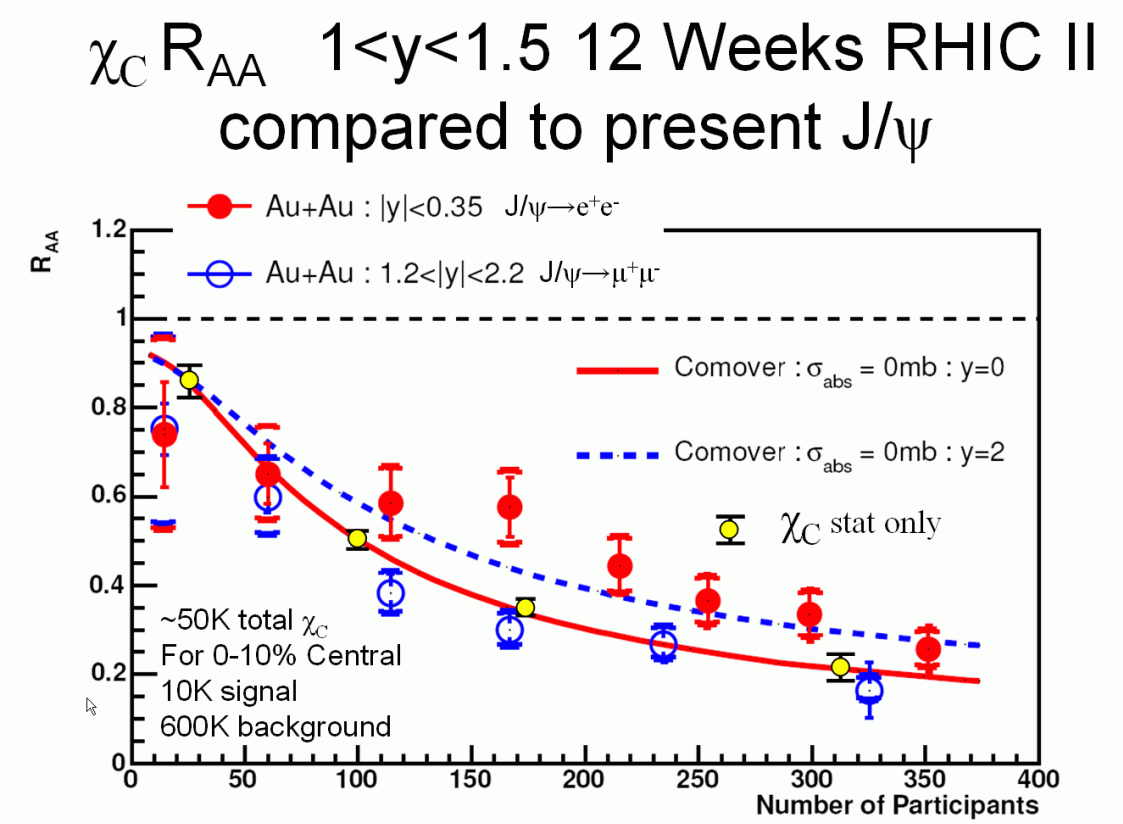

Figure 2.11: R_{AA} for the χ_C in where the χ_C decays to a $J/\psi + \gamma$ and the J/ψ is detected via its dimuon decay in the muon spectrometer. The photon detected by the NCC in the rapidity range $1<|\eta|<1.5$. This is compared to the R_{AA} of the J/ψ measured by PHENIX in Run-4. Error bars for RHIC I will be about a factor of 3-5 larger. Errors for the χ_C are statistical only. It is assumed that the p+p measurement of the χ_C adds a negligible error to the ratio.

2.1.3 Charm via Electrons

Further PHENIX upgrades include a forward silicon vertex detector with coverage matching that of the forward muon spectrometer. With the additional capability to identify displaced vertices, we greatly extend our ability to measure charm and bottom via single muon semi-leptonic decays by rejecting much longer lifetime muon backgrounds from pion and kaons decays. Additionally, we then can separate J/ψ contributions from B meson decay. This information from the forward silicon detector and the NCC may allow for the tagging of forward rapidity electrons, which has a displaced vertex. In principle, we can then separate the charm and bottom semi-leptonic decay electrons from the very prompt Dalitz decays and conversions. This could be complementary to the single muon program. In reality the kinematic coverage for both is limited by the coverage of the silicon detector and both measure essentially the same thing with quite different kinematics. We note that with a limited number of layers in the silicon detector, significant detailed studies are needed to

determine whether a clean electron sample can be obtained in proton-proton or heavy ion reactions.

2.2 Studies of Cold Nuclei, Nucleon Structure and Saturation

A system with very low viscosity to entropy ratio is formed very early (t $\approx$ 1 fm/c) in the collisions of heavy ions. As mentioned above, pQCD calculations predict thermalization times longer than this. How then, can the system thermalize so quickly? An exciting theoretical advance has emerged, in that non-perturbative methods of calculating the early stages of such collisions are now available in a formulation often referred to as the Colored Glass Condensate (CGC). Such calculations indicate that the low-x partons in nuclear collisions are packed together such that their nuclear wavefunctions overlap and saturation occurs – thereby distorting the wavefunctions. It is precisely these virtual low-x partons which are thought to lead to the formation of the real low momentum partons which make up the dense sQGP. Various ideas have been formulated which allow for thermalization of the system starting from the CGC. [50, 51, 52, 53]

The NCC upgrade will offer many new opportunities for advancing the understanding of this regime by studying p(d)+A collisions. It is important to note that the center-of-mass energy at RHIC is more than a factor of 5 greater than any existing fixed-target experiments. The Muon Piston Calorimeter (MPC), already installed in PHENIX covers a rapidity range from 3<| η |<3.7, so coverage of the NCC+MPC will be 1<| η |<3.7. These two items, an increased CM energy and a forward rapidity coverage, will make accessible new kinematic regions in PHENIX – in particular – the low-x region where CGC calculations are applicable.

It must be stressed that the CGC model, while being the most popular model for gluon saturation is certainly not the whole story. The suppression of various processes in p(d)+Acollisions at forward rapidity is also described by models of shadowing [54, 55, 56]. However we take the CGC model as a guide to possible phenomena that might be observed. These phenomena are generic enough that they will shed insight on most models. In fact, there is some evidence that the CGC and other models may be equivalent in some kinematic regions [57].

In the following we briefly discuss the CGC model and measurements which have been made by the present PHENIX detector. It will be made clear why study of the CGC must be made in the forward rapidity region. In addition, several other topics of interest in p(d)+A collisions will be discussed.

2.2.1 An Example of a Possible Model of Suppression at Large Rapidity: The Colored Glass Condensate

Recently, Mclerran and his collaborators [58, 59, 60] have used a classical approximation for the initial stage of a heavy ion collision, arguing that the occupation numbers at low x, where much of the particle production occurs are rather high (see Fig. 2.12). This model,

which is named the "Colored Glass Condensate," shows the phenomenon of gluon saturation and makes predictions that can be used to calculate the initial conditions in a heavy ion collision which in turn can then be used as input to the hydrodynamical calculations. This calculation relies on the fact that very early in the collision, gluon saturation effects at low x set a value of the parameter Q$\sim$Q$_S$, which is the value of the momentum transfer where α_S (the running coupling constant of QCD) can be considered small, but the occupation numbers are high and the approximations of the CGC model are valid. More physically Q$\sim$Q$_S$ defines the boundary at which gluons can be considered as saturated. The value of Q_S at RHIC is 1-2 GeV so $\alpha_S^2 \sim \frac{1}{10}$. Fig. 2.13 shows the region of of x and Q where this saturation should take place. The saturation assumed by these authors is present in the initial state before the nuclei collide. Hence the study of proton-nucleus collisions will be important in distinguishing these effects, from final state effects such as the formation of a quark-gluon plasma.

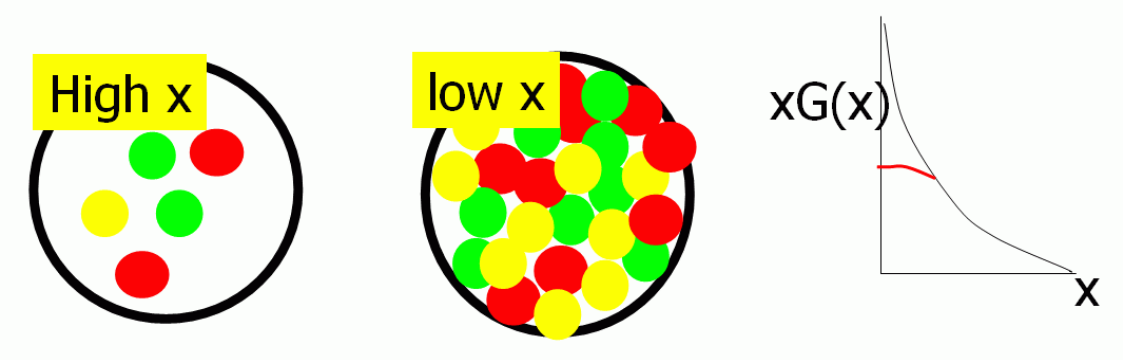

Figure 2.12: A schematic showing the saturation of the gluons at low-x. This has the effect of suppressing very low x gluons and pushing them to higher-x

Such an effect is consistent with electron-proton collisions at HERA [61]. In a heavy ion collision, the nucleus acts as an amplifier of the effect because of the thickness of the nucleus. Saturation effects which in a proton would be at x$\sim 10^{-4}$ would show up in p+A collisions at x$\sim 10^{-2}$. Investigations of CGC signals use the fact that going to forward rapidities samples a lower-x range in the nucleus.

The ratio

$$R_{CP} = \frac{Yield(central)/N_{coll}(Central)}{Yield(peripheral)/N_{coll}(Peripheral)} \tag{2.2}$$

is a measure of the yield per collision from hard processes coming from central as compared to peripheral collisions, where the peripheral collisions are taken as a baseline. If p+p data is available, it is often used as the baseline as will be done later in the definition of R$_{AA}$. Using punch-through hadrons identified in the muon spectrometer PHENIX looked at this ratio in deuteron-nucleus collisions. For a given p_T, a lower and lower value of x is sampled as one moves to higher rapidity. Since the gluon structure function increases at low x one would see a stronger suppression as one moves to higher rapidity. Fig. 2.14 shows just this effect, with the more central collisions showing a larger suppression. One interesting fact is that in the backward rapidity region, a strong enhancement is shown.

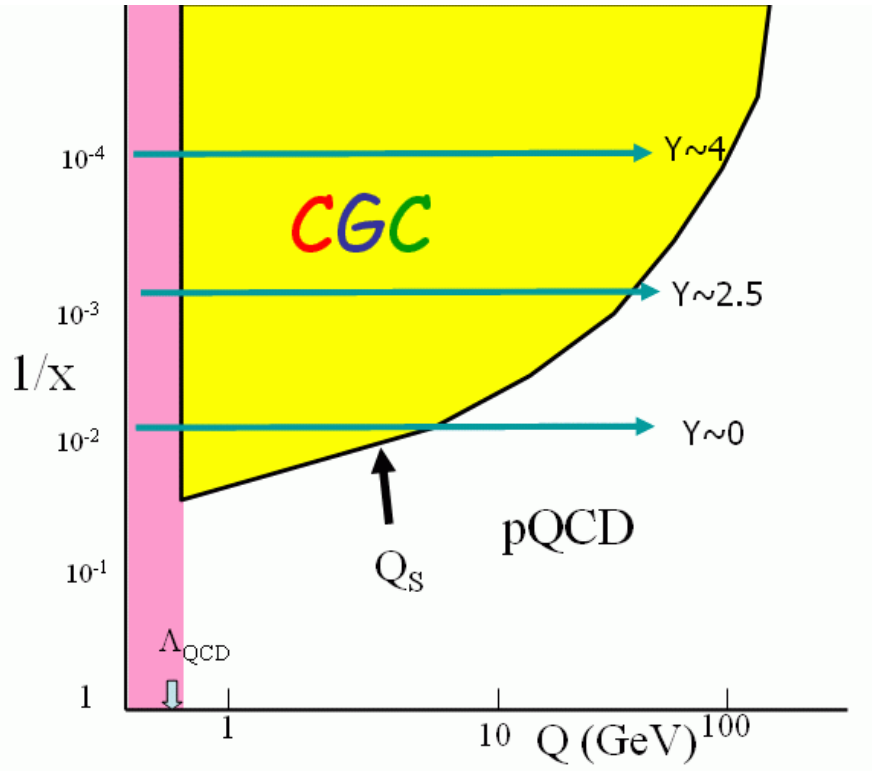

Figure 2.13: A schematic drawing of regions in the nucleus, showing the CGC region bordered by a line representing Q_S. Going forward in rapidity to regions covered by the NCC moves into the CGC region.

2.2.1.1 Contribution of the NCC

The NCC will be directly sensitive to the gluon structure function (or what is taken for a structure function in the CGC model) over a large region of x and Q^2 allowing measurements both inside and outside the saturation regions shown in Fig. 2.13. At midrapidity in central heavy ion collisions, there is a difference between the suppression of direct photons and hadrons (see Figure 2.6). This was a clear sign that the suppression was due primarily to final state interactions (the sQGP) and not due to the initial state (the CGC). By contrast, for central deuteron Gold (d+Au) collisions, neither hadrons nor direct photons, show suppression at midrapidity. As just mentioned, in the forward rapidity region, hadrons do show a suppression in d+Au collisions (see Fig. 2.14). One important test is to look at direct photons at forward rapidity. If the suppression is due to the initial state, that is the CGC, direct photons should also show a suppression. (See appendix C for a simulation of this effect.) By charting out the suppression versus centrality and rapidity the NCC will be able to map out the saturation regions shown in Fig. 2.13.

While we consider direct photon production to be the most important of the channels we will use to study saturation, it is one of many interesting channels in the forward rapidity regions that are sensitive to gluon distributions which are accessible to the NCC. These channels include (starting with our most important channel):

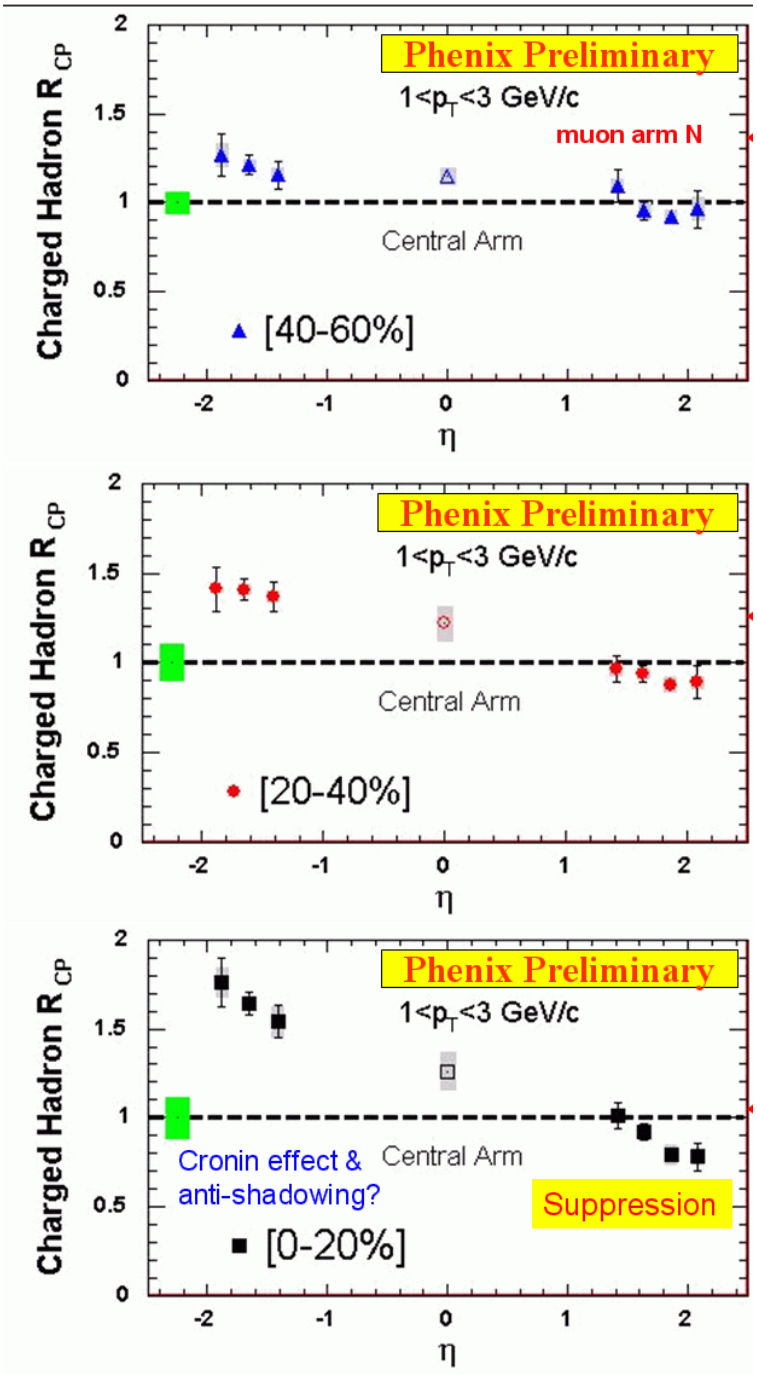

Figure 2.14: R_{CP} for charged hadrons as measured by the PHENIX muon arms for different centralities.

1. **Direct photon and jet production** – The inclusive production of direct photons at forward rapidity is sensitive to the gluon distribution. Moreover, a measurement of direct photon in coincidence with a jet would be very valuable since the kinematic variables of the gluons can be readily reconstructed. This channel is particularly important, since whatever the ultimate theory, the understanding of the gluon structure function in nuclei at low-x is a generic feature that is important to many models.

2. **Single hadron production** – Several hadrons can be readily detected by NCC via their decays to lepton/photon channels. The hadrons and their relevant decay channels include $\pi^0 \to \gamma\gamma$, $\eta \to \gamma\gamma$, $\omega \to \pi^0\gamma$, $\phi \to e^+e^-$, $J/\Psi \to e^+e^-$, $\Psi' \to e^+e^-$, $\chi_c \to \gamma J/\Psi$ followed by $J/\Psi \to e^+e^-$ and $\Upsilon \to e^+e^-$. The p+A data at forward rapidity region on the production of these particles would significantly enhance the physics reach of PHENIX, which is currently limited at forward rapidity to heavy quarkonium and punch through hadrons.

3. **Dihadron production** – The nosecone calorimeters will greatly extend the kinematic coverage for detecting dihadrons. A hadron such as π^0 or η could be detected in the NCC, while the other hadron could be measured in either the central EMCAL or the NCC. Energetic dihadrons would correspond to leading particles from dijet events and provide independent information on the gluon distributions in nuclei at small x [62]. Leading particles in jets give an estimate of the jet direction.

4. **Open charm and beauty production** – In conjunction with the Forward Silicon Tracker, the NCC can be used to measure D and B meson productions via their semileptonic decays ($D \to eX$ and $B \to eX$). These heavy-quark productions are sensitive to gluon distributions. Furthermore, the acceptance for detecting a pair of charmed particle through their semileptonic decays is significantly enhanced when the NCC is combined with the muon spectrometers ($D \to eX$ in coincidence with $D \to \mu X$).

5. **Production of monojets** – This is an intriguing signature of the CGC suggested by Kharzeev Levin, and McLerran [63]. Monojets reflect that fact that the recoiling medium (presumably a CGC) reacts as a coherent whole. Such a phenomenon would be manifest as a suppression of back-to-back jets (seen as correlated particles) even in p(d)+Acollisions at forward rapidities. Some recent theoretical work suggests that this possibility is unlikely even in the context of the CGC [64]. It remains for experiments to resolve this issue.

While experiments at the LHC will go to even higher energies and the lower x-data will lie almost entirely in the saturation region.

RHIC is at a unique energy range in which measurements made at mid-rapidity lie outside the saturation region, but measurement at forward radpities is in the saturation regime. Hence the onset of saturation can be studied at RHIC. This can be seen Figure 2.15. The top figure shows the suppression factor $R_{\rm dA}$ for 200 GeV d+Au collisions [14]. One can see that at p_T greater than 2 GeV/c, there is an absence of the suppression seen in Au+Au collisions, presumably since there is no sQGP formed. The lower plot shows the evolution of

$R_{\rm CP}$ as measured by the Brahms experiment as a function of η showing the suppression at more forward rapidities, consistent with the probing of lower x gluons in a CGC [65]. $R_{\rm CP}$ can be though of as a proxy for $R_{\rm dA}$, where peripheral d+Au collisions are used in place of p+p collisions as a normalization. As mentioned previously PHENIX has recently installed a set of lead tungstate crystals – the Muon Piston Calorimeter (MPC) [66, 67] with a rapidity coverage of $3<|\ \eta\ |<3.7$. While the MPC is too coarsely segmented to reconstruct π^0s in heavy ion collisions, it will allow PHENIX to cover $1<|\ \eta\ |<3.7$ in p(d)+Acollisions, such that we will be able to map out the region in which saturation begins.

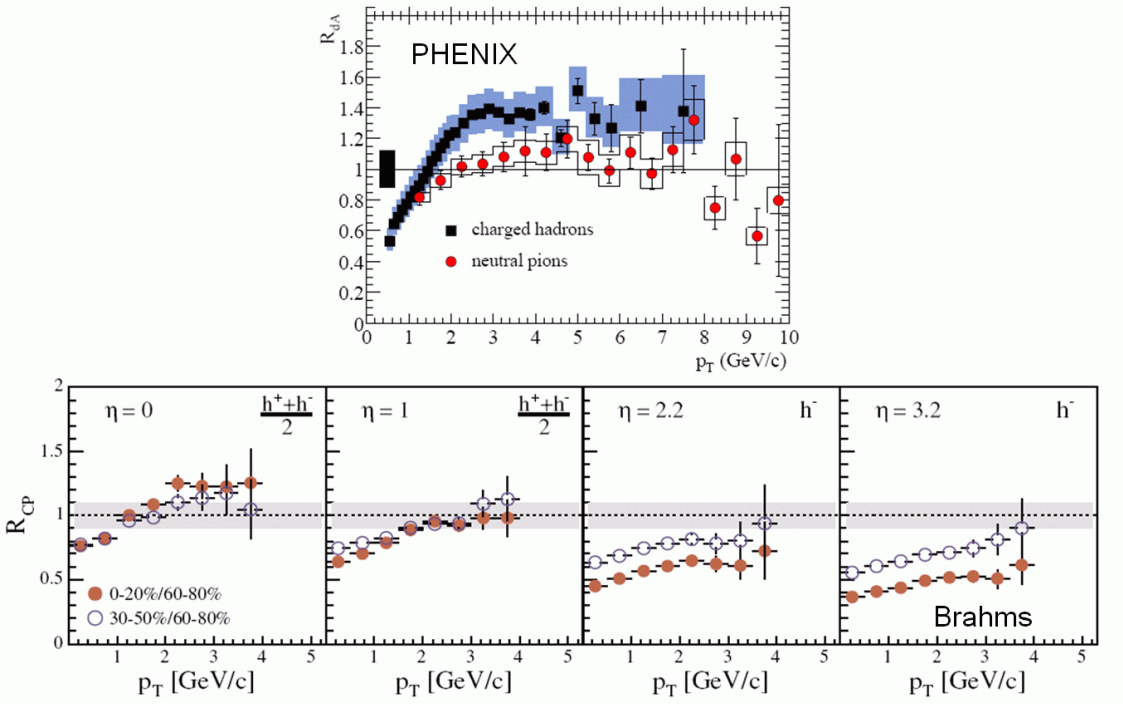

Figure 2.15: (Top) The suppression factor $R_{\rm dA}$ measured by PHENIX in minimum bias d+Au collisions at 200 GeV. (Bottom) The ratio $R_{\rm CP}$ for 200 GeV d+Au collisions as measured by the Brahms experiment. Centrality ranges used for the ratio are indicated in the plot.

2.2.2 Other Physics Topics

2.2.2.1 Antiquark distribution in nuclei at small x

In addition to the study of the CGC, other topics can also be addressed in p+A collisions in the forward rapidity region. In the past decade, nuclear shadowing at small x – has been very well characterized experimentally in DIS [68]. The experimental signature is that the DIS cross section ratio falls below unity for $x \leq 0.08$. Over the past decade there have been extensive theoretical studies of shadowing [69].

Shadowing is also expected in hadronic processes. To date, the only experimental evidence for shadowing in hadronic reactions is the reduction in the nuclear dependence seen in the Drell-Yan experiments E772 [70] and E866 [71]. The lowest x covered in these experiments is $x = 0.04$, just below the onset of the shadowing effect.

Shadowing in the $p + A$ Drell-Yan process is largely due to antiquarks in the nucleus, unlike in DIS, where valence quarks dominate for most of the explored region. Although shadowing effects are expected for antiquarks and gluons, there is no known requirement that they be identical [72] to those for quarks. There exists no experimental information on the antiquark shadowing at small x ($x < 0.04$). The coverage in x_2 will be significantly extended at RHIC. In particular, the lowest x_2 reachable at RHIC is around 10^{-3}, a factor of 40 lower than in E772. Therefore, antiquark shadowing can be well studied at PHENIX using the muon arms and the NCC to detect Drell-Yan events via the $\mu^+\mu^-$ and e^+e^- channels.

2.2.2.2 Cronin effect and x_F-scaling

Finally, the Cronin effect, first observed in fixed-target experiments, has also been seen in d+Au data at mid-rapidity. The mechanisms for the nuclear enhancement of large p_T events are still poorly understood. In particular, the dependencies of the Cronin effect on the hadron species and on the hadron rapidity (particularly the negative rapidity region) remain to be measured at RHIC energies. A universal x_F-scaling behavior [73] has been noted for hadron productions in p+A collisions. The ability to measure a variety of hadrons at the forward and backward rapidity region with the NCC would shed much light on the origin of the Cronin effect, as well as the validity of the x_F-scaling.

2.3 Spin Structure of the Nucleon

2.3.1 Physics Motivation

The nucleon is the only known stable state of quarks and gluons, the constituent which gives the atomic nucleus its mass, and therefore the mass of the visible matter which surrounds and comprises humanity. However, despite decades of study, a detailed understanding of the nucleon has eluded us. QCD, born whole as a lagrangian, describes a force which is too strong and complicated for the calculational techniques so far developed. Due to the small value of the strong coupling α_s at the high-energy scale, only in high-energy collisions has one been able to apply a quite sophisticated perturbation theory – asymptotic freedom. Recent advances in the computational power available to lattice theorists give hope that we are close to the beginning of a new era of non-perturbative QCD calculations for realistic comparisons to data.

Unpolarized deep inelastic lepton scattering and Drell-Yan experiments have provided most of the data from which we have formed our present understanding of nucleon structure at high energy, but our understanding is still primitive. The one-dimensional momentum fraction of the quarks on the light cone has been mapped out from relatively low values up to roughly 85% over a broad but unfortunately correlated range of resolution scales, i.e., Q^2.

Already this has revealed a rich phenomenology of structure which can be understood (over many orders of magnitude in Q^2), as the rapid fluctuation of color field energy into matter. Given the empirical partonic structure at one resolution scale, we now can reliably calculate the structure at some other scale, even if we cannot predict the structure *ab initio.*

Nonetheless, we still have little understanding of the physics or even the empirical distributions at large x. At very low x, we are hampered by the experimental correlation with low Q^2 (large distance scale) resolution in order to test our understanding of the observed quark-gluon fluctuations. New, precise electron scattering experiments, using both the electromagnetic and weak force, give us the spatial charge and magnetization distributions of quarks in the nucleon, but are difficult to connect to the 1-dimensional light-cone momentum distributions. The newly recognized use of exclusive reactions to determine generalized parton distributions will allow us to empirically connect these two regimes.

At high energy two fundamental aspects of the nucleon partonic structure are poorly determined by experiment. One is the nature of the quark and gluon motion transverse to the light-cone momentum direction. That is, the true 3D momentum distribution. The other is the nature of the nucleon spin. At present, we have a limited set of high-energy data which tell us that alignment of quarks along the light-cone momentum direction, as a function of x. These distributions are unknown at both high and very low x, and the resolution range in Q^2 explored is much narrower than in the unpolarized case. In fact, even these data are limited to the case where the nucleon spin is along the light-cone momentum direction. Until the advent of the RHIC polarized proton collider data, there was no precise and clearly interpretable data on the polarization of the gluons along the nucleon spin direction. The polarized lepton scattering experiments have made it clear that the quark spins only contribute about 30% to the nucleon spin. The gluons, which make up roughly 50% of the total (unpolarized) partonic momentum distribution, may be expected to carry a significant fraction of the nucleon spin, but this distribution is almost completely unknown at present. The RHIC spin program using longitudinally polarized protons promises to answer the question of the gluon spin contribution definitively. First measurements using the existing PHENIX spectrometer have already constrained the polarized gluon distribution. The NCC will allow PHENIX to make a significantly more detailed and precise investigation of the polarized gluon distribution over a much broader range of light-cone momentum fraction, and as a function of x.

Exploration of the polarization of quarks with the nucleon spin perpendicular to the light cone strongly tests our understanding of both transverse momentum and spin, which – at least in experiment – are intrinsically linked to each other. Ever since the observation of a large asymmetry in high-energy proton scattering, it has been clear that transverse effects would play an important role. These effects have been shown to persist even at RHIC energies, almost undiminished in size. Recent progress has been spurred by the observations of transverse asymmetries in lepton scattering from transversely polarized protons. First glimpses from these experiments have prompted intense theoretical activity, with new insight gained into the role of gauge links in calculating partonic field operators. We now have firm predictions relating the fragmentation process in lepton scattering to that in Drell-Yan. The possibility of a distribution arising from the correlation of spin and longitudinal momentum fraction is now widely accepted, and again there are early first glimpses from lepton

scattering. A natural explanation for this correlation is the existence of significant quark orbital angular momentum. In fact, orbital angular momentum is essentially unexplored experimentally at the partonic level. Exclusive reaction experiments, if able to determine the generalized parton distributions sufficiently well, can give us information only about the total angular momentum. Theoretically, there is now a much more thoroughly developed formalism to describe transverse measurements. The distributions are functions not only of momentum fraction and Q^2, but now transverse parton momentum k_T as well. While the dependence can be modeled, there is evidence that one can develop the transverse momentum distribution directly from perturbative QCD (pQCD). Thus, using transversely polarized protons at RHIC, one should be able to explore these new distributions in a regime where pQCD can be safely applied, for example using spin-dependent two-hadron correlation functions [74]. The addition of the NCC will clearly increase the PHENIX hadron acceptance at forward rapidity where the transverse effects are large. While extracting this new distributions is indeed more difficult, it is clear that this is a very active and developing area in high energy spin physics, and forward acceptance is required in order for PHENIX to be a major player in this area. If the longitudinal program finds that the gluon contribution to the nucleon spin is small, the transverse physics will be the only effective avenue at RHIC to study the partonic nature of orbital angular momentum.

Below we give a more detailed description of what we hope to learn from this program. In addition, we touch upon the role that the NCC may be able to play at 500 GeV in the study of the anti-quark production via W boson production.

2.3.2 Nucleon Structure: Gluon Polarization

Our present knowledge of the partonic structure of the nucleon is encoded in the so-called parton distribution functions (PDF) which depend on Bjorken x, the light-cone momentum fraction, and the momentum scale Q^2. Since the quarks are spin-1/2 particles, we can actually define two quark distributions, so-called helicity distributions, which describe the partons with the same or opposite helicity of that of a proton with helicity along the light cone direction. We will denote the polarized PDFs by $q_f^{\rightarrow}(x,Q^2)$ and $q_f^{\leftarrow}(x,Q^2)$, where f is the flavor of the quark or a gluon, however we will typically denote the unpolarized gluon distribution as $g(x,Q^2)$. In general, the unpolarized PDFs are then the sum of the helicity distributions: $q_f(x,Q^2) = q_f^{\rightarrow}(x,Q^2) + q_f^{\leftarrow}(x,Q^2)$. It is common to also define $\Delta q_f(x,Q^2) = q_f^{\rightarrow}(x,Q^2) - q_f^{\leftarrow}(x,Q^2)$.

The distributions for charged partons can be extracted directly from inclusive deep inelastic lepton scattering (DIS) experiments (in which only the scattered lepton is detected) if the Q^2 and energy ν of the photon are sufficiently high. Deep inelastic neutrino scattering allows one to separate quark and antiquark distributions, which the charged lepton scattering cannot distinguish. One can attempt to isolate the charged partons by flavor using so-called flavor tagging, where the known valence quark content of of hadrons is correlated with the flavor of the quark which absorbed the virtual photon. The detection of DIS lepton and a leading hadron, known as semi-inclusive DIS (SIDIS), necessarily depends on modeling of the fragmentation process. Lepton scattering from the gluon distribution is complicated, as

the gluon has no electromagnetic or weak charge, thus extraction is more model dependent. To date the most successful DIS program has been the analysis of dijets [75], which primarily (but not exclusively) derive from the photon-gluon fusion diagram. If there is insufficient energy to produce jets, one may attempt to substitute leading hadrons, but again, one is now more model dependent. In fact, global fits are regularly made by a number groups around the world, using not only the DIS data, but also data from hadron colliders and theoretical constraints derived from QCD sum rules [76, 77, 78].

The dependence of these functions on Q^2 can be directly related to the fluctuation of the gluons into quark-antiquark pairs and the radiation of gluons by quarks through the DGLAP equations, and this provides an means in principle to determine the polarized gluon distribution from the Q^2 evolution of the polarized quark distributions measured in DIS. The results of a recent analysis [79] of the available polarized DIS data (from SLAC, CERN, and DESY) are displayed in Fig. 2.16 (left panel) and show that the present uncertainties on ΔG are so large that even the sign of the gluon polarization is barely constrained; much more precise polarized DIS data, over a broader range in x and Q^2, would be necessary to provide better limits. The fact that the photon-quark asymmetry A_1 itself has only very small Q^2 dependence gives this type of analysis only a small "lever arm."

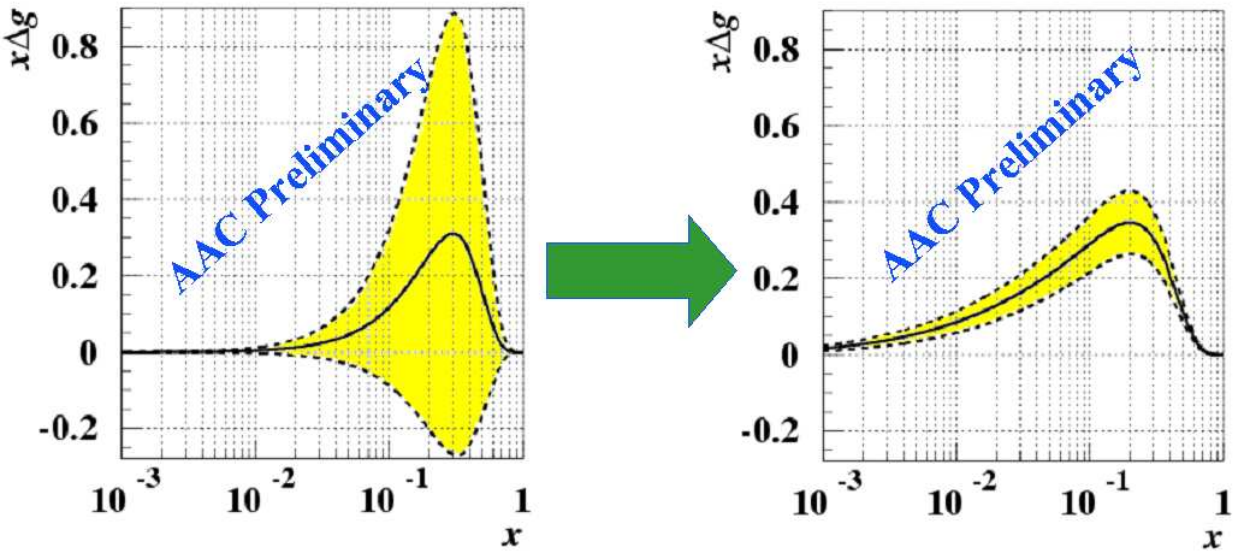

Figure 2.16: Polarized gluon distribution derived from NLO-QCD analysis of existing DIS data. The ranged limited by the dashed curves shows the range of gluon polarizations allowed by the data. The righ panel shows the effect of including the direct photon results anticipated from PHENIX data from one year at design luminosity in the same NLO-QCD global analysis.

The RHIC spin program will provide the first precise measurement of the x-dependence of polarized gluon distribution $\Delta g(x)$. The PHENIX experiment, which has excellent particle identification and high rate capabilities, is well suited to this measurement as we are sensitive to Δg through multiple channels and each of these channels has independent experimental

and theoretical uncertainties. Our main sensitivity is through inclusive hadron production, direct photon production, and heavy quark production.

In unpolarized $p+p$ experiments the gluon distribution function has been measured using single- and dijet events as well as from direct photon events. In both cases, jets or high p_t photons carry information directly from the underlying hard scattering process which can be calculated using pQCD. As the cross sections factorize into a hard scattering and a proton structure part a measurement determines the parton distribution functions connected to the processes, schematically

$$\sigma \sim q\left(x_A\right) \otimes G\left(x_B\right) \otimes \left|\mathcal{M}_{\mathrm{pQCD}}\right|^2$$

where x_A and x_B are the fraction of proton momentum carried by the partons entering the hard scattering process. The theoretical problems present in the interpretation of fixed-target data have been largely resolved for the collider environment [80, 81]. PHENIX's first direct γ cross-section measurement indicates that these calculations are valid at RHIC.

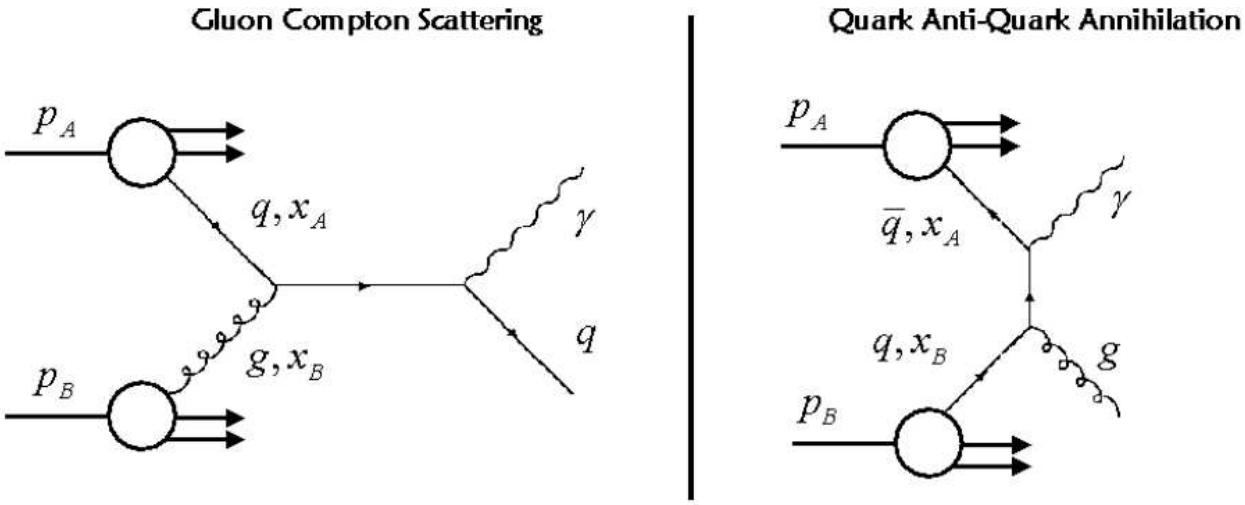

Figure 2.17: Direct photon production in the gluon Compton and quark anti-quark annihilation processes. The ratio of the two processes has been studied using PYTHIA and was found to be about 9:1.

Figure 2.17 shows that direct photon production at RHIC is dominated by quark-gluon Compton scattering. This ensures that the double spin asymmetries from direct photon production provide the cleanest theoretical access to the gluon polarization $\Delta g/g$.

Helicity conservation at the quark-gluon vertex gives rise to a double spin asymmetry

$$A_{LL} \sim \frac{\Delta q_f\left(x_A\right)}{q_f\left(x_A\right)} \otimes \frac{\Delta g\left(x_B\right)}{g\left(x_B\right)} \otimes a_{LL}^{qg \rightarrow q\gamma}$$

from which $\Delta g/g$ can be extracted. The hard scattering asymmetry $a_{LL}^{qg \rightarrow q\gamma}$ is calculated for the underlying quark-gluon Compton diagram with perturbative QCD. Background from the quark anti-quark annihilation process has been studied using the event generator PYTHIA and was found to be small.

The measurement of a double spin asymmetry for the case of detecting only the direct photon, typically as a function of p_T necessarily involves a convolution of over the momentum fractions of the colliding partons. The measurements are compared to QCD predictions based on different models of the gluon distribution. If one can also detect the opposing quark jet, then one may extract the shape of the distribution more directly, as the initial momentums fractions x_A and x_B are now known (though the flavors and gluon combinations remain unknown and are summed over). This essentially allows a much more direct determination of the polarized gluon distribution. Unfortunately, the limited acceptance, $\eta \leq |0.35|$, of the current PHENIX detector and the absence of hadronic calorimetry presently make it impossible for us to reconstruct jets.

The NCC allows us to greatly extend the x-range of PHENIX's measurement. and provide information on the x dependence of ΔG. The right panel of Fig. 2.16 displays the impact of PHENIX direct photon (inclusive) data on the range of allowed polarized gluon distributions. Despite the fact that the gluon polarization appears best constrained and falls off with decreasing x, the integral, ΔG, is dominated by contributions from $x < 0.1$ since this is the region where the gluons are most abundant [note that Δg is multiplied by x]. It is thus important to measure ΔG to values of x as far below 0.1 as feasible. Historically it is interesting to note that the quark spin crisis only arose when EMC [82] extended the measurement of quark spin contributions to low x. Extrapolations of the SLAC [83] data alone led to results for the quark spin contribution consistent with expectations from naive quark models. The additional geometric acceptance in the forward direction provided by the NCC extends the measurement of the gluon polarization from $0.01 < x < 0.3$ down to about $x = 0.001$. Further, in combination with the new PHENIX inner tracker detectors, which will allow crude jet-reconstruction in the PHENIX central arm, the calorimeter makes it possible to obtain a rough measurement of x on an event-by-event basis by detecting the away-side jet associated with the recoiling quark. The x measurement allows for a leading-order determination of ΔG as described above; this will be particularly valuable in constraining ΔG at low x and complimenting the NLO determination that will utilize the inclusive measurements. A rough jet measurement can also be made with the NCC, making possible measurements in which jets at forward rapidity can be used to constrain x on an event-by-event basis.

Overall, PHENIX is sensitive to Δg through multiple channels. The kinematic coverage for these various channels within PHENIX are shown in Fig. 2.18. The complementary measurements cover slightly different kinematic ranges, and most importantly provide alternative ways to the gluon polarization with different systematic and theoretical uncertainties. Figure 2.19 compares the x-Q^2 footprint of these channels to that of the DIS experiments.

2.3.3 Transverse Spin Physics

It is fair to say that much of the interest in high-energy spin physics can be traced to two surprising results: the observations of large lambda hyperon polarizations [84] and large single spin asymmetries in pion production from polarized nucleon-nucleon collisions [85]. The general expectation from pQCD at leading twist was that these asymmetries would be

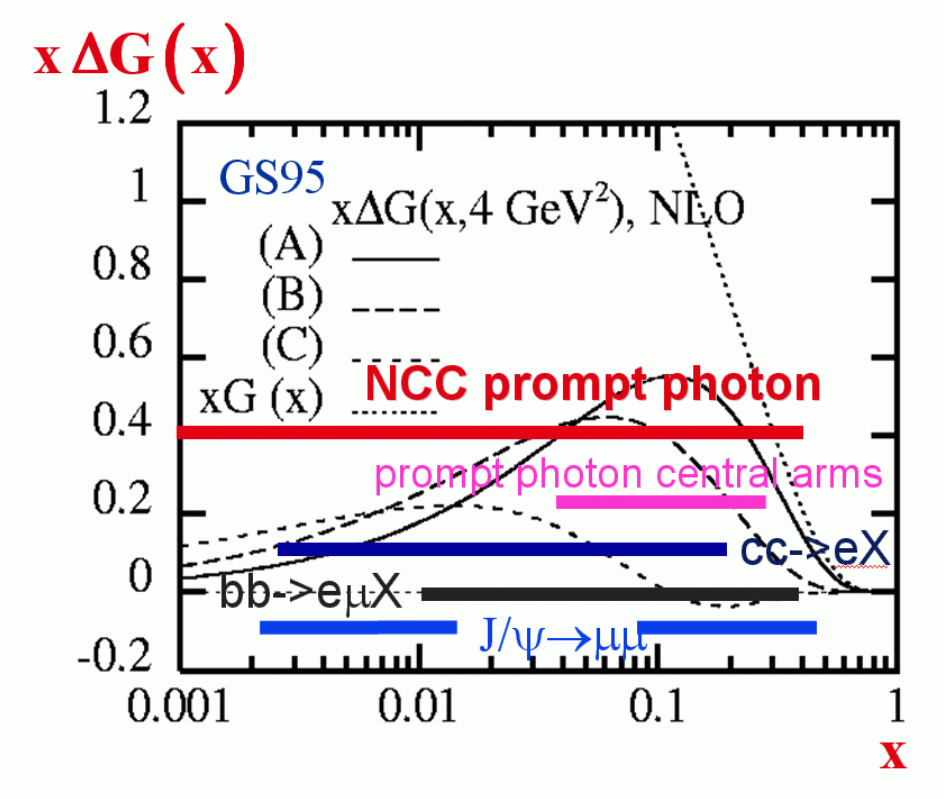

Figure 2.18: Kinematic coverage for PHENIX measurements that are sensitive to Δg. x_{Bj} range shown on-top parameterization of ΔG.

vanishingly small, due to the chiral dynamics of QCD It was therefore startling when E704 discovered very large asymmetries in pion production from polarized $p+p$ collisions at $\sqrt{s} =$ 20 GeV. The expectation that yet higher energy would cause these asymmetries to vanish, was again invalidated by the STAR discovery that these effects persisted to the much higher $\sqrt{s}$ of 200 GeV [86], since it was thought that any power corrections should be suppressed at higher energies, despite the fact that the predictions of unpolarized cross-sections agree very well with the data. The single spin asymmetries for π^0 mesons detected at STAR, as a function of Feynman x, are shown in Fig. 2.20. Given that the magnitude of asymmetries at high energies are typically only a few percent, these forward asymmetries are quite large. One might questions whether the forward reactions are too soft to apply perturbative QCD, but as shown in Fig. 2.21 the cross sections are well described by NLO pQCD [87] as well as by PYTHIA [88]. The existence of large single spin asymmetries at RHIC, along with the good theoretical understanding of the unpolarized cross-sections gives hope that transverse spin effects can be used as a tool to probe the transverse structure of protons.

There are three basic sources for the single spin asymmetries observed so far:

1. the existence of the Sivers function [89] which describes the correlation between the spin direction of the proton and the transverse momentum of the parton. Partons from the Sivers distribution fragment with the normal well-known fragmentation functions.

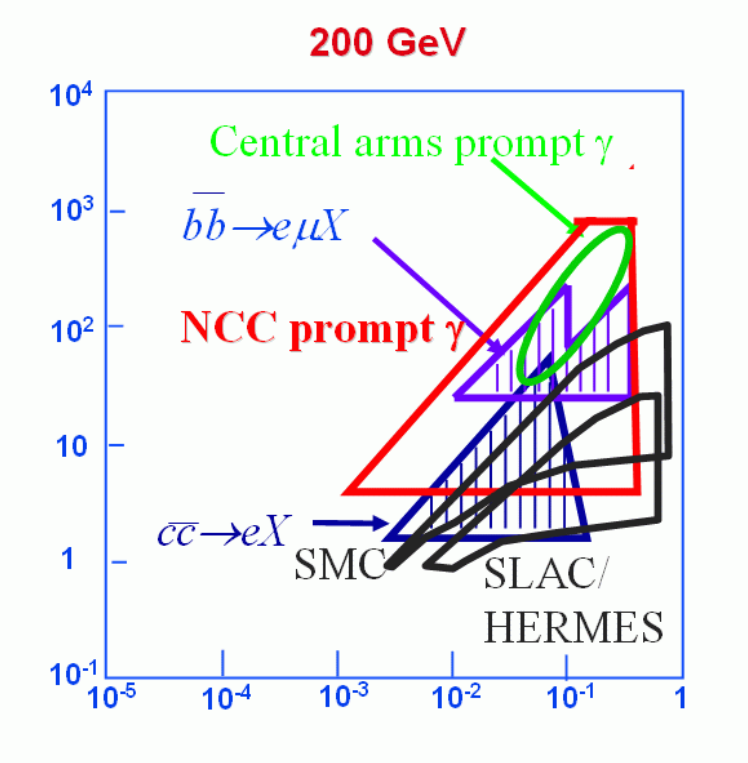

Figure 2.19: Range of x and Q^2 accessible by various DIS experiments compared to those accessible at PHENIX.

2. the existence of Collins fragmentation functions [90] which provide a correlation between the momentum of the final state particles with the direction of the initial parton spin. The initially transversely polarized quark are described by the transversity distribution [91]

3. Higher twist mechanisms in the initial and/or final state [92]

The recent observation of azimuthal asymmetries in semi-inclusive pion electroproduction at HERMES, from both longitudinally [93] and transversely polarized nucleon targets [94] along with the STAR results has sparked renewed and intense theoretical study of this physics. Using the transversely polarized target data, HERMES has made a preliminary extraction of the separate asymmetries arising from the Sivers mechanism and the Collins mechanism. Additional efforts at BELLE have made the first extraction [95] of a Collins fragmentation function for e^+e^- annihilation. Collins fragmentation functions of two pion states have also been proposed [96], and there is a preliminary observation once again at HERMES [97].

The existence of sizable Collins fragmentation functions will allow the extraction of the transversity distribution of the nucleon $\delta q_f(x)$. Just as in the case of Δq_f, the transversity is a measure of the alignment of quarks along or opposite the nucleon spin; the critical difference is that in the longitudinal case, the nucleon spin is along the light-cone direction, while in the

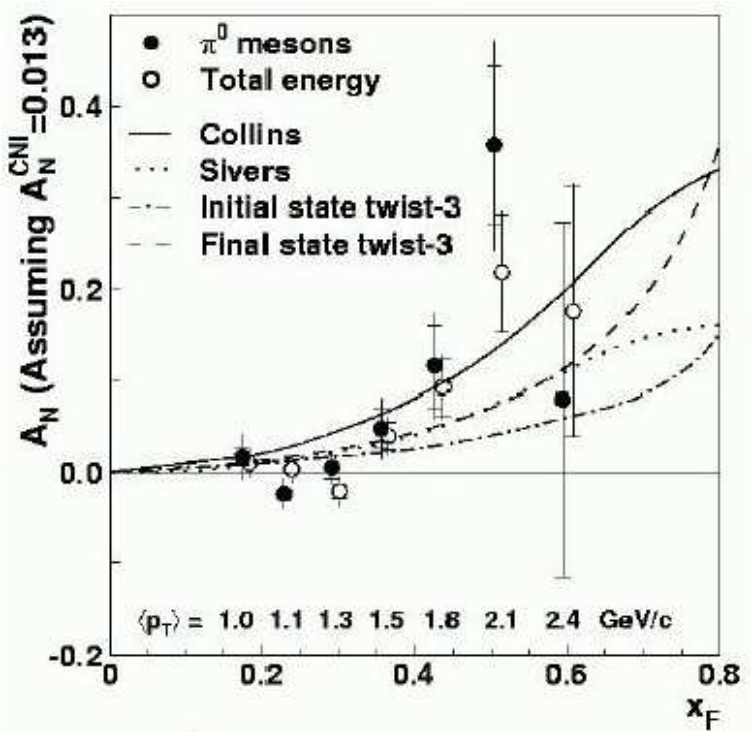

Figure 2.20: Single spin asymmetry from π^0 mesons at forward rapidity ($\langle\eta\rangle = 3.8$) as a function of Feynman x, measured at the STAR experiment from transversely polarized pp collisions at $\sqrt{s} = 200$ GeV [86].

transverse case, it is perpendicular to this direction. Non-relativistically, this is a trivially different distribution, but once on the light-cone these are "independent" distributions, of the same leading order (A common (correct) model of the of the quark-gluon structure could predict both distributions, but you cannot determine one distribution from the other). The transversity is interesting for a number of reasons. Besides completing our knowledge of the nucleon at leading order, it is notable for being mainly sensitive to the valence quark spin structure, and furthermore, its Q^2 evolution is quite different due to the lack of coupling between gluon transversity functions and quark transversity functions. These attributes provide an important test of our understanding of the longitudinal antiquark and gluon spin structure functions, especially with regard to relativistic effects.

The existence of Sivers distributions also provides an interesting window into the structure of the nucleon. This function accounts for the possibility that a parton's transverse momentum depends on the orientation of the nucleon spin. Orbital angular momentum of the quarks about the spin axis would naturally provide just such a correlation. At present, this connection is still not understood theoretically at the partonic level, but the distribution function itself is now generally accepted and well defined.

Effects in forward hadron production from transversely polarized pp collisions are somewhat more complicated than in polarized SIDIS, but as usual, the effects are typically larger and easier to study. Formally, there has been considerable progress in working out

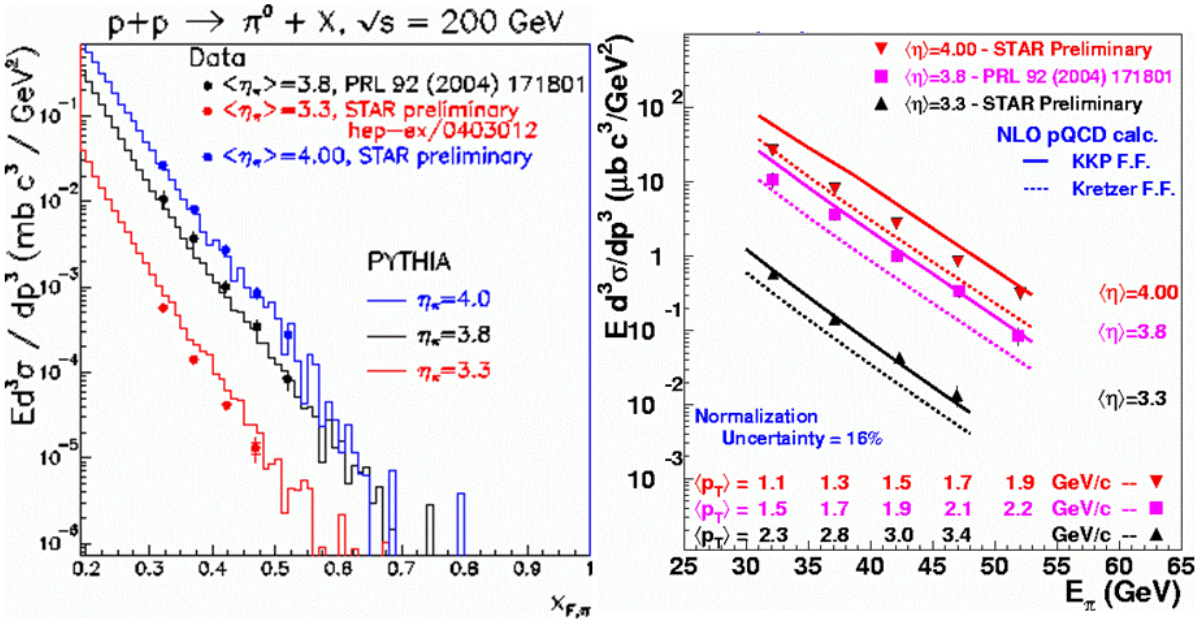

Figure 2.21: Forward inclusive π^0 cross sections measured at the STAR experiment from transversely polarized $p+p$ collisions at $\sqrt{s} = 200$ GeV [86]; the average pseudorapidity is $\langle\eta\rangle = 3.8$. In the left panel, these results are compared to predictions using PYTHIA [88] as a function of Feynman x; in the right panel they are compared to NLO pQCD [87] calculations as a function of the pion energy.

a formalism of possible distributions and fragmentation functions, for example as given in Refs. [98, 99, 100]. Predictions based on models of the nucleon are now being constrained by the data, but there is still much more data needed. As an example, the calculation of the asymmetry in pion production for the E704 experiment is shown in Fig. 2.22, taken from Ref. [100]. These models explore maximal bounds for the various distribution, but the point here is that the distributions in x_F are quite different, and they do not change much as a function of energy.

The NCC along with the recently installed Muon Piston Calorimeter(MPC) and the standard PHENIX central detectors will allow an important series of transverse spin measurements to be carried out at PHENIX. These should make it possible to separate out the mechanisms contributing to the forward inclusive asymmetry. Specifically, the Sivers distribution can be measured in the azimuthal asymmetry of back-to-back dihadrons or dijets,

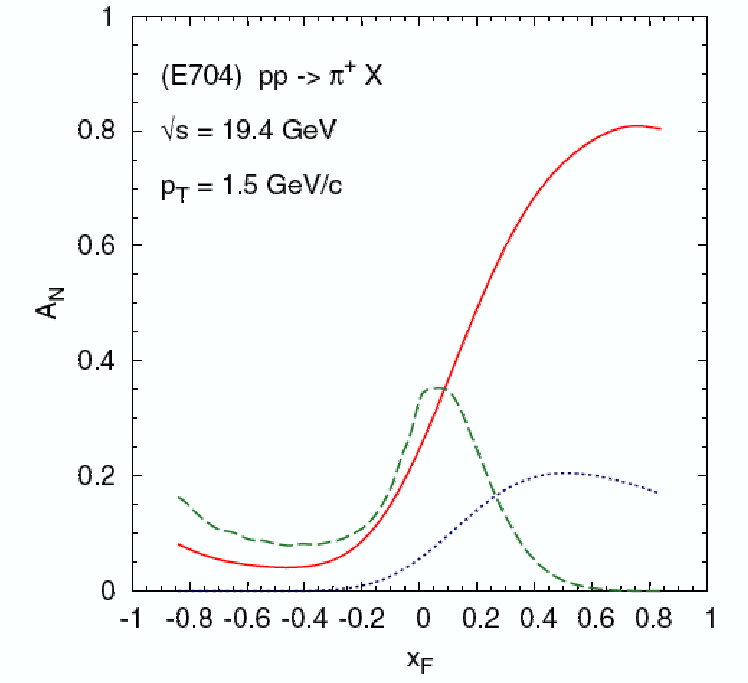

Figure 2.22: Different contributions to A_N, plotted as a function of x_F, for $p^{\uparrow}p \rightarrow \pi^+ X$ processes and E704 kinematics. The different lines correspond to solid line: quark Sivers mechanism alone; dashed line: gluon Sivers mechanism alone; dotted line: transversity $\otimes$ Collins. All other contributions are much smaller. Taken from Ref. [100].

where one of the hadrons is the forward π^0 or jet. In a second important measurement, the Sivers effect can be directly accessed through the observation of single spin asymmetries in inclusive jet production. Contributions from the Collins effect in the fragmentation of final state hadrons do not contribute to A_N^{jet} in this measurement as they average out in the integration over the azimuthal distribution of hadrons in the jet. The measurement of jet single spin asymmetries can be well carried out with the NCC by recording the jet yields for the different transverse proton spin orientations and constructing the relative luminosity corrected asymmetries between the yields for the up versus down proton spin orientations.

Transversity quark distributions can be measured through the observation of Collins fragmentation asymmetries within jets. The experimental observable in the NCC will be the azimuthal distribution of neutral pion yields around the jet axis reconstructed with the NCC. In this measurement, the azimuthal angle ϕ will be taken between the proton spin direction $\vec{S}_p$ and the transverse momentum $\vec{k}_T$ of the pion with respect to the jet axis, $\vec{p}_{jet}$. The azimuthal yield $N(\phi)$ depends on products of quark transversity distributions and Collins fragmentation functions. Schematically, we have

$$N(\phi) \sim N_0(1+A(z)\vec{S}_p[\vec{p}_{jet}\times\vec{k}_T]) = N_0(1+A(z)sin(\phi))A \sim \int_{x_1}\int_{x_2} dx_1 dx_2 \sum_q \delta q(x_1) G(x_2) H_1^{\perp}(z),$$

where $\delta q(x_1)$ are the quark transversity distributions for quarks of flavor q and $H_1^{\perp}(z)$ is the Collins fragmentation function for a final state pion which carries the momentum

fraction $z = p_\pi/p_{jet}$ of the total jet momentum p_{jet}. $G(x_2)$ is the spin averaged gluon distribution function, well known from inclusive deep inelastic lepton-nucleon scattering experiments. Recently, information on the Collins function $H_1^\perp(z)$ has become available from measurements of dihadron yields in jet-jet correlations in e^+e^- annihilation in Belle. With the experimental information on the gluon distributions and the Collins function available quark transversity distributions can be extracted through ab initio QCD analysis of the azimuthal neutral pion yields $N(\phi)$ measured in jets with the NCC.

The critical experimental performance parameters for this NCC measurement include the angular resolution for the direction of the jet axis and the resolution in the hadron momentum fraction z. Uncertainties in knowing the jet axis will dilute the amplitude of the azimuthal Collins asymmetry and uncertainties in measuring z will smear the spin analyzing power of the Collins function.

In general the exploration of transverse spin asymmetries in SIDIS and pp collisions requires one to investigate the dependence of the asymmetries on the p_T of the hadrons. This raises serious questions about the universality of the distribution and fragmentation functions which can be investigated in both experiment and theory. It has as well forced modelers to include the intrinsic k_T of the partons in some fashion. These issues are being addressed aggressively by theoretical community. In fact, if we hope to start developing a true three-dimensional understanding of the nucleon structure, this physics must be confronted and understood.

2.3.4 Nucleon Structure: Quark Polarization

While Δq has been fairly well measured, the anti-quark's contribution to Δq is not well-known. Some information has come recently from the polarized SIDIS measurement from the HERMES collaboration [101], using a flavor tagging analysis of the identified hadron asymmetries. The HERMES results on the sea polarization are accompanied by a substantial systematic error due to the observed small size of the asymmetry, and the weakness of the correlation from the flavor tagging. As usual, the weak interaction is of critical use in determining the sea quark distributions, allowing the PHENIX measurement to provide an important independent measurement of high precision and much higher Q^2, using an experimental approach completely different from that of HERMES.

The high-energy polarized proton beams at RHIC provide copious yields of W bosons, and the parity-violating nature of the weak interaction permits the extraction of light quark and anti-quark polarizations through measurements of longitudinal single spin asymmetries in W^+ and W^- production. Bourrely and Soffer first discussed this idea using QCD at leading order perturbation theory [102]. Recently Yuan and Nadolsky presented a calculation using modern resummation techniques in addition to an NLO calculation [103]. This work leads to a robust interpretation of the PHENIX quark polarization measurement in W production. In PHENIX, W production is characterized either by detecting high-energy electrons (or positrons) in the two central spectrometer arms or by reconstructing high-p_T muons in the two muon spectrometers. Due to their eight–times-larger acceptances, the PHENIX muon spectrometers will dominate the measurement statistically. The anticipated integrated

luminosity of 800 pb^{-1} will yield approximately 10^4 detected W^+ and W^- events. However, before a successful measurement can be carried out, the event selection electronics must be improved significantly. The muon trigger was designed for heavy ion running and low-luminosity proton collisions; an upgrade is required to record selectively energetic muons from W decay during the high-rate spin running. Recently, the NSF has awarded a collaboration within PHENIX funds of almost \$2M to carry out this upgrade using resistive plate chambers to be installed in each muon spectrometer.

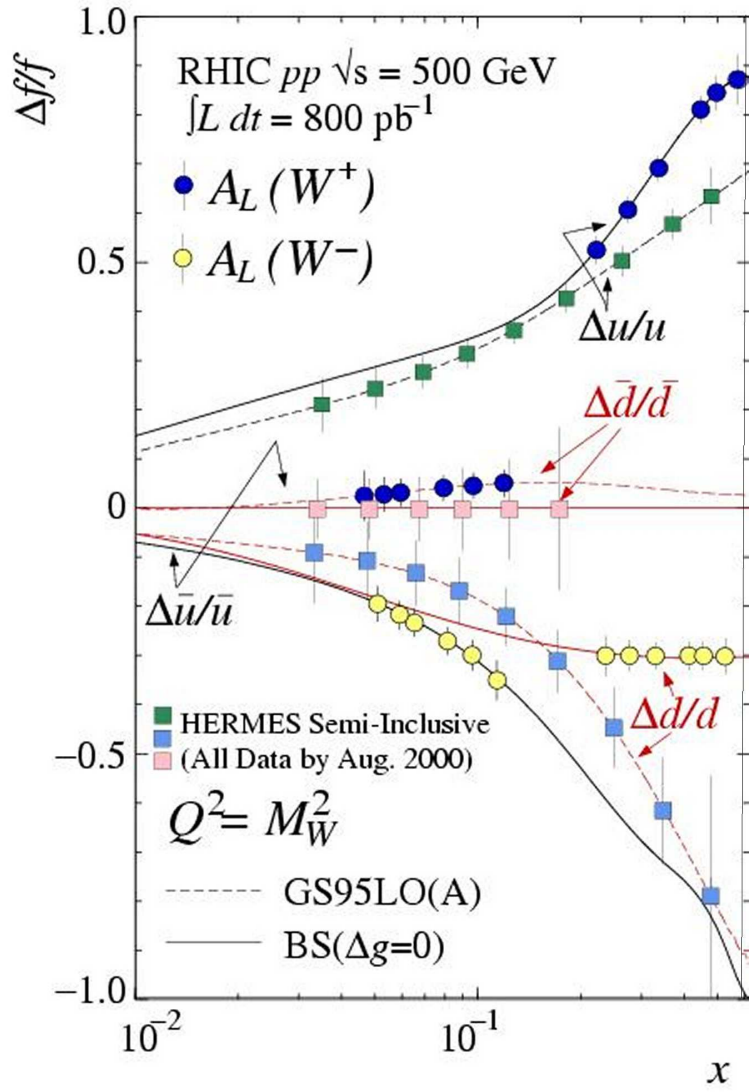

Figure 2.23: Simulation of measurements of light quark polarizations from W boson production at RHIC, compared with preliminary data from the HERMES experiment.

Figure 2.23 shows the projected precision of PHENIX on the light quark polarizations in the proton. Superimposed on the plot are projections of the accuracy achieved in preliminary results from HERMES (the figure has not yet been updated with the actual published final results). The anticipated measurements are highly complementary in nature. The HERMES

results feature more complete kinematic coverage, while the PHENIX results are of greater precision. The PHENIX technique distinguishes cleanly between the light quark flavors in a model-independent way, while the HERMES kaon asymmetries are able to probe the strange quark polarization. Finally, the systematic uncertainties in the two experiments are of completely different origin.

The measurement of the anti-quark spin contribution to the spin of the proton will be via the measurement of high p_T leptons coming from W's – a rather rare process. The NCC upgrade will extend this measurement both by allowing the detection of electrons and positrons in the forward region (though without charge determination) – in addition to the muons, and in reducing potential backgrounds. One of the potentially large backgrounds is the decay of low momentum pions and kaons within the magnet muon tracker volume, resulting in an apparently straight line (high momentum) trajectory. Such background events can be studied and, if necessary, reduced by requiring a separation between the lepton-detected by either the muon spectrometer (muons) or the calorimeter (electrons) and the jet, as detected by the calorimeter.

Chapter 3

Design of the NCC

3.1 Overview

The PHENIX[6, 104] detector shown in Fig. 3.1 is designed to perform a broad study of nucleus-nucleus (A+A), proton- or deuteron-nucleus (p+A or d+A), and proton-proton (p+p) collisions to investigate nuclear matter under extreme conditions and to measure spin dependent structure functions. It is a detector with unparalleled capabilities. Global detectors characterize the collisions, a pair of central spectrometers at mid rapidity measures electrons, hadrons, and photons, and a pair of forward spectrometers measure muons. Each central spectrometer is limited in geometric acceptance to about one steradian but has excellent particle identification. All currently existing subsystems have a proven energy and momentum resolution.

3.2 Upgrade Layout and NCC Configuration

The PHENIX Forward (Muon) spectrometers, illustrated in the bottom panel of Fig. 3.1, were built to identify and measure the momentum of muons. The ongoing upgrade to the PHENIX Forward Spectrometers includes an enhanced muon trigger able to impose cutoffs on the muon momenta, forward Si vertex detectors (FVTX) for measuring track impact parameters in the forward direction and Nosecone Calorimeters for measuring and identifying particles producing electromagnetic and hadronic showers and for measuring jets. The proposed upgrade to the forward spectrometers is shown diagrammatically in Fig. 3.2.

The space available in the PHENIX central region around the interaction region is constrained by the magnet poles to ± 60 cm along the beam line shared between the NCC and Forward and Central Silicon Vertex Trackers (FVTX,VTX). Two identical NCCs will be installed on the North and South magnet poles each occupying 19 cm of available real estate.

The space allocated to the new calorimeters is currently used by supplementary muon filters (copper nosecones, one for each magnet pole, which are brass disks 19 cm deep and $\sim$ 1m in diameter). The depth and geometry of new calorimeters is chosen to fit within the envelope of the existing copper nosecones. Fig. 3.3 is a 3D rendering of one of the PHENIX

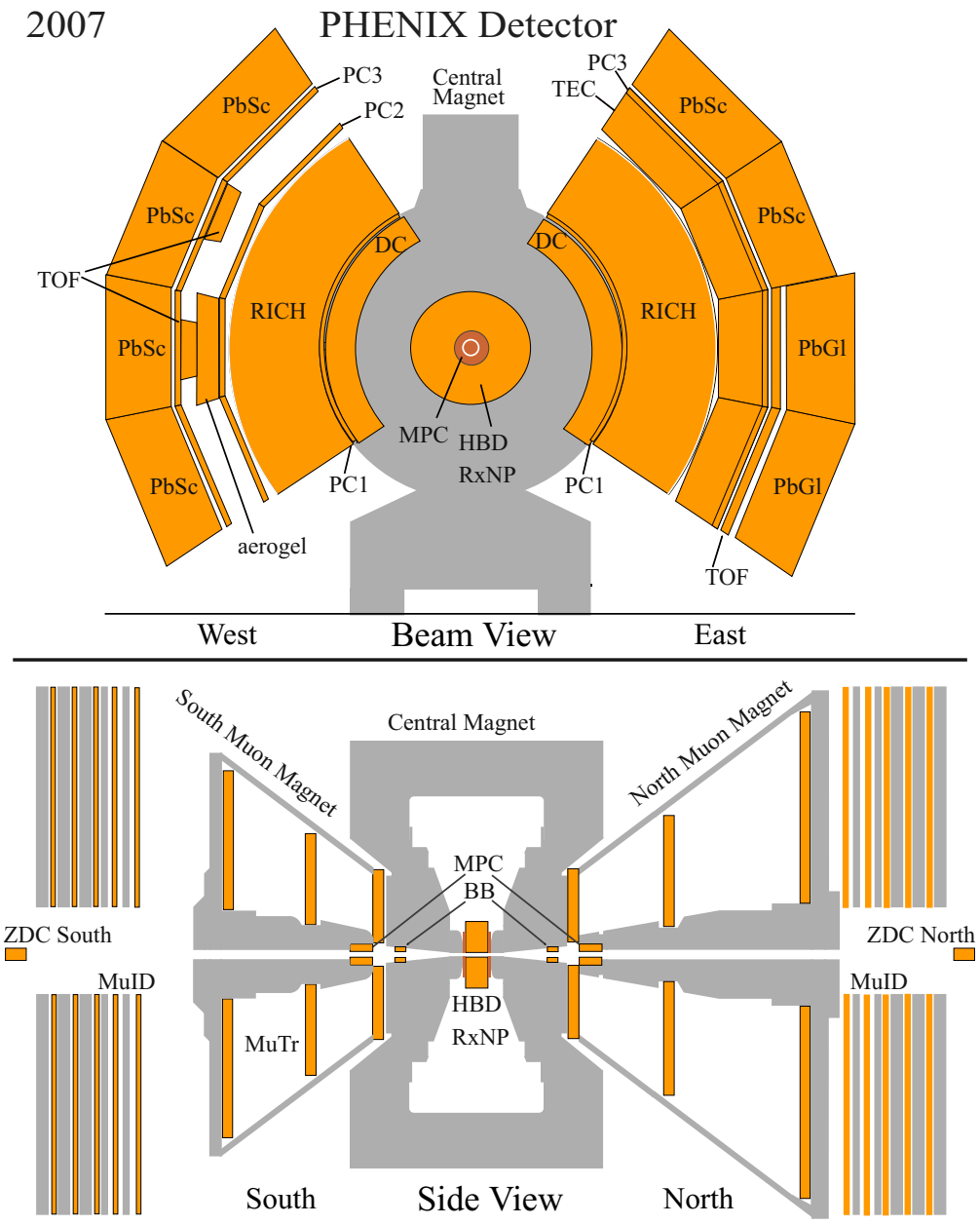

Figure 3.1: A beam view (top) and side view (bottom) of the PHENIX detector in its most recent configuration. BB-Beam-Beam trigger counters, DC-Drift Chambers, RICH - ring imaging Cerenkov counters, aerogel - Aerogel Cerenkov counters, PC-Pad Chambers, TEC - Time Expansion Chambers, PbSc/PbGl – Electromagnetic Calorimeters, MPC- Muon Piston Calorimeters, MuTr/MuId -Muon Tracking and Muon Identification, and ZDC - Zero Degree Calorimeters. The magnetic field is axial in the central region and the muon magnets generate a radial magnetic field.

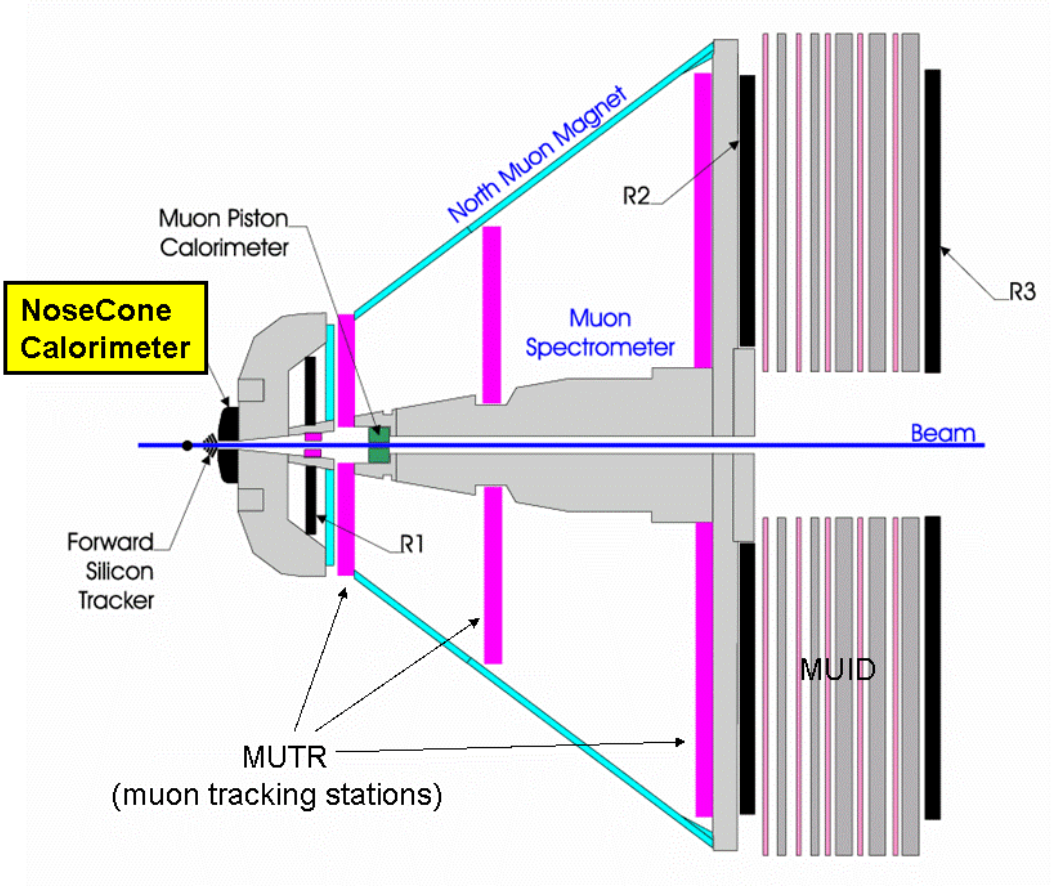

Figure 3.2: Schematic rendering of the upgraded PHENIX Forward Spectrometer.The present muon spectrometer includes the muon magnet, MUID for muon identification, MUTR for tracking, and the Muon Piston Calorimeter which covers rapidities between 3 and 4. The new components include the Nosecone Calorimeter, the Forward Silicon Tracker, and R1-R3, the new resistive plate chambers built for triggering on muons.

central magnet poles with the NCC and its analog readout crates installed. Shadowed regions indicate the PHENIX central arm acceptance which is free of any obstruction by calorimeter components. All upgrade components including NCC's are now fully implemented into PHENIX simulation chain so the upgrade influence on hit occupancy in central arms can be studied in details.

The NCC adds to PHENIX a feature that is unique at RHIC: The NCC leakage segment serves as a low resolution hadronic calorimeter allowing for a direct jet measurements. As a component of the PHENIX Forward Spectrometer, the NCC will add the following functionality:

1. precision measurements of individual electromagnetic showers;

2. γ/π^0 discrimination similar to the central PHENIX electromagnetic calorimeters;

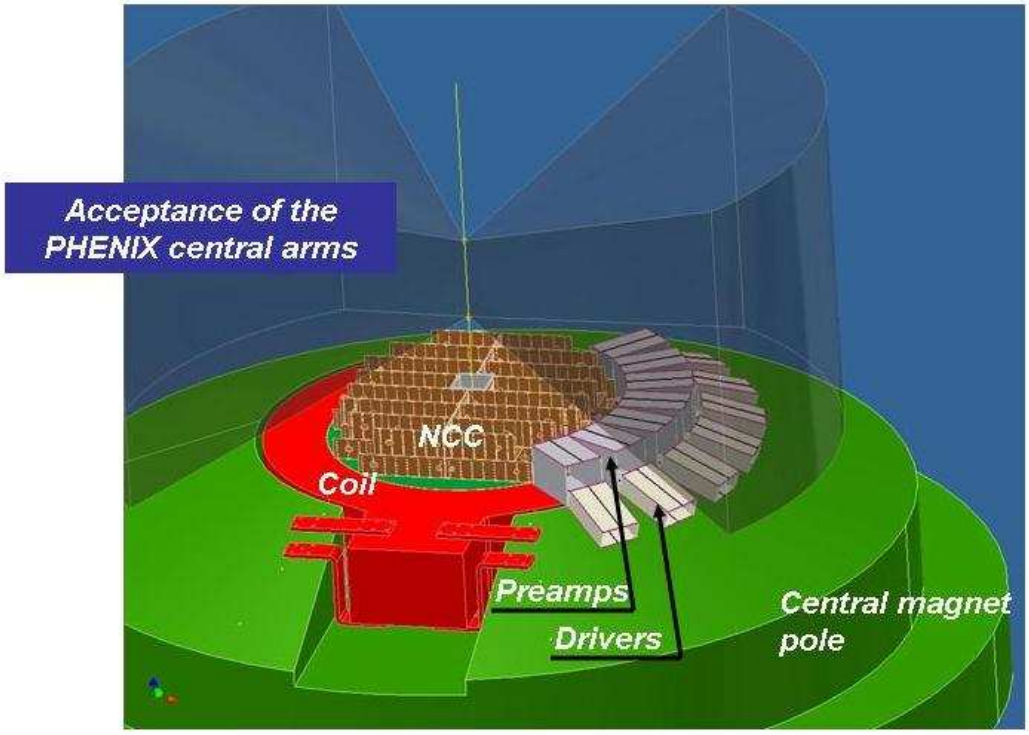

Figure 3.3: NCC assembled on the PHENIX Central Magnet pole. Shadowed is the acceptance of the Central Arms.

3. photon(electron)/hadron discrimination comparable to that in the central arms;

4. jet finding, jet energy, and impact position measurements giving jet vector measurements.

5. isolation cone energy measurements;

6. a fast trigger on local total energy deposition (jet), fast trigger on electromagnetic energy (direct photons and π^0's), qualifying primitives for fake muon rejection.

The NCC will also assist in matching muon trajectories identified in the forward muon spectrometer to tracks in the central vertexing system.

3.3 NCC Design considerations

The design requirements imposed on the detector by physics considerations are:

1. the ability to measure electromagnetic showers with a precision comparable to the sum of all systematic uncertainties characteristic of similar measurements with the PHENIX

central electromagnetic calorimeters in p+p, d+Au, and Au+Au collisions (π^0 effective mass resolution better than 20 MeV up to about 30 GeV/c),

2. the ability to discriminate between electromagnetic and hadronic showers in the calorimeter allowing extraction of the direct photon signal down to ∼5% of the π^0 yield,

3. the ability to reconstruct π^0's via effective mass measurements and shower shape analysis to the p_T extent allowed by the calorimeter acceptance and RHIC luminosity,

4. the ability to measure shower impact vectors with resolution sufficient for efficient matching to charged tracks reconstructed by the FVTX,

5. the ability to measure the total jet energy and jet angle with precision sufficient to reconstruct kinematics of photon-quark hard scattering resulting in γ-jet events with jets or direct photons in the forward direction,

6. the ability to measure energies inside the jet cone around high-p_T lepton candidates for isolation testing.

To satisfy these specifications we designed calorimeters which are a combination of highly segmented electromagnetic (EM1 and EM2) and more coarsely segmented hadronic (HAD) components supplemented by a high resolution preshower detector(PS) at a depth of $\sim 2X_0$ and a shower maximum detector (SM) at a depth of $\sim 9X_0$. The role of the PS is to count photon hits and measure hit-to-hit separation, while the role of the SM is to measure the decay asymmetry whenever the π^0 candidate is found in PS detector. The longitudinal structure of the calorimeter tower is sketched in Fig. 3.4.

The NCC's are located 41 cm from the nominal collision point on the north and south poles of the PHENIX central magnet and limited to a depth of 19 cm each. Building the instrumentation capable of attaining the required performance under the constraints of the PHENIX geometry requires the densest absorber material (tungsten) and the most versatile active media known to instrumentation in physics (silicon). Silicon provides for versatility of segmentation; tungsten has a small Moliere radius (9.3 mm) so the showers are very compact. Tungsten also has an excellent ratio of radiation and absorption lengths which is important for electromagnetic energy measurements in the presence of heavy hadronic background.

Compromises are required in order to achieve the goals of this proposal using available technology at a reasonable funding level. Based upon physics expectations, priority is given to particle identification (including resolving close showers), electromagnetic energy measurements and triggering capabilities.

The design of the NCC relies heavily on past experience in Si-W calorimetry[105, 106, 107]. Since even the upgraded PHENIX detector will have no means to measure particle momenta in the forward direction the NCC must be capable of discriminating between hadronic and electromagnetic activity as a stand alone device.

Such a calorimeter covering an area $\sim 0.7\ m^2$ with towers comparable in size to the Moliere radius will have ∼2500 silicon pixels per readout layer. A number of ongoing R&D projects

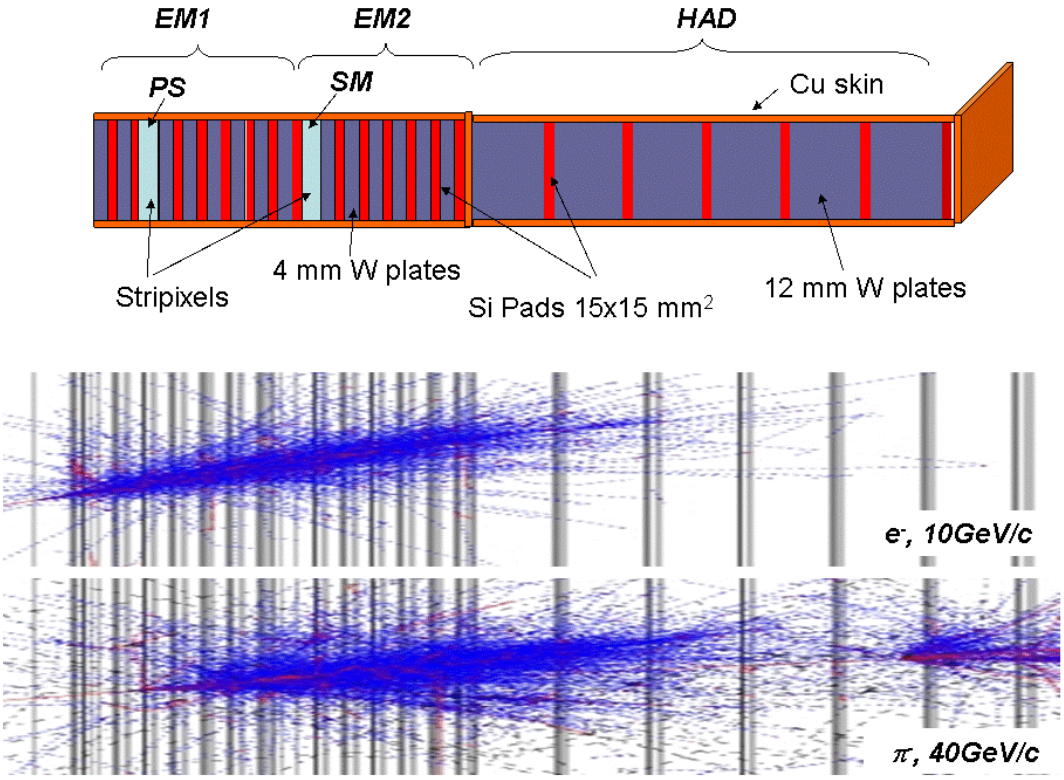

Figure 3.4: Longitudinal structure of a single calorimeter tower showing the locations of the three calorimetric segments, EM1, EM2, and HAD, and the high-resolution position preshower (PS) and shower-max (SM) detectors. Shown in the bottom panel are electromagnetic and hadronic showers due to a 10 GeV/c electron and 40 GeV/c charged pion.

aimed at building similar calorimeters for experiments at a future electron-positron linear collider are considering the option to digitize signals from every pixel in all sampling layers. The proposed solutions are in their preliminary stages and expensive. To reduce cost and complexity we decided on an option with pixels from a number of sequential silicon sampling layers ganged together and connected to the input of a single amplification/digitization circuit. Extensive SPICE simulations were done to simulate details of the ganged readout to insure that the electronics noise will never reach a level comparable with the intrinsic stochastic resolution of the device. The system prototype fully implementing all solutions presented in this document is currently under construction and will be tested in the test beam later this year.

The decision to gang the pixels allows one to reduce the number of channels in the detector by a factor of 6−7 (see below), and to use signal amplification solutions developed by the BNL Instrumentation Department for earlier projects[108]. This option also provides the solution to the problem of compatibility between a new detector and existing mechanical infrastructure in an efficient manner.

A calorimeter built to discriminate between electromagnetic and hadronic showers using shower shape measurements alone must have a hadronic (or leakage) segment to measure energies beyond the total absorption depth for electromagnetic showers. We propose to build relatively shallow electromagnetic segments of interleaved silicon and 4 mm tungsten plates, leaving as much space for the leakage section as possible. The hadronic segment (HAD) is structured following the pattern used in EM1 and EM2 (except the total absorber plate thickness is ∼12 mm). It will (1) assist in the energy measurements of photons at the extreme upper end of the spectrum, (2) serve as an effective electromagnetic/hadronic discriminator tool, and (3) guarantee low-grade hadronic energy measurements in the calorimeter. Thick hadronic plates will degrade the calorimeter energy resolution for electromagnetic shower measurements but the compromise is unavoidable to compensate for missing charged particle momentum measurements. The relative shallowness of the electromagnetic segments also serves to suppress the hadronic pile-up contribution to electromagnetic energy mostly contained in EM1 and EM2.

The W absorber plate thickness and the total depth of absorber in the calorimeter are also constrained by readout which is about 2.5 mm per layer divided up into 0.5 mm silicon, 1.6 mm of support components, and clearance gaps. The optimization process converged on a design with 20 pad-structured sampling layers and two layers of 2D position sensitive pixelated strips (preshower-PS and shower max-SM) which will serve as a very efficient photon-π^0 identifier able to discriminate between individual electromagnetic showers and overlapping photons from high momentum π^0's. Both longitudinal and lateral shower profiles can be measured in the device and are used in the particle identification.

Because of the limited total depth of a calorimeter we have chosen to apply the same lateral granularity throughout the whole depth of the calorimeter. We have chosen 4 mm W plates for the first two fine segments (EM1 and EM2) based upon the following simple considerations later tested in simulation:

- The radial shower profile, which is used to discriminate between single and multiple showers, has a pronounced central core surrounded by a halo. GEANT simulated profiles integrated over the shower depth in different materials are shown in the Fig. 3.5 where the distance from shower axis is in Moliere units (9.3 mm for pure W).

- W and Pb show nearly identical behavior with W being the material of choice if the resolving of showers is the primary goal. 50% of the shower energy is contained within a radius of 0.25 $R_{Moliere}$ which can be used as an estimate for the intrinsic limit for two-shower separation. Further improvements are constrained by fluctuations in the number of particles in the shower. Symmetrically decaying 30 GeV/c π^0's will have two photons in the calorimeter at a distance of about 5 mm (depending on the production kinematics) thus suggesting a Moliere radius of no larger than 20 mm for the NCC. Technology sets a lower limit to the thickness of readout layers (carrier boards, silicon sensors, interconnects, protection) of about 2.5 mm. To keep the Moliere radius below 20 mm the thickness of W plates in the fine sections of calorimeter must be equal to or above this value. Electromagnetic segments built of 4mm W + 2.5 mm readout sampling cells have a Moliere radius of $\tilde{1}4$ mm consistent with requirements derived

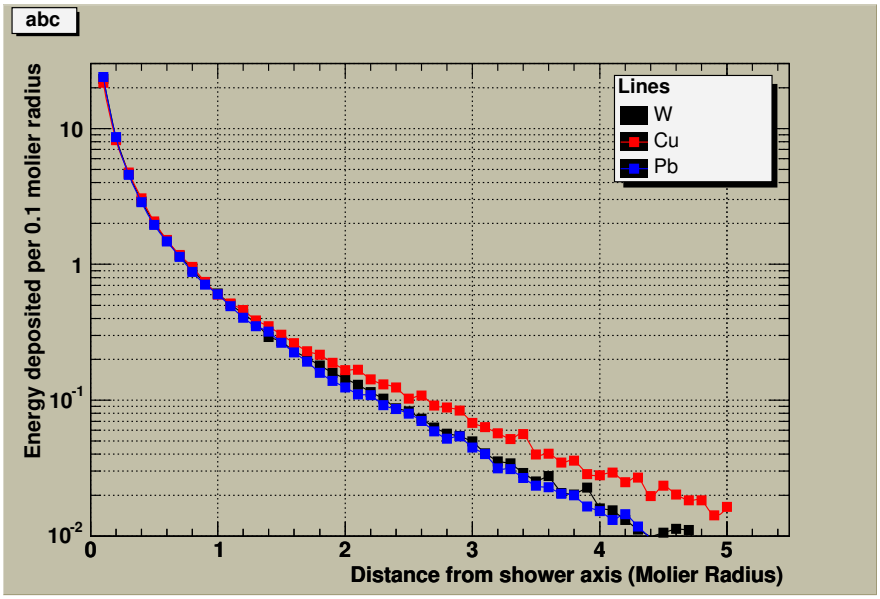

Figure 3.5: Radial profile of the electromagnetic showers in different materials(from simulation. The x-axis is in units of the Moliere radius.)

from the expected two-shower resolving power.

An infinitely deep calorimeter built of 4 mm W plates and 2.5 mm readout layers (525 μm Si sensors) will sample approximately 1.4% of energy deposited in the calorimeter by minimum ionizing particles resulting in the intrinsic limit to the energy resolution (sampling fluctuations only) of

$$\frac{\sigma}{E} \simeq \frac{20\%}{\sqrt{E}}.$$

A full GEANT simulation (discussed later) of the actual calorimeter, with thicker W plates in HAD gives an energy resolution of:

$$\frac{\Delta E}{E} = \frac{0.23}{\sqrt{E}} + 0.01$$

A short summary of the calorimeter design features is in the Table 3.1 (all counts are for a single calorimeter unit). The calorimeter will have a total depth seen by particles at normal incidence of $\sim$42 X_0 or 1.6 L_{abs}.

The remaining issue of concern for direct photons physics is the background of charged electrons impinging on NCC. The addition of the FVTX and Barrel VTX will provide tracking allowing for the differentiation of electrons and photons over most of the coverage of the NCC. At the highest $\eta > 2.2$ only statistical tools are available since this is outside the coverage of the FVTX.

Table 3.1: Nose Cone Calorimeter design features. All counts are for a single unit.

Parameter		Value	Comment
Distance from collision vertex		41 cm	
Radial coverage		50 cm	
Geometrical depth		$\sim$ 19 cm	
Absorber		W	42 X_0 or 1.6 L_{abs}
Readout		Si pads (15x15 mm^2) and pixilated strips (0.5x0.5 mm pixels grouped into 60 mm long strips)	
Calorimeter		EM1 and EM2 (14 sampling cells: 4mm W + 2.5 mm readout) longitudinally structured into two identical non-projective sections. HAD (6 sampling cells: 12 mm W + 2.5 mm readout)	
Preshower detector (PS)		StriPixel layer downstream of the first two EM sampling cells	
Shower max detector (SM)		StriPixel layer downstream of the first 9 EM sampling cells	
Sensors		calorimeter	3320 (14 x 160 + 6 x 180)
		PS and SM detectors	320 (2 x 160)
Channel count		calorimeter	8000
		PS and SM detectors	81920 (672 SVX4 chips)
Multiple scattering in NCC combined with Fe magnet pole		133 MeV	To compare with 106 MeV in the existing configuration with Cu Nosecone
Expected EM energy resolution		$23\%/\sqrt{E}$	
Expected jet energy resolution		$45\%/\sqrt{E}$	
Two showers resolved at	in calorimeter	3 cm	
	in preshower	2 mm	
	in shower max.	4 mm	

3.4 The Performance of the NCC

An extensive study of the present design including Monte-Carlo simulation and hardware R&D culminated in the construction and beam testing of a proof-of-principle detector prototype described in the Apendices. In our simulation effort the calorimeter as described above was simulated using GEANT to produce libraries of electromagnetic and hadronic showers and PYTHIA simulated events. The calorimeter was located 41 cm from the production vertex. The whole active area of the calorimeter was illuminated. The simulated data are integrated over impact angles 0 to 45 degrees.

3.4.1 Simulations - the optimization procedure

For the purposes of optimization the NCC 3D-model implemented in ACAD was converted into a GEANT3 model which is now part of both standalone and PISA based simulation chains. Unless explicitly specified, the results presented in this chapter are based upon a standalone GEANT simulation.

3.4.2 Containment, energy and position resolution

The depth and positions of calorimeter segments were optimized with respect to the shower profile to insure approximately equal energy sharing between EM1 and EM2 and a linear dependence of the energy deposited in the EM2 vs energy of the photon (see Fig. 3.6).

Most of the electromagnetic energy stays in the electromagnetic segments (EM1 and EM2) with a relatively low energy dependent leakage to the hadronic segment. The calibration coefficients used to convert energy in silicon into energies deposited in individual segments (sampling fractions) extracted from single electron simulation differ between segments and depend on the energy of the impinging electron.

A simple functional form was used to describe the behavior observed in the simulated data. When energy dependent calibration coefficients were applied, the calorimeter response was found to be linear to better than 1% (Fig. 3.6, right panel). The energy resolution for electrons averaged over NCC phase space is shown in Fig. 3.7.

The coarse structure of the hadronic segment contributes to degradation of stochastic term (23% compared to 20% prediction based upon the Wigmans compilation). It also results in a $\sim 1\%$ constant term - an important issue in statistical treatment of the data.

An estimate of the NCC position resolution based only upon energy measurements in calorimeter towers is presented in Fig. 3.8. The resolution is defined as the RMS of the distribution of the deviations of the particle impact point from the line connecting showers in calorimeter segments. Comparable lateral and longitudinal dimensions of the individual sub-towers in the electromagnetic and hadronic segments allow for independent position measurements in every segment and provide some degree of pointing capabilities. A very preliminary estimate of the calorimeter pointing resolution, which will be improved when proper treatment of the data from PS and SM detectors is established, is shown in the right panel in Fig. 3.8.

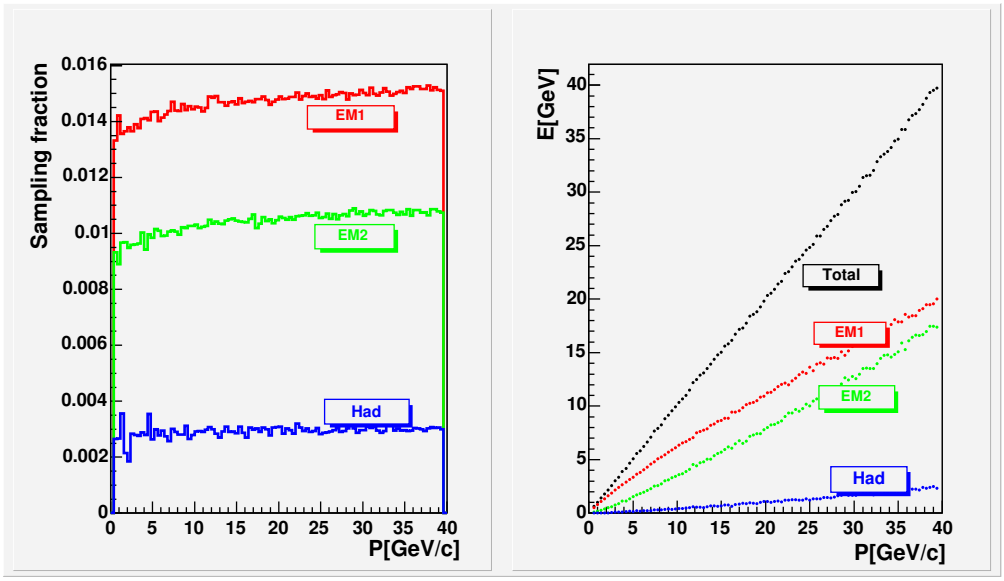

Figure 3.6: Left: Momentum dependence of the sampling faction in NCC segments; Right - energy measured in NCC segments and total energy in the NCC vs electron momentum.

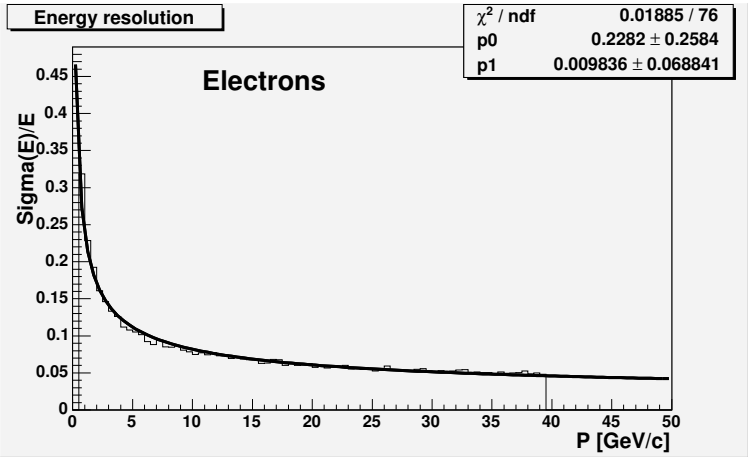

Figure 3.7: The momentum dependence of the intrinsic NCC electromagnetic energy resolution deduced from simulations. The fit is to an energy resolution function of the form $\frac{\Delta E}{E} = \frac{0.23}{\sqrt{E}} + 0.01$

As seen from Fig. 3.8, the position and pointing resolution computed applying currently implemented reconstruction algorithms only to energy measurements is ∼2.5 mm and ∼6 mrad, and it is nearly independent of electron momenta. It is interesting to note that similar values are computed for hadronic hits are not much different - a feature of predominantly large impact angles resulting in particle trajectories passing through at least two towers in a segment in most of the cases. Both position and angular resolution degrade by nearly ×2 for muons which never interact in the calorimeter.

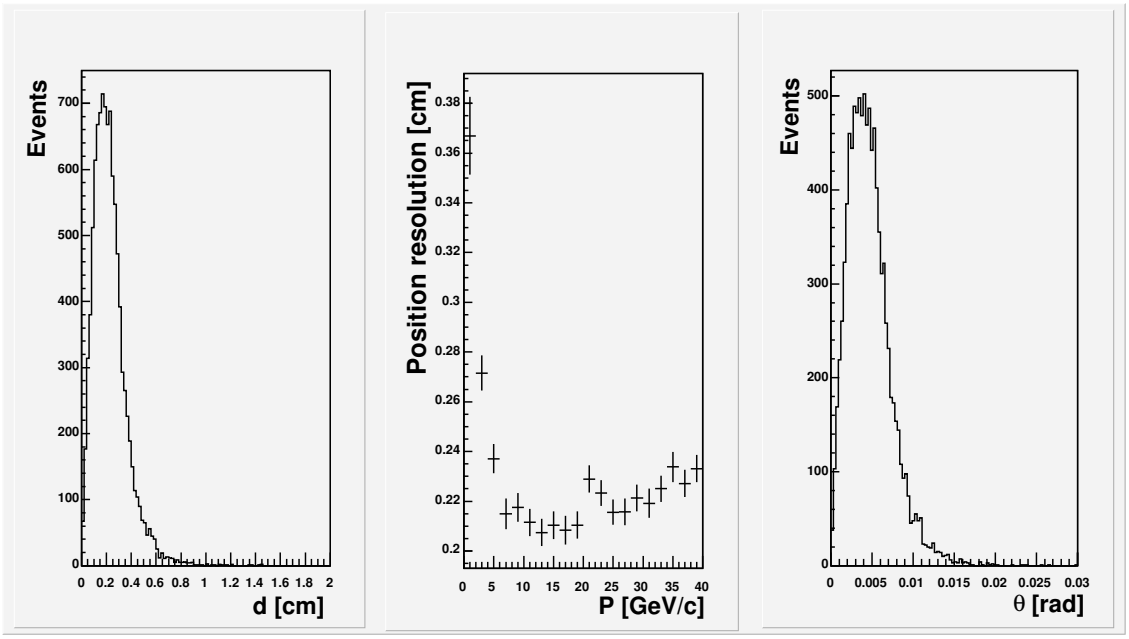

Figure 3.8: Left: radial distance between electron impact point and measured shower object; Center: the momentum dependence of the NCC position resolution (based upon energy sharing between towers only); Right: angle between impact vector and track vector measured in calorimeter.

3.4.3 Discrimination between hadronic and electromagnetic activity in NCC

At present, the rejection procedure used to test the NCC performance is entirely based upon shower shape measurements with calorimeter towers. Lateral shower shape analysis in position sensitive layers (PreShower and ShowerMax) will be added at a later stage and is expected to improve results. Electron events were used to compute average energy and variance in every segment. The results were parametrized using simple polynomial functions. Analysis algorithms implemented for the purposes of this proposal combine objects (tower clusters and strip clusters) reconstructed in NCC components into entities named tracks. The energy of the track is equal to the sum of the calibrated energies of contributing clusters. Its geometrical parameters are defined as an energy weighted average of vectors pointing from primary vertex to individual contributing objects. A χ^2 estimator quantifying the difference between track parameters and predictions based upon energy pattern parametrization was used to separate electromagnetic from non-electromagnetic showers. The χ^2 distributions for electron and pion (treated as electrons) tracks in the calorimeter is shown in Fig. 3.9.

A nice feature of the data presented in Fig. 3.9 is the nearly identical behavior of the electron χ^2 distributions based on longitudinal and transverse shower measurements which confirms the statistical validity of the underlying assumptions. A cut of $\chi^2 < 9$ was applied to the statistics of tracks due to charged hadrons impinging on the calorimeter to select those resulting in a pattern of energy in calorimeter segments consistent with an electron

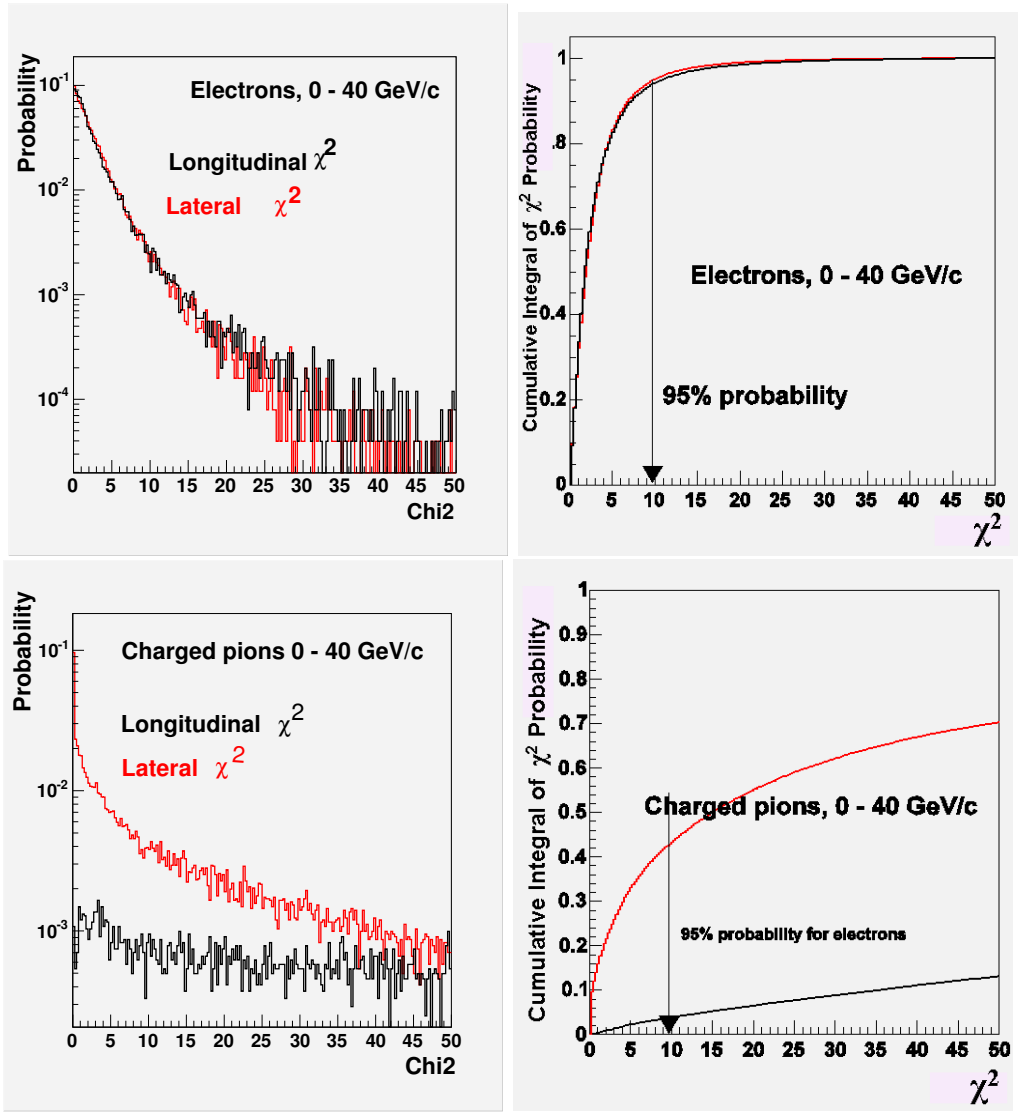

Figure 3.9: The χ^2 distributions for electrons (top) and pions (bottom) in the momentum range 0.5-40 GeV/c in NCC. The corresponding cumulative distributions are in the panels on the right. Currently, these distributions are based upon energy measurements only.

hypothesis. In the absence of independent momentum measurements for E/P matching, hadron rejection will depend on the momentum distributions of the particles we want to retain and particles we want to reject. PYTHIA was used to predict the momentum spectrum of charged particles in the calorimeter (black line in Fig. 3.10). The red line in the same figure is the energy spectrum of fake-electromagnetic showers due to charged pions. The ratio of the two histograms is the hadron suppression factor which must be applied to the spectrum of charged particles impinging on the NCC to compute its contribution to the inclusive spectrum of electromagnetic activity as seen in NCC.

Further insight into the discrimination capabilities of the NCC will require much more

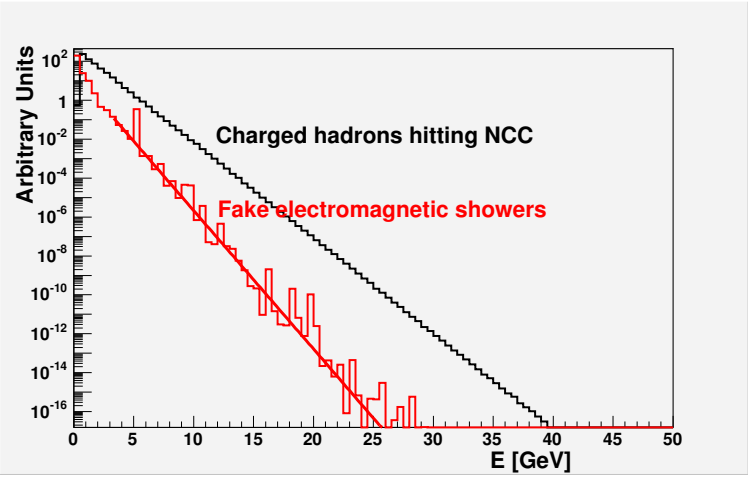

Figure 3.10: Top: Momentum distribution of hadrons impinging on NCC and energy distribution of residual tracks consistent with electromagnetic pattern after the χ^2 test described in the text. The current algorithm of hadron rejection is based upon longitudinally segmented energy measurements only.

involved simulation compared to what has been done so far. The results described in this section should improve once lateral shower development measured in the tower structured segments of calorimeter and in the PS and SM detectors are incorporated into the rejection algorithms.

Figure 3.11 illustrates the efficiency of this rejection algorithm when applied in the extraction of the inclusive photon spectrum in minimum bias events simulated with PYTHIA. The black and blue histograms are for all particles hitting the NCC (all hit energies and all track energies). The other two histograms are for photons only (all photon energies and energies of the photon tracks selected by χ^2 criteria). While the ratio of the first two histograms follow the general tendency observed in Fig. 3.10 the red and magenta lines for the photons are similar. This confirms that the NCC can actually be used to measure the forward inclusive production of photons. Of course corrections will have to be applied to correct for the photon particle identification probabilities. An accurate determination of these probabilities will take extensive work using actual calorimeter data from a prototype in a test beam.

The residual tracks due to hadrons will contribute up to 0.1% of the inclusive hadronic cross section to the photon spectra which must be processed through a subtraction procedure usually applied to extract direct photon production. The latter value is to be compared to the corresponding numbers for direct photons which can be estimated from PHENIX published data on π^0's and direct photon production in p+p interactions at 200 GeV [8,9]. In the p_T range above 6 GeV/c where direct photon yield exceeds 10% of the π^0 yield (∼5% of the charge hadron yield), fake electromagnetic showers in the proposed NCC are less than 1% of the total hadronic yield corresponding to a direct photon to fake electromagnetic showers ratio of better than 10%.

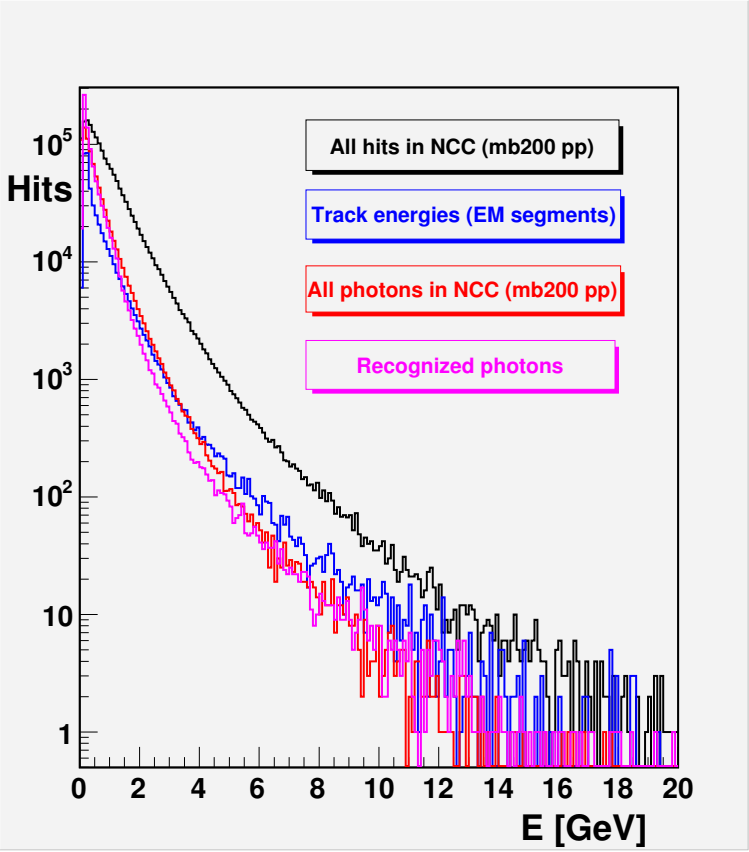

Figure 3.11: Energy distribution for all (black and blue) and photon (red and magenta) hits in minimum bias events in NCC. Black - energies from PYTHIA; blue - track energies in the NCC; red - photons from PYTHIA; magenta - identified photons.

3.4.4 Jet measurements

Jets are an important signature for hard scattering processes and a source of information on the kinematics of the underlying 2→2 scattering. PHENIX is currently studying physics involving jets in the final state mainly through inclusive measurements of high transverse momentum hadrons. Extracting information characterizing initial hard scattering and properties of partons involved in 2→2 hard process require knowledge of parton fragmentation properties which are modified by a QGP and are subject to large theoretical uncertainties. While the NCC does not have the depth in interaction lengths to completely contain the jet hadronic energy because of space constraints, information from the NCC can be used to obtain information about the energy and direction of jets. To estimate the NCCs capability to measure jets, a library of PYTHIA jets was simulated (stripping off all particles which could not be traced to the fragmenting hard scattered parton) and processed trough GEANT. Only jets due to a fragmenting parton pointing towards NCC were kept. In Fig. 3.12 the total energy of jet particles hitting the NCC is shown vs the energy of fragmenting parton (left panel). The energy measured in the NCC as function of jet energy delivered to the

NCC is shown in the central panel and the measured width of the jets (in units of NCC towers) is shown in the right panel. Jet width is peaked around 2 towers which means that a 4-tower radius cone around the center of the shower should contain a major fraction of the measured jet energy. (The characteristic width of an electromagnetic shower is ∼0.8 in the same units.)

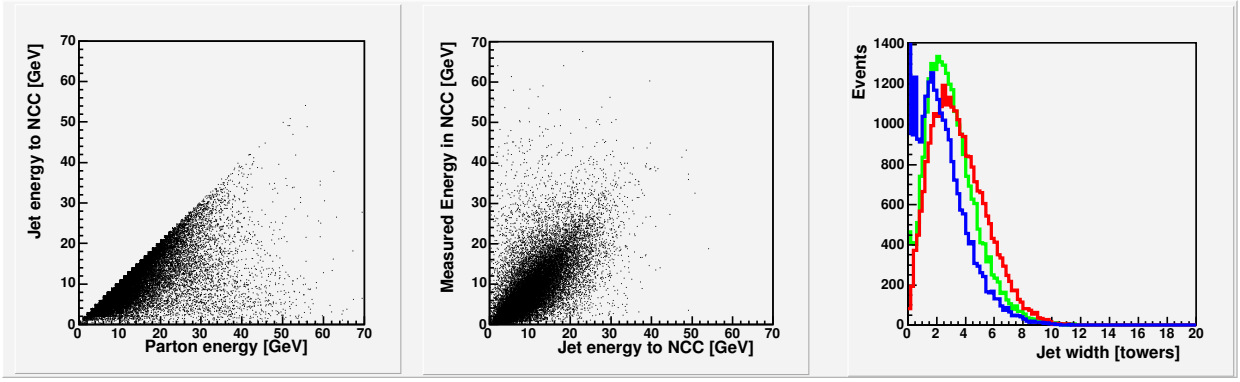

Figure 3.12: Left: Total energy of jet fragments hitting the NCC vs jet energy. (PYTHIA); Center: Measured jet energy vs energy of fragments in NCC; Right: Jet width measured in the NCC in units of NCC towers in EM1-red, EM2-green and HAD-blue.

The dependence of the measured jet energy on the total energy of jet-related particles reaching the NCC is also shown in the left panel of Fig. 3.13 as a profile histogram. The percentage of the total jet energy measured in the NCC (after an electron energy calibration) is ∼75% of the actual delivered jet energy (black points). Within the energy range studied this fraction stays constant. For comparison the energies inside jet cones of 4 - and 6-tower radii (currently considered as candidate jet-trigger granularities) are also shown. Further study involving actual jet reconstruction algorithms is required to chose between different options. In general measurements of the total jet energy (or 4-momentum) are not required to reconstruct hard scattering kinematics in photon-jet events if the direct photon parameters are measured. What is of importance is the ability to trigger on a jet, identify the jet and measure its direction. The distribution of the angular difference between the sum of fragment vectors inside the NCC aperture and the tower energy weighted center of gravity for all hits in the NCC is shown in the right panel in Fig. 3.13 (black histogram). The characteristic misalignment value is ∼20 mrad but extends to a larger values reflecting fluctuations in numbers and energies deposited by stable hadrons from the jet core. For comparison the angular mismeasurement of the fragmenting PYTHIA parton using the vector sum of particle momenta is also shown (red histogram). The simulation was done with initial and final state radiation enabled; the default value of k_T was chosen for this simulation. It is interesting to note that effects due to finite calorimeter resolution and QCD radiation (as described in PYTHIA) are of a similar magnitude.

The fluctuations of measured jet energy normalized to the total measured jet energy is shown in Fig. 3.14 as a function of total energy of all fragments hitting NCC. The NCC measures jet energies with nearly constant RMS∼40% dominated by fluctuations in the

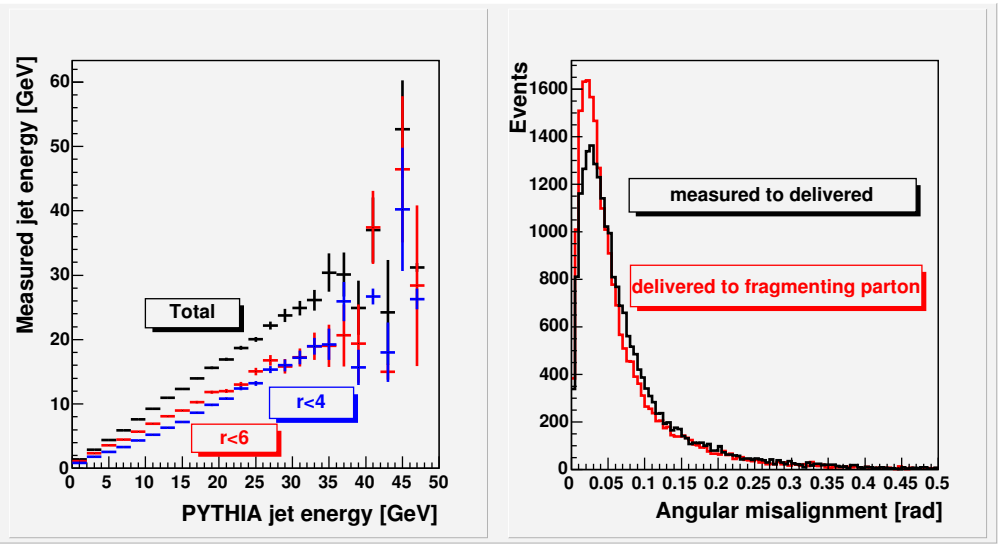

Figure 3.13: Left: total measured jet energy and energies inside 4- and 6-tower radii jet cones vs total energy of jet related particles inside the NCC aperture; Right: angular mismeasurement of the vector sum of jet particles in the NCC aperture using the energy weighted hit gravity center in the NCC (black line). The angular mismeasurement of the fragmenting parton using the vector sum of the jet particles is also shown (red line).

number of fragments and hadronic leakage. Resolution defined as an RMS of the energy seen in EM segments (where the role of hadronic fluctuations should be reduced) is shown in the same figure for comparison. Limiting measurements to EM-segments only is unlikely to improve energy resolution for jet-related measurements.

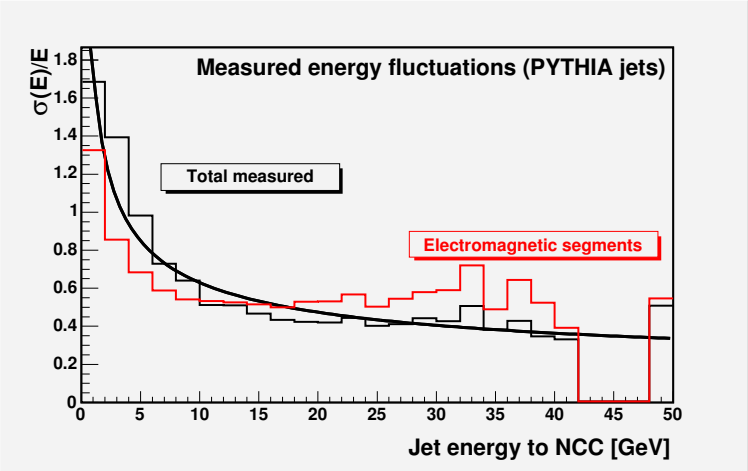

Figure 3.14: The relative RMS of the measured total and electromagnetic jet energies. The fit is to an energy resolution for jets of about $\frac{40\%}{\sqrt{E}}$

3.4.5 Muons in the NCC: Reconstruction and Rejection

The distribution of energies left in the NCC by minimum ionizing particles (MIPS) of up to 40 GeV/c momenta is shown in the left top corner of Fig. 3.15. It peaks at ∼.6 GeV with contributions peaking at 0.14 GeV, 0.12 GeV and 0.34 GeV in the EM1, EM2, and HAD segments, respectively. The NCC readout (note that all layers in each segment are ganged together) is designed to measure energies per tower up to 50 GeV (using the electron calibration) with ∼13.5 bit resolution (i.e. least bit of ∼5 MeV) and a noise contribution well below a single bit. A typical MIP signal will be seen around channel 30 in every calorimeter segment giving a good signal to noise separation for MIP signals. The muon energy pattern deposited in the calorimeter is different from both electromagnetic and hadronic showers. It typically shows a smaller number of towers and a very simple longitudinal profile. A library of muons in the NCC was used to define a χ^2 estimator based upon values and RMS of energies in segments, tower multiplicities in muon clusters and an estimated position resolution (see Fig. 3.15 top right). A very preliminary χ^2 distribution is shown in Fig. 3.15 lower left panel. Cumulative integrals of the χ^2 distributions are shown for samples of muon and pion tracks in the lower right panel. It is very encouraging to see that in a segmented calorimeter even a very coarse implementation of χ^2 estimator for muons already allows one to substantially reduce hadronic background.

A rejection procedure based on the χ^2 estimator as described above was applied to test the NCC effectiveness for suppressing fake muons where decays of low momentum punch-through hadrons are mis-identified as muons by the muon spectrometer. In general hits from fake muons will be distributed over the NCC aperture following the angular distribution of particles in minimum bias events. Testing the probability for a random hit in NCC to find an associated track with characteristics resembling a MIP was done by flipping momentum vectors of hadrons in minimum bias PYTHIA events around the collision point and comparing them to the pattern seen in NCC in the opposite hemisphere. The radial distributions for all tested hits and for those passing the filter are shown in Fig. 3.16.

The algorithm has a rejection factor for fake muons of a factor of ∼50 at angles near the beam pipe and improves at larger radii as expected since the occupancy is lower. This capability to reduce the background of fake muons, can be used in conjuntion with more the FVTX and cuts in the muon spectrumeter to reach the ncessary level needed for a variety of physics topics including the W-boson for spin measurements, high momentum muons for heavy quarks measurements, and quarkonium states decaying into dimuons.

3.4.6 π^0 reconstruction

The basis of much of the physics to be done by the NCC physics is related to the photon/π^0 measurements. For heavy ion collisions, correlated photon-jet events are of particular importance, in which the final state results from the Compton scattering of a low-x gluon on a quark - the photon gives us a calibration of the energy and the transverse momentum of the gluon. The background to this process is the double-jet final state with one jet fragmenting into a leading π^0 faking a single photon due to shower overlaps. Given the characteristic slope of the shower core ∼0.2 $R_{Moliere}$, the clear separation of the maxima due to two photons

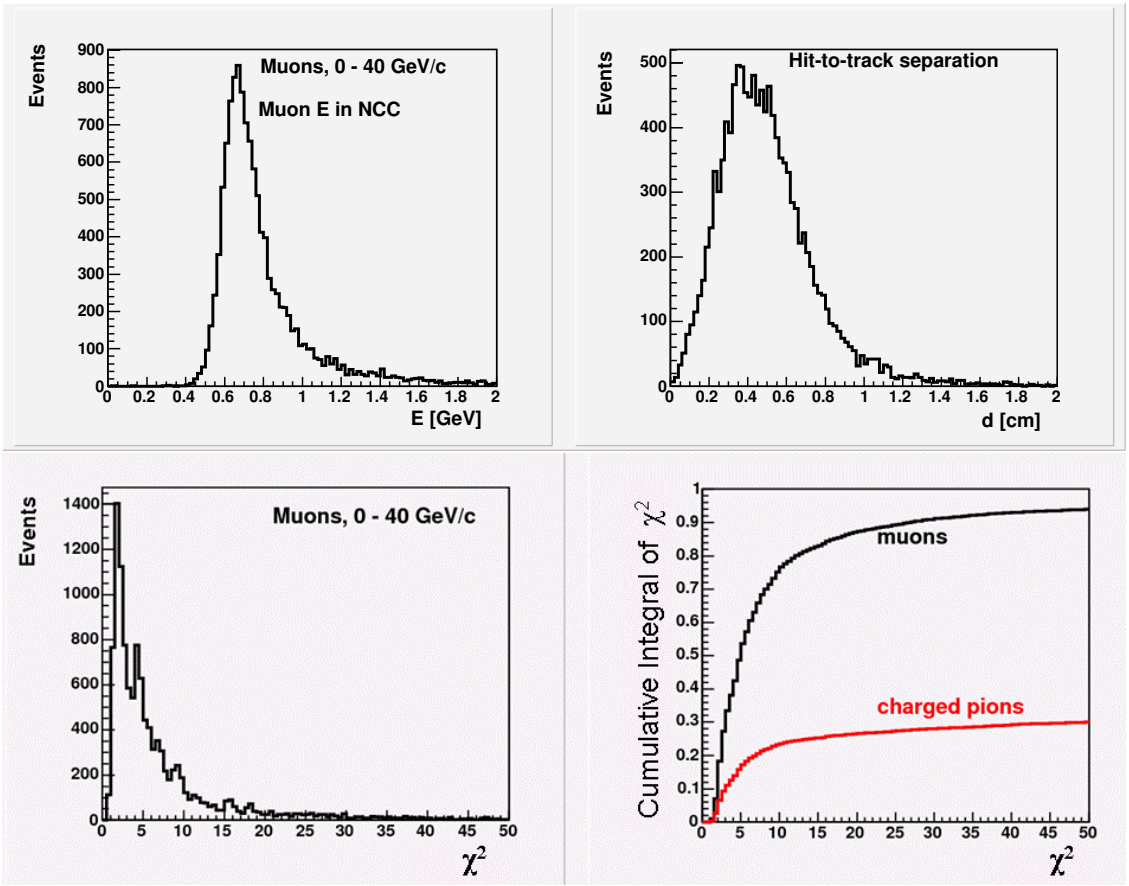

Figure 3.15: Base data used to extract fitting primitives for muons passing through NCC. Energy deposited by muons in the NCC (upper left); Distances of fitted track and hit in pads (upper right); χ^2 distribution, where the χ^2 estimator is dependent on energies and positions deposited in the NCC (lower left); cumulative integral of the χ^2 for muons and charged pions (lower right).

with close energies in a detector built of composite material with Moliere radius $R_{Moliere}$ ~18 mm should be possible down to a similar value of $\Delta \sim 0.2 R_{Moliere}$.

The problem arises when attempting to prove that observed maxima are due to independent showers and not to shower fluctuations. The separation is small compared to the average shower radius at the same energy to make meaningful quantitative tests based on lateral shower shape measurements. The following strategy is adopted for the NCC to deal with fluctuations. We are installing two layers of identical 2D position sensitive detectors (0.5 mm pitch) in the calorimeter at two depths: 2 X_0 and 9 X_0. The first layer (PreShower-PM), installed downstream of the first two sampling layers in the first EM segment (EM1), is a hit counting layer where position resolution is given by the strip width to ~150 μm. The second (ShowerMax-SM) layer will serve to measure the decay asymmetry through shower shape analysis at a depth where the shower expands to 1 $R_{Moliere}$ radius. The algorithm will first find all showers in the calorimeter. For every shower it will identify the regions of in-

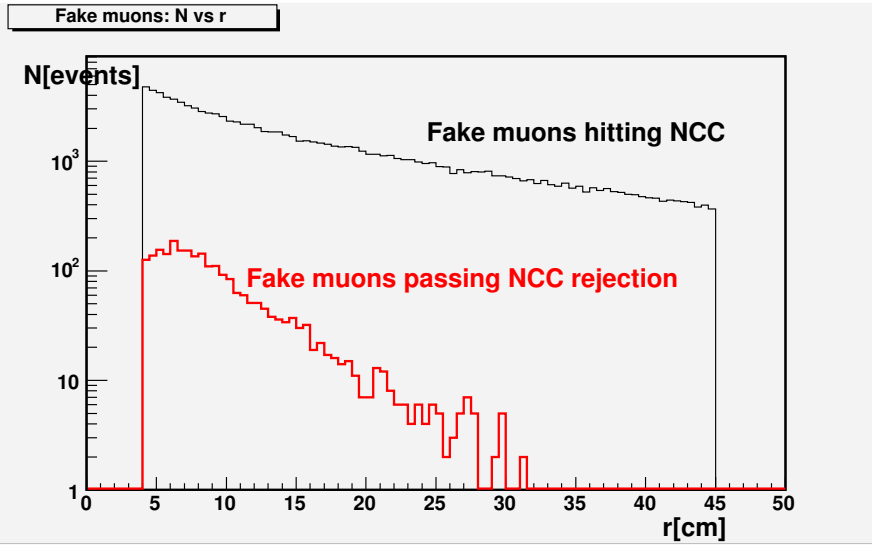

Figure 3.16: Fake muon rejection in the NCC in minimum bias PYTHIA events. Fake muons were simulated by reflecting momentum vectors of particles hitting the opposing NCC

terest in the PS and SM detectors and look for hits in the PS layer to find those which may contain overlapping candidates. These overlap candidates will be checked for consistency with the hits in the SM layer where the deconvolution will finally be made assuming that the contribution of individual photons is proportional to the peak energy values as measured in the SM detector. Simulations have shown that this approach works well to energies up to 30 GeV (effectively to the limit set by the integrated luminosity).

This section shows the proof-of-principal simulation for the algorithm as described above and will be further updated when test beam data will become available. The π^0 events were simulated with a uniform momentum distribution between 1 and 30 GeV/c. Checks were made that only those events with both photons inside NCC aperture are retained. The pattern recognition algorithm used was simple and intended to answer whether the data actually possesses the features required to separate single showers from overlapping showers using this technique. In the detector with Moliere radius ∼14 mm and tower size 15×15 mm^2 decay kinematics implies that a substantial fraction of π^0 decays will yield clearly separated photons. As in the central calorimeter, we consider two showers distinct if their maxima are separated by at least one counter i.e. there is a visible valley between the showers.

A clustering algorithm was applied to the hits seen in the longitudinal segments of the calorimeter. The clustering was done separately in all segments. Showers ordered by energies were combined into "tracks" originating from the collision vertex. Whenever the algorithm produced more than one track in the NCC, an attempt was made to compute an effective mass. The comparison of the effective mass distributions for e- and π^0's events producing multi-track configurations is shown in the left panel in Fig. 3.17. A scatter-plot of the effective mass vs π^0 momentum in "multi-track" π^0-events is shown in the right panel.

A clear π_0 signal with a width of $\sim$ 25 MeV/c^2 is seen in π^0 events. The distribution for electron events is totally consistent with background. This approach works reasonably

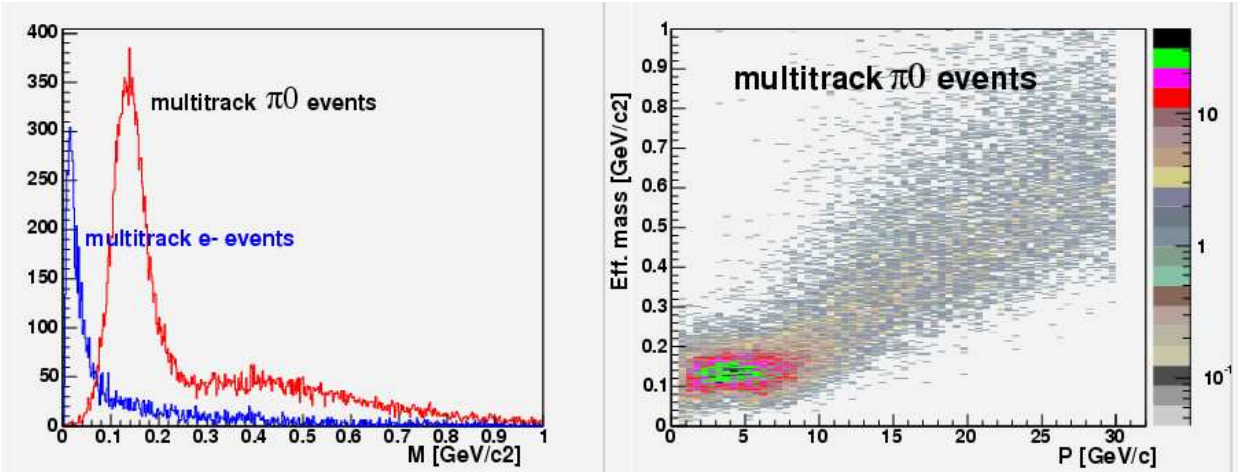

Figure 3.17: Two-shower effective mass distribution in the events with two distinct maxima found in the pattern of deposited energy in NCC.

well for π^0 momenta below 7 GeV/c and fails at higher momenta where the showers begin to merge. The computed probability to find two distinct showers in the event with both photons from π^0 decay in the detector aperture is shown in Fig. 3.18.

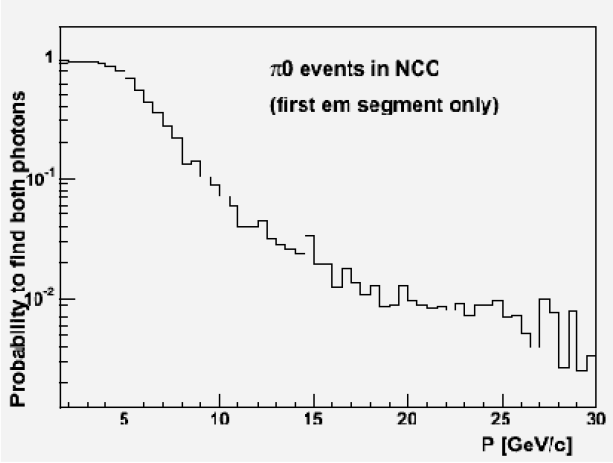

Figure 3.18: Probability to find both showers from π^0 decay as two distinct maxima in NCC vs momentum of π^0.

The events with effective mass outside the two standard deviation window around the π^0 mass as well as single "track" events were further subjected to a reconstruction procedure relying on the pre-shower (PS) detector for shower separation measurements and on the shower-max (SM) detector for decay asymmetry measurements. All fired strips in the PS and SM detectors were subjected to a simple clustering algorithm which assumed all strips around a local amplitude maxima being part of a single cluster. For illustration in Fig. 3.19 the hit pattern produced by 12 GeV/c π^0 is shown in the PS and SM detectors. The multiplicities of fired strips in the two detectors are very different. The clusters are obviously separated

in both detectors but fluctuations are the limiting factor adversely affecting the resolving power.

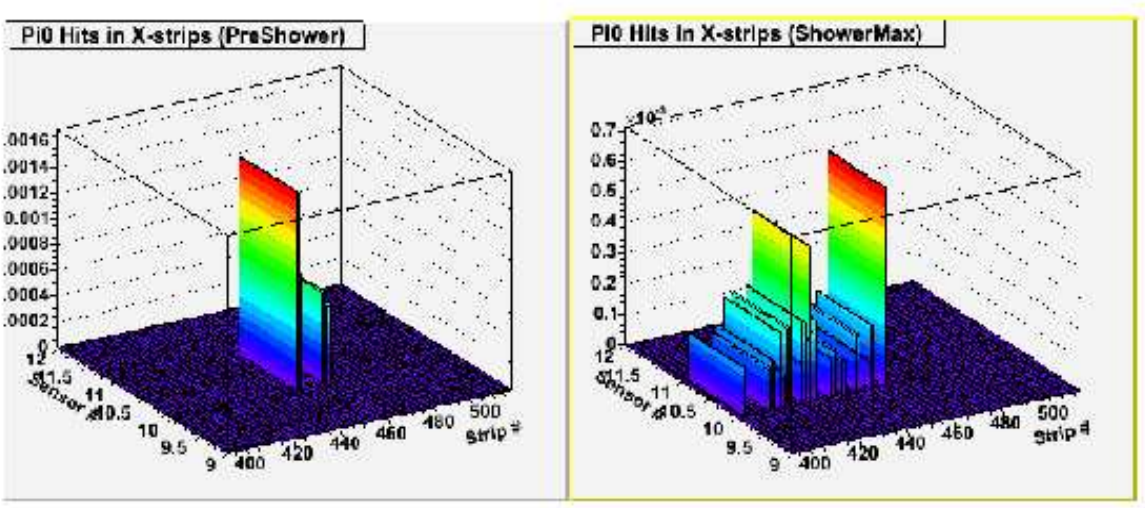

Figure 3.19: Energy patterns in the PreShowr and ShowerMax detectors due to two overlapping photons from 12 GeV/c π^0 decay. (The vertical axis is an energy per strip in GeV).

The total energy is obtained from the sum of energies in EM1, EM2 and HAD. The decay opening angle is obtained using hits in PS. The decay asymmetry is obtained from the SM shower profiles. Once these three factors are known, the effective mass can be computed using formulas based upon decay kinematics. The comparison of the distributions of effective masses reconstructed using this procedure in electron events and π^0 events is shown in Fig. 3.20.

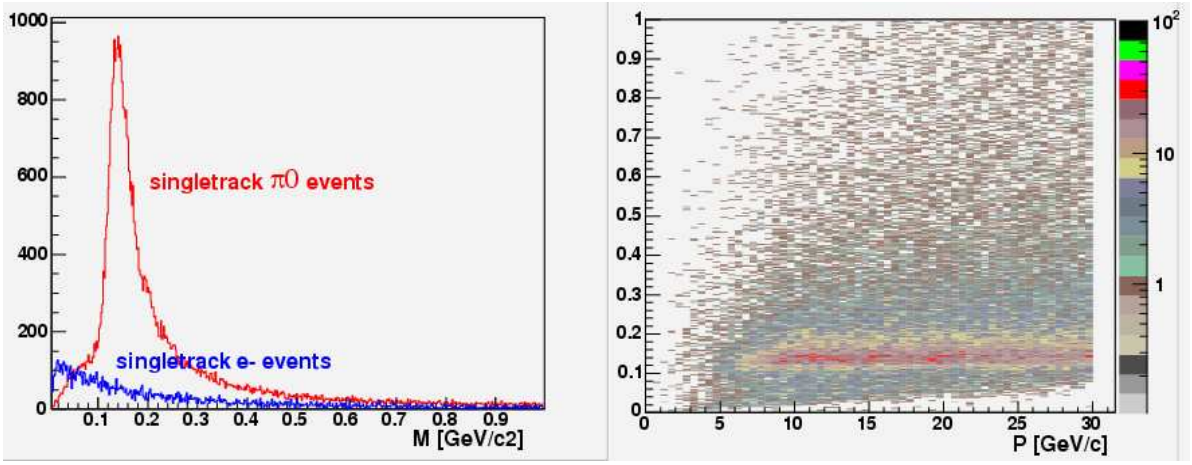

Figure 3.20: Reconstructed effective mass distribution in the events with a single distinct maximum found in the pattern of deposited energy in NCC.

The π^0 peak is present in π^0 events only, whereas the distribution for e-events is totally consistent with background. The shape of the π^0 peak as it is reconstructed by this procedure is a subject for further improvements. Currently it has a central peak characterized by $\sigma \sim$ 20 MeV/c2 consistent with detector energy resolution on top of a wide distribution which would usually be considered as a background. The real composition of the peak reflects correlations between the decay asymmetry and the effective mass resolution intrinsic to this approach. While asymmetric decays result in better separated showers, asymmetry measurements in the SM detector get less and less precise when the energy in one of the showers decreases. There are also flaws and shortcuts in the current implementation of this procedure resulting in a failure to properly reconstruct very asymmetric decays. Addressing such issues will require further development. The losses and failures to reconstruct π^0's by the currently available algorithm are summarized in Fig. 3.21. We expect to make considerable improvements in the algorithm using data collected with prototype in a test beam.

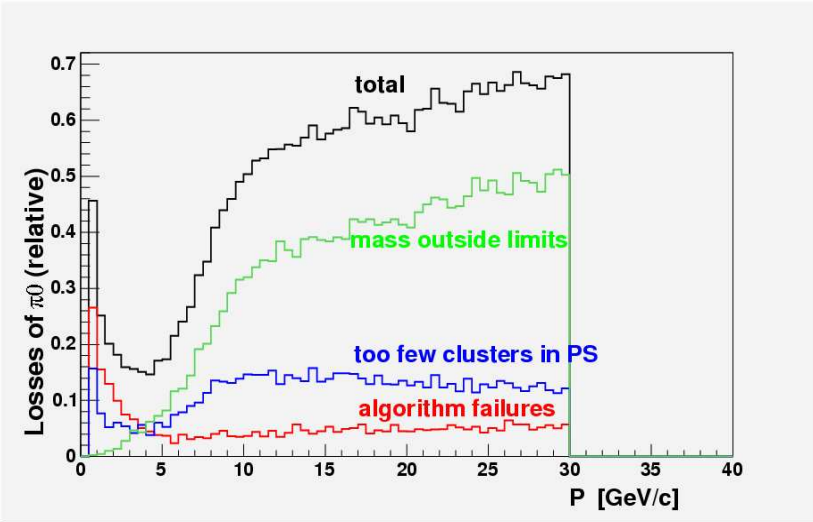

Figure 3.21: Probability for π^0 in NCC to fail in reconstruction or to end up outside 2σ mass window.

Mass cuts 2 standard deviations around the central peak applied to π^0 masses reconstructed in "single track" events result in loosing 50% of π^0's from the peak region. All other losses are less than 15% combined. If events producing reconstruction failures are excluded the estimated efficiency of algorithm to reconstruct π^0 both via multi-track and single-track algorithm in the NCC is shown in Fig. 3.22.

Even at this early stage in the development the efficiency stays above 40% up to 30 GeV. For comparison the π^0 reconstruction efficiency in the PHENIX central calorimeters drops to zero around 15 GeV/c.

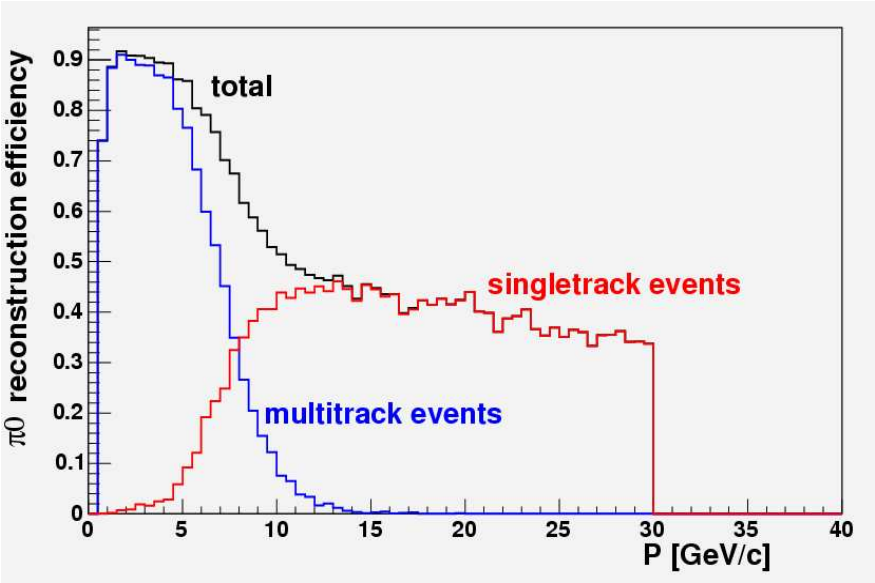

Figure 3.22: Probability for π^0 in NCC to be reconstructed within 2σ mass window.

Further progress in understanding NCC π^0 reconstruction capabilities strongly depends on availability of test beam data which can be used both to improve the quality of Monte-Carlo simulation and to further tune reconstruction algorithms. We are currently constructing the 12x12 cm^2 prototype which will serve to verify design ideas presented above (beam time is reserved at SPS CERN for September 2007). We are also planning to use the first production NCC brick as a detector system prototype and to test it extensively in the beam at FNAL in preinstallation period.

3.5 NCC Occupancy and Dynamic Range Considerations

In the NCC the energies of showering particles are shared between three segments of the calorimeter. This sharing is uneven, with most of the electromagnetic energy deposited in the EM segments, and most of hadronic energy in HAD. In p+p interactions it is sufficient to set the upper limit of the dynamic range per tower per section to $\sim$ 60% of the W mass to cover the whole range of physics topics we are planning to study at a 500 GeV collision energy.

In heavy ion collisions, the calorimeter located at 40 cm from the collision vertex will see a high occupancy environment resulting from hits due to the pile of particles. The potential impact on the calorimeter dynamic range was estimated by merging contributions from individual minimum bias events to simulate the environment typically observed in the central heavy ion collisions. The 50 GeV dynamic range was found equally fitting for the needs of both physics programs.

The question of NCC performance in heavy ion collisions is complicated. To illustrate

the problem, an event with a few hundred particles hitting each NCC (merged min bias events-simulated mid-centrality event) is shown in Fig. 3.23.

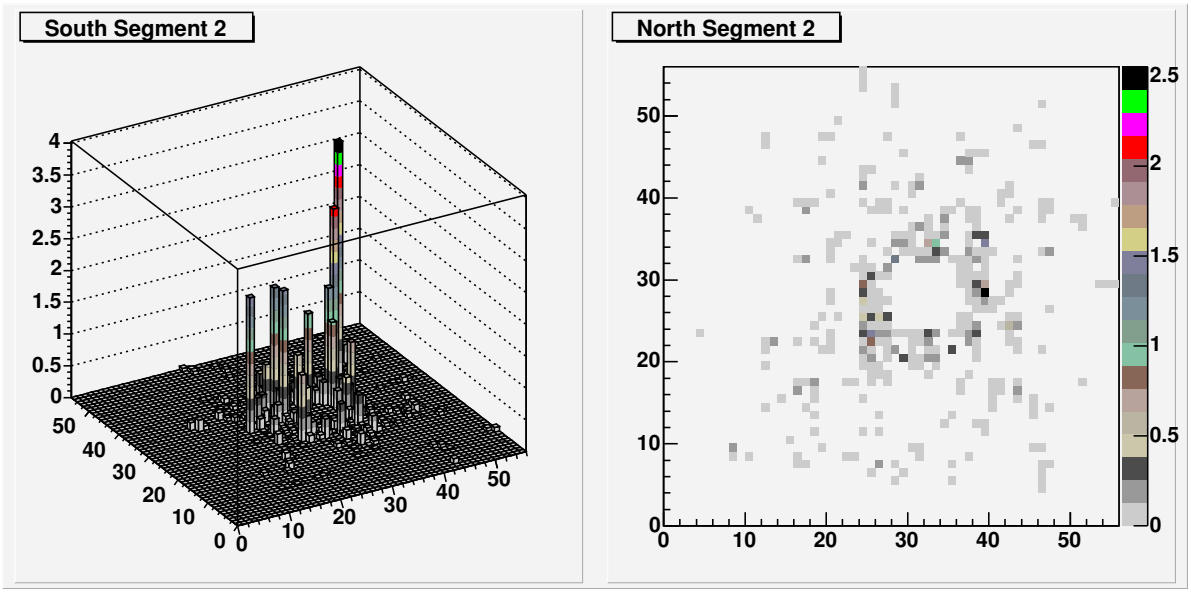

Figure 3.23: Mid-centrality Au+Au event in NCC. Data for South(left) and North(right) calorimeters are shown in different formats to illustrate two different aspects of handling high multiplicity events in NCC: rapidity dependent sensitivity to jet activities and centrality dependence of the acceptance for low p_T physics. x and y axis indicate tower numbers, z-axis indicates energy deposition per tower in GeV.

Different data representations are chosen for North and South detectors. In central events the occupancy in the forward rapidity region of the calorimeter will be too high for meaningful low energy shower reconstruction. With increased centrality this region will extend towards smaller rapidities. The correlation between event centrality and the extent of the saturated regions are subject for further studies. Event centrality will also affect triggering on jets and jet recognition except in rare events with very high-p_T jets or photons which will still be visible above underlying event background.

3.6 NCC Mechanical Design

A modular design illustrated in Fig. 3.24 was developed for the NCC to allow for a relatively easy industrialization of the construction project. The NCC mechanical design, implemented in the form of an Autodesk Inventor 3D-model, is now under the responsibility of the PHENIX engineering group so any potential modifications can be easily handled. The calorimeter is built of "bricks". Two kinds of bricks (see Fig. 3.25) are used to build two quasi-independent calorimeters: the electromagnetic (EM1 and EM2) and hadronic (HAD). All bricks are a double 6.2 × 6.2 cm^2 silicon sensor wide. There are three standards for the brick length in the electromagnetic and hadronic segments (7/6/5 sensors in HAD, 6/5/4

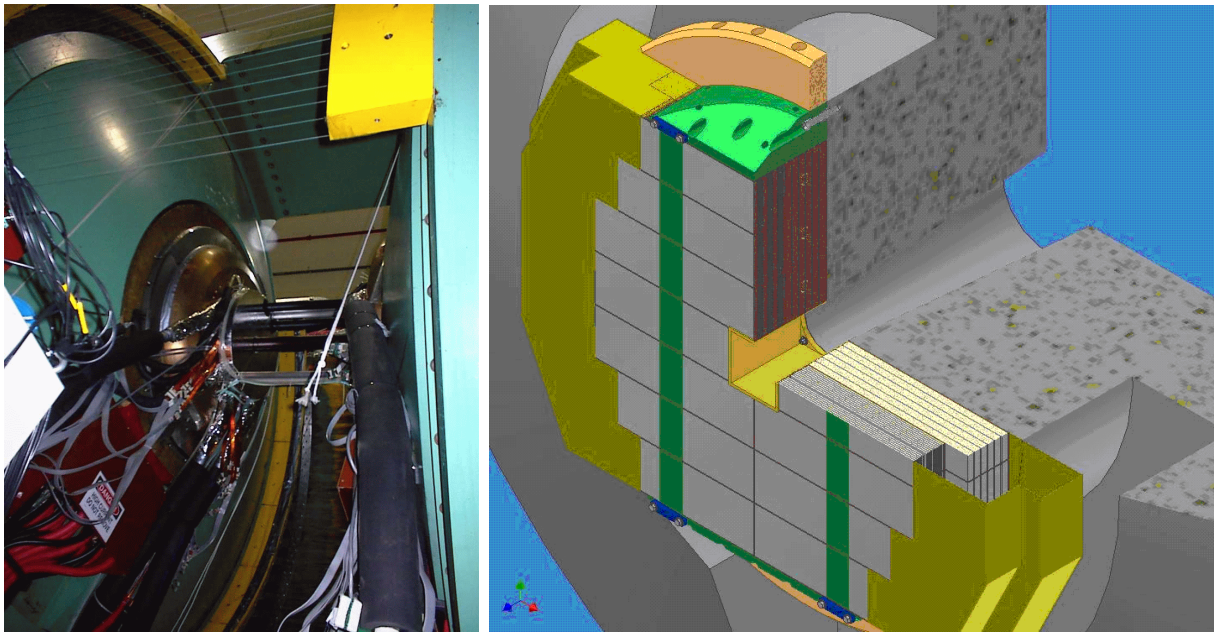

Figure 3.24: Present PHENIX Nose Cone (left panel). Cutaway view of Nose Cone Calorimeter (right panel). Boxes upstream are electromagnetic segments (EM1 and EM2), downstream boxes are HAD.Crates with preamplifiers and cable drivers are also shown

sensors in EM1 and EM2). The electromagnetic bricks are much more demanding in terms of the readout as compared to the hadronic bricks. Electromagnetic bricks are composed of two electromagnetic segments (EM1 and EM2) built out of fine calorimeter sampling cells, preshower detector (PS) and shower max detector (SM). A hadronic brick consists of a single hadronic segment built out of coarse sampling cells. Each brick has a W plate facing upstream and Cu skin enclosing it on all other sides save one for connections to external electronics.

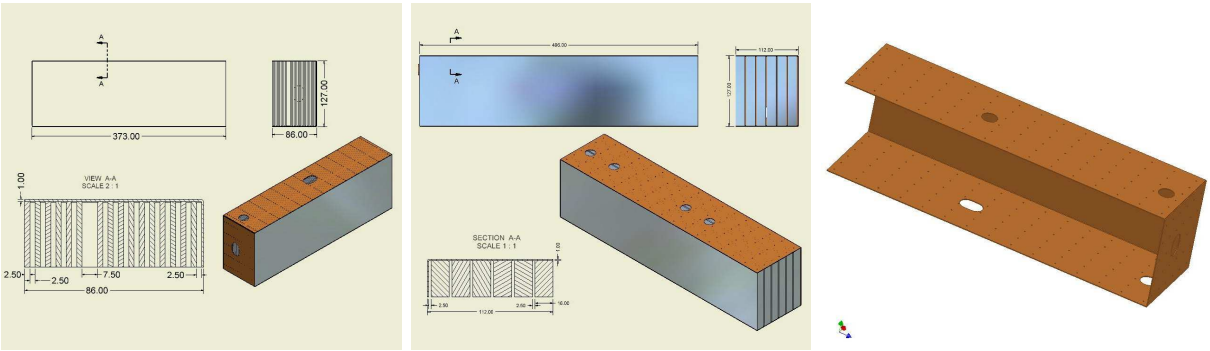

Figure 3.25: NCC building bricks. (left) electromagnetic (center) hadronic, (right) Cu skin for the electromagnetic brick.

When assembled, the bricks form two vertical walls one made of EM bricks, the other of HAD bricks. Small locking pins are used to maintain the geometry. For mechanical reasons

the two walls have the same size vertically, giving up some of the acceptance in hadronic segment. Horizontally the hadronic wall is two sensors wider compared to electromagnetic wall. This geometry allows us to minimize the cost while still measuring all particles originating in the area ±30cm with respect to the nominal collision point. The calorimeter walls are supported by two shelves above and below, and thin pretensioned front braces (strips of stainless steel or Kevlar) which the walls from buckling outward.

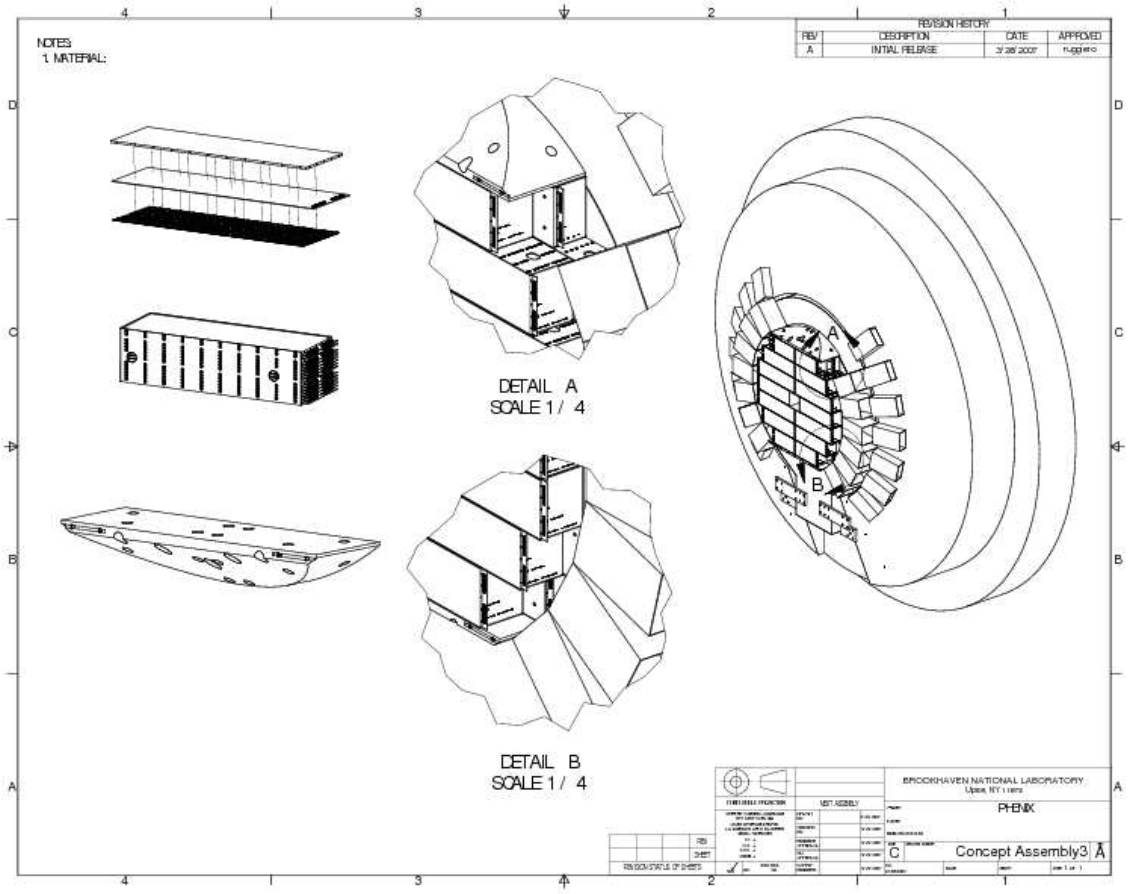

Figure 3.26: The main components of NCC design: sampling cell, brick, cutouts showing different pats of the assembled calorimeter, and assembled calorimeter with analog readout electronics on the magnet pole.

3.7 NCC Readout

3.7.1 Sensors

Two kinds of silicon sensors are used in the NCC readout: pad structured sensors and pixelated strips. These will be described in more detail below and in the Appendices. Sili-

con detectors in the calorimeter provide for precise shower energy measurements via charge measurements in silicon pads and for precise tracking measurements via energy sharing measurements in silicon strips. The sensors must be robust and radiation hard. The pad size chosen for the NCC is ∼1.55x1.55 cm^2. The strip size for PS and SM is ∼0.5x60 mm^2. All silicon detectors in the NCC are 6.2x6.2 cm^2 diced from 4" wafers 525 μm thick. Critical to the success of the experiment will be reliable operation of these sensors in a radiation environment. The estimates based upon ionization losses by collision related particles produced in pp-interactions at $\sqrt{s}$=500 GeV at a luminosity of $10^{32} cm^{-2} s^{-1}$ result in radiation dose of ∼ 10 Krad/year close to the beam pipe. Albedo neutrons from the calorimeter absorber will constitute 3 to 10 % of the value of the MIP fluence but will induce ×10 higher damage effectively doubling the radiation dose to ∼ 20 Krad/year of operation [109]. In 10 years of running at RHIC II luminosity the sensors in the central region of NCC will begin showing signs of radiation damage. To alleviate the possible consequences of exposure all sensors in NCC are used in AC coupled mode (external RC decoupling network) thus allowing us to handle at least ×10 increase in the leakage current. In addition, the mechanical design of the readout units allows for replacement of problematic sensors without collateral losses (although it can be done without moving calorimeter bricks to "gray" repair area).

In our design of sensors and selection of raw material we were guided by the experience and work done within the scope of the D0 (FNAL) and ALICE (LHC) projects and recent published data from the R&D in radiation hard silicon technology. In particular we followed a few simple rules:

- We use single sided sensors from established vendors to insure high yields and less trouble due to the simplicity of the design. In addition double sided sensors suffer more radiation damage,

- A minimal number of different sensor designs (only two in the NCC case). Design to successful completion of the project using a single vendor. Transfer the design to additional vendors when ready. This will speed production,

- Use short strips to reduce the number of ghosts hits to avoid creating pattern recognition problems. We use 4" wafers only,

- Specially designed guard ring structures. Such guard rings are important in order to keep breakdown voltage before and after irradiation as high as possible.

Following these recommendations the pad layers in the Nose Cone Calorimeters are built using single-sided single-metal p+ on n- bulk silicon devices. The technology of pad structured sensors is well tested. We have three established vendors ready to manufacture the 6.2x6.2 cm^2 pad-structured sensors using nearly identical design files, corrected for specifics of technology. The pixelated strips (StriPixels) are novel detectors developed at BNL and currently selected as a base design for the silicon sensors in another of PHENIX upgrades - the central silicon tracker. The design chosen by PHENIX are interleaved StriPixel detectors where each pixel is divided into two parts: an X-cell (or pixel) and Y-cell. X-strips and Y-strips connect X-cells and Y-cells, respectively, in a strip detector readout scheme. In this

detector two dimensional (2D) position sensitivity is achieved with single-sided processing. A short summary of sensor parameters is given in Table 3.2.

Specifications	Pad-structured sensors	StriPixel sensors
Wafer thickness	525 μm	525 μm
Depletion voltage	100-120 V	100-120 V
Diode capacitance	25 pF	3 pF
Bias voltage	Full dep. V + 20V	Full dep. V + 20V
Leakage current	< 300nA total, <20nA/pad	< 1nA total
Junction breakdown	> 300V	> 300V
Implant area	15 x 15 mm^2	
Al area	15.02 x 15.02 mm^2	15-60 mkm prototyped. Decision pending.
Polysilicon bias resistor		1 MΩ
Interpad (strip) capacitance	< 2pF (pad-pad) or < 8 pF (pad-all neighbors)	TBD
Maximum heat dissipation from the bulk material	$<\sim$ 50 mW / sensor	$<\sim$ 50 mW / sensor
Heat dissipation from on-the-sensor electronics	no major heat sources	0.5 W / sensor

Table 3.2: NCC Silicon Sensor parameters

Both pad sensors and StriPixels have been prototyped at ELMA (Russia), ON Semiconductor's (Czech Republic) and SENS/ETRI(Korea). The R&D program to develop pad-structured sensors is now completed. We are currently in the last stage of developing and prototyping StriPixel sensors. The delivery of sensors of the final design manufactured following double-metal technology is expected in June 2007.

We briefly review the design of the sensors and related infrastructure in this section. R&D results are presented in the Appendices.

3.7.2 Pad-Structured Readout Layers

The pad structured Si layers (20 in total) are built of 6.2x6.2 cm^2 silicon detectors subdivided into 16 identical square cross section pads (diodes).

The individual pad-structured sensors will be assembled into stacks consisting of the silicon crystal, a single layer interconnect board and ceramic substrate glued together using silicon-based adhesive. Assembled and exploded stacks are shown in Fig. 3.27.

Sensors are first glued to the dielectric side of the interconnect board, a ceramic spacer laminate (silicon based glue is used everywhere so the effects of thermal expansion mismatch are alleviated). The interconnect board is made of FR4 ceramic spacer alumina tile 0.8 mm thick. The spacer will provide for rigidity of the sensor stack and prevent the sensor-interconnect laminate from warping.

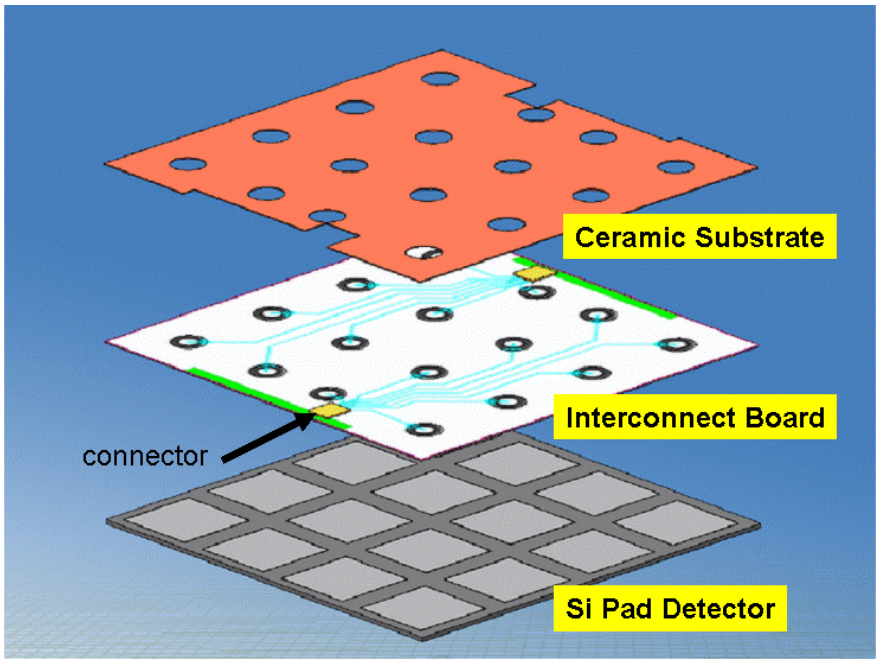

Figure 3.27: Pad-sensor stack. From bottom to top: silicon pads, interconnect board, and ceramic substrate.

The interconnect board is further wire bonded to the pad centers through 3 mm diameter vias. Low-profile RC-network components are placed on the carrier board opposite to the bonding point locations (hidden inside large diameter vias in the ceramic spacer now separating the interconnect and carrier boards). A single sided polyimid cable bonded and glued to the sensor common side and soldered to the ground pad on interconnect is used for the ground connection. Two 20 pin low profile (0.9 mm total height) connectors are installed close to the edges of the interconnect board to connect the sensor stack to traces on the carrier board which is conductively glued to the tungsten plate (see Fig. 3.28).

The laminate of the 4 mm W plate and carrier board with installed sensors stacks form a readout unit (sampling cell) which is used throughout the whole calorimeter depth. To increase the amount of absorber in the hadronic segment an additional 8mm W plate is screwed to the 4 mm plates prior to assembly of the brick.

The interplate gap reserved for the readout unit is 2.5 mm thick. 0.5 mm of this space is silicon, ∼0.2 mm is FR4 (motherboard), 0.2 mm is the FR4 interconnect. 0.9 mm partially filled with ceramic spacer is used to accommodate connectors and RC-network distributing bias voltage to individual diodes. The remaining ∼0.2 mm gap is to insure that no pressure is applied to the surface of the sensors. Such pressure may result in increased noise due to the piezoelectric effect.

This particular design is developed to insure an easy repair of the assembled readout unit. If the sensor fails, the sensor stack can be removed from the carrier board and a new stack can be installed. The very same approach can be used if repair will ever become needed due to for example unplanned beam loss in the area close to detector location. It would

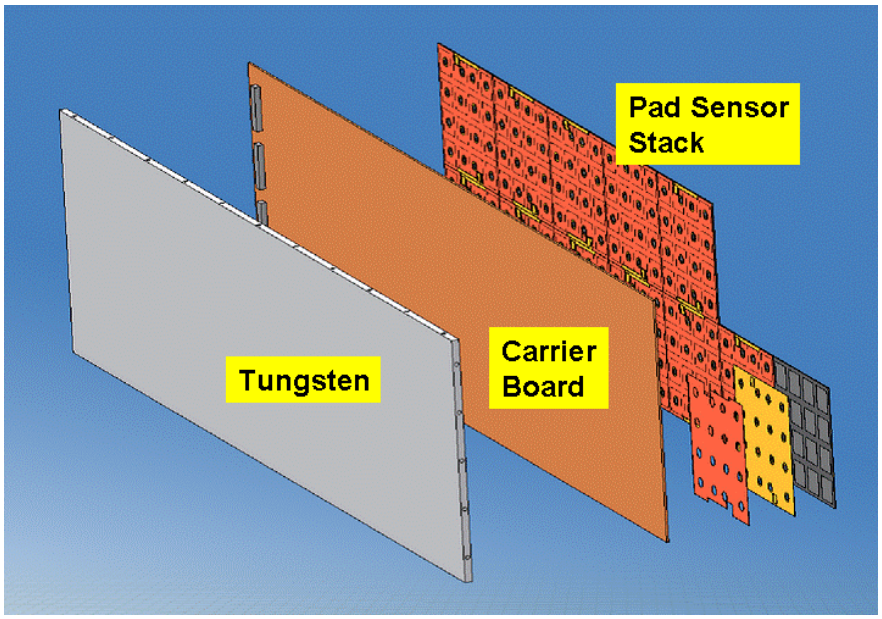

Figure 3.28: Exploded NCC pad-readout unit. Left to right: Tungsten, Carrier Board, Pad sensor stack described in Fig. 3.27.

certainly require removal of the detector from the pole tip, disassembly of affected bricks into individual sampling cells, and replacement of damaged sensor stacks – all of which are well within the scope of work typically planned for RHIC shutdowns. The NCC will use five different readout units, all of which are a double sensor wide, with the number of sensors varying between 8 and 14.

3.7.3 StriPixel readout layers

We have chosen a novel detector of interleaved pixelated strips ("StriPixel") developed at BNL and already in use for the Central VTX in PHENIX. This novel detector generates X-Y two dimensional position sensitivity with a single-sided processing and readout. Fig. 3.29 is an illustration of the concept. It consists of a comb shaped structure with 250 μm prongs to cover a pixel area of 500x500 mm^2. Prongs are interleaved with similar prongs from two overlapping pixels on the right and on the left.

Alternate combs are connected either in the X direction (for measurement of the Y coordinate) or in the Y direction (for measurement of the X coordinate). The pitch between prongs belonging to different strips is chosen comparable to the charge diffusion distance to insure uniform charge sharing. While it is easy to predict that an optimal pitch for a 525 μm wafer must be in the range of 15 mm, it may still be affected by the comb geometry and needs prototyping to optimize the pitch. Other critical issues are interpixel connections and crosstalk, the latter depends on the total length of the strip edge and strip implant which in turn is correlated to the pitch. While the PHENIX central VTX employs double metal technology for interpixel interconnects, for the NCC we began with an attempt to

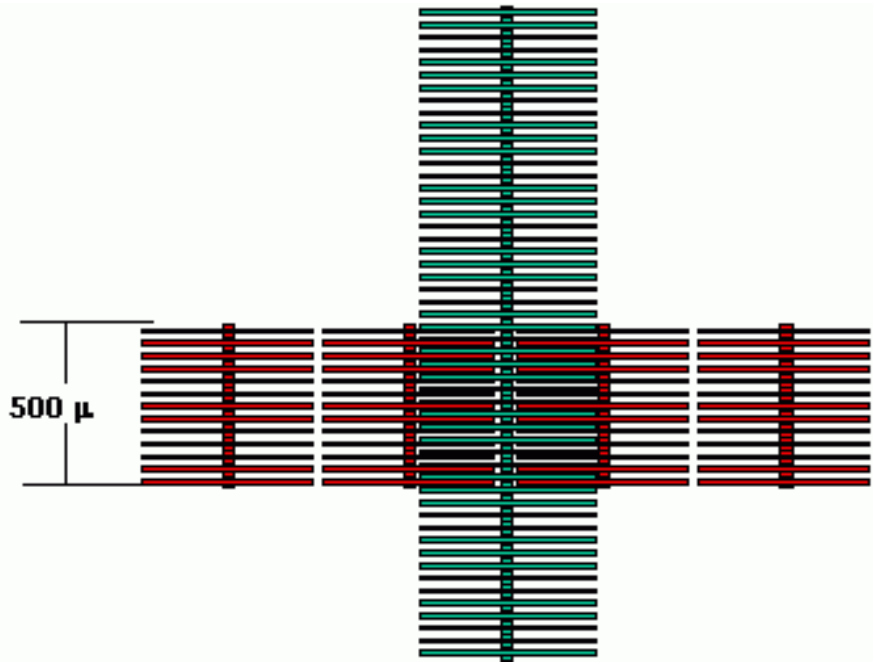

Figure 3.29: Design of the detector with interleaved pixilated strips giving 2D position sensitivity. Ionization charge produced by charged particles is shared between X and Y oriented strips.

use n+ implants to create conductive regions in the bulk silicon separated from Al with a layer of SiO2. This technology has in principle better promise for radiation hardness. The first prototypes produced at ELMA has shown very asymmetric charge collection and produced some hints of a large crosstalk between orthogonal strips (see Appendices). Our next prototype will have double metal readout and will be available for testing in June of this year.

The readout system for the StriPixel silicon detectors is based on the SVX4 chip developed at FNAL for the D0-detector Upgrade and the existing PHENIX data acquisition system. Strips are connected to Data Collection Modules(DCM's - part of the PHENIX DAQ system). The StriPixels are connected through hybrids with an RC network, to SVX4 chips daisy chained, to an interface board with a sequencer, and then connected to DCM's. The hybrids will be glued directly onto the sensors with the common of the sensor glued to a ceramic substrate and then to the carrier board.

Preliminary results of R&D work on StriPixel structures and a detailed proposal for readout electronics for StriPixel NCC layers developed in collaboration between the BNL NCC group, the BNL Instrumentation Department and the JINR LHE (Dubna) group can be found in the Appendices.

If further tests of StriPixel design with double metal technology will show that cross-talk between adjacent strips is unacceptable we will cancel further development of the StriPixel sensor and will use the well established **silicon strip detectors**, designed and tested for the NUCLEON experiment in cosmic ray physics (Moscow State University). These detectors

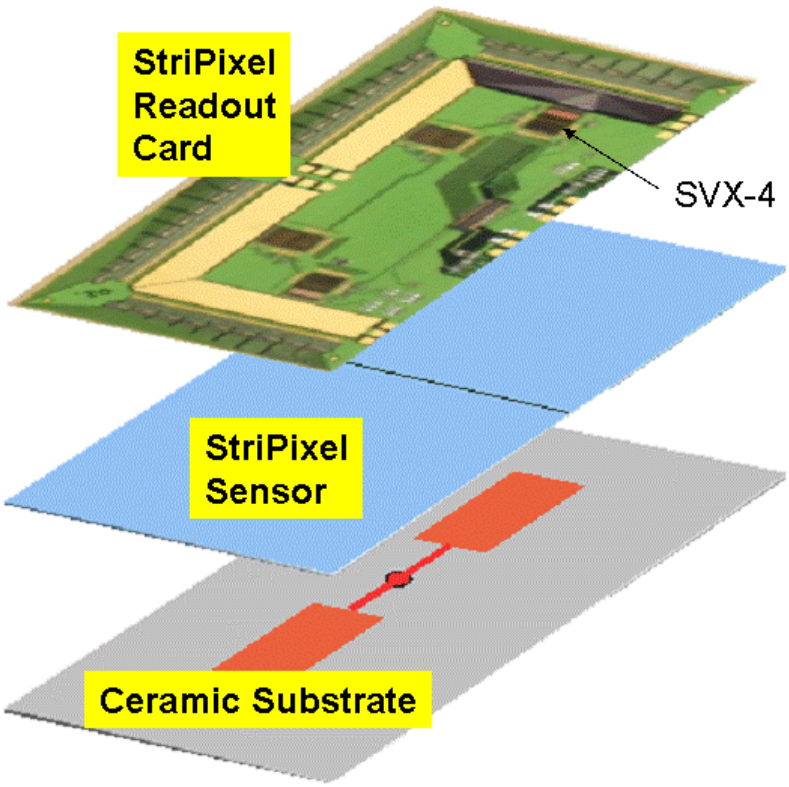

Figure 3.30: Expanded view of StriPixel stack, from top to bottom: StriPixel Readout Card, StriPixel Sensor, ceramic substrate. The assembly is then mounted on a carrier board which is not shown.

have the same pitch and are compatible with StriPixel Readout Card (SRC) boards. Figure 3.31 shows the two strip readout ladders (X and Y orientation) that could in principle be mounted on both sides of the single ladder ceramic substrate. Replacing stripixel sensors with strip sensors will have almost no ramifications on detector cost: sensors itself are $\sim 50\%$ cheaper than stripixel option, the number of readout channels and readout design will stay the same.

In contrast to the passive pad layers, the StriPixel layers carry active components (readout chips) to dissipate heat. The maximum amount of dissipated heat is 0.5 W per sensor or 7 W per layer. Extensive measurements of the heat dissipation inside enclosed cavity formed by W-plates made by S. Stoll (BNL) have shown the temperature of the inside layer stabilizing 8° C above ambient temperature which is acceptable. We also considered different ways of removing heat from stripixel layers (active ventilation, conductive strips etc). These had a modest effect - i.e. drop of 3° C in the middle of the brick. The final design of the detector will have a ventilating plenum between the detector and readout crates. Air from this plenum will be used to help with heat removal from inside the position sensitive NCC layers.

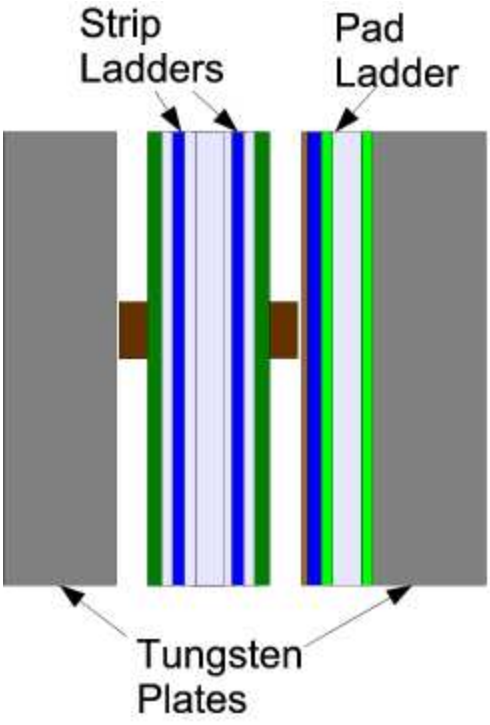

Figure 3.31: Arrangement of strip ladders between pad sensor assemblies on tungsten plates. This is one of the options allowing to implement 2Dimensional readout using single sided uni-directional strip sensors.

3.8 NCC Electronics

For readout purposes the calorimeter is longitudinally segmented into two fine and one coarse tower-structured segments and two 2D sensitive coordinate layers. In total the silicon tungsten calorimeter will have close to 60,000 silicon pixels and 80,000 strips. This calls for a compact, economical readout.

3.8.1 Readout electronics for tower structured NCC segments

Signals from geometrically matching silicon pads are first ganged together to create calorimeter towers, then conditioned by external preamplifiers and sent over 10 m long cables to a digitization plant on the bridge above the central magnet. 14 bit octal ADC chips running at 50 MHz digitization frequency are used to sample signals from the calorimeter towers. Weighted sums of 8 digitization samples are used as an energy estimate and stored for the further event analysis. The block diagram of the NCC analog signal processing plant is shown in Fig. 3.32.

As previously mentioned we will sum up signals from pads in each longitudinal segment of the calorimeter. A simple passive (on the cable) summation scheme is implemented on the outskirts of the detector. Signals from individual pads are carried over the traces on the carrier boards to the low profile connectors daisy chained using a custom designed FPC cable

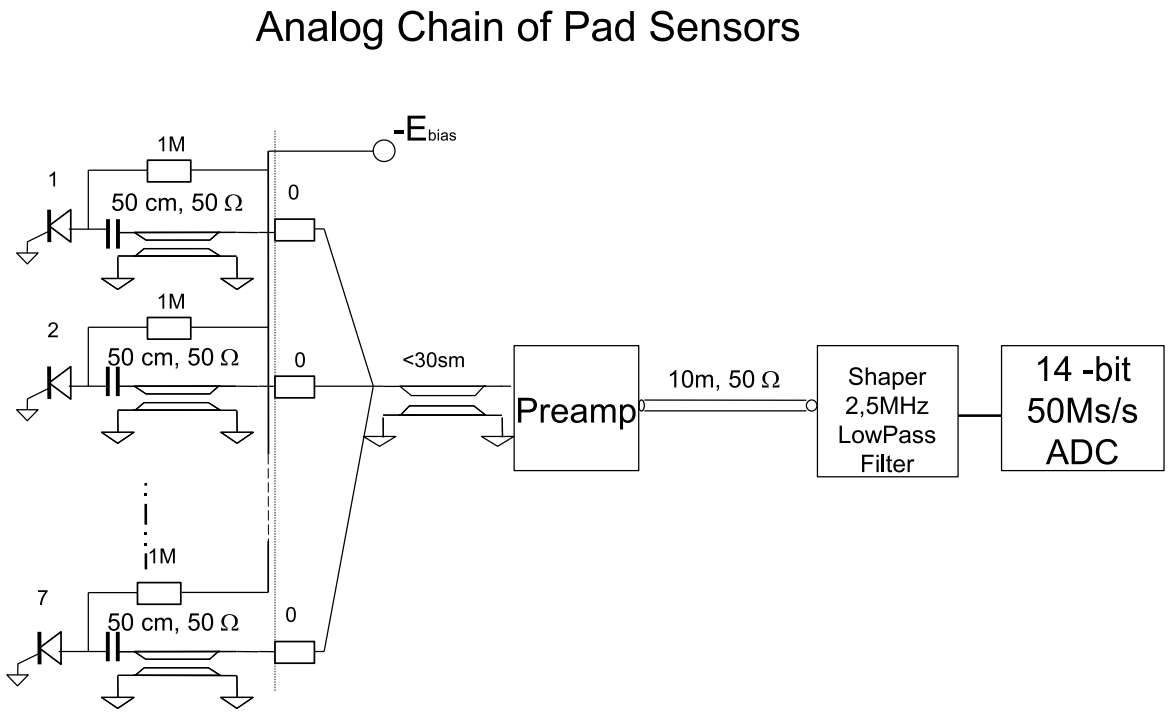

Figure 3.32: Signal processing block-diagram for NCC towers

which is further plugged into the input connector in the preamplifier crate (see Fig. 3.33).

Rather modest goals for the electromagnetic energy resolution allow us to disregard the potential contribution to resolution due to the spread in the gains between individual pixels. Summed signals are amplified using hybrid line terminating amplifiers developed at BNL for the ATLAS liquid argon calorimeter. Modifications to the existing design include a polarity change for all transistors (to work for positive swing signals) and the addition of differential drivers to drive the differential signals over Meritec 2mm parallel pair cables to the digital signal processing plant.

Depending on the location in the calorimeter the readout unit will deliver between 64 and 112 signal lines to the preamplifier carrier board. In order to minimize the number of individually designed components in the detector, we are planning to use the same design for the preamplifier carrier boards everywhere with only live channels populated. Each carrier board host up to 14 octal preamplifier hybrids hosting preamps, shapers and differential drivers.

Details of the signal processing chain for NCC towers were simulated using a full component model built within the LT SPICE electronics simulation framework. All related

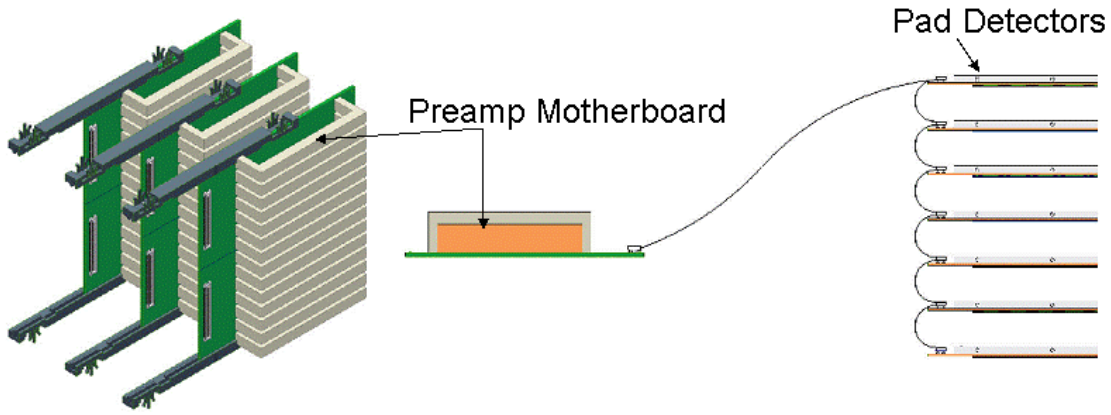

Figure 3.33: NCC custom built crate with preamplifiers and differential drivers for analog conditioning of signals from calorimeter towers.

information can be found in the Appendices. Our main concern and reasoning for implementing the simulation with this degree of sophistication was related to the necessity to measure signals due to minimum ionizing particles in the NCC towers. The simulation concluded that by using the transresistance preamplifier developed at BNL complemented by the optimal low frequency bandpass filter, the electronics noise can be reduced down to ENC$\sim$2000. This allows us to reach a dynamic range of the $\sim$10000 (close to 14 bits) in signal processing with an ENC equivalent of LC/4.

The amplified differential signals are driven from the detector to the FEM through 2mm Hard Metric (HM) parallel pair cables. This cable is made from 2 isolated 26 gauge parallel wires with overall shield and 100 ohms impedance. The 2mm HM connector has 5 pins per row and can host 2 signal pairs plus central ground pin per row. A block-diagram of the digital signal processing plan including low level triggering is shown in Fig. 3.34.

The NCC Front-end Module (FEM) has the function of receiving the NCC preamp signals, digitizing the signals and sending them to the Data Collection Module (DCM) and NCC local level 1 modules (LL1). The FEMs are hosted in the 6U VME crates located on the platform above the central magnet. Each FEM station will receive 64 channels of signals. A custom dataway will be used as a bus for the serial data and to chain FEM data between adjacent modules. A crate interface module will serve to interface with the PHENIX granule timing module (GTM) as well as to the PHENIX slow download interface used for setting voltages etc. The level 0 (L0) and level 1 (L1) timing signals and serial data will be generated from the interface module and sent to the FEM.

The cable receiver, as shown in Fig. 3.34, will receive, shape and drive the signals differentially to the ADC. Final gain adjustment can be done by changing the feedback resistors. An 8 channel 50MHz 14-bit ADC running at 40 MHz will be used to digitize the signal. The ADC will sample the signal 4 times per RHIC beam crossing. Ignoring the voltage shift of the ADC, the full range of the ADC is +1V to -1V. The amplifier and receiver arrangement can only swing the voltage from 0V in a positive direction. To avoid losing half of the dynamic

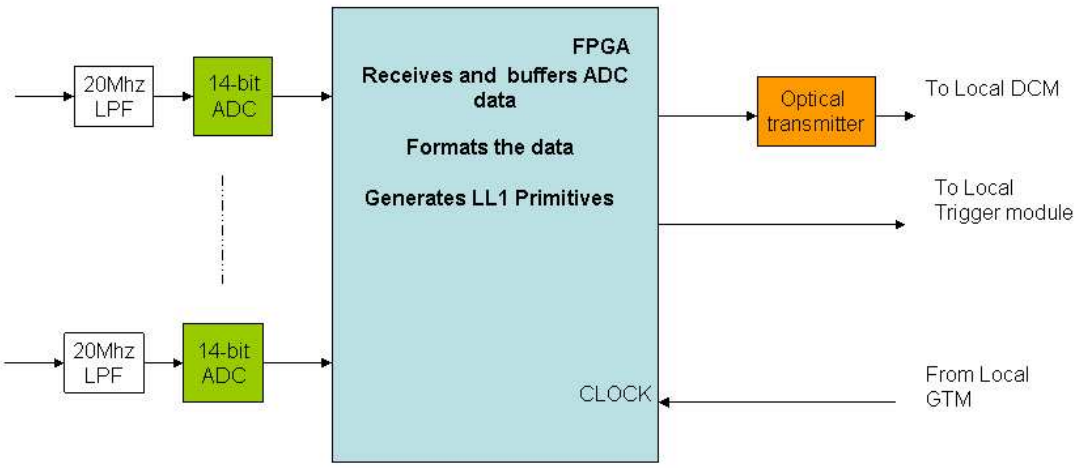

Figure 3.34: Digital signal processing diagram for the NCC pad electronics.

range the input signal will be biased towards -1V using the reference voltage existing on the ADC chip. The ADC data is serialized using a 12 times sampling clock running at 720MHz. An FPGA will be used to receive the serialized data. The same FPGA will provide the 40 beam crossing L1 delay buffers, 5 L1 trigger event buffers and data formatting. Upon receiving a L1 trigger, a weighted sum of 12 samples of data per channel will be output to the DCM. Data output of the FEMs will be connected through a token passing dataway. Four modules of data will be sent per optical transmitter to the DCM.

Similar ADC boards were recently developed in PHENIX for the Hadron Blind Detector Project (HBD) and are already in use. An example board is shown in Fig. 3.35

3.8.2 Readout electronics for position sensitive NCC layers

Position sensitive (stripixel) sensors are bonded to integrated readout chips (SVX4) developed for the upgraded D0/CDF detectors at FNAL. Each sensor is serviced by two SVX4 chips. The Ionization signal in each strip is locally digitized with 8 bit resolution (60 fC dynamic range), zero suppressed and shipped to data collection modules upon receiving an accept signal. Details of the SVX4 based readout as implemented for the NCC including results of noise measurements made with prototype readout boards can be found in the Appendices.

3.9 NCC Event Based Triggering - Hardware

In order to pursue its rare-event physics program, (e.g. $\gamma - jet$ events) the PHENIX experiment requires high luminosity from the RHIC accelerator and highly selective Level-1 and Level-2 triggers. In particular, the Level-1 trigger system is limited to a maximum rate of 12.5 kHz by the readout rate of the detector front-end electronics. This will require an overall

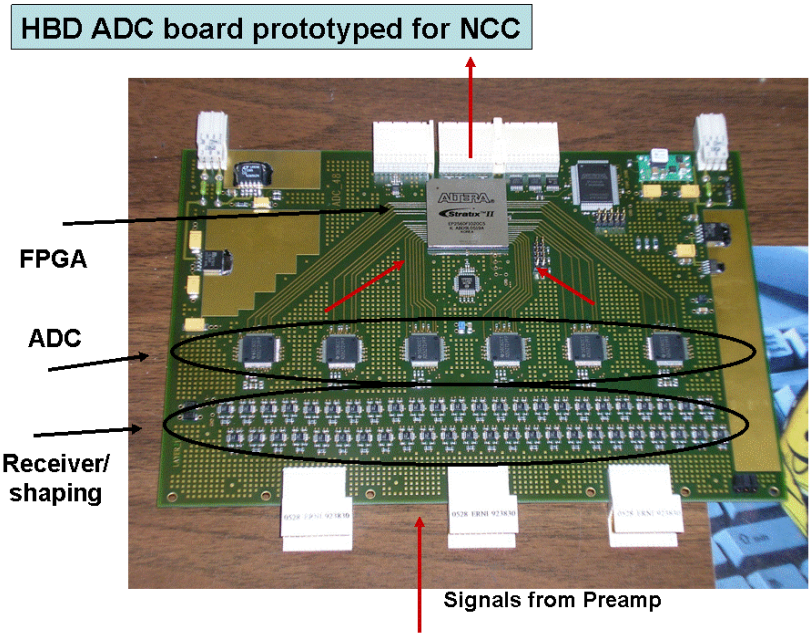

Figure 3.35: HBD ADC board used as a prototype for the NCC pad FEM.

event rejection of up to ∼1000 when RHIC reaches its goal of ten times design luminosity for protons in future run. Since we anticipate the parallel acquisition of several rare event channels, the rejection for an individual trigger channel must be larger by a factor 5-10.

The PHENIX Level-1 trigger is fully pipelined and provides an event decision in less than 4.2 μs (40 RHIC clock ticks). The Level-1 Trigger consists of two separate subsystems. The Local Level-1 (LL1) system communicates directly with the participating detector systems. The input data from these detector systems is processed by the LL1 algorithms to produce a set of reduced-bit input primitive data for each RHIC beam crossing. The Global Level-1 system receives and combines this data to provide a trigger decision. In addition, busy signals (both global and trigger) are managed by GL1. The PHENIX detector system readout is divided into two sets of elements: granules and partitions. A granule is the smallest detector element that communicates with the PHENIX timing and control system via a Granule Timing Module (GTM). The GTMs distribute the local 9.4Mhz RHIC beam clock as well as control bits and event accepts to the granule. A partition is an administrative configuration of granules that share both busy signals and Level-1 triggers.

In this PHENIX upgrade the NCC LL1 primitive system will generate primitive information on jets, as well as single and multiple high energy clusters. The NCC LL1 system will be based on a set of generic "trigger tile" cards being developed by Iowa State University and Northern Microdesign as part of a DOE STTR grant. It is intended that these trigger daughter cards will also be used in the PHENIX muon trigger upgrade and a possible LL1 system for the Forward Vertex (FVTX) detector as well. These daughter cards are designed for a very high input bandwidth, with up to ten serial inputs per card operating at 2.5 Gb/s. Four cards will be used in a standard VME 9U format motherboard, which will include

interconnected multi-Gbit serial connections for inter-tile communication. Each trigger tile will include two Xilinx Virtex-5 FPGA's, and the board is being design to accommodate several varieties of the Xilinx Virtex-5 so that the logic density (and cost) can be tailored to the particular application.

A block diagram of the trigger tile is shown in Fig. 3.36. Because the NCC front end electronics will be sending digitized trigger primitives (4x4 and 8x8 overlapping tiles), the NCC LL1 system will fit in one 9U VME card containing four trigger tiles.

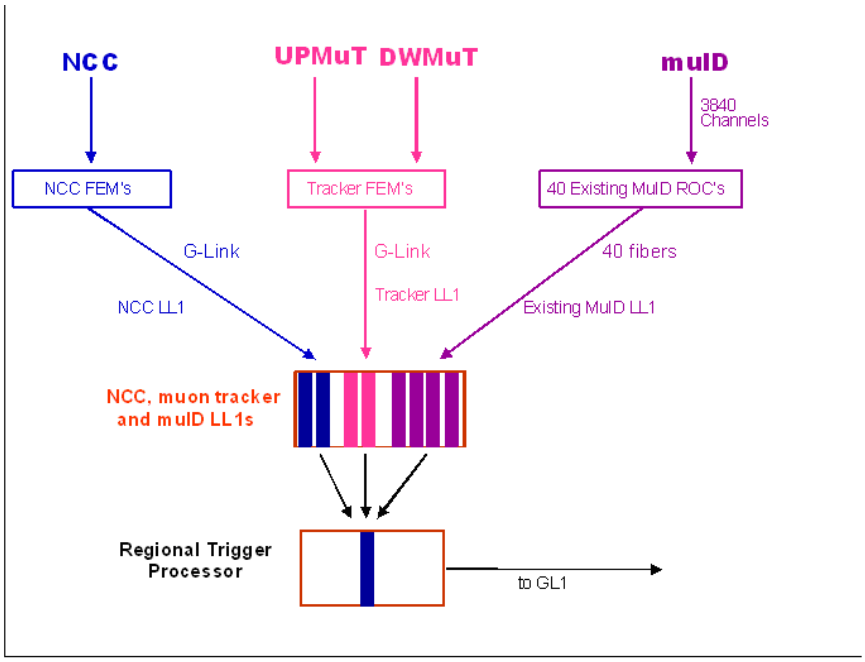

Figure 3.36: Block diagram of a generic LL1 trigger tile for use in the NCC LL1 system. The trigger tile features high input I/O bandwidth as well as the ability for inter-tile communication using Gbit serial links.

3.9.1 The NCC Event Based Triggering - Simulations

The NoseCone calorimeter will use a Local Level-1 (LL1) trigger to select events with a high-p_T photon or jet in the calorimeter acceptance. As is typical of PHENIX LL1 systems the processing will consist of a set of pipelined stages. First, a set of primitive data will be digitized on the front-end modules (FEMs). Second, this data will be transferred to an LL1 system, and finally the bit-reduced trigger information is sent from the LL1 system to the PHENIX Global Level-1 trigger system, possibly via a new regional trigger processor to combine Level-1 information from the different forward detectors.

The NCC front end electronics will aggregate the NCC pad data and form two types of tiles for trigger processing. The first, a set of 4x4 tower overlapping trigger tiles will be available for prescaled triggering at any p_T. The second set will be a collection of 8x8 tower overlapping trigger tiles. The 8x8 overlapping size was chosen to fully contain high-p_T

electromagnetic showers as well as a good match the η width of a jet of hadrons. For both the 4x4 and 8x8 triggers the algorithm will begin by examining the relevant trigger tile in the EM2 section of the calorimeter. If energy is found in the EM2 tile, a corresponding tile is constructed in the EM1 and HAD calorimeter sections based on the center of the trigger tile in EM2 and the assumption that the incident energy came from a vertex location at $z = 0$. This "steering" in theta angle accounts for the fact that particles do not enter the NCC at normal incidence.

A sum is formed from the trigger tile energies in the EM1, EM2 and HAD sections, and this energy sum is compared to a threshold based on the desired E_T trigger threshold and theta angle of the trigger tile in the EM2 section. In this way the total energy threshold varies as a function of theta in such a way as to keep the E_T threshold approximately constant. If the energy is above threshold, a trigger bit is set in the reduced bit output to Global Level-1. The reduced bit output of the NCC LL1 trigger, in the form of a set of bits indicating satisfied algorithms, would be transmitted to the GL1 system over optical fiber.

In order to separate electromagnetic from hadronic showers using the trigger tiles, an additional selection is made based on the fraction of the total shower energy that is in the HAD calorimeter section, HAD/(EM1 + EM2). If this ratio is less than one, the trigger tile is tagged as an EM (electromagnetic) trigger. Simulation studies show that this separation in 99% efficient for high-energy photon showers. Note that the 8x8 trigger is inclusive of the 8x8 EM trigger.

Studies of the anticipated rejection from the NCC LL1 have been done using the simulated events and the PHENIX detector simulation application (PISA). For proton-proton collisions at $\sqrt{s}$ = 500GeV, approximately one million minimum bias events were generated and simulated in the PHENIX apparatus. Rejection factors for the 8x8 and 8x8 EM trigger tiles were calculated, and are shown in Fig. 3.37. A table of the rejection factors is available in Table 3.9.1. We note that rejections in the range of 10000 for the 8x8 EM trigger can be obtained with an E_T threshold between 10-12.5 GeV.

In order to examine the expected event rejection in heavy ion collisions, the event generator Hijing was used. To cover the full range of potential colliding species at RHIC we chose to simulate Au+Au, Cu+Cu and Si+Si collisions. The expected rejection factors for the 8x8 EM and 8x8 trigger tiles are shown in Fig. 3.38 and Fig. 3.39. As expected, substantial event selectivity can be obtained for collisions of light ions, but the very high multiplicity in Au+Au collisions limits the overall rejection that can be achieved. The rejection factors are shown in tabular form in Table 3.9.1. These results are based on simulations of 500 events for Au+Au, 1600 events for Cu+Cu, and 3700 events for Si+Si.

Finally, we examined the expected event rejection in d+Au collisions (again using the event generator Hijing). The expected rejection factors for the 8x8 EM and 8x8 trigger tiles are shown in Fig. 3.40 and Fig. 3.41, with the rejection for each arm of the NCC identified separately due to the nature of the asymmetric colliding species. The rejection factors are shown in tabular form in Table 3.9.1. These results are based on simulations of 5000 d+Au events.

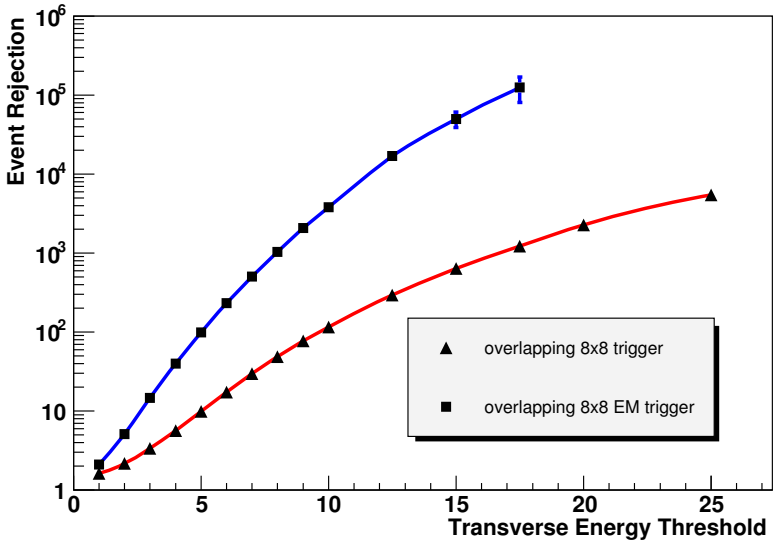

Figure 3.37: Anticipated NCC LL1 rejection factors of minimum bias proton-proton collisions at $\sqrt{s} = 500$GeV for the 8x8 EM and 8x8 trigger tiles, as described in the text.

E_T Threshold (GeV)	8x8 EM	8x8
1.0	2	1.6
2.0	5	2.0
3.0	15	3.5
4.0	40	5.7
5.0	99	10.0
6.0	233	17
7.0	505	30
8.0	1032	49
9.0	2083	77
10.0	3808	116
12.5	16910	295
15.0	49900	636
17.5	125000	1230
20.0	-	2300
25.0	-	5500

Table 3.3: Anticipated NCC LL1 rejection factors of minimum bias proton-proton collisions at $\sqrt{s} = 500$GeV for the 8x8 EM and 8x8 trigger tiles.

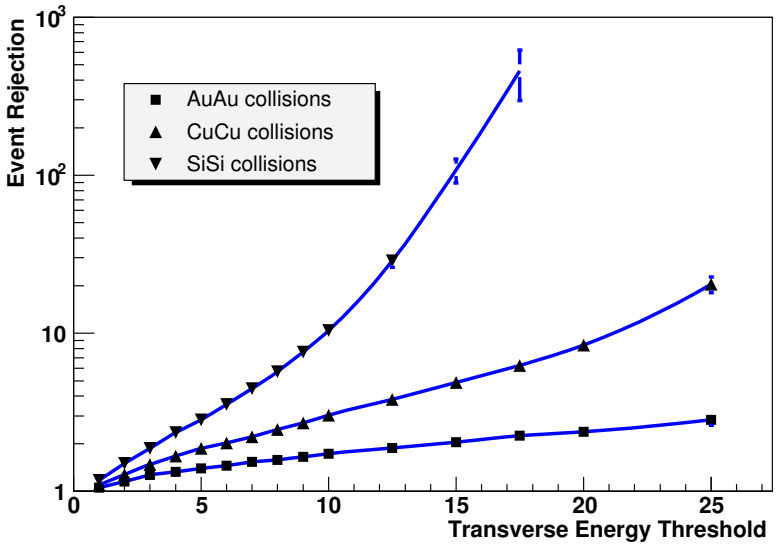

Figure 3.38: Anticipated NCC LL1 rejection factors of minimum bias heavy ion collisions at $\sqrt{s} = 200$GeV for the 8x8 EM trigger tile, as described in the text.

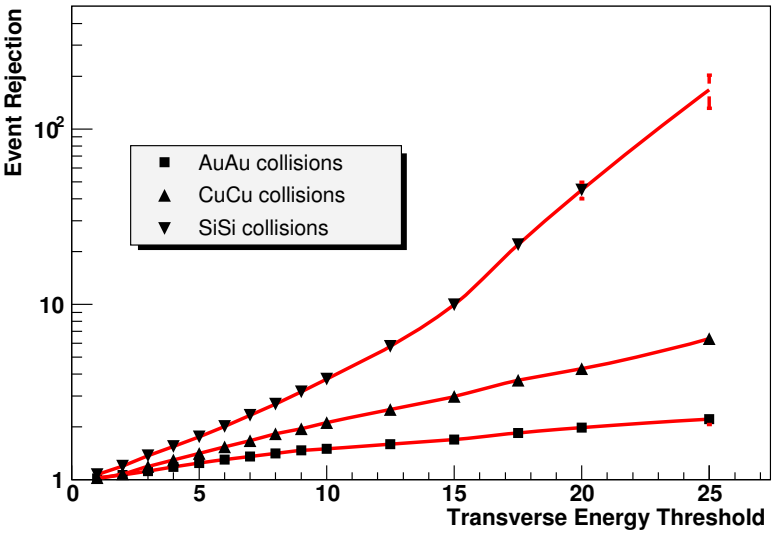

Figure 3.39: Anticipated NCC LL1 rejection factors of minimum bias heavy ion collisions at $\sqrt{s} = 200$GeV for the 8x8 trigger tile, as described in the text.

	Si+Si		Cu+Cu		Au+Au	
E_T Threshold (GeV)	8x8EM	8x8	8x8EM	8x8	8x8EM	8x8
1.0	1.2	1.1	1.1	1.0	1.1	1.0
2.0	1.5	1.2	1.3	1.1	1.2	1.1
3.0	1.9	1.4	1.5	1.2	1.3	1.1
4.0	2.4	1.5	1.7	1.3	1.3	1.2
5.0	2.8	1.8	1.9	1.4	1.4	1.2
6.0	3.5	2.0	2.0	1.5	1.5	1.3
7.0	4.5	2.3	2.2	1.7	1.5	1.4
8.0	5.7	2.7	2.5	1.8	1.6	1.4
9.0	7.6	3.2	2.7	2.0	1.7	1.5
10.0	10.4	3.7	3.0	2.1	1.7	1.5
12.5	29	5.8	3.8	2.5	1.9	1.6
15.0	108	10	4.9	3.0	2.0	1.7
17.5	459	22	6.3	3.7	2.3	1.8
20.0	1225	45	8.4	4.3	2.4	2.0
25.0	-	167	20	6.4	2.8	2.2

Table 3.4: Anticipated NCC LL1 rejection factors of minimum bias heavy ion collisions at $\sqrt{s} = 200$GeV for the 8x8 EM and 8x8 trigger tiles.

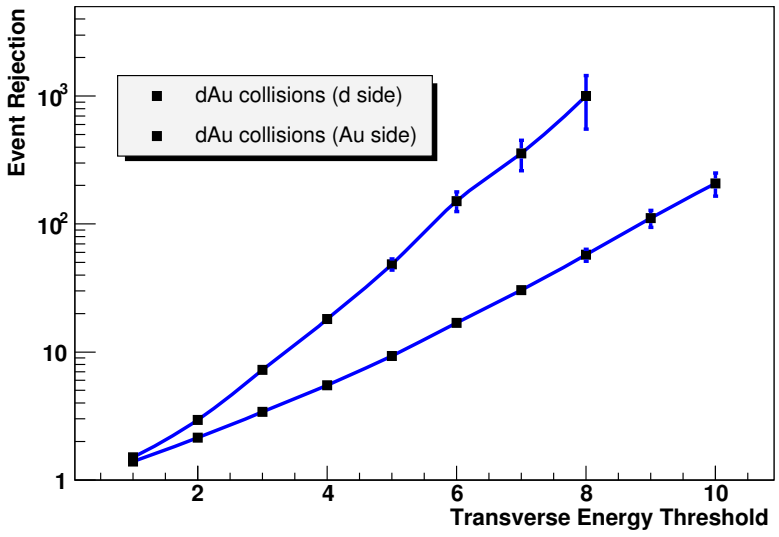

Figure 3.40: Anticipated NCC LL1 rejection factors of minimum bias d+Au collisions at $\sqrt{s} = 200$GeV for the 8x8 EM trigger tile, as described in the text. Note that the trigger rejections depend on whether the NCC arm in in the d-going or Au-going side of PHENIX.

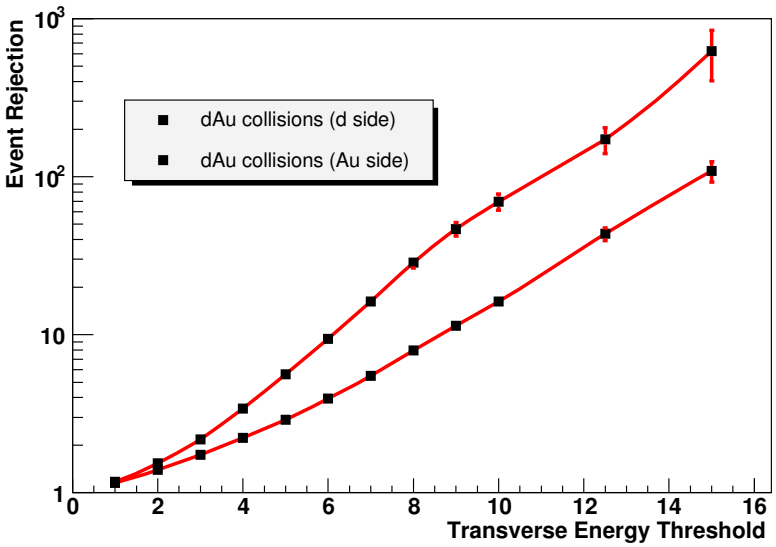

Figure 3.41: Anticipated NCC LL1 rejection factors of minimum bias d+Au collisions at $\sqrt{s} = 200$GeV for the 8x8 trigger tile, as described in the text.Note that the trigger rejections depend on whether the NCC arm in in the d-going or Au-going side of PHENIX.

	d side		Au side	
E_T Threshold (GeV)	8x8EM	8x8	8x8EM	8x8
1.0	1.5	1.2	1.4	1.2
2.0	2.9	1.5	2.1	1.4
3.0	7.2	2.1	3.4	1.7
4.0	18	3.4	5.5	2.2
5.0	48	5.6	9.3	2.9
6.0	151	9.4	17	3.9
7.0	357	16	30	5.5
8.0	1000	29	57	7.9
9.0	-	47	111	11.4
10.0	-	69	208	16.2
12.5	-	172	1666	43
15.0	-	625	-	109

Table 3.5: Anticipated NCC LL1 rejection factors of minimum bias d+Au collisions at $\sqrt{s} = 200$GeV for the 8x8 EM and 8x8 trigger tiles.

3.9.2 Ongoing R&D Program

With the help of institutional contributions it was possible to maintain a small, but well focused, effort over the past three years to explore technologies for silicon detectors suitable for the PHENIX NCC. The Collaborating groups in US, Japan, Russia, Korea, Finland and Czech Republic were able to design, manufacture, and test batches of DC-coupled pad-structured Si sensors, AC-coupled pad-structured sensors and first ever samples of StriPixel sensors with effective strip width of 0.5 mm. Their were enough DC coupled sensors for the proof-of-principle prototype calorimeter which was completed and beam-tested in November 2005 (Figs. 3.42, 3.43). The main results of completed R&D program are presented in the Appendices.

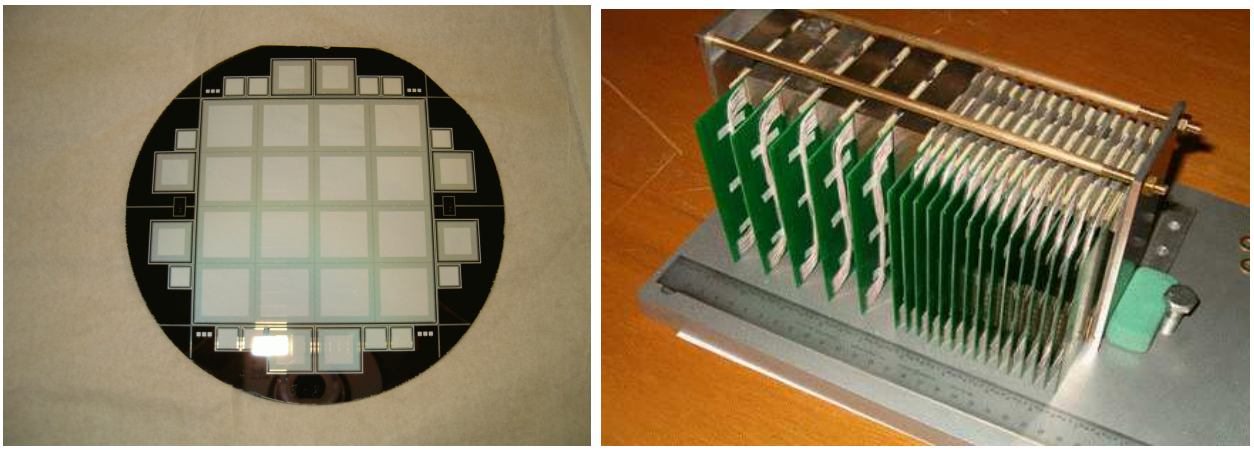

Figure 3.42: (Left) The NCC Silicon sensor. An undiced wafer is shown. The active area is subdivided into 16 readout pads 1.5x1.5 cm^2 each. (Right) First proof-of-principle prototype calorimeter (2005). Electronics designed for cosmic ray satellite experiments were used for readout (not shown).

The ongoing R&D effort is aimed towards finalizing technology choices. We closely follow the development of the digital signal processing plan for the HBD, which is functionally identical to what is proposed for the NCC. In addition SVX4-based readout is currently under development for the two outer layers of the PHENIX Barrel Silicon Vertex Detector (VTX).

The key issues still to be resolved are the noise (capacitative and pick-up) in the detector operating with ganged sequential pads and optimization of the StriPixel sensor design. The solution to the noise issue requires extremely careful design with care taken of grounding the detector components and readout electronics. We benefited from help from the D0 silicon laboratory at FNAL in the detector design and will further rely on their expertise in large silicon systems and detector mechanics.

We continue StriPixel sensor development (Fig. 3.44). We retain the option of single sided strip detectors of a similar geometry as a backup solution. We plan to make the final technology choice in the summer of 2007.

For many parts of the NCC, the technology choices have been made, and R&D is focusing

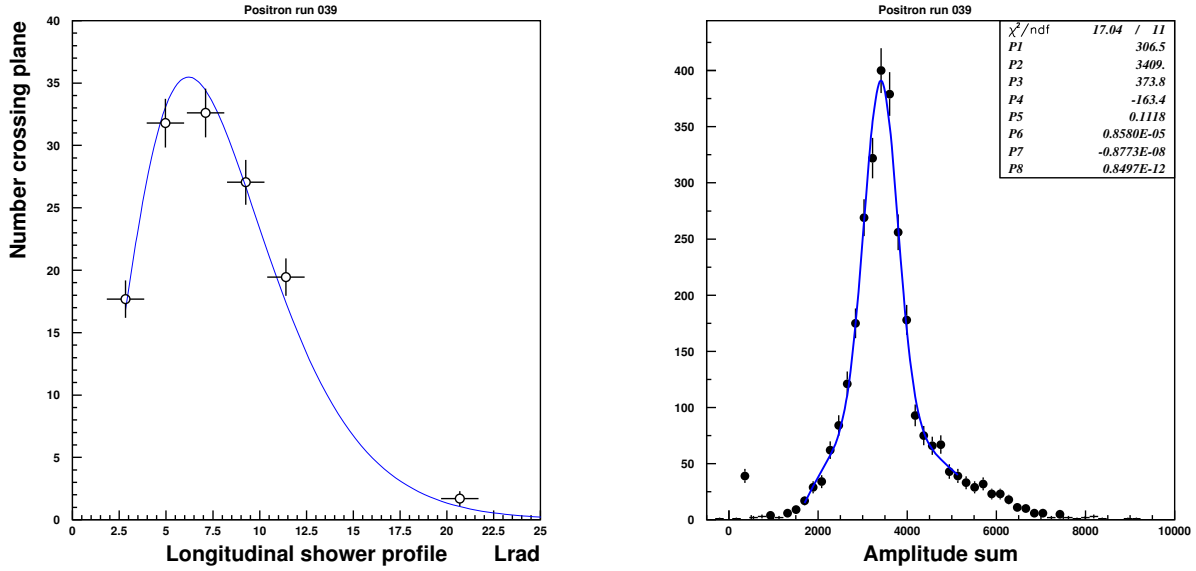

Figure 3.43: (Left) Longitudinal profile of electrons in prototype detector shown in Figure 3.42. (Right) Energy distribution in the NCC prototype measured exposing detector to a 10 GeV/c positron beam.

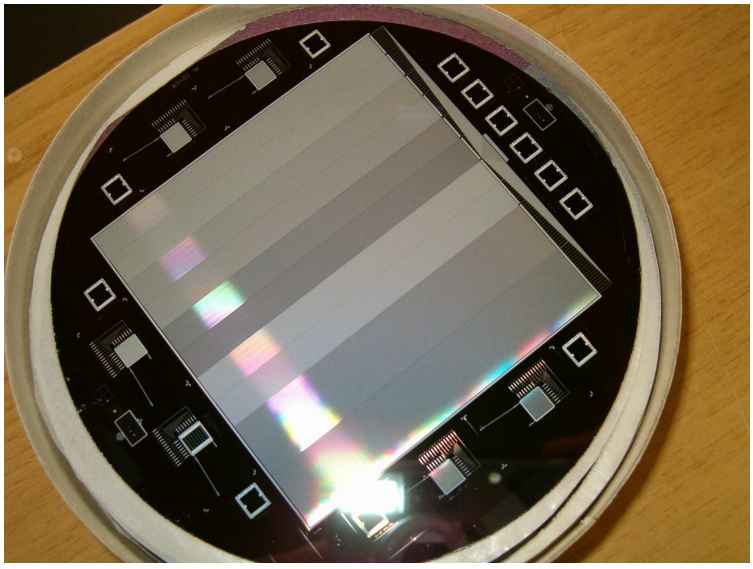

Figure 3.44: Prototype wafer with 5 different StriPixel structures in both the X and Y directions produced by ELMA. The technology is single-metal with implanted bridges in the orthogonal direction.

on prototyping the designs. The following topics will be pursued so the construction of the NCC can start in FY08:

- Production and testing of StriPixel test sensors to study the influence of inter-pixel pitch on the charge sharing and crosstalk between strips;
- Finalizing the choice of the sensors for position sensitive layers;
- Finalizing design of the readout units for both kind of sensors;
- Testing heat dissipation in position sensitive layers. If required - designing and testing a heat removal scheme for the SVX4 based readout electronics;
- Finalizing conversion of ATLAS preamps for the PHENIX NCC application. Implementing a new version of amplifier with 2-sided hybrid technology;
- Development of the readout electronics for the NCC;
- Small scale production runs of pad-structured and StriPixel sensors to equip a fullscale brick-sized NCC prototype for on-the-bench and test beam measurements of the detector performance;
- Finalizing detector mechanical design;
- Constructing system prototype (single brick) and running test-beam experiment in the Fall of 2007 or early 2008.

Chapter 4

Project Management and Responsibilities

The organization and management of the proposed effort is embedded in the management structure of the PHENIX experiment, which is part of the BNL RHIC project. The new organization satisfies a number of requirements including an interface to the existing RHIC and PHENIX management structure and roles and responsibilities within the existing PHENIX subsystem structure. Particular attention has been paid to the fact that a significant portion of the project efforts is carried by PHENIX groups belonging to the international component of the PHENIX collaboration. Deliverables, responsibilities for deliverables and the accountabilities of the participating institutions are defined. These responsibilities will be formalized in memoranda of understanding (MOU's) between PHENIX and the participating institutions. In this section, we outline our proposed management organization and delineate responsibilities within the project.

4.1 Project background

The proposed project is part of a detailed upgrades program to enhance the physics capabilities of PHENIX. The development of the PHENIX upgrade program started in response to the recent NSAC long-range plan, which was developed in 2000. The PHENIX Upgrade program spans the next 8 years. Realizing this plan will enable PHENIX to remain competitive in the study of relativistic heavy ion collisions well beyond the turn on of LHC expected for 2008. It will also advance our understanding of QCD by fully exploiting the unique spin physics capabilities of RHIC. The plan covers a broad range of measurements in A+A, p(d)+A, and p+p and its goal is to provide key measurements that currently can either not be addressed at RHIC or only with limited accuracy.

The calorimeter component of the PHENIX upgrade program was first proposed in the fall of 2004 when a Letter of Intent (LOI) for an upgrade of the forward region of PHENIX was written and presented to the PHENIX management. This LOI included the NCC, and a trigger for the muon spectrometer which is now being funded by the NSF. The forward LOI was reviewed at a joint meeting of the PHENIX detector council (DC) and executive

council (EC). Following their recommendations PHENIX management (PM) endorsed both projects and the group was charged with preparing the NCC proposal for presentation to the DOE through BNL.

The NCC project was reviewed in December 2004 by a panel, including PHENIX Detector Council and Executive Council members, as well as external members who are not PHENIX collaborators. The recommendations of the review panel were very helpful to prepare the proposals. All recommendations were addressed and answers were incorporated. Subsequently, in March of 2006 a formal BNL review was undertaken and a recommendation was made by the review panel that the project begin funding in FY 2008. In addition technical recommendations were suggested to the NCC collaboration and again the recommendations of the review panel were addressed.

4.2 The management plan for the NCC

4.2.1 DOE/BNL management

The DOE Office of Nuclear Physics (NP) has overall DOE responsibility for the project. Jehanne Simon-Gillo is the Federal Program Manager for the project. The BNL project oversight manager is Thomas Ludlam, BNL. The BNL project oversight manager will keep the BNL management and the DOE informed about the technical goals and progress of the project.

4.2.2 PHENIX management structure

The NCC project is part of the PHENIX project and as such integrated into the PHENIX management structure as described by the PHENIX bylaws. The PHENIX Collaboration Management has overall responsibility for the successful execution of the scientific operation of the PHENIX detector. Barbara Jacak (Stony Brook) is the PHENIX Spokesperson.

The PHENIX Detector Council (DC) will advise PHENIX management on the design, construction, and integration of the NCC. The DC is co-chaired by the Operations Manager (Edward O'Brien) and the Upgrades Manager (Axel Drees). The NCC subsystem manager will serve as a member of the DC.

4.2.3 PHENIX subsystem leadership

We expect that the proposed NCC project will be funded through the DOE Office of Nuclear Physics (DOE-NP) beginning in 2008. The collaborating institutions will jointly fund remaining R&D efforts (2006-2007) resulting in construction and beam-testing of a W-Si prototype calorimeter serving as NCC system prototype. A successful completion of the NCC will require close collaboration between participating institutions with a well-defined matrix of responsibilities and contributions in terms of deliverables. These deliverables and planned sources of contributions are outlined below. Within PHENIX the responsibility for the NCC subsystem will be shared by the subsystem leader, Richard Seto (UCR) and his

two deputies, Itaru Nakagava (RIKEN) and Edouard Kistenev (BNL). The subsystem leader reports to PHENIX PM and will represent the NCC in the PHENIX DC.

Simultaneously, Edouard Kistenev will serve as the DOE contract project manager (CPM), and will have the fiscal and construction responsibility for the DOE funded deliverables as outlined in this proposal. Of course, this involves appropriate planning, budgeting, and reporting.

4.2.4 Role of BNL

Because we expect that all DOE funding for this effort will be directed through the BNL Physics Department, BNL line management will have ultimate fiscal and managerial responsibility for the construction of the NCC and for its subsequent operation.

Fig. 4.1 shows a management chart of the NCC project. The subsystem manager has general responsibility for the implementation of the project and is assisted by two deputies. In addition the manager and his deputies will have fiscal responsibilities. As mentioned Edouard Kistenev will have responsibility for DOE funds. As a separate but related item, Itaru Nakagawa will have the fiscal responsibility for RIKEN funding which may go to the construction of a second NCC. Similar to other upgrade projects in PHENIX, the PHENIX operations manager will assist the project in all integration matters and is responsible for installation of the detector into the PHENIX experiment and for the safety of operations. The institutions that will participate in the implementation of individual tasks are given in the bottom of every task block in Fig. 4.2. When our international collaborators, notably Russia, Czech, Finland, and Korea, are represented by several institutions working together they are indicated by nation, rather than by individual institution. PHENIX safety, DAQ, and infrastructure are common to all subsystems, so they are not listed as an explicit part of NCC management.

4.2.5 Specification of deliverables

The NCC is divided into subprojects, which themselves are divided into tasks detailed in an NCC Microsoft Project File. The main tasks identified as blocks in Fig. 4.2 are closely related to deliverables, which need to be completed before the NCC construction project can be considered complete. Below are the major deliverables and responsible institutions and a brief review of institutional responsibilities. Note that JINR involves three laboratories - the first headed by Anatoly Litvinenko primarily responsible for mechanical design and construction, the second headed by Sergey Bazylev, responsible for electronics, and the third headed by Nikolai Zamyatin responsible for silicon detector testing and assembly.

4.2.5.1 Calorimeter

- Silicon pad-structured sensors designed and implemented to the specification: **MSU/JINR/Czech/Korea**

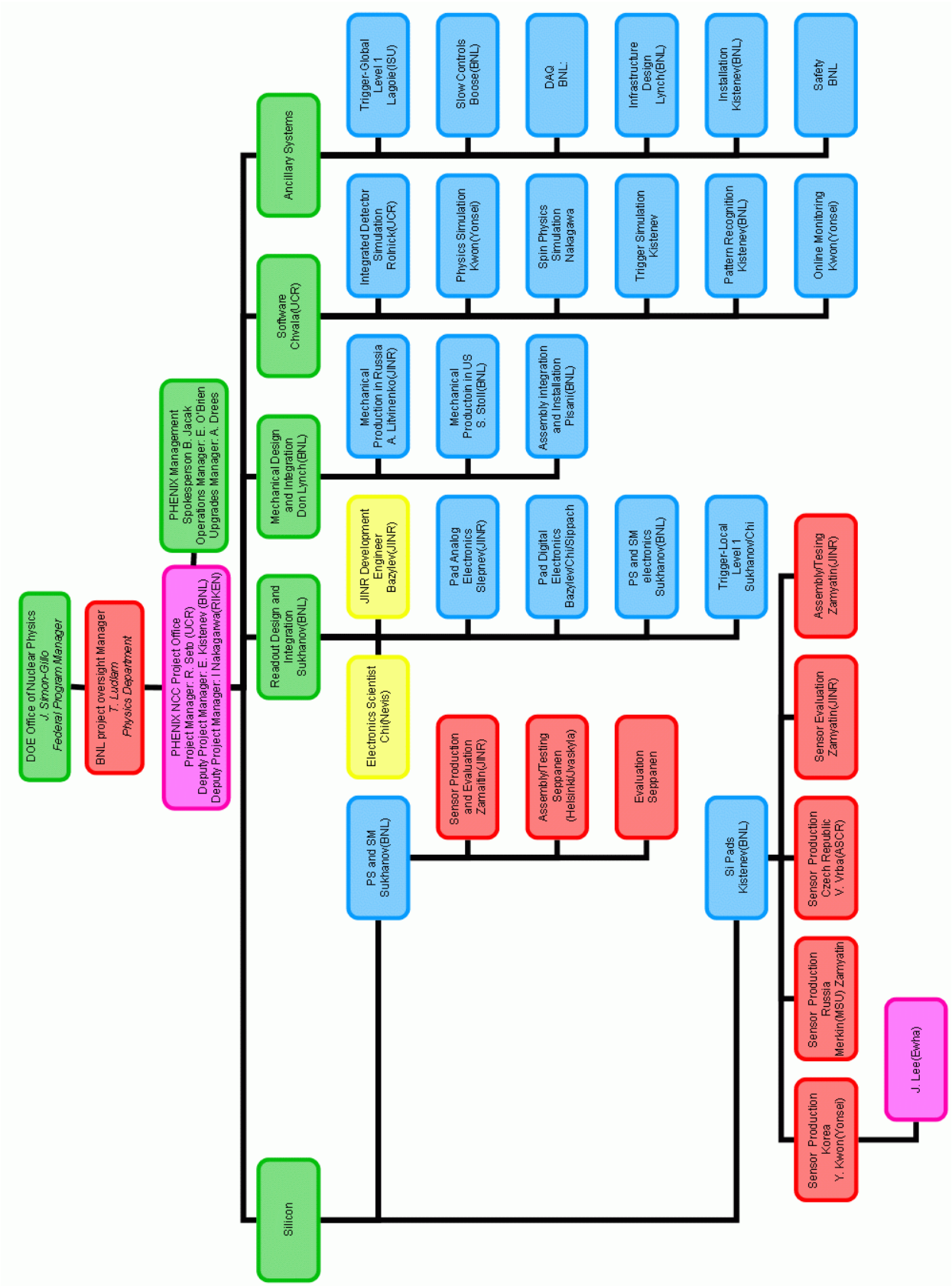

Figure 4.1: Management chart of the NCC project.

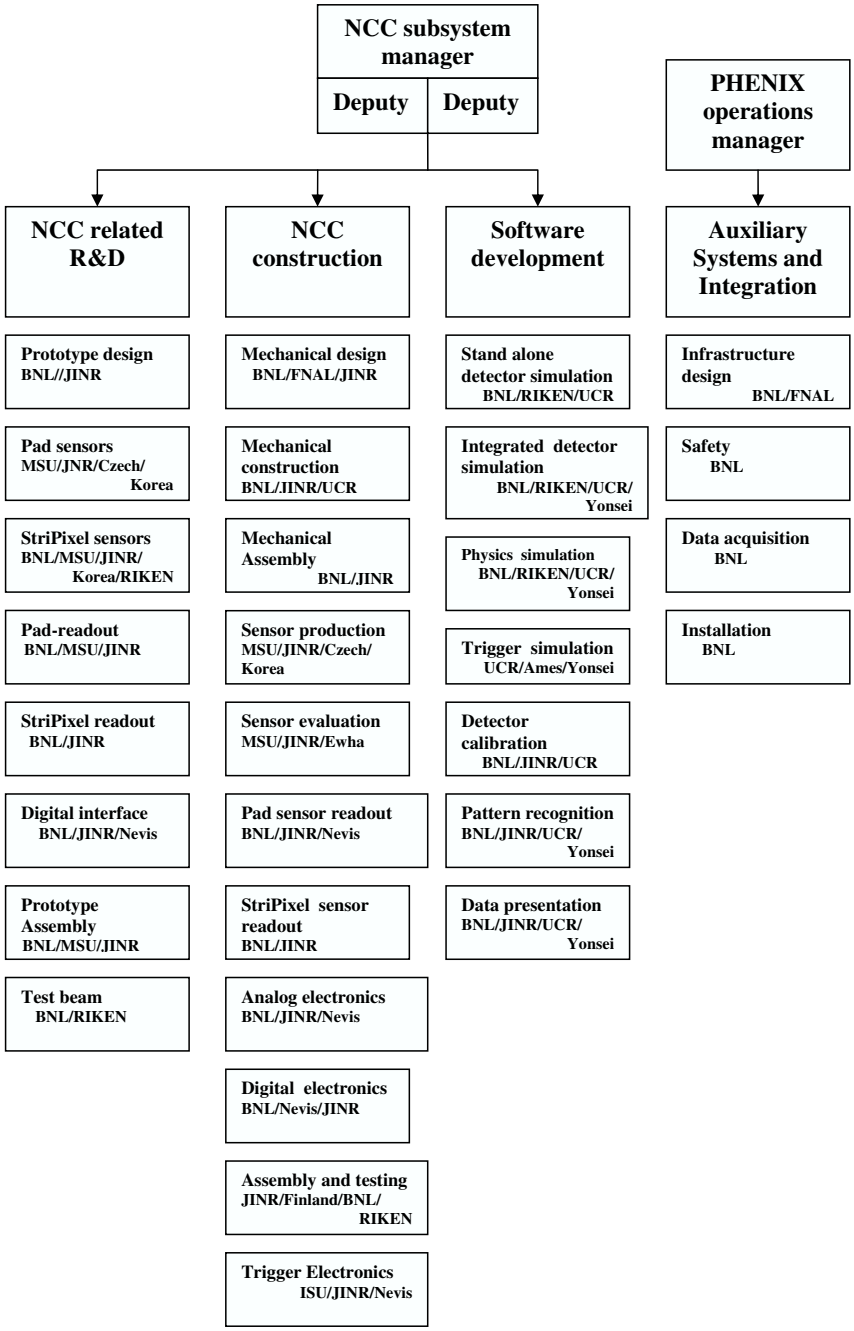

Figure 4.2: Institutional tasks for the NCC project.

- Silicon strip sensors designed and implemented to the specification: **MSU/JINR/BNL/Korea**
- Pad detector electronics
  - Readout units for the pad-structured calorimeter layers: **MSU/JINR/Nevis**
  - Analog data processing electronics for pad-structured layers (EM1/EM2/HAD segments of NCC): **BNL/JINR/Nevis**
- StriPixel detector electronics
  - Readout units for PS and SM detectors: **BNL/JINR**
  - Detector-end data processing for StriPixel PreShower and ShowerMax layers: **BNL/JINR**
- Digital data processing: **BNL/Nevis/JINR**
- Trigger electronics: **ISU-Ames/JINR/Nevis**
- Support structure and absorber plates: **BNL/UCR/JINR**
- Calorimeter mechanical components: **JINR**
- Assembly and testing of Pad Senor Modules **JINR/Ewha/Yonsei**
- Assembly and testing of StriPixel Modules **Jyvaskyla/Hensinki/Ewha/Yonsei**
- Assembly and testing of calorimeter bricks: **BNL/UCR/RIKEN**
- Assembly and testing of calorimeter: **BNL/UCR/RIKEN**

4.2.5.2 DAQ system

- Data collection modules: **BNL/Nevis**
- Software development for data collection, monitoring and analysis: **BNL/UCR/RIKEN**

4.2.5.3 Auxiliary Systems and Integration

- System support requirements specified, including heat loads, power distribution, mechanical tolerances and grounding scheme: **BNL/FNAL**
- Ancillary systems operational, including power distribution and cooling system: **BNL**
- Installation and integration:**BNL**
- Commissioning of full detector system: **BNL/UCR/RIKEN**

4.3 Institutional involvement

4.3.1 US based Institutions

Currently 20 institutions with over 70 individuals are involved in the NCC project. The different institutions bring in diverse research backgrounds, physics interests and expertise, which form a broad base to carry out the proposed project. Each group assumes specific responsibilities and will participate actively in the NCC project. According to their expertise and interests these groups will be involved in construction, installation, commissioning, operation, and data analysis. Formal commitments of the involved institutions will be specified in Memoranda of Understanding (MoU). Many of these groups have been actively involved in the R&D effort through institutional contributions, while others have joined the project only recently. Below are brief descriptions of expertise and potential involvement of the institutions.

The PHENIX group at University of California, Riverside has taken primary responsibility for Simulations and Software development, and is heavily involved with ongoing NCC related R&D. As the subsystem manager, UCR group leader Richard Seto has played a leading role in the management of the NCC, and was instrumental in bringing the project to the proposal stage.

The BNL physics group brings management and physics experience and broad experience with silicon detector and calorimeter technology. Individual group members bring specific technical skills that will be important for the successful construction, installation, commissioning and operation of the NCC in the RHIC environment. Edouard Kistenev of BNL will serve as the DOE contract project manager (CPM). He has taken a leading role in developing the concept and design of the NCC.

The PHENIX Group, led by Don Lych from the BNL Physics Department provides infrastructure and technical support as part of Systems Engineering and Integration (SE&I) for the entire PHENIX experiment. It has a staff of mechanical and electrical engineers and a group of experienced technicians who are intimately familiar with the detector, and work closely with the BNL Collider-Accelerator Department for operations and any modifications to its present design. They designed much of the infrastructure for the baseline detector, including racks, cable trays, electrical power, cooling, access, safety systems and numerous other services, and carried out the installation of all of the present subsystem detectors. This group will now be closely involved with the design of the infrastructure and support for the PHENIX Forward Calorimeters, and with its installation into PHENIX.

BNL's Instrumentation Division's Silicon Detector Development and Processing Laboratory (SDDPL) will be involved in the development of silicon strip detectors for PHENIX Upgrades. Zhen Li is the primary designer for the StriPixel detectors. The activity of the group will include detector simulation, design, and processing of prototype detectors. SDDPL will also be involved in laser scan tests of those prototypes, these tests will be carried out in close collaboration with the BNL Physics Department and RIKEN. The BNL Instrumentation Department proposed the solution based upon hybrid amplifiers earlier developed for the ATLAS experiment at CERN to serve as a basis for the analog signal processing for NCC. The further activities will involve modification to the schematics for the amplifiers to

work with positive polarity signals, compactification of the layout, testing and participation in production. This work is being done in collaboration with engineers at JINR.

The PHENIX group from Iowa State University (led by John Lajoie) will take responsibility for the design, implementation, construction, and support of the NCC Level-1 trigger system (similar to their earlier work on the design, construction and maintenance of the PHENIX Level-1 trigger system).

The BNL PHENIX group has primary responsibility for a number of major subsystems. These include Electronics Facilities and Infrastructure (EF&I), Online Computing Systems (ONCS) and Offline Computing. These groups will participate in the electronic integration and readout of the NCC detector into the PHENIX data acquisition system, and will be involved with track reconstruction and offline data analysis.

The PHENIX group from the University of Illinois (led by M. Grosse-Perdekamp) has primary interest in the use of the NCC for spin analysis and will not have any formal hardware responsibilities, because of other commitments.

The BNL PHENIX group will also serve as host institution for the project and will provide the lab space for the final detector assembly and testing.

4.3.2 International participation

The Joint Institute for Nuclear Research in Dubna has broad expertise in all aspects of experimentation in Nuclear and particle physics. The JINR PHENIX group can draw on expertise of their local and international collaborators in mechanics, electronics and sensor development. As mentioned previously there are three major groups of physicists at JINR involved with the NCC. The first group, headed by Anatoly Litvinenko, has already contributed to the initial design of NCC mechanical structure, and will continue this work in collaboration with group from FNAL, and will take major responsibility for production of major mechanical components for NCC. The second group, headed by Sergey Bazylev, has taken major responsibilities in the electronics design for the pad modules - both for the preamp boards and the FEM. The third group, headed by Nikolai Zamyatin, will take major responsibility for the assembly and testing of the pad sensor modules. They will also act as a liaison to ELMA, which is producing pad and StriPixel detectors in Russia.

The Moscow State University group, led by Michael Merkin has internationally recognized expertise in silicon detectors and their application in experimental physics. MSU contributed to the ZEUS experiment at DESY (silicon hadron rejector), the D0 experiment at FNAL (central tracker), and a number of smaller projects. Together with JINR, RIKEN, BNL and UCR the MSU group built and tested a "proof-of-principle" NCC prototype, which demonstrated robustness of the technology. MSU will share the major responsibility for production and evaluation of pad-structured sensors for the calorimeter together with JINR.

The Finnish group at Jvaskyla, led by Jan Rak and Helsinki, led by Henri Seppanen have now taken the responsibility for the testing and assembly of the StriPixel layers. They bring a great deal of experience in this as they have assembled silicon detectors for the ALICE experiment at CERN at their laboratory at the Helsinki Institute of Physics. This work has just come to an end and the facilities will now be used for the NCC. Jyvaskyla has hired a

physicist to oversee the operation at the laboratory in Helsinki.

The Korean groups at Yonsei University, led by Ju Kang and Yongil Kwon and Ewha University, led by Il Park and Jik Lee have become involved in the work on both the pad and StriPixel sensors. Ewha has built the Silicon detector for the CREAM balloon project working together with industrial partners SENS Technology - a small company specializing in Silicon detectors. The group is currently working on prototyping the NCC pad and StriPixel detectors and has taken a major responsibility of a test beam prototype to be put into the CERN test beam in September. The group at Yonsei will also take major responsibilities in software, simulation and data analysis.

The Czech Republic group, led by Miroslav Finger and Vaclav Vrba, involves physicists from the Institute of Physics, Charles University and the Czech Technical University, who are primarily interested in the PHENIX spin physics program and silicon detector development. The Czech group has a history of collaboration with groups from JINR Dubna and an established relationship with the major silicon processing plant in the Czech Republic (ON Semiconductors). As part of their contribution to the NCC project, Prague collaborators have already initiated the first round of sensor prototyping at ON Semiconductors. This development will allow better estimates of the potential benefits of sensor production in the Czech republic and will help management to apportion the sharing of silicon production efforts between MSU, Korea, and ON Semiconductors.

Chapter 5

Budgets and Schedule

5.1 Overview

The PHENIX Forward Calorimetry Upgrade Project naturally splits into three subprojects namely:

- W-Si Calorimetry R&D to culminate in construction of a W-Si calorimeter system prototype in late 2007 or early 2008;
- Construction and installation of DOE funded NCC staring in 2008 and ready for physics in the fall of 2010;
- Construction and installation of a second NCC starting in 2009 and ready for physics in 2011.

The project is based on a cost sharing between the DOE Office of Nuclear Physics and the PHENIX NCC Group, as introduced in this Proposal. The group is jointly responsible for funding the ongoing W-Si Calorimetry R&D program, which is planned for completion in 2008 with construction and beam testing of the Calorimeter System Prototype. The DOE Construction funding is expected to start in 2008 and continue for three years with peak funding in 2009. It is important to note that in these plans the DOE funding will be for the complete construction of one of the pair of NCC detectors. Remaining detector development issues will be resolved using institutional engineering manpower. Sufficient funds to cover the cost (R&D and Construction) of the second PHENIX NCC unit will be provided by non-U.S. collaborators.

In what follows we discuss cost and scheduling issues related to the DOE Construction Project to allow implementing the proposed upgrade in the minimal configuration consisting of a single calorimeter unit. The decision to deploy this unit as an upgrade to North or South muon arms will depend on RHIC running schedule and configurations for collisions of different ion species. Note that for p(d)+A collisions this would mean placing the NCC on proton/deuteron going direction.

The cost and schedule for the NCC Upgrade project has been developed using engineering estimates, vendor quotes and experience from the construction of silicon detectors from

participating Institutions. The production schedule of the two subprojects (First and Second NCC) are not totally independent, and unless extra production capacity is identified the starting date for the Second Calorimeter Project will be constrained by funding and by the rate of production of Si sensors at the ELMA (Russia), ON Semiconductors (Czech Republic) and SENS (Korea) facilities. While the estimated base costs of the North and South detectors are identical, the real cost to the PHENIX NCC Group can be different depending on accounting practices specific to collaborating countries. In this section, we outline only those costs which concern the DOE.

5.2 Contingency Analysis

The contingency is calculated according to the presecription described in the Appendix. The average contingency for the construction project is 25%.

5.3 Overhead Estimate

The overhead applied to funds requested from the DOE is based on the standard rate for capital construction projects at BNL. This overhead is applied to base cost prorated for contingency and spares and included into "Cost to Project" in our budget tables. The additional overhead charged by local institutions is not listed separately. However, these costs are included in the budget table via cost estimates for items ordered in foreign countries through collaborating institutions. In particular, all manpower costs are fully burdened costs, including local overhead.

5.4 Tungsten-Si Calorimeter R&D

The ongoing collaboration funded R&D efforts are aimed at confirming design ideas developed in the course of earlier 2005/2006 R&D and at constructing and testing a full scale brick-wide prototype of the W-Si calorimeter including the SM and PS layers. When this portion of the project is completed the Collaboration will be in possession of

- the final design and production documentation for DC-coupled pad-structured Si sensors developed to NCC specifications;
- the final design and production documentation for the pixelated strip Si sensors (StriPixels) developed to NCC specifications;
- the final design and production documentation for the pad-structured readout units. The design documentation for readout unit components (carrier and interconnect boards) will be ready for submission to pc-board production houses;
- the final design and production documentation for the pixelated strip readout units including sensor-readout hybrids, brick-end receiver boards, trigger and timing control board and front-end modules interfacing the NCC to PHENIX DAQ;

- prototype 12x12 cm^2 W-Si calorimeter assembled and tested in a test beam.

The completion of this the R&D program is a major milestone and is necessary to address the challenges of this Upgrade Project. It is important for the collaboration to accumulate test beam data using a detector that, in all essential aspects, is identical to the NCC the Collaboration proposes to build. To this purpose the collaboration is also planning a test beam exposure of a very first production calorimeter brick prior to its installation into PHENIX. Exposing part of the real detector to high energy particle test beams will confirm performance expectations, and provide the experience and test data necessary for successful use of the detector in the PHENIX experiment.

This R&D program will be supported by the Collaboration with major funding provided by BNL (BNL Generic R&D funds) and other collaborating institutions in the US and Japan, and in-kind and man-power contributions from other collaborating Institutions. Most of the funding required to carry this program in 2006 is already committed.

5.5 NCC Construction

The total cost of the Nose Cone Calorimeter Construction Project to DOE in 2007 $US including contingencies and overhead is **4.3 million $US**. This number is detailed in the table below where the base cost estimates (including spares), contingency requests and overheads are first quoted separately. We have also separated the costs directly related to construction of a single NCC unit and those for ancillary systems (PHENIX DAQ, infrastructural and installation costs).

The funding from the DOE will cover

- the construction of a single Calorimeter unit comprising two fine electromagnetic and one coarse hadronic pad-structured segments, PreShower and ShowerMax detectors in 2008-2010,
- an upgrade to the PHENIX infrastructure to allow for installation of this detector in 2010,
- installation and commissioning of a single Nose Cone Calorimeter in 2010.

Funding request for NCC-One Construction Project (k$US)

Year	2008	2009	2010	Base Cost	Contingency	Overhead	Total
NCC Construction	1400	1600	1071	2626	862	628	4116
Ancillary Systems			227	130	24	28	182
Total DOE Construction	1400	1600	1298	2756	886	656	**4298**

Figure 5.1: Profile of DOE cost estimates for first NCC.

As indicated in Fig. 5.1, the first NCC unit is planed to be ready for physics for the RHIC run that begins in the fall of 2010. Below are the budgetary and scheduling details.

WBS	Task Name	Funding Request
1.	**NCC Project**	
1.1	**Generic R&D**	$105,300
1.2	**W-Si Calorimeter R&D**	$94,100
1.3	**Calorimeter mechanical design**	$55,000
1.4	**Calorimeter Prototyping**	$138,238
1.5	**Final NCC Design Review**	$0
1.6	**NCC Construction Project**	
1.6.1	**NCC One: Grand Total**	$4,297,613
1.6.1.1	**NCC One: Construction**	$4,115,893
1.6.1.1.1	Stock components (connectors etc)	$76,700
1.6.1.1.2	**Silicon Sensors**	$1,988,506
1.6.1.1.2.1	Silicon wafers	$324,479
1.6.1.1.2.2	Pad sensor production [each]	$1,234,044
1.6.1.1.2.3	Certification [each]	$49,362
1.6.1.1.2.4	Strip sensor production [each]	$356,832
1.6.1.1.2.5	Certification [each]	$23,789
1.6.1.1.3	**Pad-structured readout units**	$464,624
1.6.1.1.3.1	Ladder carrier boards	$56,697
1.6.1.1.3.2	Stack kits	$155,137
1.6.1.1.3.3	Assembly and testing [stacks]	$246,809
1.6.1.1.3.4	FPC cables	$5,981
1.6.1.1.4	**Pad front-end (preamps)**	$133,482
1.6.1.1.4.1	Mather boards	$32,710
1.6.1.1.4.2	Preamp hybrids	$90,860
1.6.1.1.4.3	Crates	$9,912
1.6.1.1.5	**Strip-structured readout units**	$129,826
1.6.1.1.5.1	SVX4's	$0
1.6.1.1.5.2	Ladder Carrier Boards	$2,442
1.6.1.1.5.3	Sensor Readout Modules (SRM)	$43,613
1.6.1.1.5.4	Dual sensor stack kits	$19,937
1.6.1.1.5.5	Assembly and testing [stacks]	$59,472
1.6.1.1.5.6	Interstack jumpers	$2,181
1.6.1.1.5.7	FEM cables	$2,181
1.6.1.1.6	**Strip front-end (data collection)**	$19,081
1.6.1.1.6.1	Front End Modules [FEM]	$16,900
1.6.1.1.6.2	Trigger and timing module	$1,558
1.6.1.1.6.3	Bias Power	$623
1.6.1.1.7	**Mechanical Structure**	$580,454
1.6.1.1.7.1	W plates for a single NCC	$566,400
1.6.1.1.7.2	Components for brick construction	$3,717
1.6.1.1.7.3	FEM crates	$425
1.6.1.1.7.4	Support structure	$7,080
1.6.1.1.7.5	Cooling system	$2,832
1.6.1.1.8	**Assembly of bricks**	$37,878
1.6.1.1.8.1	Assembly of pad sampling cells	$4,956
1.6.1.1.8.2	Assembly of pad ROU's	$9,912
1.6.1.1.8.3	Certification of pad sampling cells	$9,912
1.6.1.1.8.4	Assembly of PreShower layer	$6,549
1.6.1.1.8.5	Assembly of ShowerMax layer	$6,549
1.6.1.1.9	Digital signal processing [channels]	$560,736
1.6.1.1.10	HM Cables	$124,608
1.6.1.1.11	System test	$0
1.6.1.2	NCC One: DAQ	$113,280
1.6.1.3	NCC One: Integration	$40,120
1.6.1.4	NCC One: Installation	$28,320

Figure 5.2: Budgetary and scheduling details covering major tasks involved in construction of the first NCC unit (extracted from the project file).

The major cost item and the critical item in the project are silicon sensors. The two kinds of sensors used in the calorimeter are responsible for nearly half of the unit cost. The other half is spread relatively uniformly among mechanics and electronics. The production of sensors drives the schedule. At this time we have identified three suppliers, Russia(ELMA), Czech Republic (ON Semiconductors) and in Korea (SENS), interested in producing Si sensors following our design. ELMA and ON Semiconductors both have an experience with production of sensors close to NCC specifications, hence cost estimates and schedules presented in this proposal are based upon quotations from ELMA. It will take two years to produce sensors for a single NCC unit if all production is done at ELMA. To shorten this time down to the 18 months reserved for this task in our schedule we will have production running both at ELMA and ON Semiconductors. with the Korean option being seriously investigated. SENS has produced a first pad sensor module which will be tested soon.

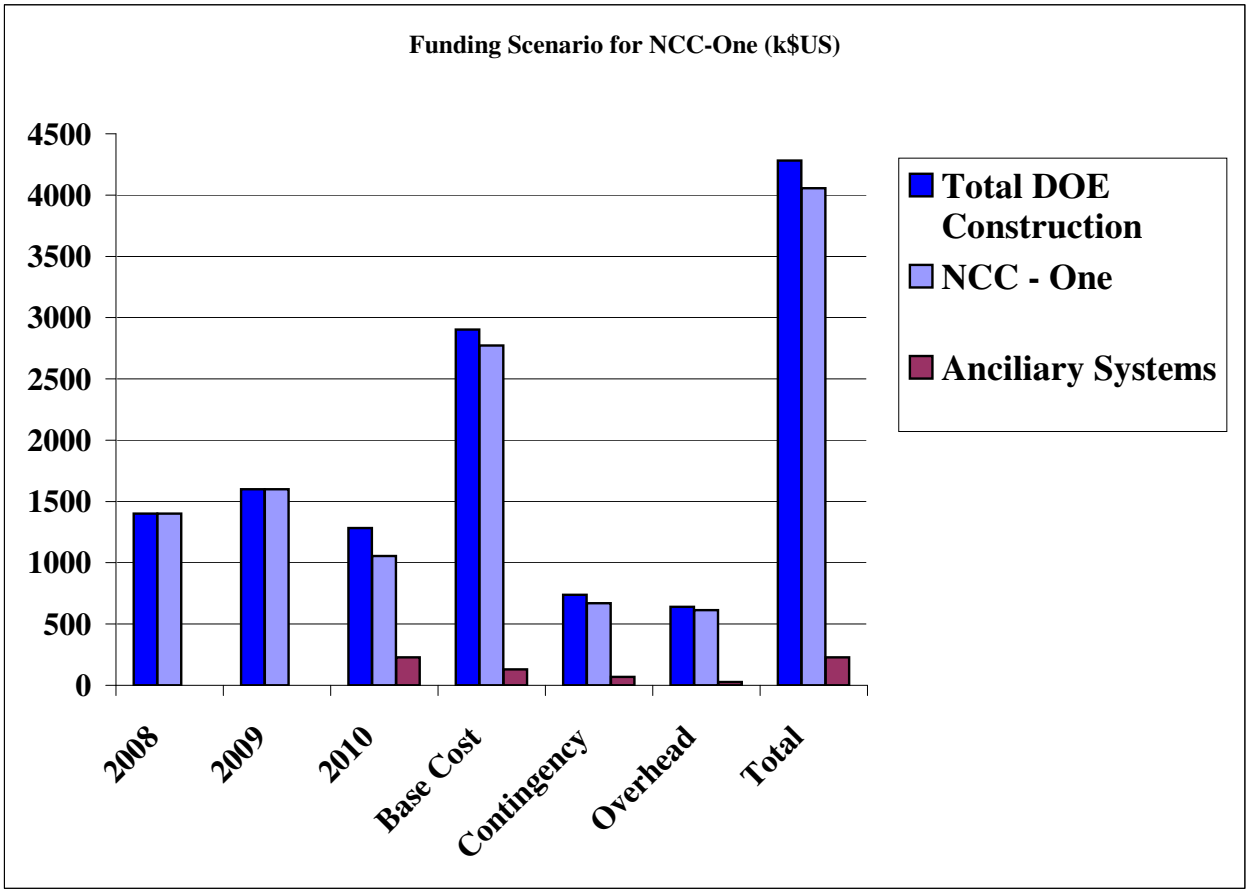

Figure 5.3: Proposed funding profile for DOE Construction project (also see first three columns in Fig. 5.1.)

In 2008 funding is required to purchase silicon wafers, start sensor production and to set assembly areas at collaborating institutions. Funding in 2009 covers all major purchases including tungsten plates and electronics components (US Industry and Russia), most of the Si (foundries in collaborating countries) and detector assembly (collaborating institu-

tions). We are planning for the last task to be carried mainly in the students laboratories in collaborating Universities.

5.6 Additional NCC to complement DOE Construction project

As stated above, the PHENIX Collaboration is pursuing the design and construction of a complimentary second PHENIX NCC to (a) avoid RHIC running time losses when running asymmetric collision species, (b) to double the yield of rare probes (thereby reducing RHIC running time), and (c) to access the production kinematics resulting in associated production of particles the in forward-backward directions (for example, electrons from Z decays). The PHENIX collaboration is actively pursuing now all possible venues for funding this part of the project through international contributions.

5.7 Acknowledgments

We thank our PHENIX collaborators for the support and encouragement of the proposed NCC upgrade and for fruitful discussions. We acknowledge R&D and participant funding support from the Department of Energy, Office of Science, Office of Nuclear Physics, the National Science Foundation, and the Research Foundation of SUNY (U.S.), Ministry of Education, Culture, Sports, Science, and Technology and the Japan Society for the Promotion of Science (Japan), Ministry of Education, Youth and Sports (Czech Republic), Korea Research Foundation, Center for High Energy Physics, and Korea Science and Engineering Foundation (Korea), and Ministry of Education and Science, Russian Academy of Sciences, Federal Agency of Atomic Energy (Russia).

Appendix A

Event Rates

Here we estimate the event rates for a single NCC for selected physics processes corresponding to some of the major goals of the NCC detector.

Table A.1: Luminosity guidance from CAD for RHIC II. We assume a 50% duty cycle for RHIC to give a weekly integrated luminosity. We then assume a 12 week run and a 60% uptime for PHENIX to give an total integrated luminosity. The max rate is the interaction rate at peak luminosity.

Species CM Energy	p+p 200 GeV	p+p 500 GeV	p+Au 200 GeV	d+Au 200 GeV	Cu+Cu 200 GeV	Au+Au 200 GeV
lum ($s^{-1}cm^{-2}$)	1×10^{32}	5×10^{32}	2.5×10^{29}	1.9×10^{29}	8×10^{28}	7×10^{27}
interaction rate	4200	21000	320	585	248	47 kHz
lum/wk ($pb^{-1}wk^{-1}$)	33	166	0.083	0.062	0.025	0.0025
Int Lum (pb^{-1})	238	1195	0.6	0.45	0.18	0.018

Table A.2: Luminosity for RHIC I with same assumptions as in Table A.1.

Species CM Energy	p+p 200 GeV	p+p 500 GeV	p+Au 200 GeV	d+Au 200 GeV	Cu+Cu 200 GeV	Au+Au 200 GeV
lum ($s^{-1}cm^{-2}$)	3×10^{31}	–	–	0.09×10^{29}		0.92×10^{27}
lum/wk ($pb^{-1}wk^{-1}$)	9.9	–	–	0.0028	–	0.000327
interaction rate	4200	21000	320	585	248	47 kHz
Int Lum (pb^{-1})	71.3	–	–	0.02	–	0.0024

Table A.1 shows rates for RHIC II and Table A.2 shows rates for RHIC I. Table A.3 lists typical losses in efficiency, which are based on our experience from the first 5 years of data

Table A.3: Efficiency factors added into the rate calculations. In the analysis we typically require that the vertex be within 10 cm of the nominal collision point (a requirement set by the barrel VTX detector), which results in a loss of 0.55 for RHIC II. For RHIC I, the beam spread is larger and results in a loss of 0.31. For A+A collisions the minimum bias trigger formed by the Beam-Beam counters are essentially 100% efficient, however in p+p and p+A collisions there is some loss.

Species	p+p 200 GeV	p+p 500 GeV	p+Au	d+Au	Cu+Cu	Au+Au
vertex cut RHIC II	0.55	0.55	0.55	0.55	0.55	0.55
vertex cut RHIC I	0.31	0.31	0.31	0.31	0.31	0.31
min bias trigger eff	0.75	0.75	0.90	0.90	1.0	1.0
reconstruction eff	0.80	0.80	0.80	0.80	0.80	0.80
total eff factor RHIC II	0.33	0.33	0.40	0.40	0.44	0.44
total eff factor RHIC I	0.19	0.19	0.23	0.23	0.25	0.25

taking. The first loss arises from a vertex cut, which we take to be $\pm$ 10 cm from the nominal collision point. We assume 55% efficiency from losses due to the spread of the beam. For RHIC I this will be a 35% efficency since the spread of the beam is larger. Secondly, the minimum bias trigger uses the Beam-Beam Counters (BBC) located up and downstream of the collision point. In the high multiplicity environment of heavy ion collisions, this trigger is almost 100% efficient. However in low multiplicity p+p and p+A collisions, the efficiency drops since in some cases, no particles actually trigger the BBC. Finally we have taken 80% for the reconstruction efficiency, a reasonable number from our experience in the last several years.

Pythia was used to obtain p+p cross sections for direct photons, π^0's, W's, and the χ_c. To obtain heavy ion yields we assumed a point-like cross section; that is, the cross sections were scaled by the product of the atomic weights of the incoming nuclei. For π^0's and the χ_c a suppression factor was assumed consistent with the data from Runs 1-5 or about a factor of 2 for minimum bias collisions. Tables A.4 and A.5 give the yields for a 12 week run for p+p, p+A, Cu+Cu and Au+Au collisions for a single NCC.

We are studying the effect of triggering as described in section 3.9.1. A simple 8x8 tile trigger should be sufficient for p+p and p+A collisions given a DAQ bandwidth of 8kHz. However, at present a simple 8x8 trigger will be ineffective in heavy ion collisions giving rejections of less than 2. Using a minimum bias trigger for heavy ion collisions results in substantial loss of a e.g. a factor of 6 in Au+Au collisions and 30 in Cu+Cu collisions. This does not affect the χ_c since this depends on a dimuon trigger and will not come from triggering using the NCC. The work on the trigger is in its very early stages and more sophisticated trigger schemes will be explored. In addition improvements are envisioned to the DAQ to increase its rate by a factor of 2 or more.

Table A.7 gives a summary of the physics program addressed by the Nosecone Calorime-

Table A.4: Yields in p+p collisions of various processes into the acceptance of a single NCC for a 12 week RHIC II run with efficiency factors listed in Table A.3

Species	process		Yield
pp 200 GeV	π^0 production	$p_T(\pi^0) > 5$ GeV	62M
		$p_T(\pi^0) > 10$ GeV	260K
		$p_T(\pi^0) > 15$ GeV	8K
		$p_T(\pi^0) > 20$ GeV	450
pp 200 GeV	direct photon production	$p_T(\gamma) > 5$ GeV	1M
		$p_T(\gamma) > 10$ GeV	33K
		$p_T(\gamma) > 15$ GeV	2.6K
		$p_T(\gamma) > 20$ GeV	280
pp 200 GeV	W$\rightarrow e + \nu_e$	$p_T(e) > 5$ GeV	16
		$p_T(e) > 10$ GeV	11
		$p_T(e) > 20$ GeV	5
pp 200 GeV	$\chi_{c1} \rightarrow \gamma J/\psi \rightarrow \gamma\mu\mu$		26K
	$\chi_{c2} \rightarrow \gamma J/\psi \rightarrow \gamma\mu\mu$		42K
pp 500 GeV	π^0 production	$p_T(\pi^0) > 5$ GeV	1300M
		$p_T(\pi^0) > 10$ GeV	17M
		$p_T(\pi^0) > 15$ GeV	1.3M
		$p_T(\pi^0) > 20$ GeV	190K
pp 500 GeV	direct photon production	$p_T(\gamma) > 5$ GeV	24M
		$p_T(\gamma) > 10$ GeV	1.7M
		$p_T(\gamma) > 15$ GeV	270K
		$p_T(\gamma) > 20$ GeV	65K
pp 500 GeV	W$\rightarrow e + \nu_e$	$p_T(e) > 5$ GeV	4.9K
		$p_T(e) > 10$ GeV	4.4K
		$p_T(e) > 20$ GeV	2.8K
pp 500 GeV	$\chi_{c1} \rightarrow \gamma J/\psi \rightarrow \gamma\mu\mu$		790K
	$\chi_{c2} \rightarrow \gamma J/\psi \rightarrow \gamma\mu\mu$		1.1M

ter. Rates for direct photons and π^0's are typically about 5 times that which will be available in the central EMC in A+A collisions. Without the NCC the χ_c would be impossible in heavy ion collisions. The rate into the central EMC is simply too small. The NCC, by contrast utilizes the large acceptance of the muon arms to detect the J/ψ, and is itself a large acceptance detector. For both p+p and p+A collisions, the crucial aspect of the NCC is the forward rapidity coverage which allows one to reach low x$\tilde{1}0^{-3}$.

Table A.5: Yields in p+Au, Cu+Cu and Au+Au collisions of various processes into the acceptance of a single NCC for a 12 week RHIC II run with efficiency factors listed in Table A.3.

Species	process		Yield
p+Au 200 GeV	π^0 production	$p_T(\pi^0) > 5$ GeV	37M
		$p_T(\pi^0) > 10$ GeV	150K
		$p_T(\pi^0) > 15$ GeV	4.7K
		$p_T(\pi^0) > 20$ GeV	270
p+Au 200 GeV	direct photon production	$p_T(\gamma) > 5$ GeV	610K
		$p_T(\gamma) > 10$ GeV	20K
		$p_T(\gamma) > 15$ GeV	1.5K
		$p_T(\gamma) > 20$ GeV	170
p+Au 200 GeV	$\chi_{c1} \to \gamma J/\psi \to \gamma\mu\mu$		10K
	$\chi_{c2} \to \gamma J/\psi \to \gamma\mu\mu$		16K
Cu+Cu 200 GeV	π^0 production	$p_T(\pi^0) > 5$ GeV	130M
suppressed		$p_T(\pi^0) > 10$ GeV	545K
		$p_T(\pi^0) > 15$ GeV	16K
		$p_T(\pi^0) > 20$ GeV	942
Cu+Cu 200 GeV	direct photon production	$p_T(\gamma) > 5$ GeV	4.1M
		$p_T(\gamma) > 10$ GeV	130K
		$p_T(\gamma) > 15$ GeV	10K
		$p_T(\gamma) > 20$ GeV	1.1K
Cu+Cu 200 GeV	$\chi_{c1} \to \gamma J/\psi \to \gamma\mu\mu$		40K
suppressed	$\chi_{c2} \to \gamma J/\psi \to \gamma\mu\mu$		65K
Au+Au 200 GeV	π^0 production	$p_T(\pi^0) > 5$ GeV	100M
suppressed		$p_T(\pi^0) > 10$ GeV	440K
		$p_T(\pi^0) > 15$ GeV	13K
		$p_T(\pi^0) > 20$ GeV	1.1K
Au+Au 200 GeV	direct photon production	$p_T(\gamma) > 5$ GeV	4M
		$p_T(\gamma) > 10$ GeV	130K
		$p_T(\gamma) > 15$ GeV	10K
		$p_T(\gamma) > 20$ GeV	1.1K
Au+Au 200 GeV	$\chi_{c1} \to \gamma J/\psi \to \gamma\mu\mu$		43K
suppressed	$\chi_{c2} \to \gamma J/\psi \to \gamma\mu\mu$		70K

Table A.6: Yields of various processes into the acceptance of a single NCC for a 12 week RHIC I run with efficiency factors listed in Table A.3

Species	process		Yield
p+p 200 GeV	π^0 production	$p_T(\pi^0) > 5$ GeV	10M
		$p_T(\pi^0) > 10$ GeV	43K
		$p_T(\pi^0) > 15$ GeV	1.3K
		$p_T(\pi^0) > 20$ GeV	75
p+p 200 GeV	direct photon production	$p_T(\gamma) > 5$ GeV	167K
		$p_T(\gamma) > 10$ GeV	5.5K
		$p_T(\gamma) > 15$ GeV	433
		$p_T(\gamma) > 20$ GeV	50
p+p 200 GeV	$\chi_{c1} \rightarrow \gamma J/\psi \rightarrow \gamma\mu\mu$		4K
	$\chi_{c2} \rightarrow \gamma J/\psi \rightarrow \gamma\mu\mu$		7K
Au+Au 200 GeV	π^0 production	$p_T(\pi^0) > 5$ GeV	7.7M
suppressed		$p_T(\pi^0) > 10$ GeV	32K
		$p_T(\pi^0) > 15$ GeV	980
		$p_T(\pi^0) > 20$ GeV	58
Au+Au 200 GeV	direct photon production	$p_T(\gamma) > 5$ GeV	290K
		$p_T(\gamma) > 10$ GeV	9.6K
		$p_T(\gamma) > 15$ GeV	750
		$p_T(\gamma) > 20$ GeV	81
Au+Au 200 GeV	$\chi_{c1} \rightarrow \gamma J/\psi \rightarrow \gamma\mu\mu$		3.1K
suppressed	$\chi_{c2} \rightarrow \gamma J/\psi \rightarrow \gamma\mu\mu$		5K

Table A.7: The coverage by the NCC of some of relevant kinematic variables given the rates mentioned previously.

Process	Species	Physics Goal	
π^0 production	p+Au 200 GeV	saturation	$1< y <3$; p_T ~15 GeV
	p+p 200 GeV	"CGC"	$1< y <3$; p_T ~15 GeV
direct photon production	p+Au 200 GeV	saturation	$1< y <3$; p_T ~15 GeV
	p+p 200 GeV	"CGC"	$1< y <3$; p_T ~15 GeV
π^0 production	Au+Au 200 GeV	parton energy loss	$1< y <3$; p_T ~15 GeV
Heavy Ions	Cu+Cu 200 GeV		$1< y <3$; p_T ~15 GeV
	p+Au 200 GeV		$1< y <3$; p_T ~15 GeV
	p+p 200 GeV		$1< y <3$; p_T ~15 GeV
direct photon production	Au+Au 200 GeV	jet tomography	$1< y <3$; p_T ~15 GeV
"photon-jet"	Cu+Cu 200 GeV		$1< y <3$; p_T ~15 GeV
Heavy Ions	p+Au 200 GeV		$1< y <3$; p_T ~15 GeV
	p+p 200 GeV		$1< y <3$; p_T ~15 GeV
$\chi_{c1} \rightarrow \gamma J/\psi \rightarrow \gamma\mu\mu$	Au+Au 200 GeV	confinement	$1< y <2$
Heavy Ions	Cu+Cu 200 GeV		$1< y <2.5$
	p+Au 200 GeV		$1< y <3$
	p+p 500 GeV		$1< y <3$
π^0 production	p+p 200 GeV	$A_{LL}(p_T)$	
Spin	p+p 500 GeV		
direct photon production	p+p 200 GeV	ΔG(x)at low x	$x \sim 3 \times 10^{-3}$
Spin	p+p 500 GeV		$x \sim 1 \times 10^{-3}$
W$\rightarrow e + \nu_e$ *Spin*	p+p 500 GeV	$\Delta\overline{q}$	
Spin			

Appendix B

Physics Simulations

This appendix outlines the progress made in understanding the capabilities of the NCC in the study of a variety of physics topics. The physics analysis topics addressed by the NCC require:

- The measurement of π^0 spectrum to 30 GeV (15 GeV p_T) in AA, p+A, and p+p collisions.
- The measurement of the direct photon spectrum in AA, p+A and p+p collisions, and correlations of direct photons and high momentum π^0's.
- the measurement of jets in p+p collisions for extraction of Bjorken x.
- the ability to use isolation cuts to identify direct photons and leptons from W bosons and heavy quarks in p+p and d+Au events on an event-by-event basis.

In what follows, all plots assume the luminosities stated in Appendix A.

As mentioned previously, electromagnetic calorimetry in the central region ($-0.35 < y < 0.35$) has been a very powerful tool for the PHENIX detector. The purpose of the NCC is to extend these measurements to higher rapidity, and to increase the statistics for low event processes such as direct photon events. The increase in statistics can be rather large. RHIC II gives us a factor of about 10 increase in luminosity in Au+Au while a single NCC will give us an increase in acceptance of an order of magnitude. Theoretically this leads to an increase of two orders of magnitude. Practically however, the increase is somewhat less than this since the p_T spectrum drops off as a function of rapidity.

The increase in statistics is critical for many measurements. For example for correlation measurements in the case of photon-jet events in Au+Au collisions- we wish to divide the event sample into bins of transverse momentum and rapidity in order to be able to reconstruct the energy loss of partons as a function of momentum as well as the energy density of the collision.

For the signals we are interested in for heavy ion collisions, namely the χ_c, high momentum direct photons, and π^0's, we have tools we can use to isolate the signal. For the χ_c the tool is the invariant mass difference $m_{\gamma\mu\mu} - m_{\mu\mu}$. For the direct photon measurements in

Au+Au and d+Au we will use the method of looking at the comparison of the γ to π^0 ratio measured vs expected, where we must make a very good measurement of the π^0 spectrum. This method was used to generate the direct photon signal shown in Fig. B.1. In p+p and p+A collisions, for event-by-event measurements of the direct photon to measure x_{BJ}, we will use higher momentum photons and isolation cuts. In what follows we assume RHIC II luminosities as shown in table A.1.

B.1 Direct Photons

The method used in this the PHENIX data analysis to extract the direct photon signal (Fig B.1) makes use of the fact, that we can measure the precise π^0 spectrum. We will use the same method in the NCC, which will be possible because the PS/SM detectors should give us a good identification of showers associated with π^0's as explained in section 3.4.6. Once a π^0 spectrum is measured, the direct photon analysis proceeds as follows: A simulation is used to calculate the expected γ to π^0 ratio using the measured π^0 spectrum, putting in all known sources except direct photons. In the simulation a ratio is made between the photon spectrum and the π^0 spectrum. The same is done in the data and a double ratio is made i.e.

$$R = \frac{(\gamma/\pi^0)_{measured}}{(\gamma/\pi^0)_{expected}} = \frac{(\frac{\gamma_{\pi^0}+\gamma_{direct}}{\pi^0})_{measured}}{(\frac{\gamma_{\pi^0}}{\pi^0})_{expected}} \sim 1 + \frac{\gamma_{direct}}{\gamma_{\pi^0}}$$

This method cancels many systematic errors. In particular overlapping showers will cancel in the ratio if the simulation is done correctly. Fig. B.1 shows the estimated statistical errors for such an analysis in Au+Au collisions.

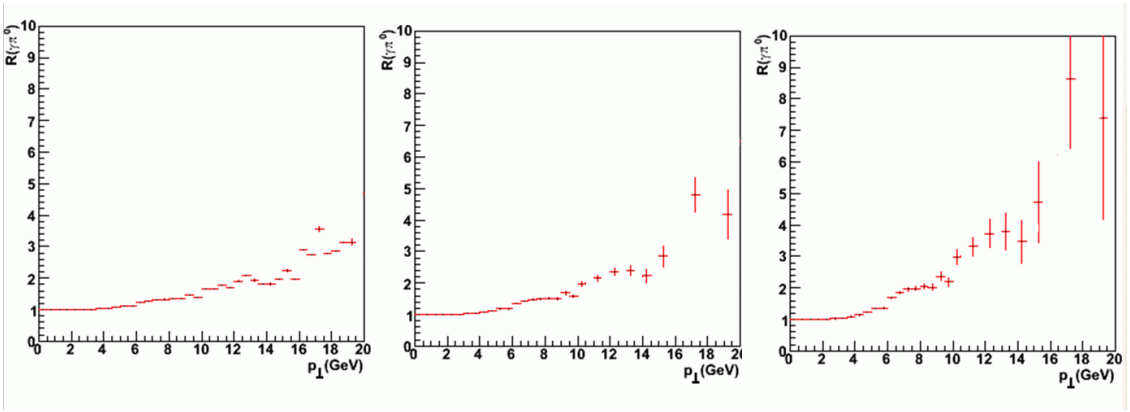

Figure B.1: Simulation of the direct photon signal, i.e. the ratio $R = \frac{(\gamma/\pi^0)_{measured}}{((\gamma/\pi^0)_{expected})}$ as measured by the NCC. R in p+p collisions[left]; R in p+Au collisions[center]; R in Au+Au collisions [right]. Our final analysis will require a comparison of all three systems. Error bars are from the statistics we expect to get in the experiment. The fluctuations of the points arises from lack of statistics in the simulation.

In a single run at RHIC II luminosities the NCC should be able to make measurements of

the direct photon spectrum to 15 in p_T at rapidities between 1 and 3 nicely complementing the results to be obtained at central rapidity.

The study of direct photons opposite a high momentum hadron allows for a study of a calibrated jet since the photon does not undergo any quenching. While the process is most easily visualized on an event by event basis, in practice it is done using correlation functions where the angular correlation between photons and high momentum π^0's are plotted. The combinatorial background is subtracted using a mixed event technique. Using the technique of recognizing showers which actually arise from the decay of π^0 described in section 3.4.6 a background sample of decay photons opposite high momentum π^0's can be constructed and subtracted from the original distribution to yield a correlation function of direct photons and hadrons. As was mentioned in 2.1 such studies can be done as a function of the reaction plane to enable a 3D tomography of the system.

B.1.1 Isolation cuts for direct photon in p+p and p(d)+A collisions.

It is well known that isolation criteria can be used in p+p collisions to identify direct photons. Fig. B.2, left panel shows the yield of photons from decays in QCD events (blue) and direct photons (red) in 500 GeV p+p collisions. After requiring a separation criteria, $E_{cone}/E_{direct-photon} < 0.1$, where E_{cone} is the amount of electromagnetic energy in a cone of size $\Delta\eta\Delta\phi$=0.8, the direct photons dominate over decay photons above a p_T of 7 GeV. See fig. B.2 (right panel).

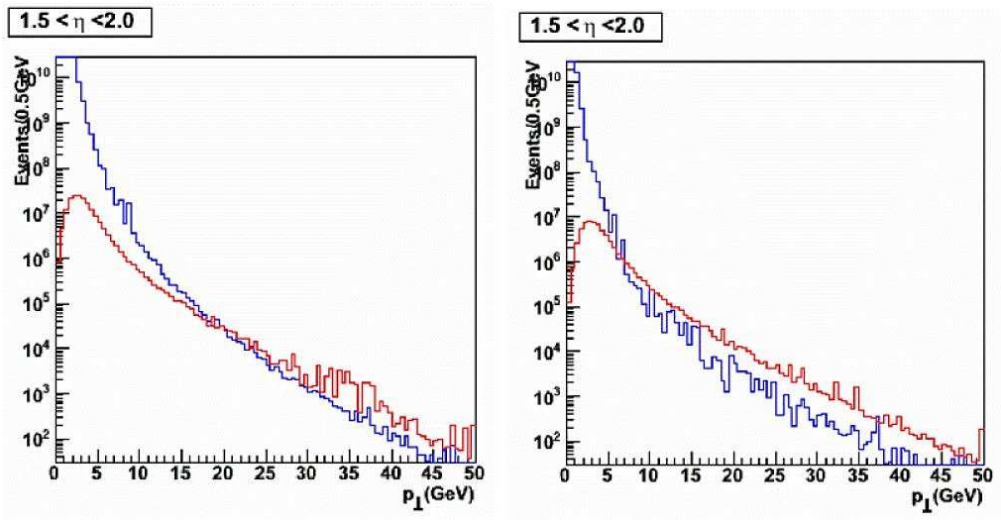

Figure B.2: Yield of photons between $1.5 < \eta < 2$ from decays in QCD events (blue) and direct photons (red) in 500 GeV p+p collisions [left]; Yield of photons between $1.5 < \eta < 2$ from decays in QCD events (blue) and direct photons (red) in 500 GeV p+p collisions after an isolation cut as explained in the text [right].

The method works in p+A collisions as well since the photon is generally separated from

the bulk of the produced particles. Fig. B.3 shows the yield of photons from decays in QCD events (blue) and direct photons (red) in p+Au collisions. Of course, one can also use a method similar to that used in heavy ion collisions and obtain the direct photon spectrum on a statistical basis, which would then allow one to go to low p_T. An important point, mentioned previously, is that in the case of suppression due to the initial state (i.e., the CGC) direct photons should should experience a similar suppression as the hadrons. Photons, which to first order, do not interact via the strong interaction, should not be sensitive to final state effects (i.e., nuclear matter or any sQGP) and should be a clean indication of suppression due to initial state effects.

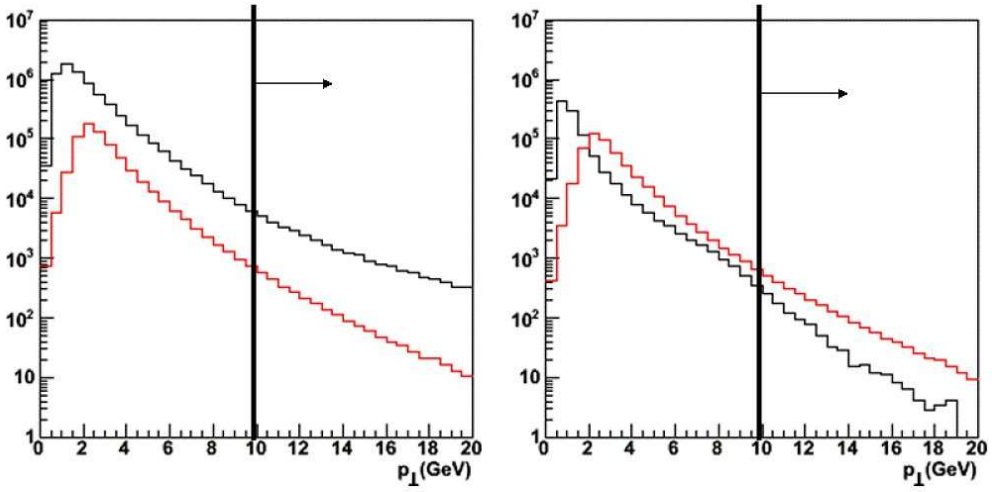

Figure B.3: (left) Photons from decays in QCD events [black] and direct photons [red] in p+Au collisions between $1 < \eta < 3$. (right) For the QCD background, only the highest energy photon in each event is plotted. Photons between $1 < \eta < 3$ from decays in QCD events [black] and direct photons [red] in p+Au collisions after an isolation cut in which $E_{cone}/E_{direct-photon} < 0.1$, where E_{cone} is the amount of electromagnetic energy in a cone of size $\Delta\eta\Delta\phi$=0.8. Unlike the other figures in this section, the simulation was done using a heavy ion event generator HIJING. For the generation of QCD background events a cut of 10 GeV was made on the hard scattering of partons, hence one should look at the region to the right of the line in these plots.

B.2 Direct photons in p(d)+A collisions: Looking for a CGC

The above method can be used in p(d)+A collisions to measure the suppression of the gluon distribution via the gluon Compton scattering diagram shown in Figure 2.17. As an exercise, a model of the saturated gluon function [110] was used to understand what one might see in the simplest cases for the direct photon signal in d+Au collisions. Other models are now on the market with parameterizations that can used for such studies. However, the GBW model is simple in that it simply flattened out the Gluon distribution below some value of x, depending on the value of the saturation scale for the particular centrality and rapidity in question. Fig. B.4 shows an example.

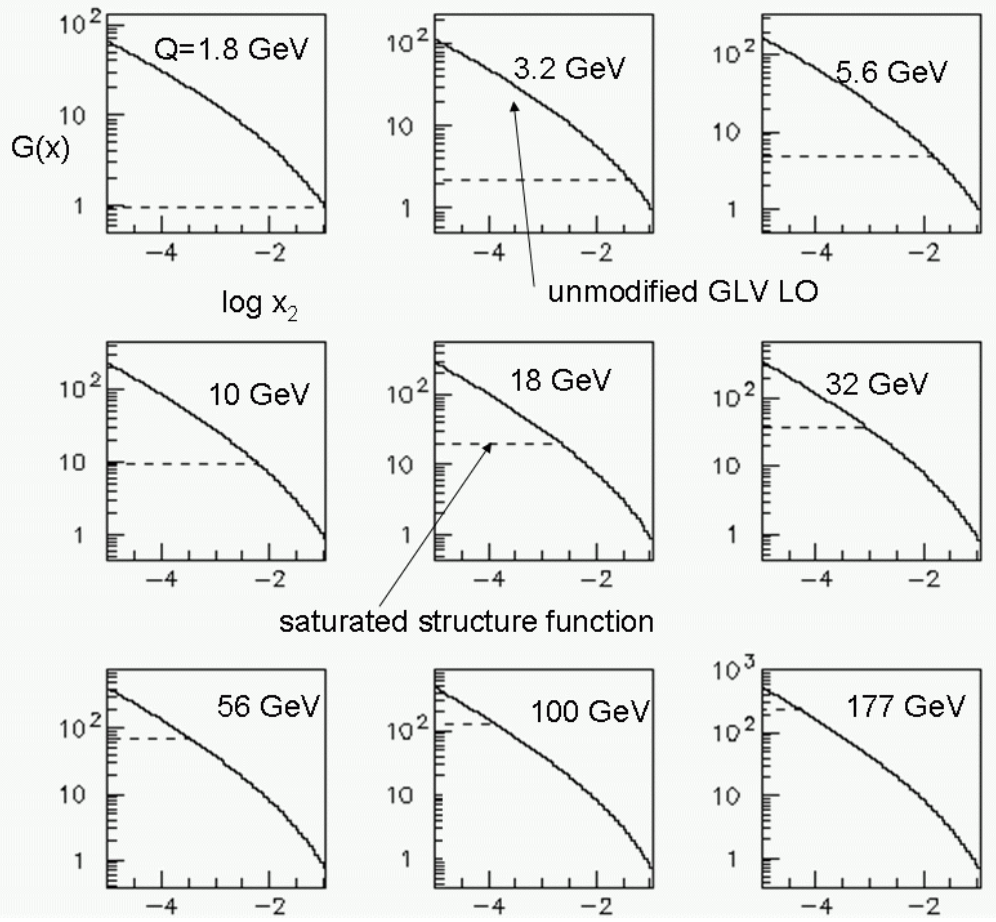

Figure B.4: Modified gluon structure function

R_{dAu} was then generated with these new distributions and checked against the measured values of R_{dAu} as measured by the PHENIX and Brahms collaborations for consistency. R_{pA} is defined similarly to R_{AA}

$$R_{pA} = \frac{dN_{pA}}{< N_{coll} > \times dN_{pp}} \tag{B.1}$$

where dN_{pA} is the differential yield for a point-like process in a p+A collision, and dN_{pp} is the differential yield for the same process in nucleon-nucleon collisions. The new gluon distributions were then used in Pythia for the production of direct photon events and a ratio R_{pA} was constructed from the simulated data. Note that in Pythia there is no Cronin enhancement. Fig. B.5 shows R_{pA} as a function of η in various bins of p_T.

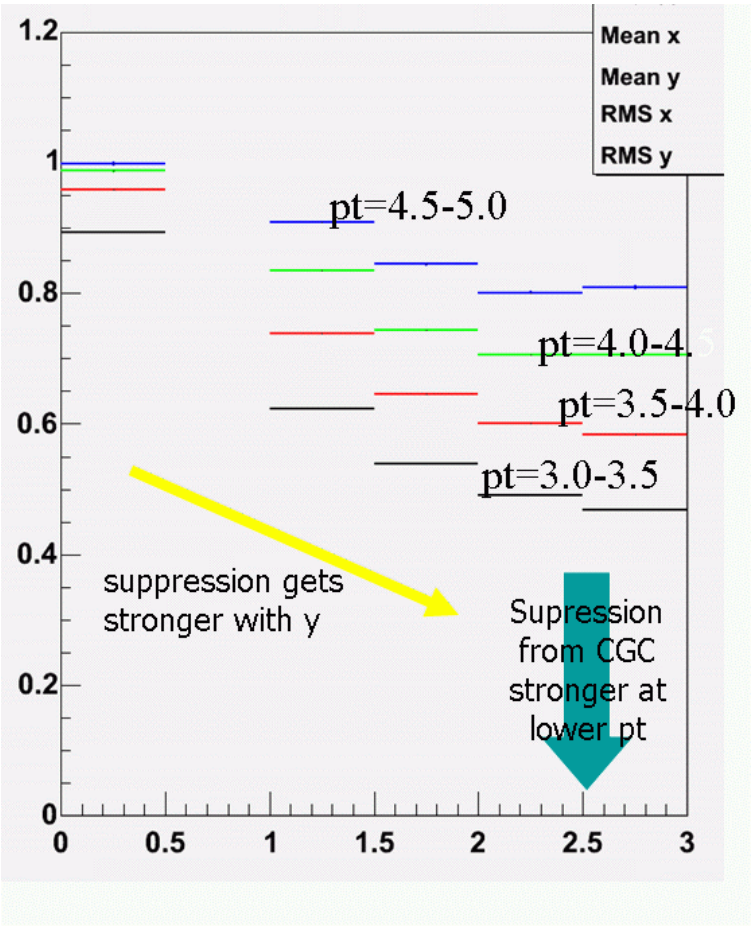

Figure B.5: R_{pA} shown as a function of η for various values of pt using a particular modified gluon structure function [110].

There are two characteristics that one sees: (1) The suppression increases for increasing rapidity, which makes sense because forward rapidity implies lower x. (2) The suppression is stronger at low p_T.

B.3 The χ_c

The χ_c decays into a J/ψ and a photon. We first identify the J/ψ via its dimuon decay – it may also be possible to also use the dielectron channel. For χ_c's, in which the muons are detected in the muon arms, the photon is accepted in the NCC more than 60% of

the time(Fig. B.7). In order to see the χ_c one reconstructs the $\mu^+\mu^-\gamma$ invariant mass and subtracts off the $\mu^+\mu^-$ invariant mass where the dimuon mass is required to be in the J/ψ peak. The χ_c should show up as a peak at the χ_c-J/ψ mass difference of about 400-500 MeV. There are actually 2 χ_c states which decay with large branching ratios to the J/ψ with masses 3511 and 3556 MeV, however our resolution will now allow us to separate these two states. Note that the resolution is now primarily due to the resolution of the photon and not the resolution of the muon spectrometer. This technique has actually used by PHENIX to identify the χ_c in p+p collisions using the central arms, where we have electromagnetic coverage. See Fig. B.6.

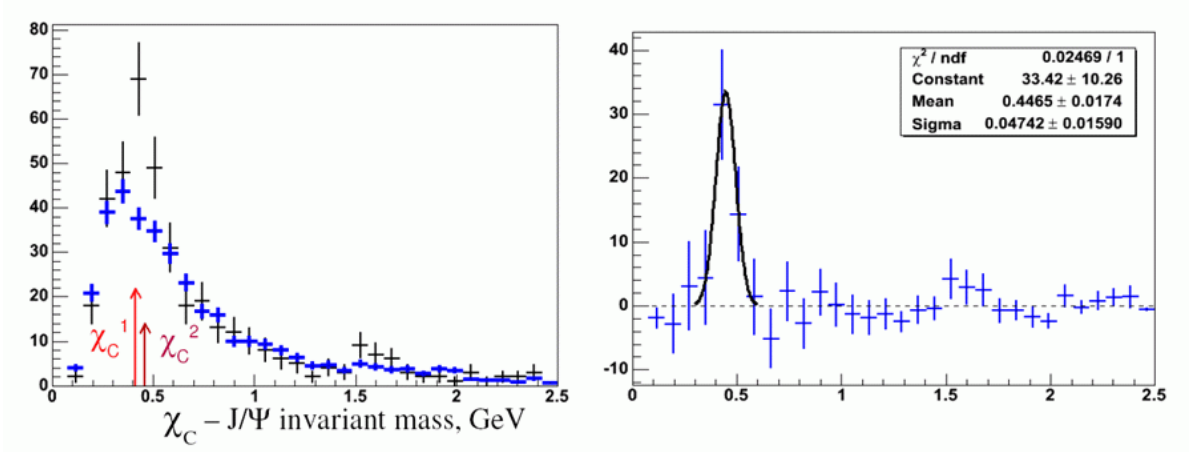

Figure B.6:
$J\psi\gamma J\psi$ invariant mass spectrum showing the χ_c peak in p+p collisions as seen by the PHENIX central arm in run-5. We see about 50 χ_c. Background subtracted spectrum is shown on the right. The resolution of the peak is about 50 MeV consistent with the resolution of the EMCAL.

A simulation was done in which single χ_c events were generated using PYTHIA which were overlaid on a background of photons corresponding to a variety of cases from p+p collisions to central Au+Au collisions. The S/B on the J/ψ was taken from present data, where we have assumed an improvement in resolution and background rejection of decay muons from the FVTX. In the case of central Au+Au collisions this lead to a S/B of about 1/5. The J/ψ was then reconstructed and paired will all photons in the event to form a γJ/ψ invariant mass distribution. We assumed that the background could be subtracted using a mixed background technique.

As an example fig. B.8 shows the invariant mass difference for simulated full events in p+p collisions for rapidity between 2 and 2.5. The background distribution is shown in black with a subtracted spectrum shown on the right. The resolution is about 120 MeV. Note that the typical energy of the photons is about 1 GeV. The energy resolution for showers contained in in EM1 and EM2 is $0.03 + \frac{0.18}{\sqrt{(E)}}$. When higher energy showers greater than 10 GeV enter the HAD compartment however, the resolution becomes $0.03 + \frac{0.27}{\sqrt{(E)}}$. We believe that out estimate of the calorimeter resolution is reasonable. If however, the calorimeter resolution

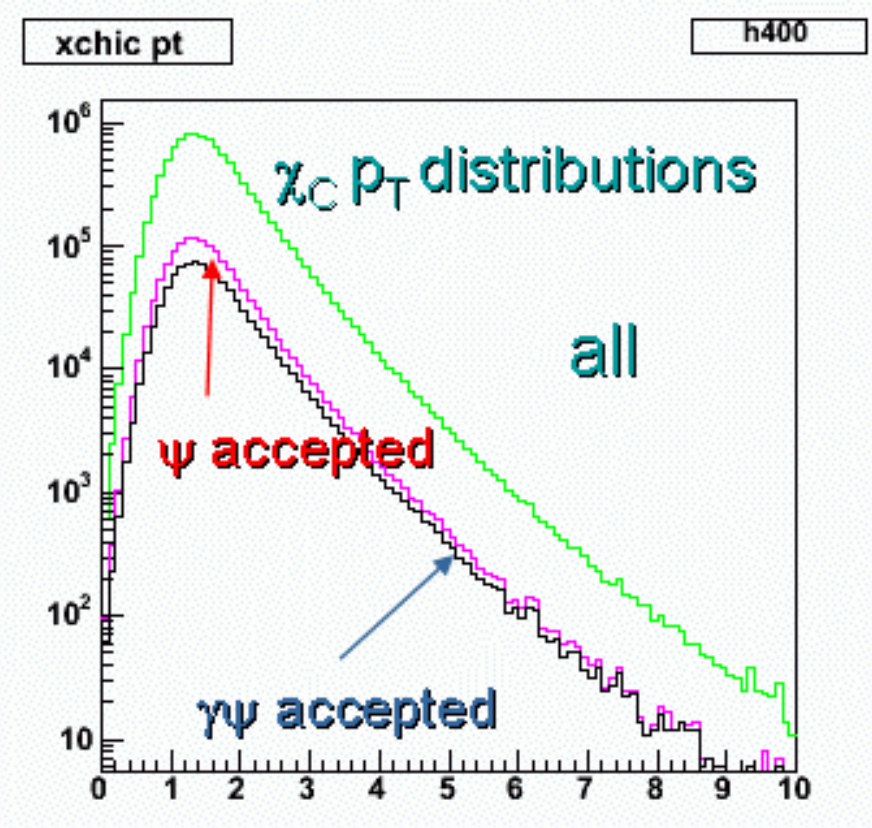

Figure B.7: p_T distributions for the χ_c. Green-all, red-J/ψ accepted in the muon spectrometer, blue-χ_c decay photon accepted in NCC and J/ψ accepted in the muon spectrometer.

is much worse the χ_c can still be reconstructed, at least in p+p events. Fig. B.9 shows the resolution if the resolution is degraded to $\frac{0.50}{\sqrt{(E)}}$.

In heavy ion collisions, the combinatorial background is considerably larger. Fig. B.10 and B.11 show the χ_c signal for the top 10% ccentrality in Cu+Cu and Au+Au events. Even in central Au+Au events, the signal at rapidities 1-2 should be clear.

We can then form the R_{AA} for the χ_C. This is shown in Fig. B.12 where the J/ψ is detected via its dimuon decay in the muon spectrometer. The photon detected by the NCC is in the rapidity range $1<|\ \eta\ |<1.5$. This is compared to the R_AA of the J/ψ measured by PHENIX in Run-4. Errors for the χ_C are statistical only. It is assumed that the p+p measurement of the χ_C adds a negligible error to the ratio. The errors are of the order of 10% which simply comes from the fact that about 10K χ_C's are detected over a background of 600K. Since this is a S/B of less than 2%, systematic errors on the background subtraction must be evaluated carefully. This needs to be pursued. Ultimately we will need test beam data to understand how well we can the multi photon background to the signal photons, and a test where the prototype is put into PHENIX for a short while to measure the level of expected backgrounds.

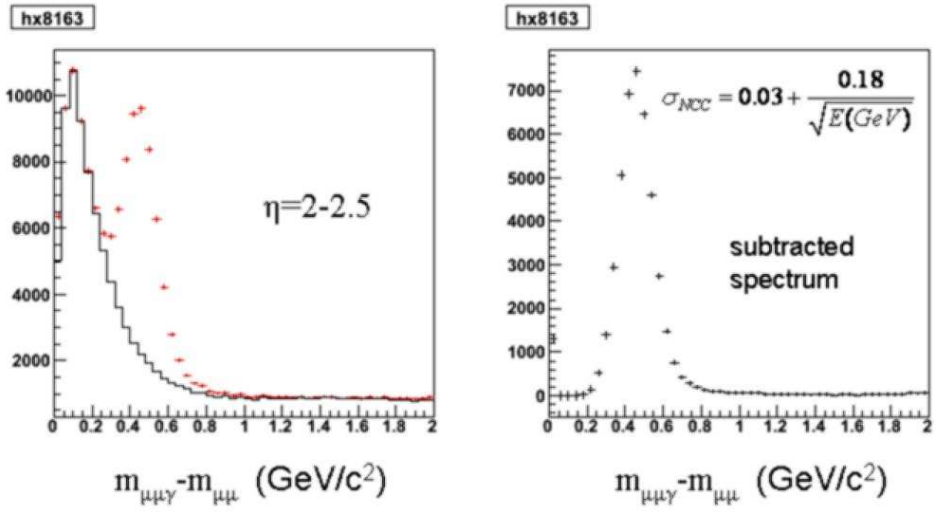

Figure B.8: The $M_{\gamma\mu\mu} - M_{\mu\mu}$ invariant mass distribution in p+p events. The left plot shows the raw mass difference spectrum (red) and background (black). The right shows the subtracted spectrum.

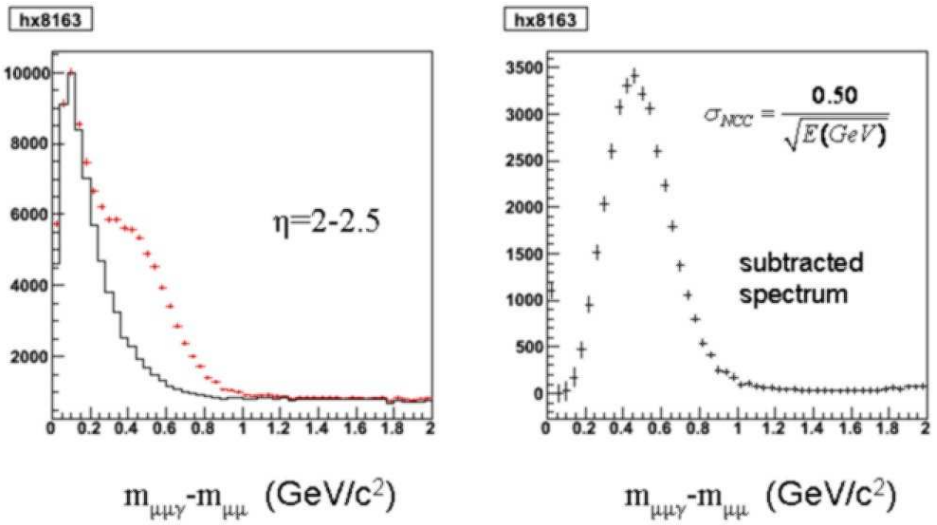

Figure B.9: Same as the previous figure with the resolution of the NCC degraded to $\frac{0.50}{\sqrt{(E(GeV))}}$

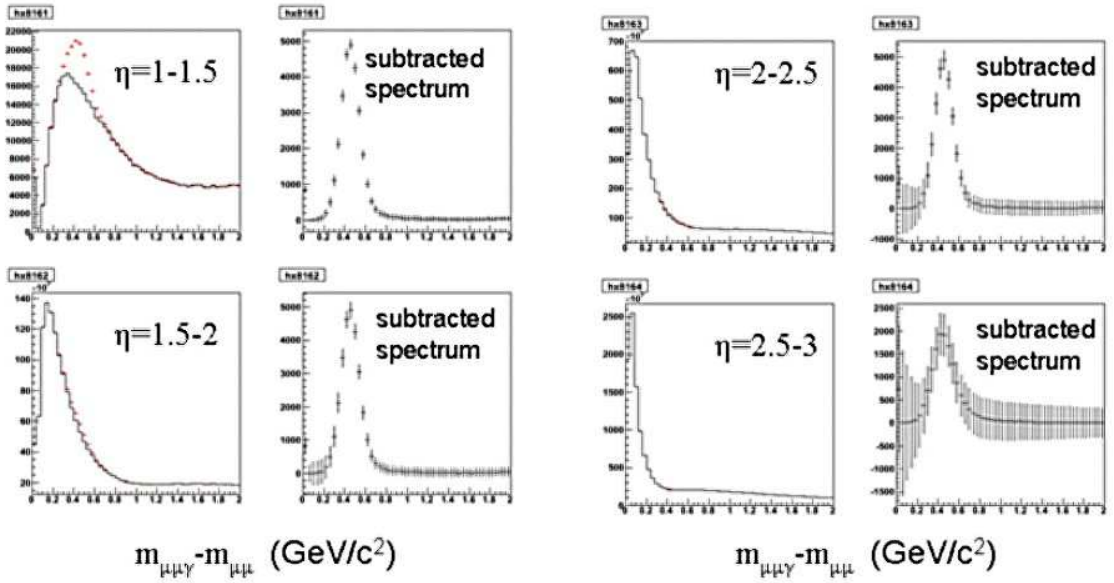

Figure B.10: Central 10% Cu+Cu events at various rapidities. The left plot of each pair show the raw mass difference, the right plot shows a background subtracted distribution.

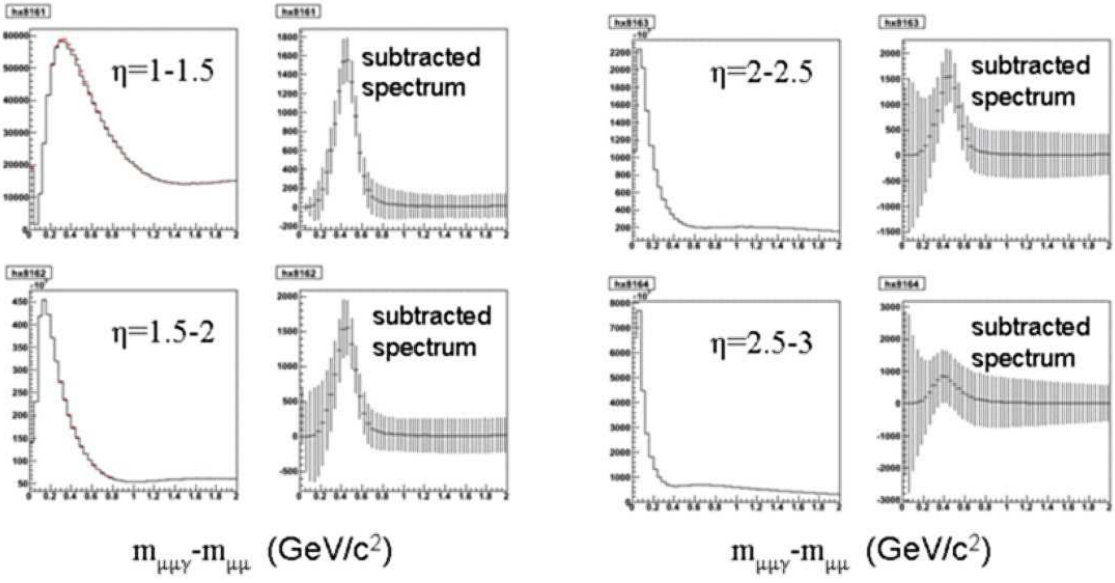

Figure B.11: Same as the previous plot for central Au+Au events.

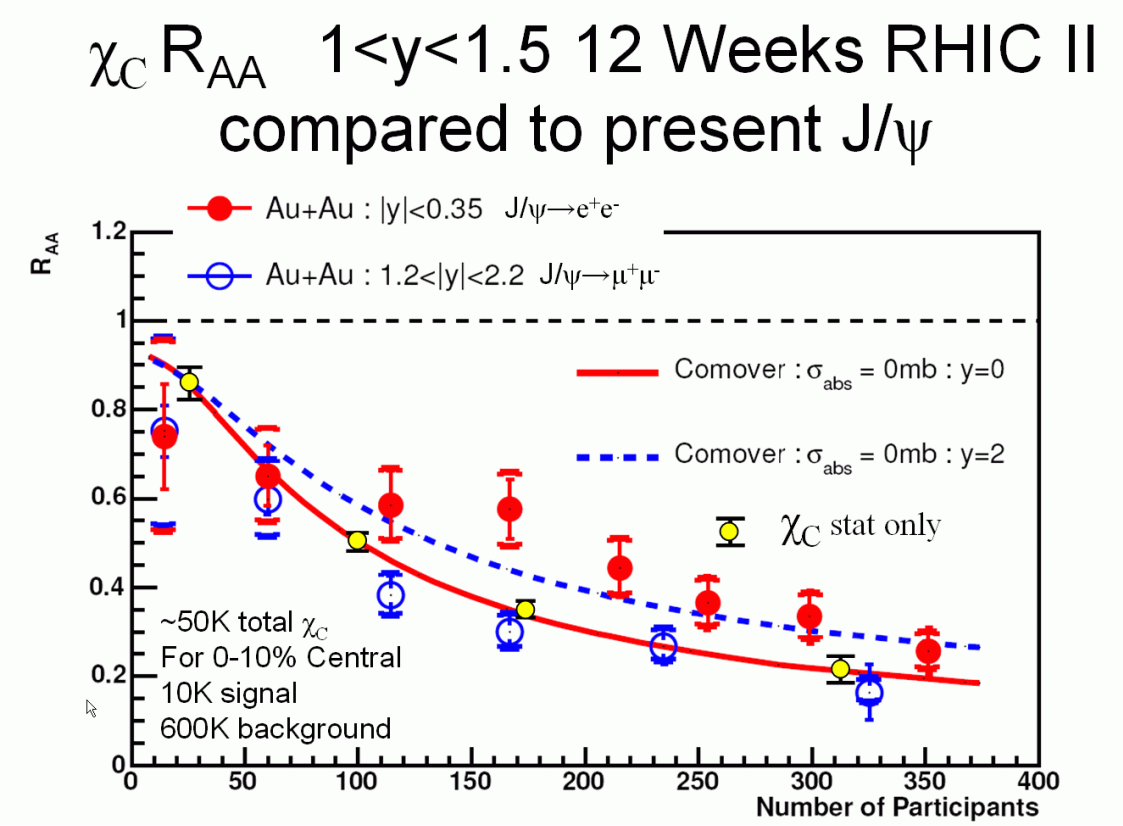

Figure B.12: R_{AA} for the χ_C in where the χ_C decays to a $J/\psi + \gamma$ and the J/ψ is detected via its dimuon decay in the muon spectrometer. The photon detected by the NCC in the rapidity range $1<|\eta|<1.5$. This is compared to the R_{AA} of the J/ψ measured by PHENIX in Run-4. At RHIC I before the RHIC II luminosity upgrade the error bars on the χ_C will be increased by a factor of 3-5 making a reasonable measurement. The increased statistics of RHIC II will allow for binning in both centrality and transverse momentum. Errors for the χ_C are statistical only. It is assumed that the p+p measurement of the χ_C adds a negligible error to the ratio.

B.4 Spin Simulations

The double longitudinal spin asymmetry A_{LL} for direct photon events gives the most theoretically clean access to the gluon polarization of the nucleon $\Delta g(x)$ because it is dominated by a single subprocess (Figure 2.17) and because one does not need to include the effects of fragmentation into a leading hadron. Jet events, if they can be reliably isolated, also allow one to avoid fragmentation uncertainties, but at the cost of a larger number of subprocesses which contribute to the asymmetry. Given a limited experimental acceptance, the asymmetry for production of a high p_T particle will typically yield the highest statistical precision, but one loses information about the particular kinematics of each event, in other words, the momentum fractions x_g of the gluon and x_q of the quark.

The present PHENIX spectrometer is only instrumented to detect photons and hadrons in the central rapidity region $\eta < |0.35|$, allowing an excellent measurement of A_{LL} with single photon and π^0 detection, but with limited ability to determine jet kinematics. The central rapidity is most sensitive to the gluon polarization at intermediate x. Given that the unpolarized gluon distribution is larger at somewhat lower x_g, there is strong interest to explore the gluon polarization to as low x_g as possible. The addition of the NCC immediately extends the range x accessible at PHENIX by nearly an order of magnitude lower, just by extending the acceptance for single photons. At the same time, it expands the range in rapidity for "jet" (or at least leading hadron) detection, thus giving a significant range over which the parton event kinematics, and hence x_g, can be determined. This range is further extended if the central (VTX) and end cap (FVTX) silicon vertex detectors are included.

In photon-jet events, assuming the dominance of the leading order graphs, one can measure x_g on an event-by-event basis by assuming that the lower x is that of the gluon and by measuring the angle of the jet, for example, as follows:

$$x_q = \frac{x_T}{2}\left(e^{+\eta_\gamma} + e^{+\eta_{Jet}}\right)$$

$$x_g = \frac{x_T}{2}\left(e^{-\eta_\gamma} + e^{-\eta_{Jet}}\right)$$

where

$$x_T = \frac{2p_{\gamma T}}{\sqrt{s}}$$

using the γ to determine p_T (this assumes intrinsic k_T effects are negligible in the kinematics).

In the following, we present the results of simulations of the accessible kinematics of the PHENIX spectrometer instrumented with the NCC, and assuming hadron detection for $\eta <\sim |2.5|$ (actually, the recoil parton η); this assumes therefore the inclusion of the VTX barrel and FVTX. Studies were performed for collision energies $\sqrt{s}$ of 200 and 500 GeV. The event generation is performed by PYTHIA using GRSV98 parton distribution functions Polarization effects are added by hand using the parton polarizations determined in AAC. The hard scattering asymmetry is calculated from the parton kinematics to leading order only. We have further applied a 10 GeV/c cut in p_T to photons.

The x_g range of the events are shown Fig. B.13, the number of gluon Compton scattering events which are detected as a function of $\log_{10} x_g$. The red points display the events with only

the existing (central) PHENIX photon detection, while the green points show the extension provided by the NCC. The black points provide a reference for the case in which there was full photon acceptance up to an η of 3. There are also clear regions of overlap between the NCC and central detectors which should allow crosschecks of the measurement of the gluon polarization.

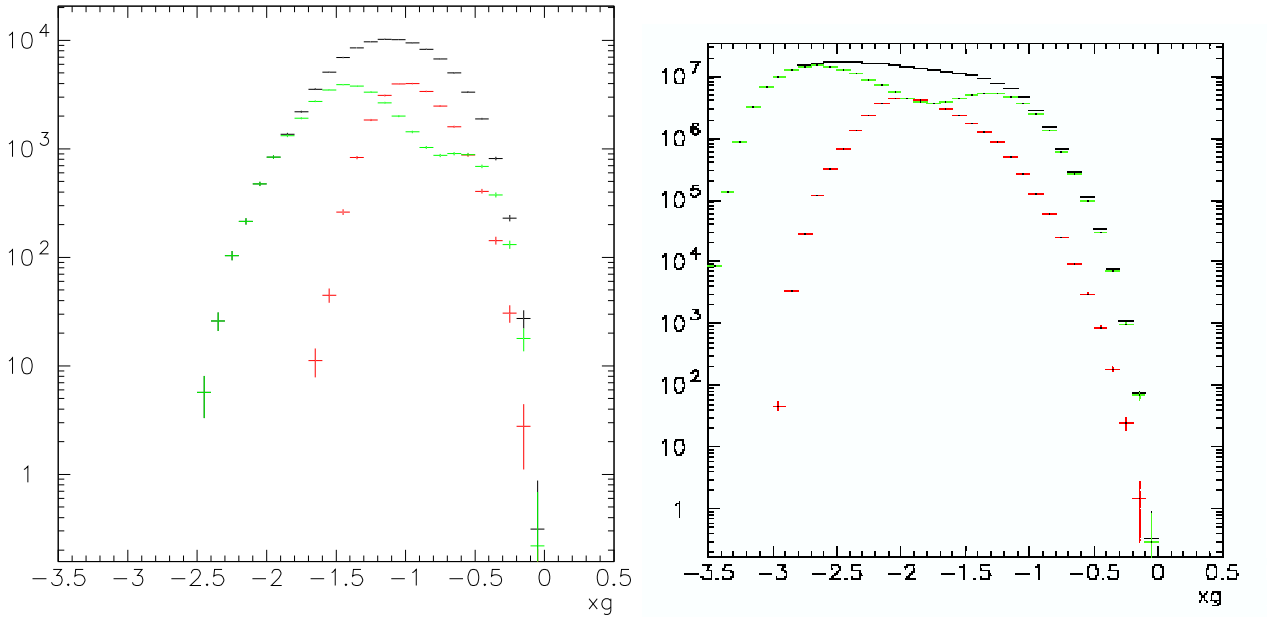

Figure B.13: Distribution of direct photon events at $\sqrt{s}$ of 200 (left) and 500 GeV (right). Red points refer to photons in the central detectors ($\eta < |0.35|$), while green points include the addition of the NCC ($1 < \eta < 3$). Black points show a hypothetical full acceptance ($\eta < |3|$).

This is where the power of the full PHENIX spectrometer will come into play. Using the tracking in the central SVX, the FVTX and the NCC PHENIX should be able to measure the jet angle over a large range. This together with the central EMC and the large acceptance of the NCC will give a measurement of both the photon and the jet over a nearly 5 units of rapidity giving access to $x_g \sim 10^{-3}$. It may be also be possible to disentangle events where the gluons are carrying a large momentum fraction to measure the spin structure functions at large x as well.

The actual double spin asymmetry as a function of photon p_T is shown in Fig. B.14, for $\sqrt{s} = 200$ GeV. The left panel shows the asymmetry measured in the central detectors, while that on the right shows the asymmetry for photons detected in the NCC. The simulation allows us to replot the asymmetry as a function of $\log_{10} x_g$, shown in Fig. B.15, clearly showing the range to which each acceptance is sensitive. One can directly see the range of $\Delta g(x_g)$ accessed (again via the simulation) in Fig. B.16.

Results of the simulation for $\sqrt{s} = 500$ GeV are shown in Figs. B.17. As expected, these measurements are sensitive to even lower x_g.

Further studies are underway to determine the effects of smearing from the actual photon

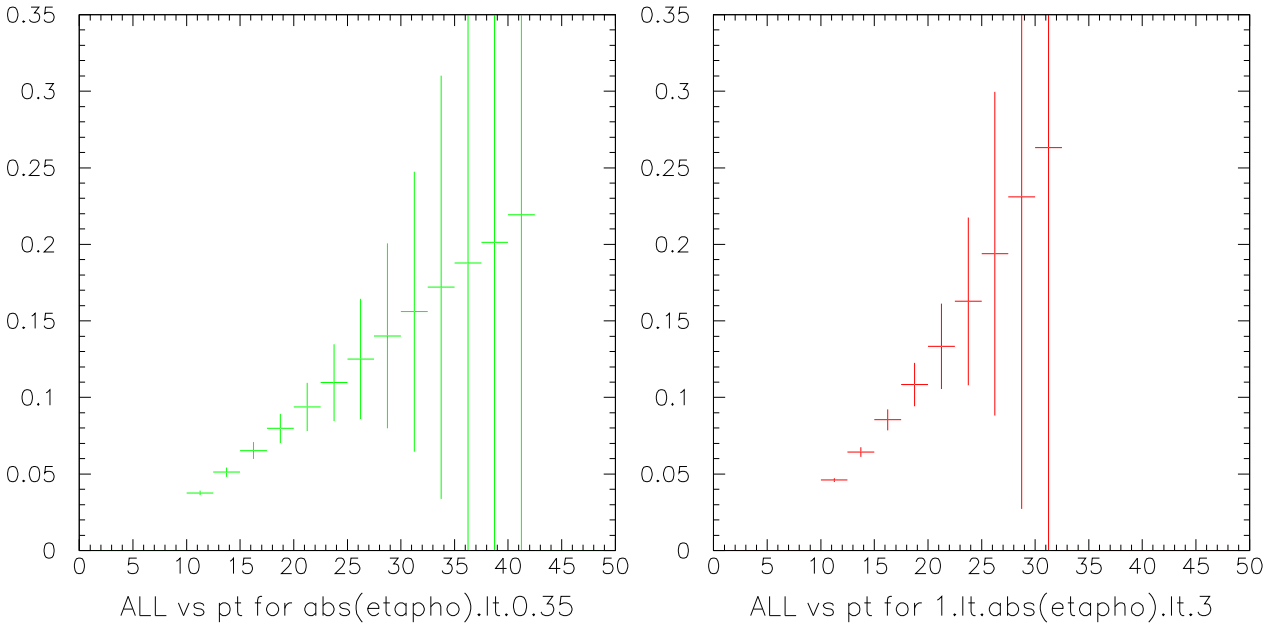

Figure B.14: Double longitudinal spin asymmetry for direct photon events at $\sqrt{s}$ of 200 GeV, as a function of photon p_T. The left panel shows the direct photon asymmetry measured by the central detectors ($\eta < |0.35|$), while the right panel shows the asymmetry measured by the NCC ($1 < \eta < 3$).

detection and jet angle resolutions for different detector configurations.

B.4.1 W isolation cuts: the quark structure of the nucleon.

While a cut on the pt of the muon can select W events, isolation cuts are traditionally used to clean up the signal offline. This is particularly important if there are fake muons coming from hadrons or hadron decays in the muon spectrometer. The isolation cut has been traditionally used to suppress the QCD background. Fig. B.18 shows that the one can get a suppression of the QCD background by a factor of 10, while loosing only 20% of the W's using at cut of 5 GeV for a radius of R¡0.75.

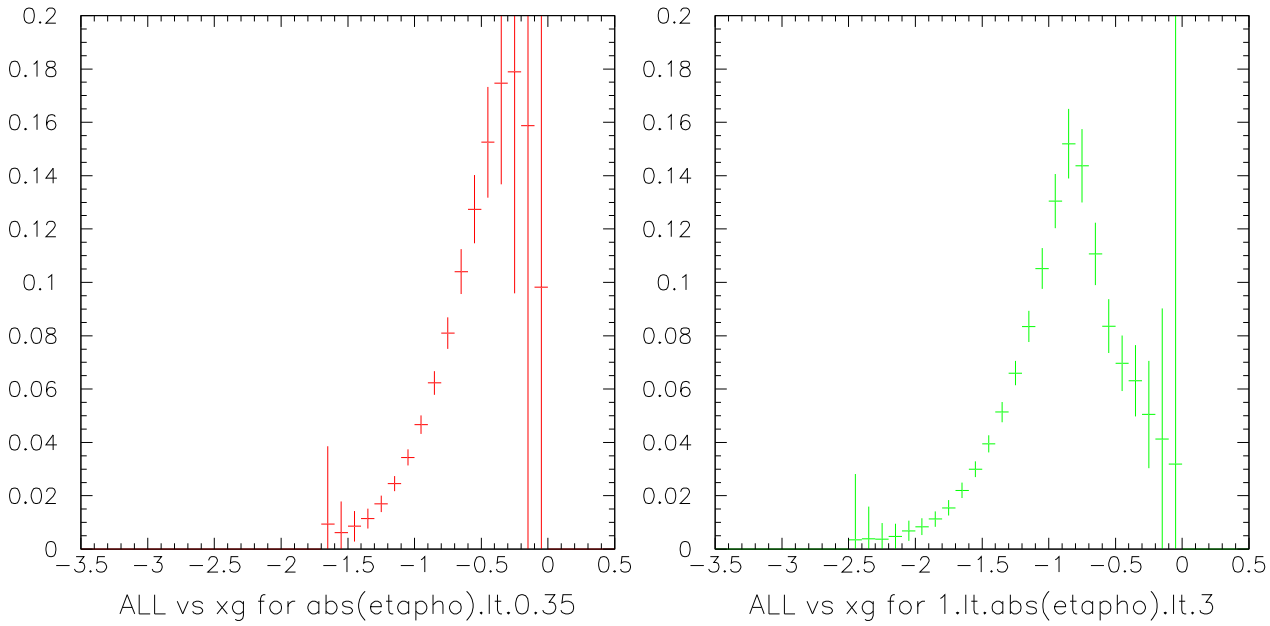

Figure B.15: Double longitudinal spin asymmetry for direct photon events at $\sqrt{s}$ of 200 GeV, as a function of $\log_{10} x_g$, as determined from the simulation. The left panel shows the direct photon asymmetry measured by the central detectors ($\eta < |0.35|$), while the right panel shows the asymmetry measured by the NCC ($1 < \eta < 3$).

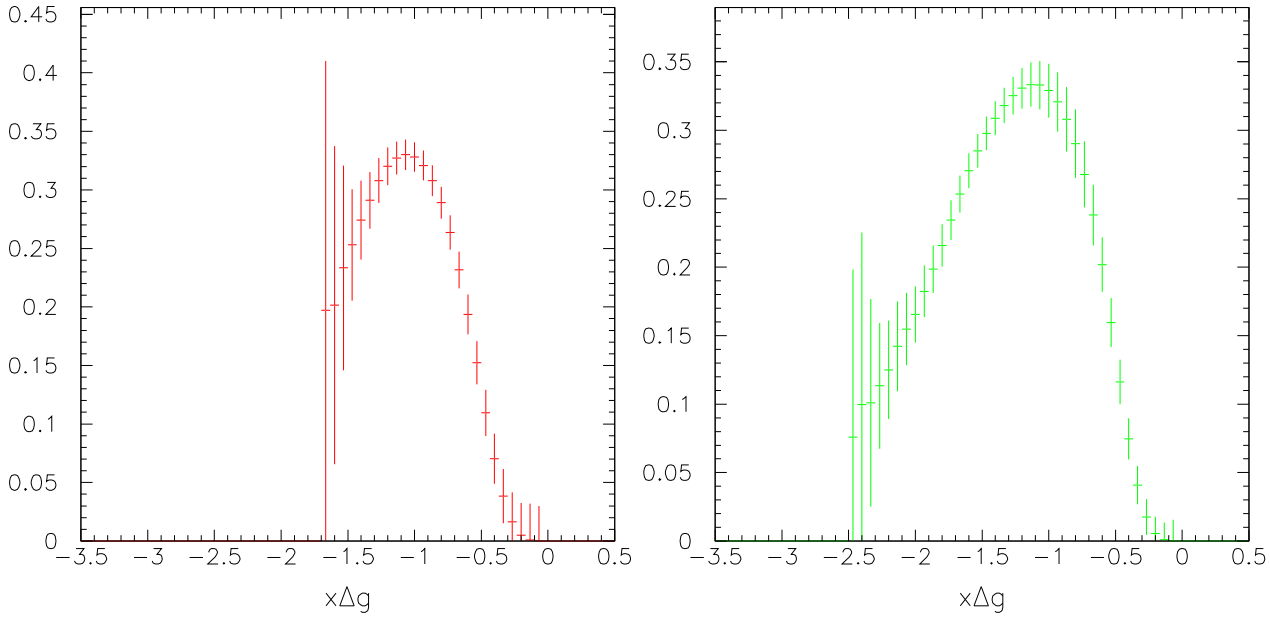

Figure B.16: Polarized gluon distribution function Δg for direct photon events at $\sqrt{s}$ of 200 GeV, as a function of $\log_{10} x_g$, as determined from the simulation. The left panel shows Δg measured by the central detectors ($\eta < |0.35|$), while the right panel shows Δg measured by the NCC ($1 < \eta < 3$).

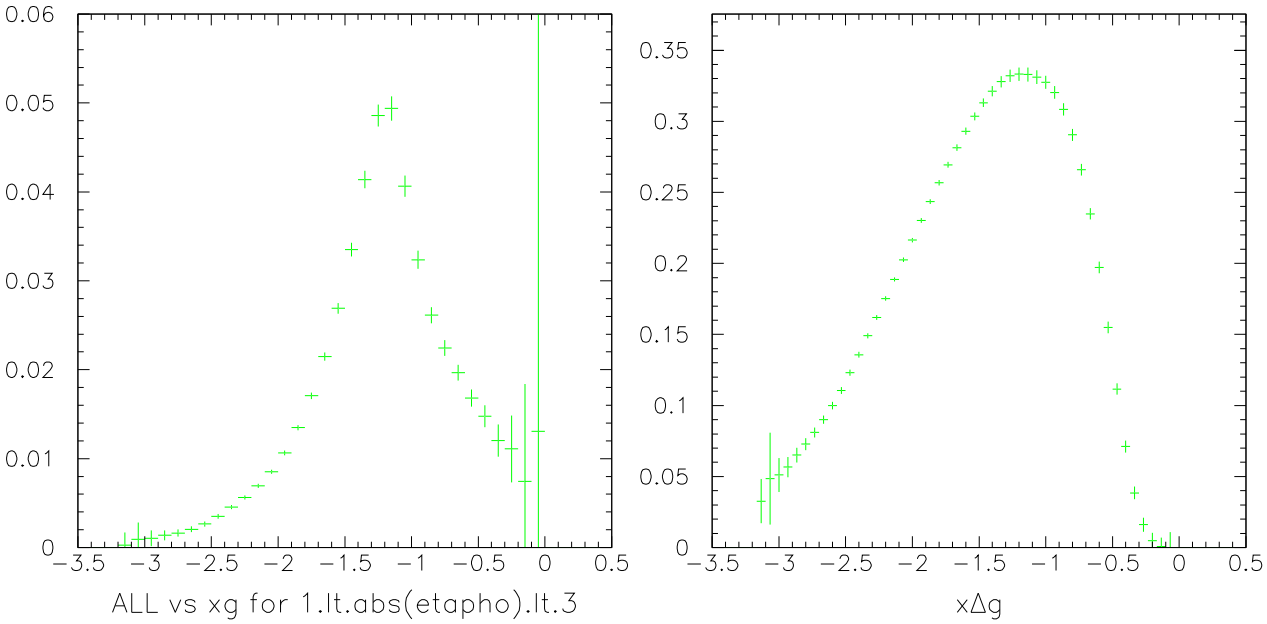

Figure B.17: Distributions for direct photon events at $\sqrt{s}$ of 500 GeV measured by the NCC ($1 < \eta < 3$) showing the reach to $x_g \sim 10^{-3}$. Double longitudinal spin asymmetry as a function of photon x_g (left). Δg (right).

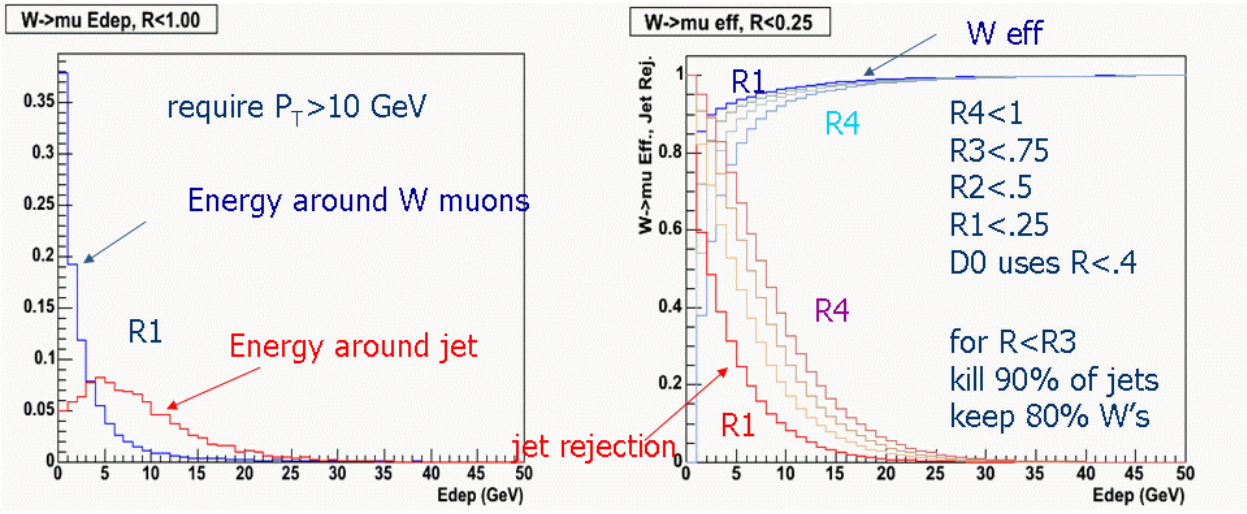

Figure B.18: (left) energy deposited around the muon in W events and jet events. (right) Suppression of background via isolation cuts.

B.5 A Simulation Study of the Reaction Plane by the NCC

When two nuclei collide slightly off-center, the initial high-density volume has the shape of their overlap region during the collision. That region is elongated along an axis perpendicular to the reaction plane–that is, the plane defined by the beam direction and the line between the centers of the two nuclei as they collide. This asymmetry gives a natural way to vary the distance a parton travels in the collision volume before escaping. Using the correlated direct photon-high p_T particle measurements versus the reaction plane will give information on the energy loss as a function of the distance traveled in the medium. A measure of the reaction plane resolution is $< cos\psi >$ where $< cos\psi >$ is the correction factor of the reaction plane resolution and is simply called the "reaction plane resolution". Measurements are as a function of reaction plane are diluted by a factor $(\frac{1}{<cos\psi>})^2$. Hence larger values of $< cos\psi >$ refer to a better reaction plane resolution. Present measurements using the Beam-Beam counters have a reaction plane resolution of $< cos\psi >$=0.4. A reaction plane detector is being proposed to increase this to $< cos\psi >$=0.7. The NCC will have a reaction plane resolution $< cos\psi >$=0.9. The following explains the simulation work to obtain this resolution.

The NCC detector is defined and installed in PISA GEANT simulation to replace the entire nosecone. Using the given geometry, a single particle simulation with charged and neutral pion was performed to prepare a mapping file, which covers full phase space (rapidity, p_T, ϕ) with uniform distribution. The mapping file is then used in the 2^{nd} step of simulation, which include realistic multiplicity (charged pion and π^0) and flow (v_2) depending on the p_T and rapidity. Therefore, the backgrounds from other detector elements as well as NCC itself are included. Fig. B.19 shows an overlay of several single track events.

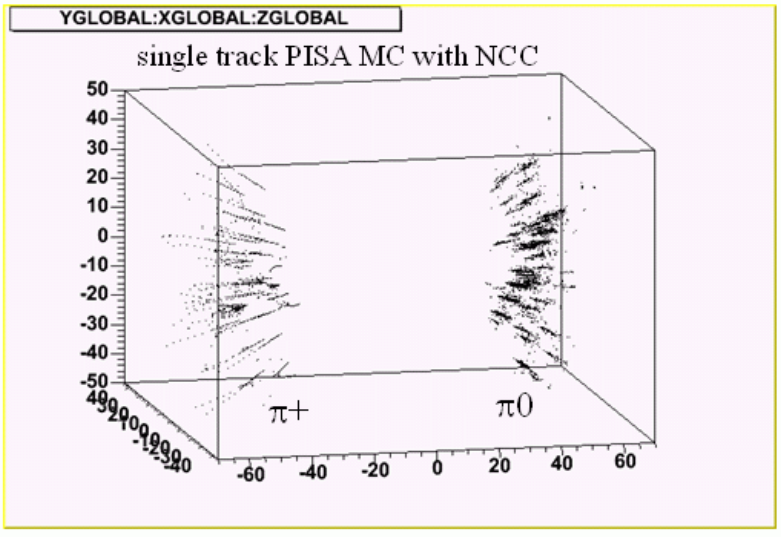

Figure B.19: An overlay of GEANT events in the NCC

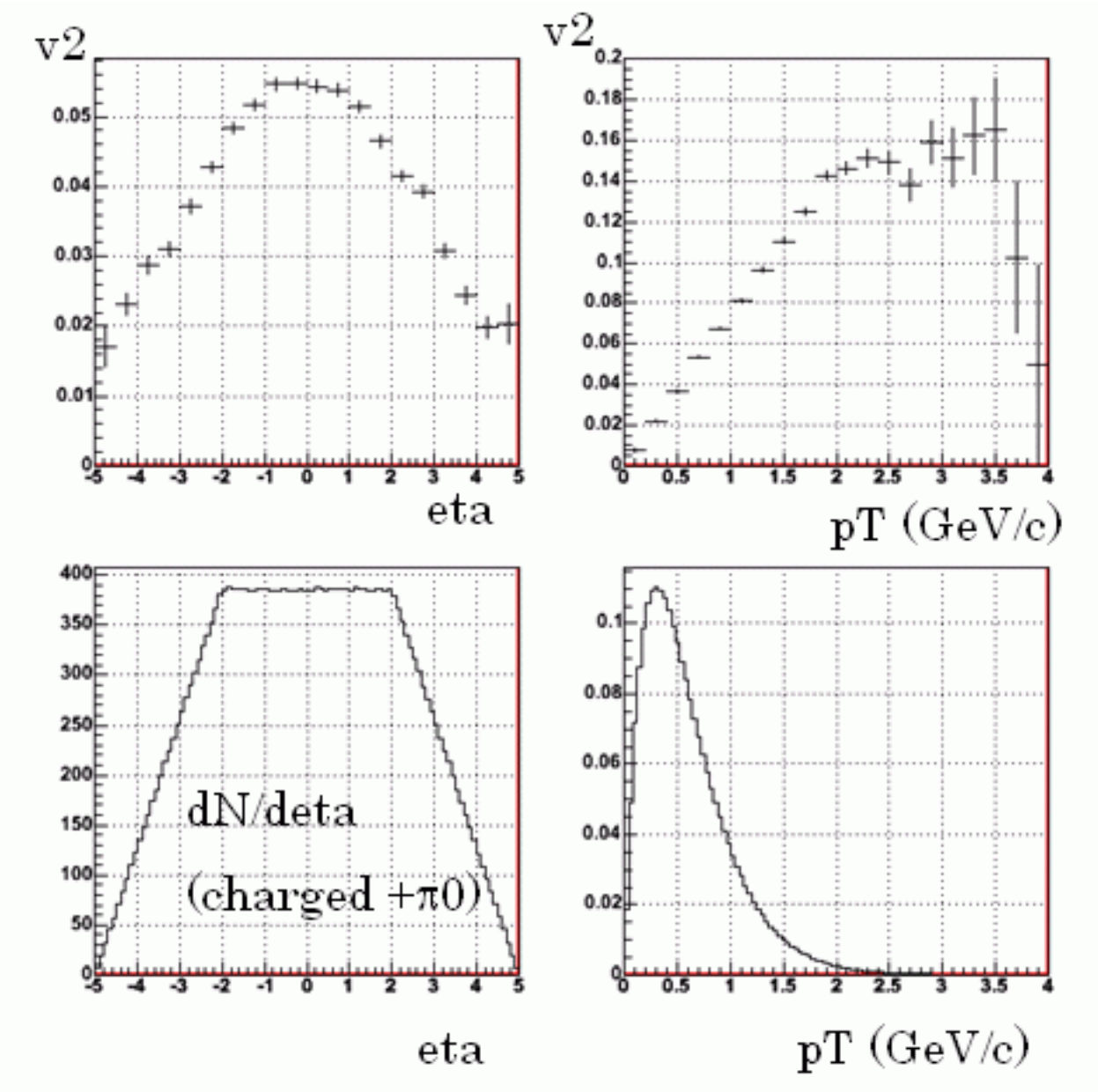

Figure B.20: Input flow (v_2) values as a function of η and p_T used in the simulation [top two panels]. η and $p_T$distributions used in the simulation [bottom two panels].

Input flow values and multiplicity used in the 2^{nd} step of simulation are shown in Fig. B.20. The top 3 panels in Fig. B.21 show the hit position in x-y on the NCC detector for 3 different z sectors, the first electro-magnetic sector (EM1) and the second electro-magnetic sector (EM2) after SM ID strip layer and the third hadronic sector (HAD). The radial hit distribution, azimuthal hit distribution with respect to the generated primary track and azimuthal hit distribution with respect to the simulated reaction plane orientation are shown in the bottom three panels in Fig. B.21.

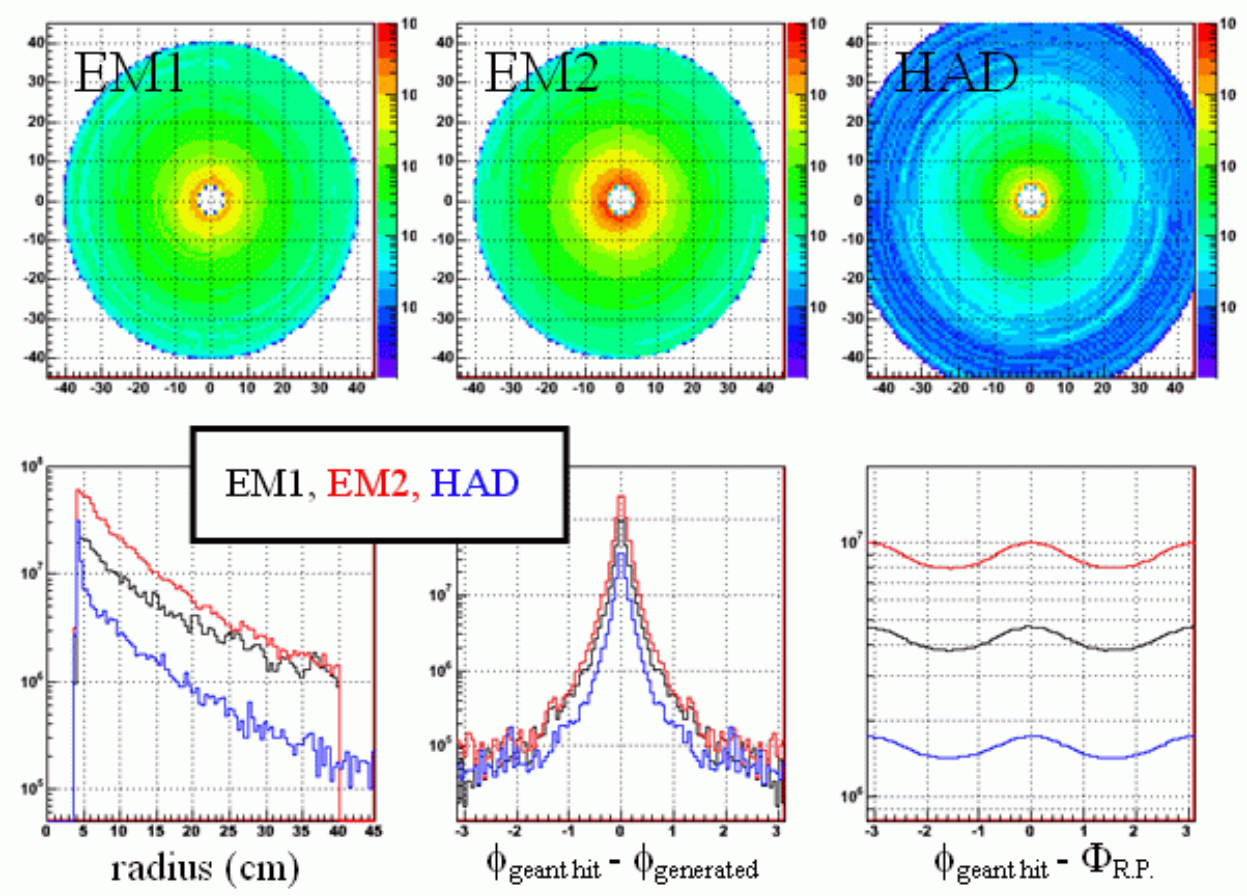

Figure B.21: Hit position in x-y on the NCC detector for in EM1, EM2, and HAD(top 3 panels). Radial hit distribution, azimuthal hit distribution with respect to the generated primary track and azimuthal hit distribution with respect to the simulated reaction plane orientation(bottom 3 panels).

Fig. B.22 shows the reaction plane distribution ($\Phi_{calc} - \Phi_{true}$) with different weighting methods described in the figure caption. The bottom panel shows the reaction plane resolution with different cases as described in the figure caption. The resolution goes up from about 0.8 in the case (2) with charged particle alone to about 0.9 case (7) by including $\pi 0$ conversion, dE/dx weighting and optimizing the weight. The three regions in the bottom panel show the radial dependence of the reaction plane resolution for each z sector, the pink dashed lines show parameterized function of radial dependence of resolution, which is used to weight each reaction plane to get the best resolution in the case (7).

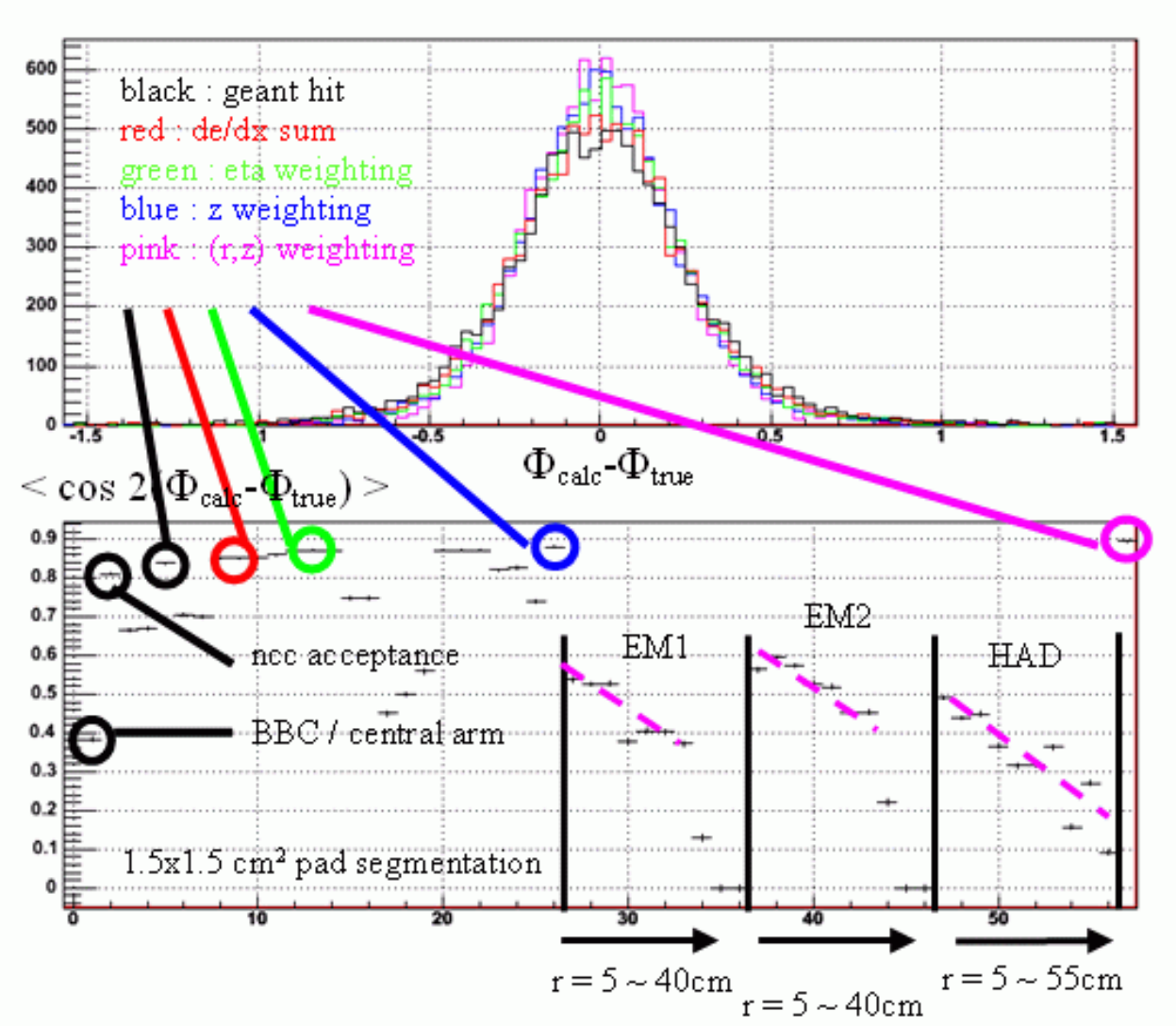

Figure B.22: (top) The reaction plane distribution ($\Phi_{calc} - \Phi_{true}$) with different weighting methods. (Bottom) Reaction plane resolution for different cases, where the conditions marked with circle are described in the following. (1:black) BBC or central arm reaction plane resolution is about 0.4, (2:black) use all charged particles in NCC acceptance, (3:black) use all GEANT hits in NCC, (4:red) weighting all the GEANT hits with dE/dx, (5:green) v2 weighting according to eta dependence of v2 in addition to (4), (6:blue) z sector depending weight in addition to (5), (7:pink) 2 dimensional r, z weight in addition to (5). The resolution goes up from about 0.8 in the case (2) with charged particle alone to about 0.9 case (7) by including π^0 conversion, dE/dx weighting and optimizing the weight.

B.6 Muons and Background

In addition to the topics covered in the main text, the NCC can be used together with other detectors to solve some problems; for example, the identification of muons. The major sources of hard muons are:

1. the semi-leptonic decay of heavy flavored quarks in the intermediate p_T (transverse momentum) range of $2 \sim 15$ (GeV/c),

2. the decays of W bosons above very high p_T of above 20 (GeV/c).

Heavy flavor production and W boson productions at RHIC are of great interest. As an example, the major focus of the ongoing muon trigger upgrade is to understand spin structure of the protons through very high p_T muon measurement. With the luminosity upgrade and the muon trigger upgrade, we will reach very high p_T regime beyond our current statistical limit.

Beyond the statistical limitation, one of the major challenges in achieving high p_T muon measurement is a fake high p_T background. The background originates from a small fraction of the soft light hadrons, $\pi^{\pm}$ and $K^{\pm}$ which penetrate the front absorber composed of the NCC and magnet yoke, and subsequently decay into muons between muon tracking station 1 and station 3 , and are reconstructed by chance. The rigidities of the reconstructed trajectories are determined by the bend angle between tracking station 1 and tracking station 3. Decays can fool this rigidity determination and generate seemingly hard tracks with a rare, but significant occurrences. Fig. B.23 shows the reconstructed p_T distribution from various p_T ranges of the light hadrons generated with realistic multiplicity for p+p collisions at $\sqrt{s} = 500GeV$. For each range, a small fraction (10^{-3} to 10^{-4}) contributes to the fake hard p_T distribution. Due to the large multiplicity, low p_T hadrons dominate the real muon contribution from W decays even at very high p_T.

The NCC is positioned between the collision location and the tracking station 1, and measures crossing locations of the reconstructed trajectories at the accuracy of about 150 μm at two independent planes, using PS and SM. While real high-p_T tracks travel along a straight line trajectory between the collision location and the tracking station 1, fake high-p_T tracks do so with large deflections inversely proportional to the momenta. So, for a chosen momentum or p_T, we can select a narrow window of possible deflection ranges and reject fake high-p_T tracks with large deflections my matching hits in the PS or SM. Figure B.24 shows the reconstructed p_T distribution similar to Fig. B.23, but with a window optimized for $p_T \sim 25$ (GeV/c). According to a preliminary study, the finite NCC occupancy in p+p collisions at $\sqrt{s} = 500$ GeV does not degrades the performance, but performance degradation due to the large occupancy in Au+Au collisions must be investigated.

In conclusion, nose cone calorimeter (NCC) can reject fake high p_T tracks effectively, and will help prompt muon measurements.

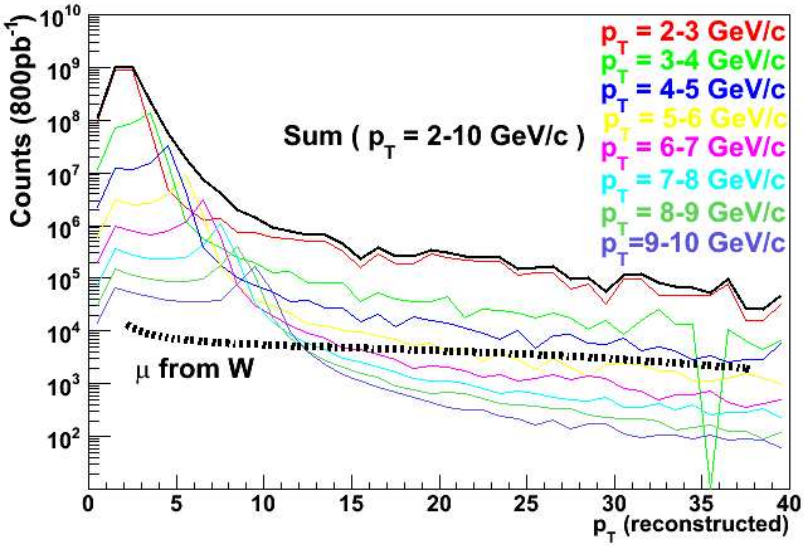

Figure B.23: . Reconstructed p_T distribution from various p_T intervals of produced light hadrons. Muons from W boson decays are also shown.

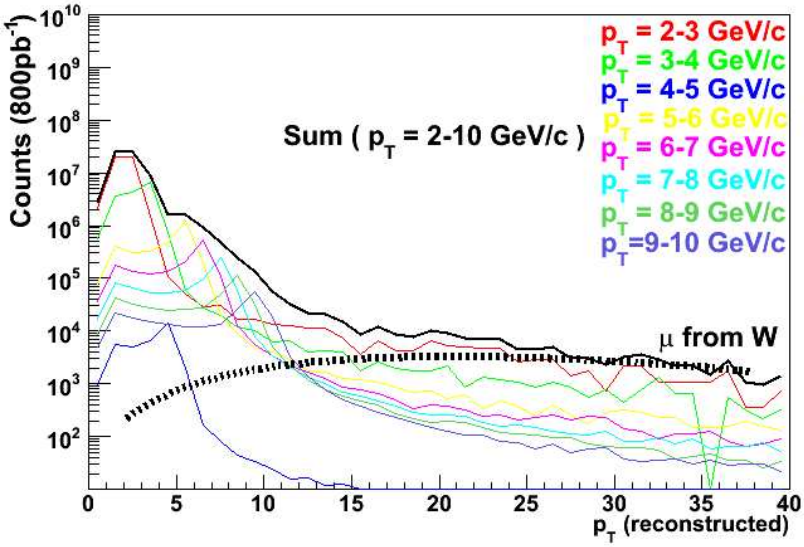

Figure B.24: Distribution similar to Fig. B.23, but with the background suppression by matching tracks from the muon spectrometer to the NCC.

Appendix C

Test Beam Results

A prototype NCC was designed as a proof-of-principle device for the Collaboration to acquire experience in silicon detector production, and to test one possible assembly scheme and the robustness of technology. The prototype calorimeter design included 22 sampling layers, with the first 16 cells grouped into 6 cell and 10 cell segments. These were designed as the as electromagnetic segments (2.5 mm W + 2.5 mm readout). The last 6 cells (15 mm W and 2.5 mm readout) served as the hadronic segment. The calorimeter was built to allow installation up to 4 sensors per layer (12x12 cm^2). We used one position in every layer to install prototype DC coupled sensors. Fig. C.1 is the photograph of a single assembled ROU (readout unit) connected to the preamplifier board.

In actual test beam experiment we used preamplifier boards developed at MSU and equipped with CR1P4 16-channel preamplifier chips provided by A.Vacchi (Trieste, Italy). To make optimal use of available electronics the number of geometrically matching pads from individual layers ganged together was limited to 4 thus resulting in the prototype being segmented into 6 longitudinal segments (4 fine and 2 coarse). Ganged and amplified signals were digitized using an off-the-shelf multi-channel ADC unit. The assembled prototype is shown in Fig. C.2.

The prototype calorimeter was exposed to electron and proton beams from the IHEP U70 proton synchrotron in Protvino (Russia) in November 2005. Here, we present data accumulated exposing the calorimeter to 70 GeV/c protons and 10 GeV/c positrons.

C.1 Data analysis

The amplitude distributions recorded in proton runs were used to establish values of the pedestals, the shape of the signal, minimum ionizing peak values and the signal/background ratio. The result is illustrated in Fig. C.3 which shows the pedestal and MIP signal. The signal/noise ratio is 4-5 with good MIP resolution. (For comparison we expect it to be $\sim$40 the final detector.)

In the electron analysis the individual pedestals computed using data from proton run were subtracted to get signal amplitudes in every segment. The MIP peak varied segment-to-segment but was nearly independent of hit position in the plane. The recorded data

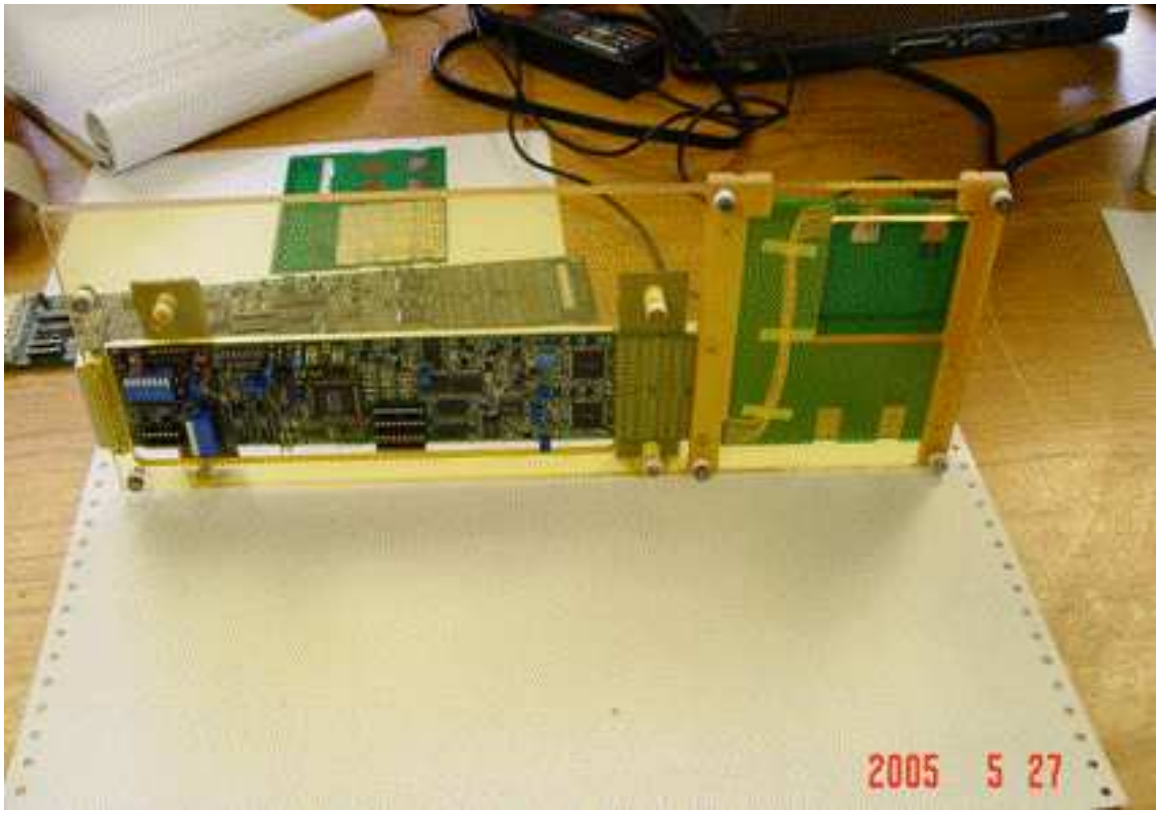

Figure C.1: Single assembled readout layer for the prototype NCC connected to readout electronics.

are strongly affected by common mode noise. Pads outside the base matrix of 3x3 towers centered at the tower with maximum amplitude were used to measure the common mode noise value which was subtracted from all 16 measured amplitudes prior to normalization. In addition the following cuts were applied to clean the data of hadronic contamination present in the electron beam:

- The amplitude sum in segment 1 was required to be smaller then amplitude sum in segment 2 (to exclude tails of showers started upstream of the prototype detector),.
- The amplitude sum in segment 1 was required to be smaller then 600 counts (to exclude events with multiple hits).

.

A typical event in the prototype calorimeter exposed to positrons of 10 GeV/c momenta cleaned of common mode noise is shown in Fig. C.4.

The average energy in the segment when exposed to positrons is plotted as function of the calorimeter depth at the geometrical center of the segment in Fig. C.5.

The observed behavior is consistent with the expected electromagnetic shower shape. The maximum in the distribution of deposited energy is reached at a depth of $\sim 7\ X_0$ in the calorimeter.

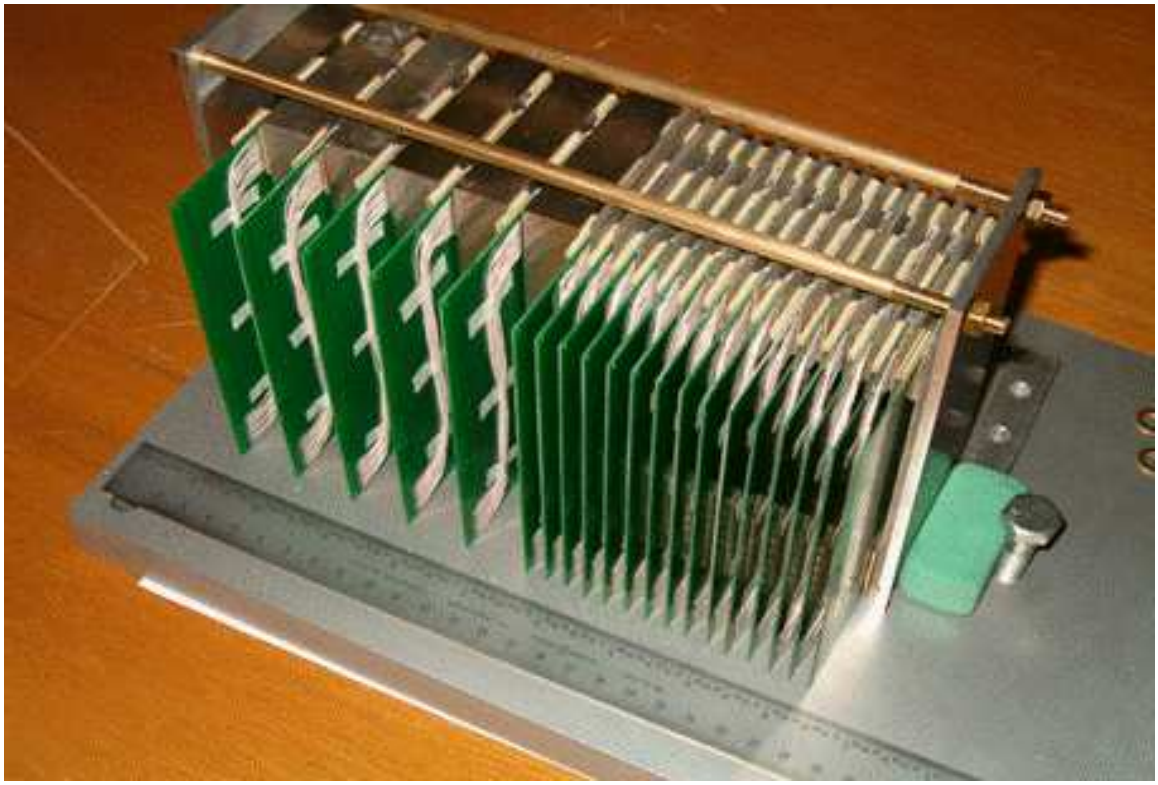

Figure C.2: Assembled prototype calorimeter. Readout electronics not shown.

The mean longitudinal profile was fitted with the functional form $k \times X_0^{(a-1)} \times \exp -bt$ and describes the data with good accuracy.

In order to improve the experimental resolution an additional weighting procedure based upon measured longitudinal shower shape was applied to the positron data. The final distribution of the weighted amplitude sum is shown in Fig. C.6. The data were fitted by sum of the Gaussian peak and polynomial background resulting in measured resolution of 11% (90% CL) for the 10 GeV/c positron beam consistent with predictions in earlier chapters of this CDR i.e. $\sim \frac{20\%}{\sqrt{(E)}} + 4\%$.

The positron data recorded in every segment of the prototype were further used to study the dependence of position resolution measured in individual segments on the depth position of the segment in the calorimeter. In the absence of beam tracking, the resolution was computed subtracting measured coordinates from those computed using straight line fit to all six measured points (see Fig. C.7).

As expected the best result ($\sigma = 1.4mm$) at 10 GeV is reached using data from segment near the shower maximum. Using all 6 points we may estimate the pointing resolution of prototype calorimeter (Fig. C.8).

A value ∼6 mrad was measured in the X- and Y- views which corresponds to a pointing resolution $\sim 9mrad$. This then corresponds to a 5 mm resolution in impact parameter with respect to the collision vertex.

The pointing capability is a byproduct of the longitudinal segmentation and introduced

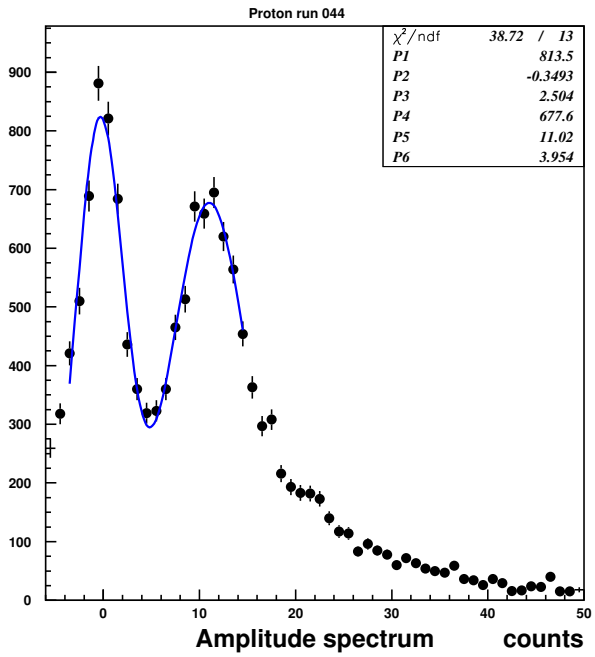

Figure C.3: Amplitude distribution of the signal from the pad nearest beam impact point. Data from prototype.

a tool to remove hadronic contamination from the photon sample. While probably not crucial, this feature may be important in reducing contamination from non-beam sources such as cosmic rays which are important backgrounds to photons with very high momenta.

Finally in Fig. C.7 we show the 3-d plot illustrating the particle identification capabilities of a calorimeter with the proposed longitudinal segmentation. Each shower is represented by a point in 3D-space: E_1/E_{Tot}, E_2/E_{Tot}, E_3/E_{Tot} where E_1, E_2, E_3 are energies measured in properly combined calorimeter segments. Red points are 10 GeV/c electrons, blue points are 70 GeV/c protons. The two sets of points are well separated.

In conclusion we would like to emphasize the following: the construction of of the prototype and its exposure in the particle beam was probably the most important achievement of our initial R&D efforts. It proved

- the robustness of technology,
- the soundness of the idea to passively sum signals from multiple Si pixels,
- the ability to handle and calibrate data from a longitudinally segmented calorimeter,
- the ability of simulations to correctly predict detector performance,
- the ability of a collaboration which has a very brief prehistory and is composed of institutions from all over the world to coordinate its efforts and reach the desired goals.

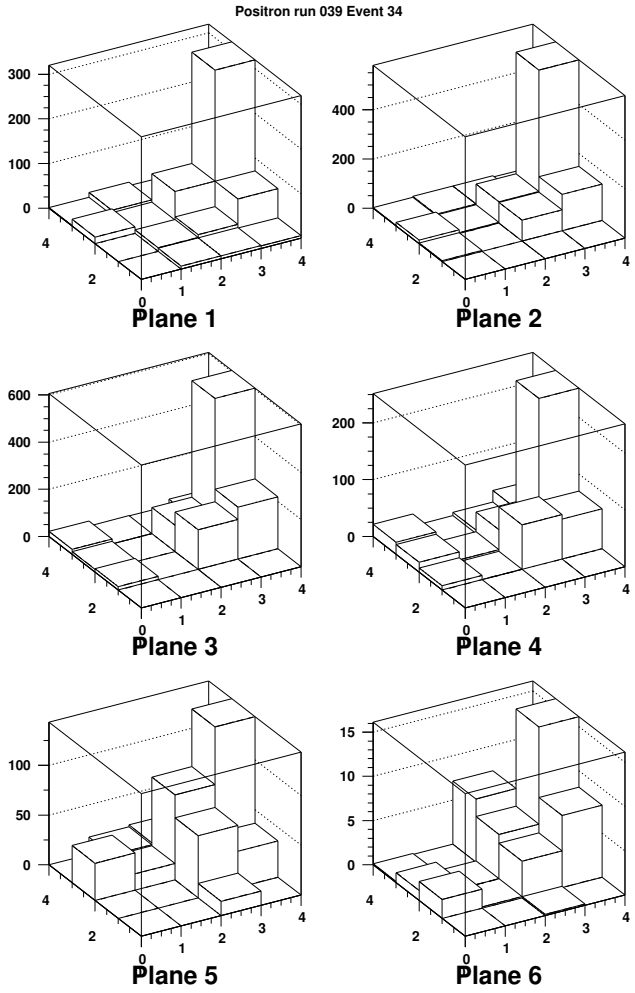

Figure C.4: Example of the electromagnetic shower in prototype W-Si calorimeter

The results of this project were very encouraging and gave us confidence that we will be able to reach similar successes with the design and prototyping of a real detector and as well as with construction project.

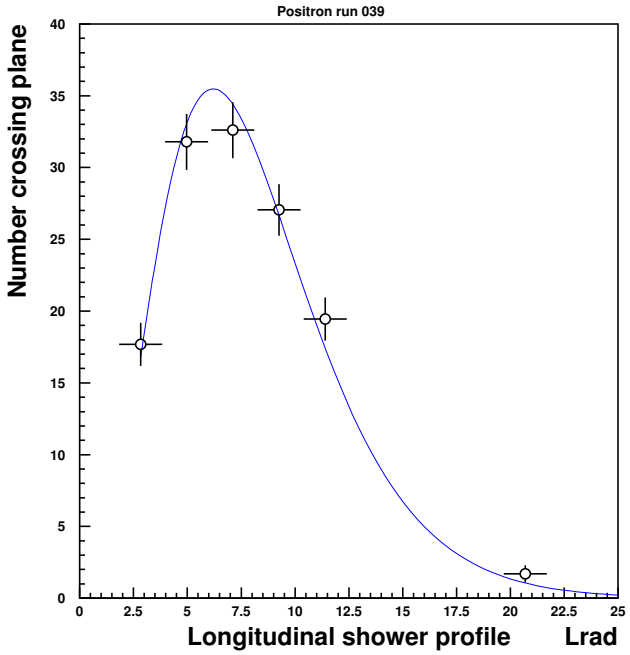

Figure C.5: Longitudinal profile of electromagnetic shower.

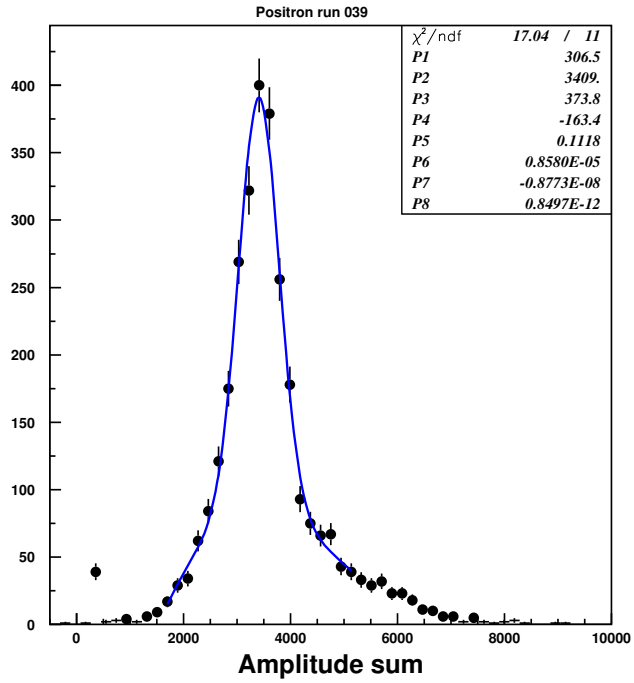

Figure C.6: Energy distribution in the NCC prototype measured exposing detector to a 10 GeV/c positron beam.

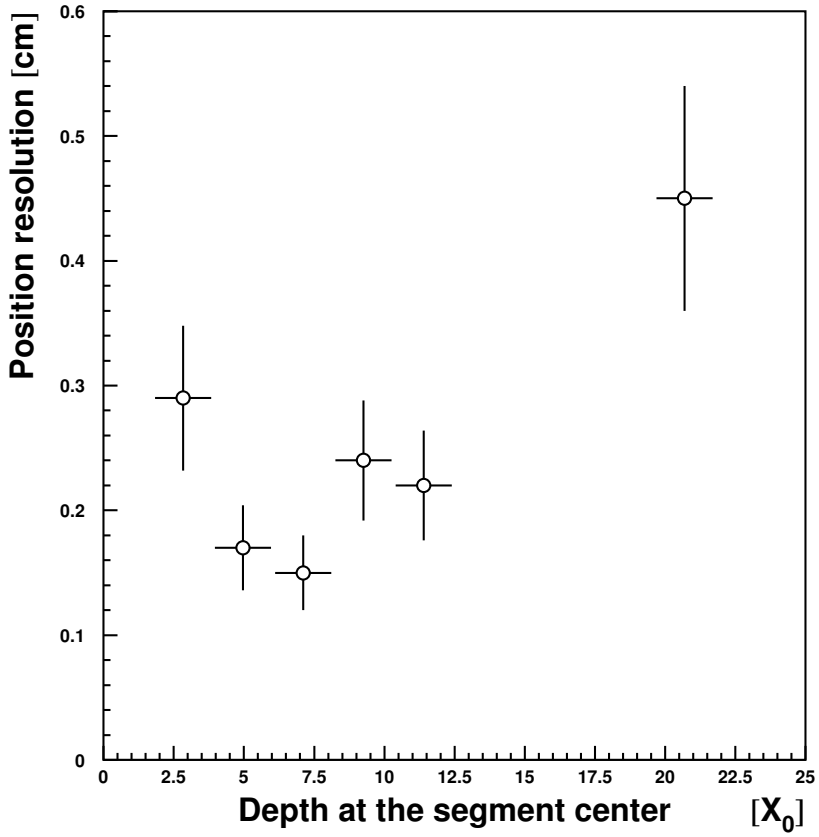

Figure C.7: Precision of the impact point measurements in the longitudinal segments of the prototype detector. The location of the geometrical center of the segment in the prototype is plotted along X in units of X_0.

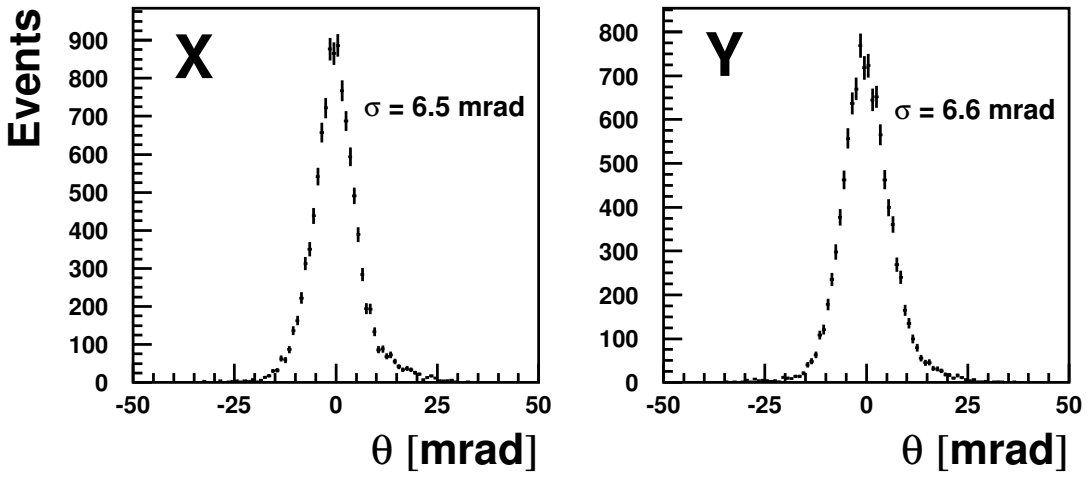

Figure C.8: Pointing resolution measured in the prototype calorimeter exposed to 10 GeV/c positrons. Both X- and Y- planes are shown.

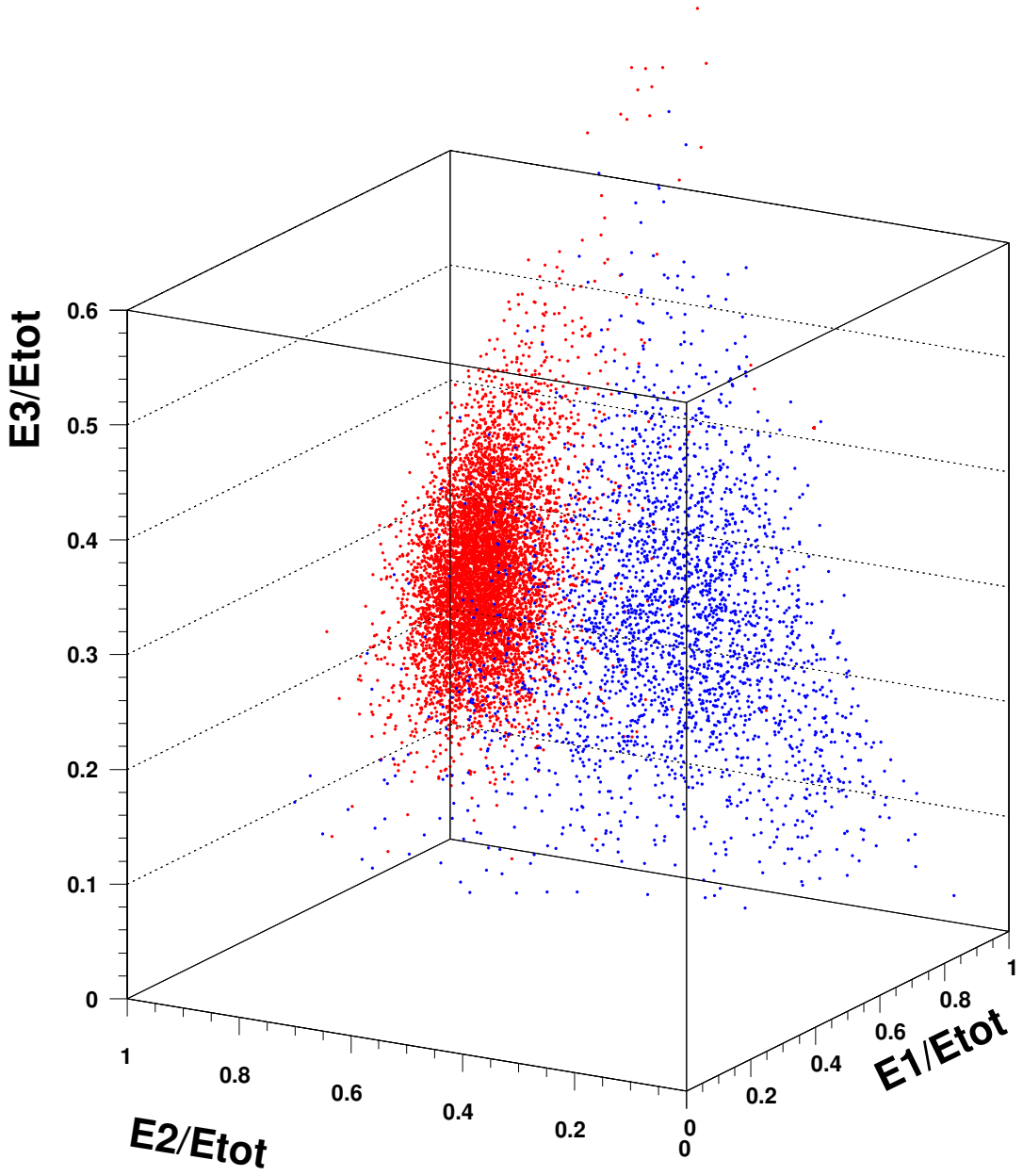

Figure C.9: Shower identification in longitudinally segmented calorimeter. E_1, E_2, E_3 are energies measured in calorimeter segments, E_{Total} is the total energy. Red points are 10 GeV/c electrons, blue points are 70 GeV/c protons.

Appendix D

Sensor Research and Development

Prototype pad-structured DC coupled silicon sensors were produced at the ELMA subsidiary of the Research Institute of Material Science and Technology (RIMST), Moscow, and delivered to our collaborators at Moscow State University (MSU). Following the design specifications discussed earlier in this document, these test sensors were optimized for radiation hardness. The design was largely influenced by previous experience at MSU (pad-structured sensors for CALICE W-Si calorimeter prototype). A picture of the sensor together with the guard-ring structure is shown in Fig. D.1. The 5kΩ, 300 μm thick FZ- wafers from Wacker (Germany) available at MSU were used for this submission. In total 30 sensors were produced; IV and CV measurements at MSU resulted in 25 sensors accepted and 5 sensors rejected because of large leakage currents. Results of the depletion voltage (CV) and leakage current (IV) measurements are shown in Fig. D.2.

Both the yield and performance of sensors are satisfactory. The good sensors were then used to build a proof-of-principle NCC prototype later tested in the test beam in Protvino, Russia (IHEP).

As part of the R&D effort we also tested a number of extreme options illustrated in Fig. D.3 (with decoupling RC networks on and partially on sensors).

The sensors with built-in RC networks are a good option for detectors intended for mass use as they are easy to test and need only a minimal set of external passive components for connection to preamplifiers. Unfortunately this technology routinely results in increased cost and reduced yield associated with the extra steps required to grow large capacitances on pad surfaces. In addition, it leaves no choice but using detectors with bias voltage applied to the common side. In the case of the PHENIX NCC where individual pixels are ganged together to allow a single preamplifier to handle the analog sum of the pixel currents, the AC coupled design has disadvantages. For instance it makes biasing the sensors and insulating them from detector construction elements difficult.

Our project was reviewed by the unofficial panel of Si detector experts at the SiDet Laboratory at FNAL, the recommendation which we accepted were to either use DC coupled sensors or to limit the upgrades to growing polysilicon resistors on the sensors (keeping external decoupling capacitances). While no firm commitment was made at a time the modified design was proposed for consideration by several companies: ELMA(Russia), ON Semiconductor (Czech Republic), and SENS (Korea). ON Semiconductors delivered test

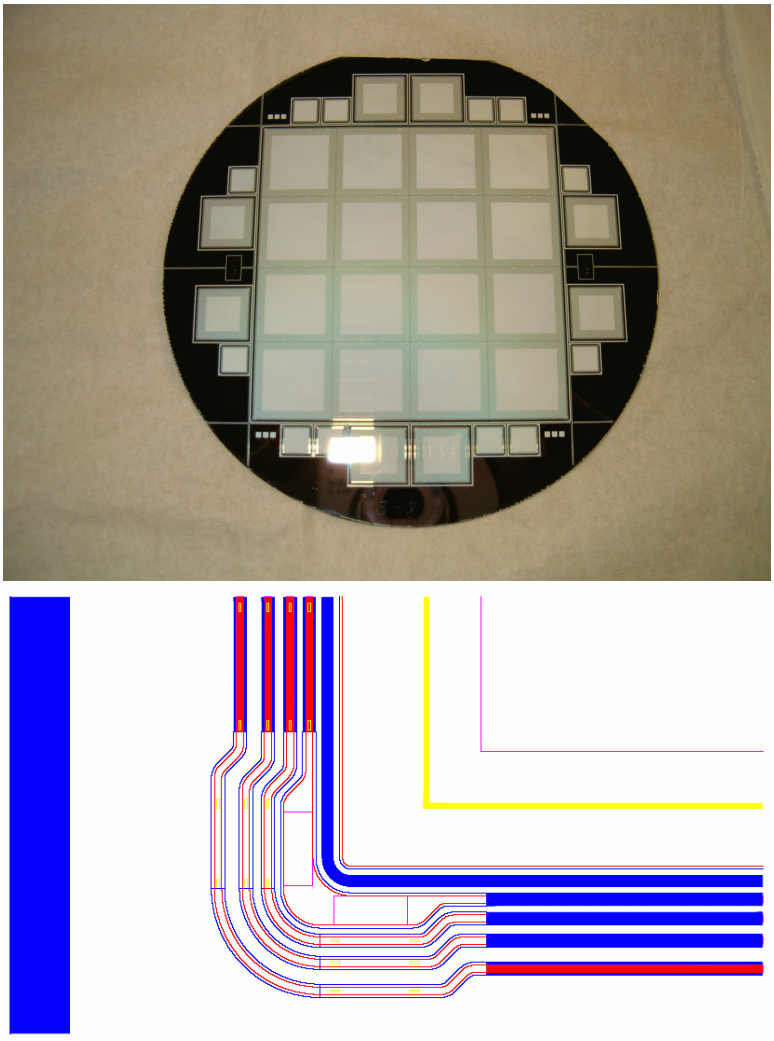

Figure D.1: The NCC Silicon sensor. An undiced wafer is shown. The active area is subdivided into 16 readout pads 1.5x1.5 cm^2 each. The structure of the guard rings which prevents voltage breakdowns after radiation exposure is also shown below.

samples to our Collaborators in Prague for evaluation. The uniformity of resistances was found to be better than 15% and all other characteristics were found acceptable. The very first AC coupled sensors manufactured at ELMA were received at MSU and measured. Given the relatively low yield, we decided not to pursue this option.

Within the same framework we began development work aimed at optimizing the StriPixel sensor design. This project has an obvious urgency since critical aspects of charge sharing and crosstalk between crossing strips are very difficult to simulate and final choice cannot be made without prototyping a variety of structures. The first prototype prototype wafers delivered from ELMA in Russia have shown the expected behavior on test structures, however, the sensors happened to be shortened because of the mismatch between design (made at BNL) and technology used at ELMA. A new submission resulted in the production

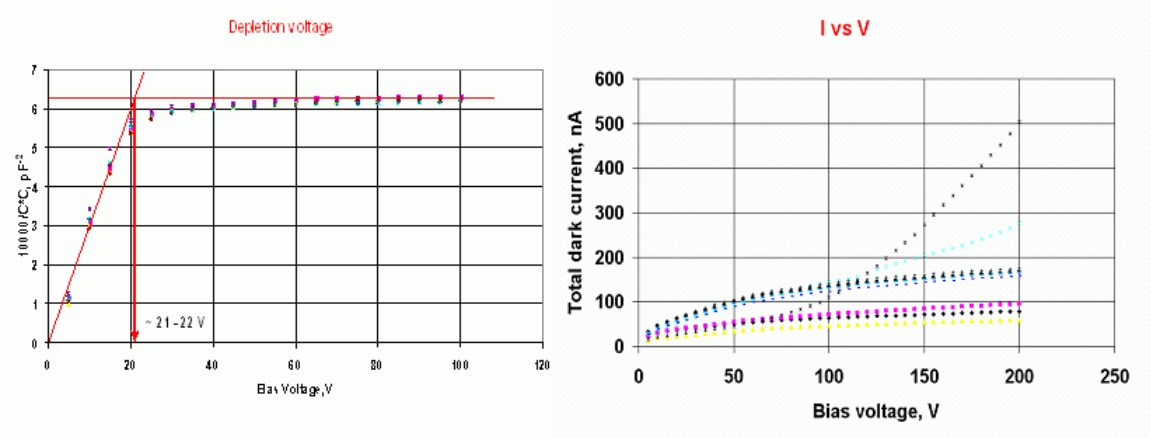

Figure D.2: CV and IV measurements for the test batch of 30 PHENIX NCC pad-structured sensors produced at ELMA.

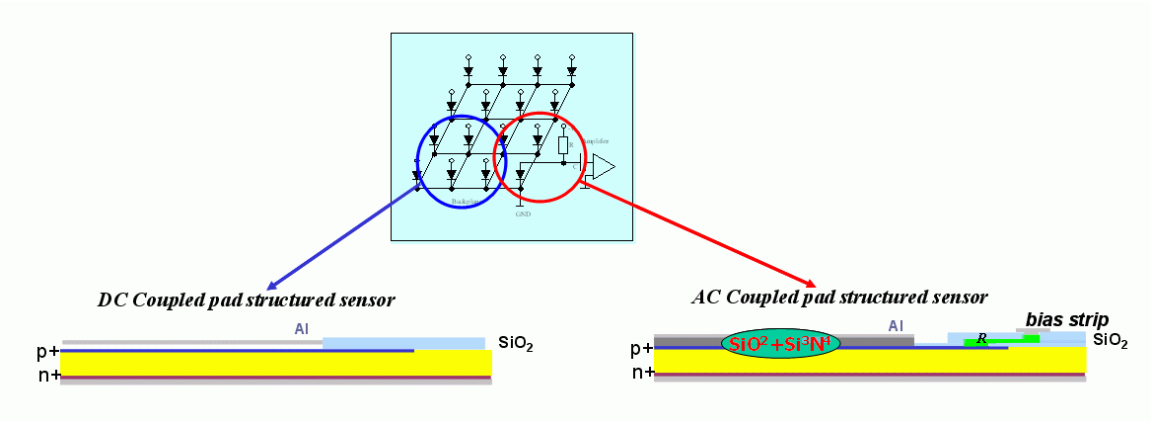

Figure D.3: Two designs for the pad-structured Si sensors. DC on the left and AC (decoupling capacitances and bias resistors are on sensor) on the right

of a few good wafers Figure D.4 and is being subjected to testing in the Silicon Laboratory in JINR (Dubna).

The prototype Sensor were exposed to α-particles from a 241Am (E=5.486 MeV) source. Reasonable (but very asymmetric) charge sharing between X and Y pixilated strips was measured(Figure D.5).

The charge sharing is improving for the finer structures. The minimum inter-strip separation tested is 15 μm). Asymmetry in the charge sharing was traced to the effect of implanted bridges. The high resistance of the implanted bridges caused asymmetrical signal degradation and excessive noise which makes them unacceptable. There are also hints of significant crosstalk between neighboring strips- capacitative coupling between p+ "wires" implanted into bulk n- silicon. Further results forthcoming.

In many aspects results from StriPixel detector testing are still inconclusive. The observed problems are related to (a) technical difficulties in measuring simultaneously X and Y strips;

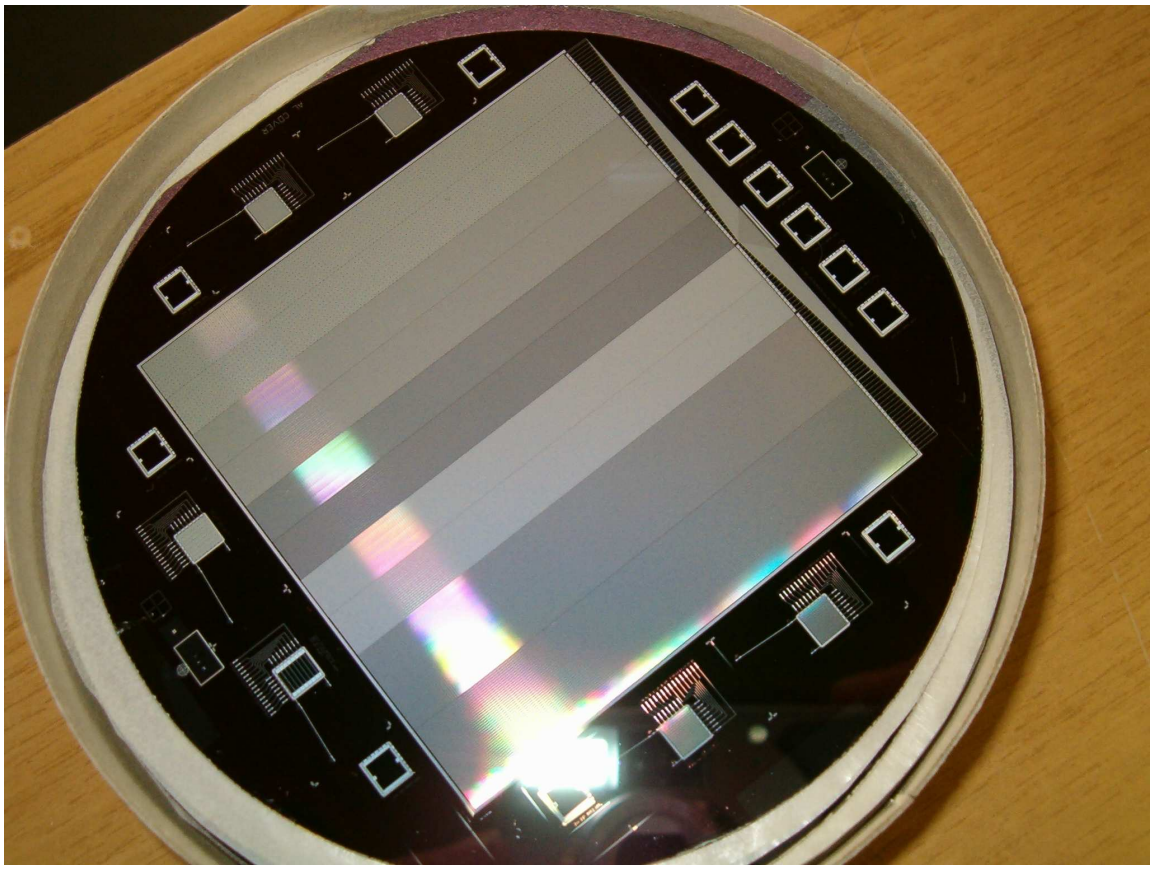

Figure D.4: Prototype wafer with 5 different StriPixel structures in both the X and Y directions. The technology is single-metal with implanted bridges in the orthogonal direction.)

(b) the short path range of alpha particles; (c) multiple scattering of alpha particles in the air. A test with beta source is crucial for final evaluation of StriPixel sensors. We have built a setup for irradiating StriPixel sensors with beta particles Figure D.6. The setup consists of a collimated source and two trigger counters in front of a precisely movable table where the SRM module will be mounted. The measurements will start as soon as we will have a stable StriPixel readout functioning.

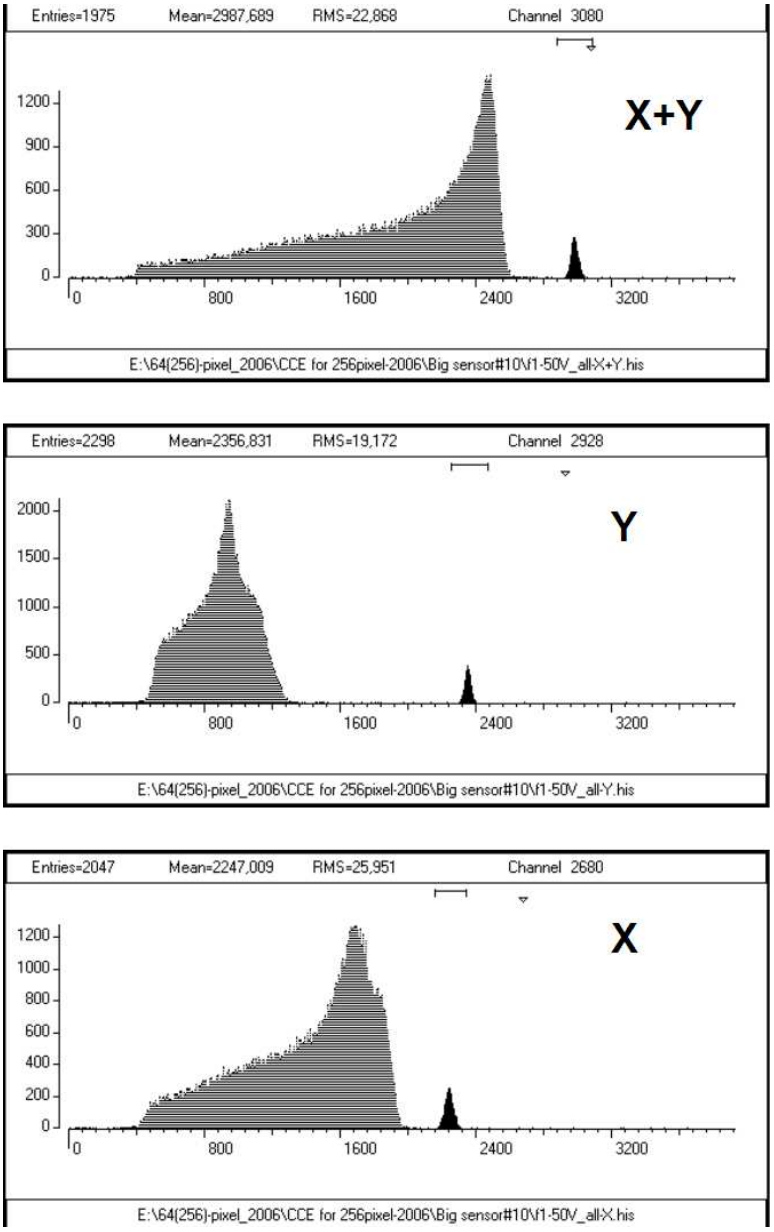

Figure D.5: Alpha particles spectra.

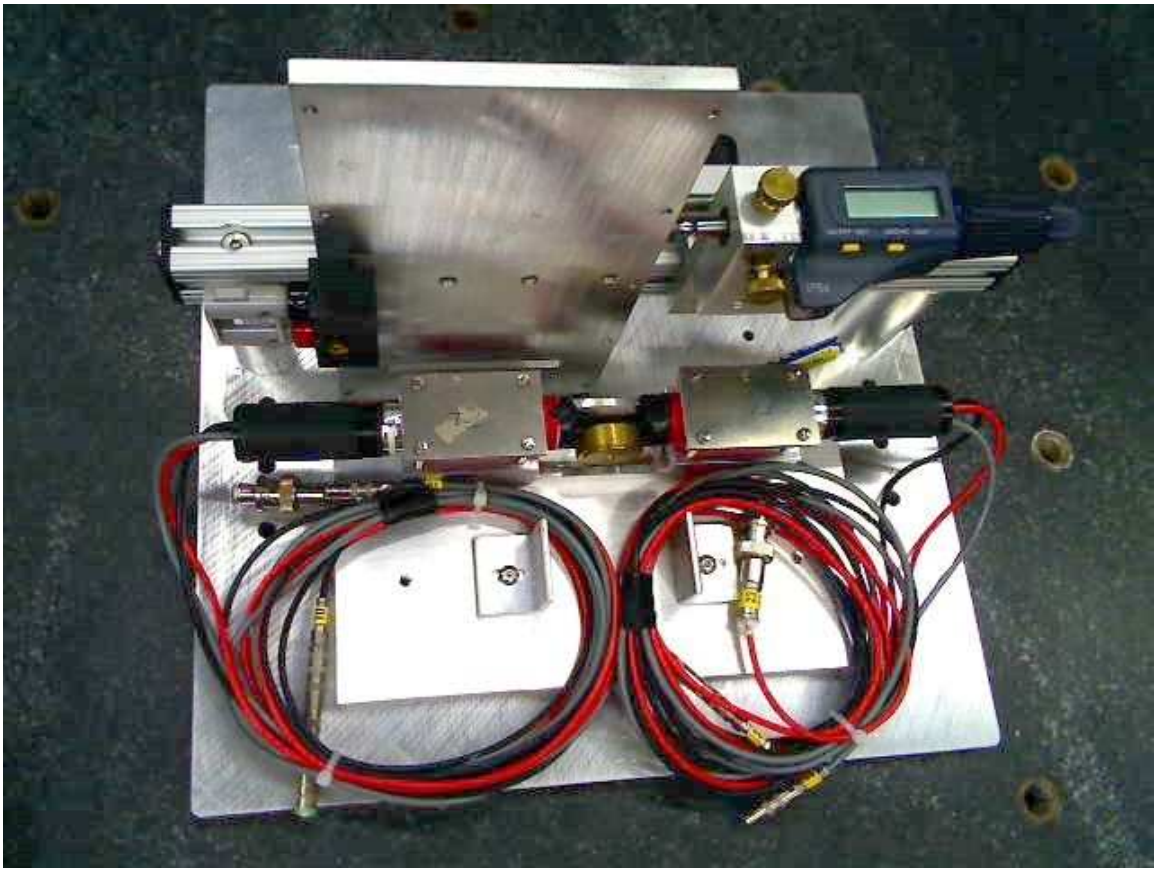

Figure D.6: Test source for StriPixel studies with collimated electron source.

Appendix E

Pad Readout Chain

E.1 SPICE Simulation Of The Pad Sensor Readout Chain.

The readout chain for pad sensors was simulated using LTspice[1] and is illustrated in Fig. E.1. In this simulation the pad sensors are represented as 50 pF capacitors. Seven pads are AC decoupled by capacitors Cd1-Cd7 and connected to the summation point via lossy transmission lines Tcar1-Tcar7. The bias is applied on each pad individually over the resistors Rb1-Rb7. From the summation point the signal goes through a short transmission line Tpa to a preamp E1. The preamp is connected to a differential driver E3, which drives 10 m of differential cable represented by a transmission lines Tpa1 and Tpa2. The other side of the cable is connected to an integral shaper LT6600-2.5 (low noise differential amplifier and 4^{th} order 2.5 MHz low-pass filter), which acts as an antialiasing filter. From here the differential signal will go directly to an ADC.

The current pulse in the pad detector is a result of charge induction due to the drift of electrons and holes originating along the track. The pulse has a very sharp front, and a tail which is a sum of two components of equal area: a fast component ∼10 ns due to the drift of electrons, and a slow component ∼30ns due to the drift of holes [109, 111]. The input signal is simulated as a 2mA double-exponential current pulse with rising time constant of 2 ns, a flat top of 1 ns and a falling time constant of 20 ns. The injected charge is 4000 fC, corresponding to 1000 MIPs, which is half of the maximum signal expected from a single pad.

The preamp is modeled as an ideal trans-conductance amplifier with gain of 10 KOhm and with input impedance of 50 Ohm. This impedance is divided into two parts: noisy Rin_hot=8 Ohm and noiseless Rin_cold=42 Ohm.

The differential driver (AD8132 or AD8137) is modeled as an ideal voltage regulator.

[1] Available free from http://www.linear.com/company/software.jsp

E.2 Simulation Model of the Pad Sensors Readout Chain

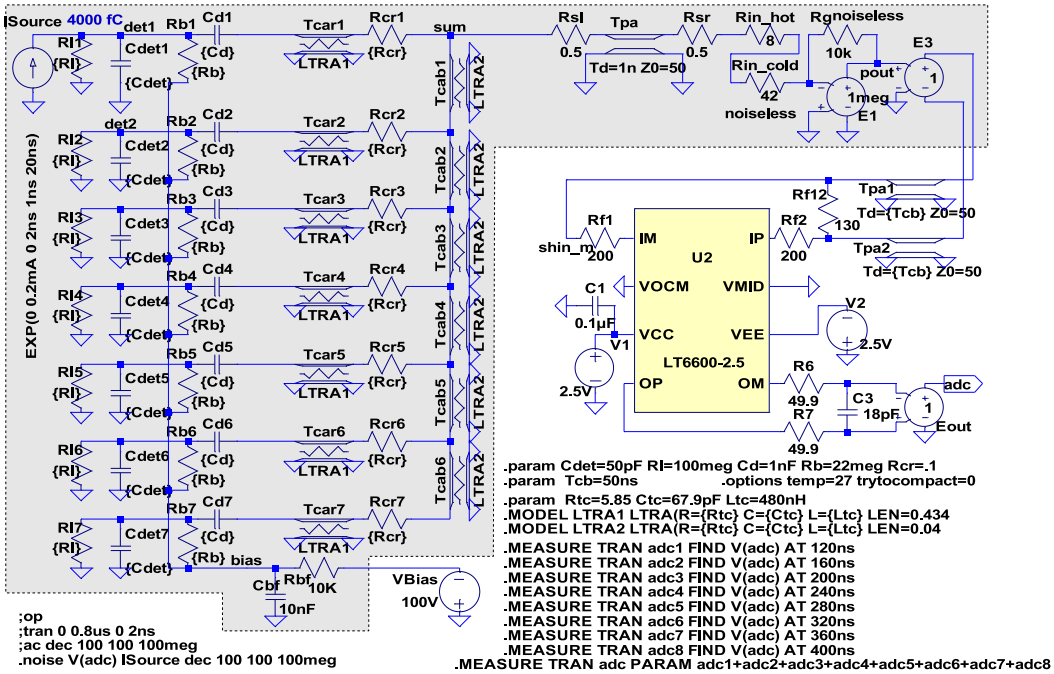

Figure E.1: Simulation model of the pad sensor readout chain.

The lossy transmission line parameters are represented in MODEL and PARAM statements on Fig. E.1 and they are explained in the next section. For this simulation the following parameters were used:

1. Unit resistivity Rtc = 5.85 Ohm/m
2. Unit capacitance Ctc = 67.9 pF/m
3. Unit inductance Ltc = 480 nH/m
4. The line lengths of Tc1-Tc7 vary from 62 mm to 434 mm

The line impedance of each line is Z=sqrt(Ltc/Ctc) = 84 Ohm.

E.3 Transmission Line Analysis

The following references and source code was used for the transmission line analysis.

Source: "High-Speed Digital Design A Handbook of Black Magic". Howard W. Johnson and Martin Graham, Prentice Hall, 1993; ISBN 0-13-395724-1

Mathcad source: http://www.sigcon.com/lib/htm/MSTRIP.htm

local source:
http://www.phenix.bnl.gov/šuhanov/ncc/electronics/signal_processing/mstrip.mcd

E.4 Selection of Cut-Off Frequency of the Low-Pass Filter

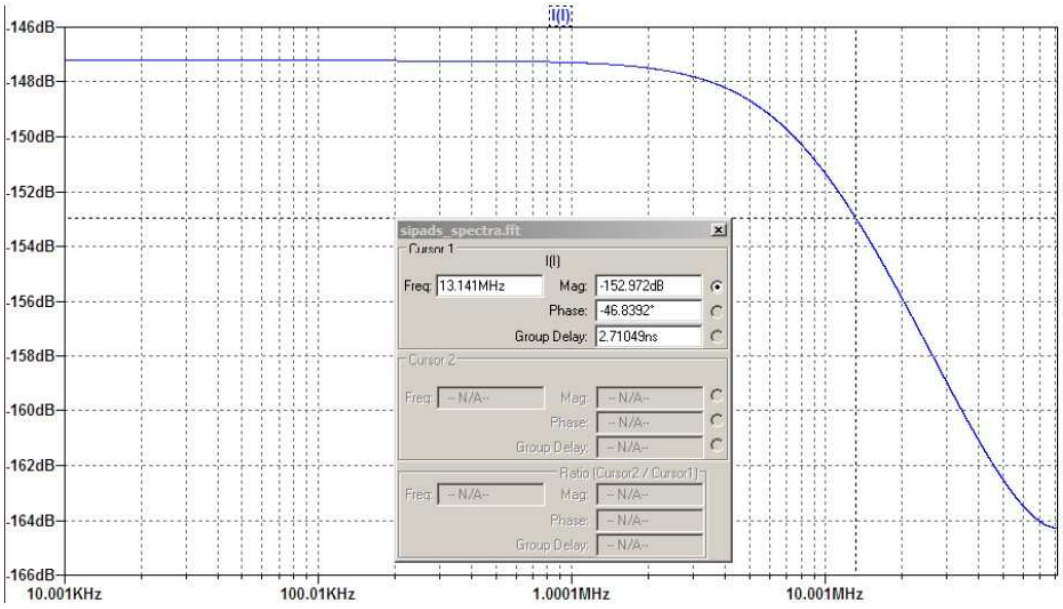

Figure E.2: Spectrum of the source signal. The bandwidth where amplitude drops by 6 dB is 13 MHz.

Figure E.2 shows that the bandwidth of the source signal is 13 MHz. Figure E.3 shows the gain of the system from the source to the preamp output, which is determined by a combination of the detector capacitance, transmission lines, and the input impedance of the preamp. Also shown on Fig. E.3 is the noise at the preamp output (red) and the contribution to the noise from the noisy part of the impedance Rin_hot (green). We select the cut-off frequency for the low-pass filter based on this figure. At frequencies around 2.5 MHz the gain starts to decline and at the same time the noise is rising. The cut-off frequency of 2.5 MHz ensures an optimal signal to noise ratio.

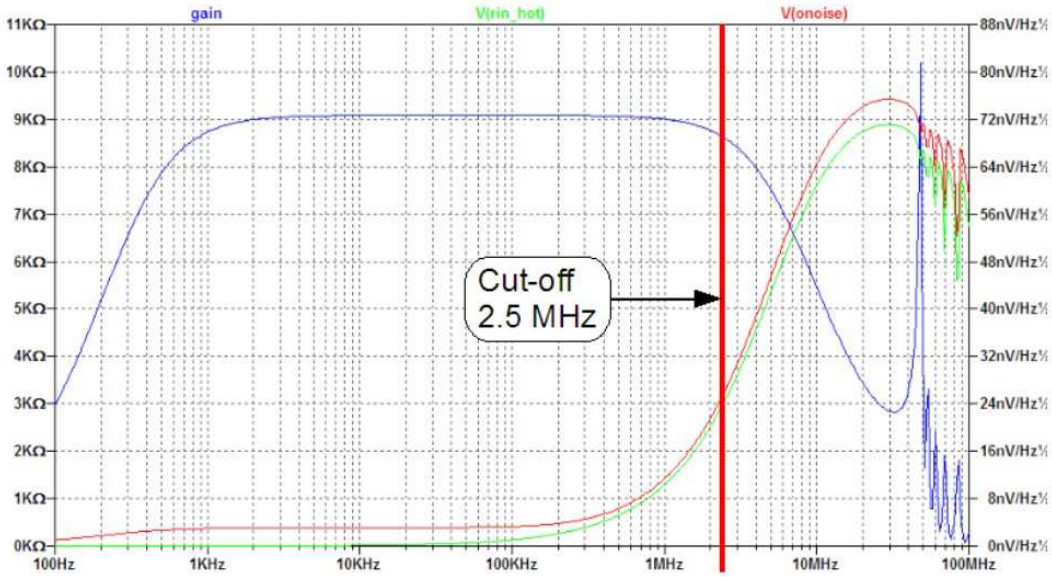

Figure E.3: Gain (blue) and noise (red) at preamp output.

E.5 Transient Analysis

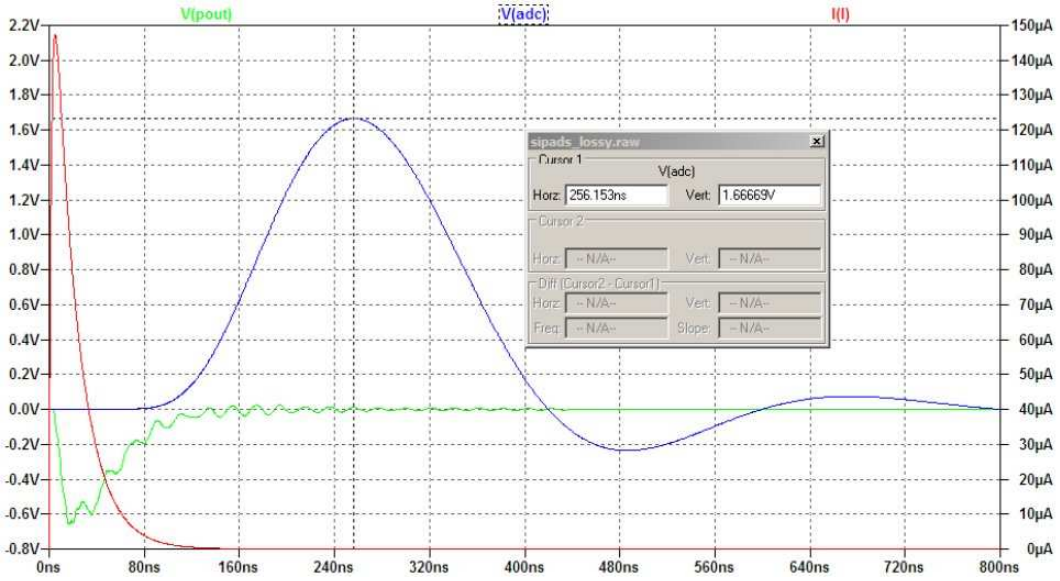

Figure E.4: Transient analysis of the pad readout chain.

Figure E.4 shows the transient analysis of the readout chain. The blue line is the output of the shaper, the green curve is an amplitude at the preamp output. One can see that there are significant reflections caused by mismatched impedances of lines Tcar1-Tcar7 and Tpa. These reflections are fully integrated and do not appear on the output signal.

The reflections could be eliminated by introducing resistors Rcr1-Rcr7 with values in the range of 35-70 Ohm (see Figure E.5). As shown later, these resistors would significantly contribute to the system noise and therefore are not implemented.

E.5.1 Nonlinearity

The simulation for small signals shows exactly the same shape with no deviation from linearity.

E.6 Noise Analysis.

The noise analysis at the shaper output is represented in Figure E.6. The figure shows the system noise (red), the noise contribution from serial resistor *Rin_hot* (green), and the system gain (blue). The flat area of the system noise below 200KHz comes from the shaper. The increased noise above 5MHz is mainly due to *Rin_hot*. This resistor is the main contributor to the total RMS noise.

By comparing Fig. E.6 with Fig. E.3 one can see that the gain is high in the region where the noise is low and the gain is sharply cut for the region with high noise.

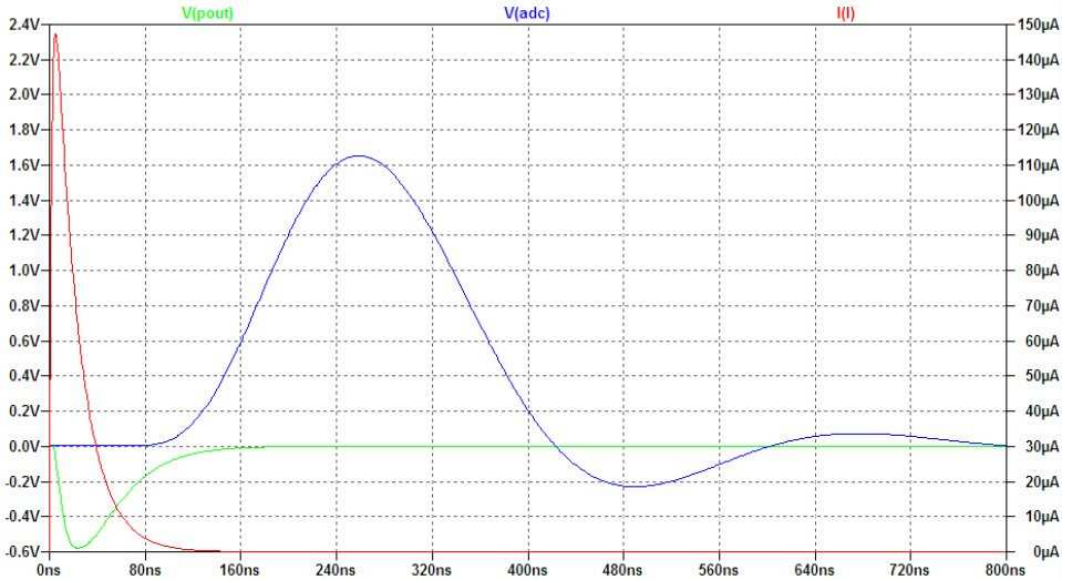

Figure E.5: Transient analysis, Rcr = 35 Ohm.

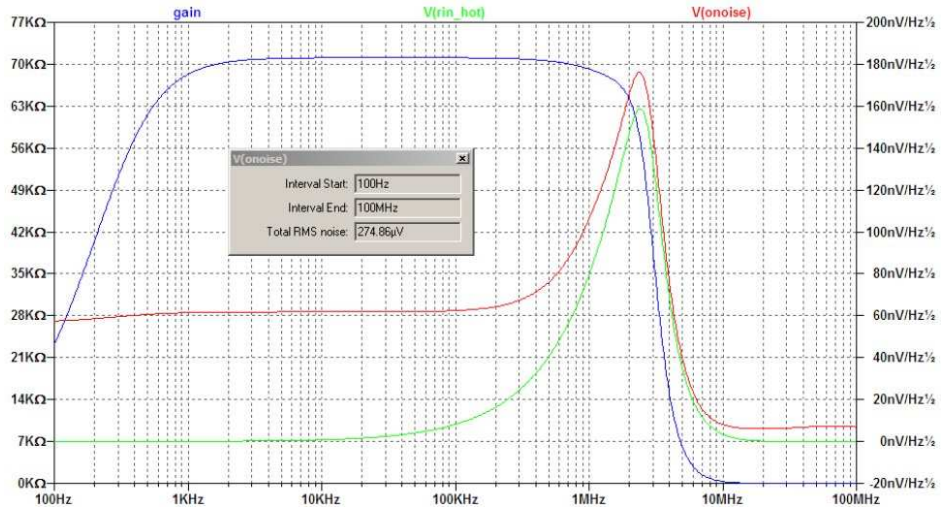

Figure E.6: Gain in kΩ (blue), noise in nV/$\sqrt{\text{Hz}}$ (red), and noise contribution of *Rin_hot* (green) at the output of the filter.

E.7 Summary Table

Figure E.7 shows the noise at the filter output (RMS1) and the signal-to-noise ratio (S/N), calculated as a non-weighted sum of eight ADC samples at different operational parameters.

The row 1.1 and 1.2 are 10 MHz cut-off and 50 MHz ADC sampling, while all other rows are 2.5 MHz cut-off and 25 MHz sampling. The improvement from using multiple sampling can be derived as ratio of S/N to S/N1 and is about 50%. The best signal to noise ratio for

RMS of ADC for diff input 2V p-p = 1.25E-004

	Rcr	SA	PA	PP	ADCsum	RMS1	S/N1	RMS	S/N
	Rcr	Signal Average over 400ns	Peak amplitude	Peak position	ADC sum of 8 samples 50MHz starting at 80ns	RMS Noise 100Hz-100MHz	S/N one sample at a peak	Total RMS noise for 8 samples	S/N including RMS of ADC
	Ohm	V	V	'ns	V	V		V	
1	**Cdet=42pF**, Rin_cold=42, R1=130, R3=R4=200, R2=10K, **LT6600-10** **Cut-off at 10 MHz, 8 samples every 20ns starting at 80 ns**								
1.1	0	0.177	1.240	117.0	3.50	4.37E-004	2.84E+003	1.24E-003	2817
1.2	35	0.177	1.200	118.0	3.50	4.97E-004	2.41E+003	1.41E-003	2480
2	**Cdet=42pF**, Rin_cold=42, R1=130, R3=R4=200, R2=10K, **LT6600-2.5** **Cut-off at 2.5 MHz, 8 samples every 40 ns starting at 120 ns**								
2.1	0	0.347	1.700	251.0	7.39	2.55E-004	6.67E+003	7.32E-004	10096
2.2	35	0.347	1.700	256.0	7.38	2.98E-004	5.70E+003	8.52E-004	8661
	Cdet=50pF, Rin_cold=42								
2.3	0	0.342	1.670	256.0	7.27	2.70E-004	6.19E+003	7.74E-004	**9395**
2.4	35	0.342	1.654	259.0	7.26	3.23E-004	5.13E+003	9.21E-004	7883
	Cdet=60pF, Rin_cold=42								
2.5	0	0.336	1.620	258.0	7.10	2.98E-004	5.44E+003	8.52E-004	8332
2.6	35	0.336	1.605	261.0	7.10	3.51E-004	4.57E+003	1.00E-003	7096

Figure E.7: Noise at the filter output (RMS1) and the signal-to-noise ratio.

a detector capacitance of 50 pF is 9395 (row 2.3). Row 2.1 shows the same ratio for smaller detector capacitance of 42 pF, and as expected, it is higher at 10096. The RMS noise level at the filter output 270 uV is shown in row 2.3, column RMS, and can be converted to ENC using:

$$ENC = \frac{RMS0}{PA} \times \frac{4000 \text{ fC}}{e} ENC = 4042 \text{ electrons}$$

In this formula RMS0 is the RMS noise level = 270 uV, PA is peak amplitude = 1.67V, 4000fC is the charge applied to the input, e – electron charge. The RMS noise after non-weighted sum of 8 samples is 7740 uV (see column RMS in row 2.3) but the effective signal increased to 7.27 V (ADCsum) from 1.67 V. This corresponds to an ENC of the readout chain = 2665 electrons.

E.8 Dynamic Range of Signal Measurement

The problem of achieving the dynamic range of signal measurement better than 12 bits comes from the fact that the effective number of bits (ENOB) of any off-the-shelf fast ADC is less than 12 bits no matter what resolution they have. That is if we take for example a 16-bit ADC with ENOB=12 and make a single sample then we cannot achieve resolution better than 12 bit.

The obvious solution is to make several samples and sum them up. In the simplified case when the output shape of the filter is flat and we take N samples on a plateau then the

signal-to-noise ratio will improve by $\sqrt{N}$. In the case of arbitrary signal shape, the optimal signal-to-noise ratio will be achieved using a weighted sum of the samples where the weights follow the shape of the signal. Using a weighted sum will give an improvement of better than 20% over a non-weighted sum.

Rule:

If dynamic range of a system is D (linear scale) and the resolution of the ADC is A bits (N<2**A) then the dynamic range can be improved K$\sqrt{N}$ using a weighted sum of N samples. The coefficient K<=1 depends on the signal shape; for a flat shape K=1. The N should be chosen less than (log2(D) - A). The sampling rate of the ADC should be higher than B*N where the B is the bandwidth of the input signal.

E.9 Summary

- The readout chain of NCC silicon pad sensor pad is simulated using LTspice program.
- The cut-off frequency of the shaper should be 2.5 MHz. Above this frequency the system gain is decreasing and the system noise is rising.
- The ADC sampling rate should be 25 MHz or higher.
- The number of samples should be 8 or larger. This will provide at least 50% improvement of S/N relative to a single-sample measurement.
- Using a weighted sum provides 20% improvement as compared to non-weighted sum.
- The impedance-matching resistors Rcr1-7 should be avoided. They add to the noise.
- Simulations did not show any nonlinearity.
- For 7*50pF pads a dynamic range of above 9350 can be achieved when the gain of the preamp is 10KOhm and the noisy part of the input impedance is equivalent to 8 Ohm.
- The Equivalent Noise Charge (ENC) at the input is 2700 electrons, or 0.43 fC.

Appendix F

Silicon Strip Sensors and Readout

F.1 Strip Sensors

We plan to instrument the preshower and shower max layers of the NCC with silicon strip detectors of a novel design, as illustrated in Fig. F.1. The sensors developed by the BNL Instrumentation Division provide two-dimensional position sensitivity. The readout of sensors is based on SVX4 chips, which were developed for silicon strip detectors by FNAL and LBL. In the final readout system the SVX4 chips would be arranged on sensor readout cards (SRCs) and mounted directly on the sensors.

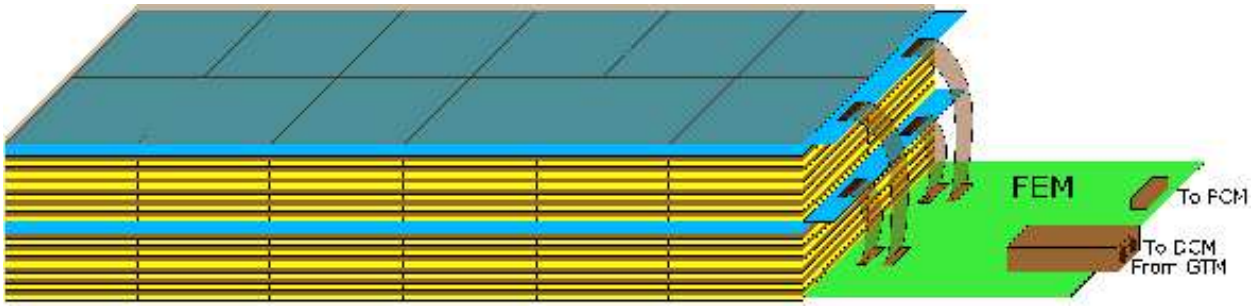

Figure F.1: Conceptual layout of the NCC electromagnetic brick. Blue layers are silicon-strip planes (preshower and shower max); brown layers are tungsten plates, yellow layers are silicon-pad readout planes. Both silicon strip planes are read by FEM boards located inside the bricks envelope. The FEM sends data to PHENIX DCM boards over optical fiber. Power and ground are distributed from a PCM (Program and Control) board located near the detector.

F.1.1 Design Principle

The concept of the StriPixel detector is described in publication of Zheng Li[112]. The sensor is a segmented detector with 0.5x0.5 mm pixels.

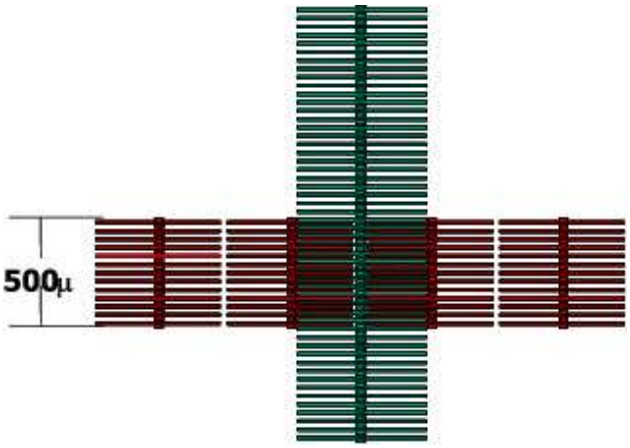

Figure F.2: Comb structure

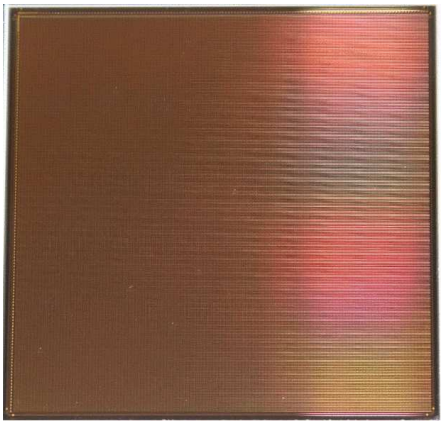

Figure F.3: Prototype of StriPixel sensor.

Figure F.2 illustrates that each pixel region has two comb-shaped metal strips to collect charge produced by an ionizing particle that transverses the silicon. A hit by an ionizing particle will deposit charge on two combs. In the original design vertical combs are connected by metal strips and horizontal combs by implanted bridges. Figure F.3 shows the prototype StriPixel produced by SENS in Seoul, Korea for Yonsei University.

The decision to use StriPixel sensors in **DC-coupled** mode was based on the following considerations:

1. Higher production yield,

2. Higher reliability during operation and

3. 25% lower cost.

The biasing resistors are implemented directly on sensors. This will simplify the production tests and characterization procedures by allowing simultaneous biasing of all strips. The readout pads are arranged on two orthogonal edges of the sensor.

F.1.2 SVX4 Readout Chip

The strips are read out with the SVX4 chip developed by FNAL/Berkeley collaboration [113]. The SVX4 is implemented in the 0.25 μ TSMC process and is inherently rad-hard. It is a 128-channel chip with a 46-deep pipeline cycled by the beam-crossing clock, thus providing the LVL1-latency required by the PHENIX DAQ. LVL1-accepted events are stored for future pipelined readout. The SVX4 allows up to 8 bits of analog information, although the number of bits are programmable. Several pedestal-subtraction steps offer robust protection against common-mode noise. On-board zero suppression is provided for, but can be turned off (see discussion below). The SVX4 also provides for four-deep multi-event buffering required by the PHENIX DAQ.

F.2 StriPixel Ladder

Figure F.4 shows the StriPixel ladder, which comprises 5 to 7 Sensor Readout Modules (SRM). Each SRM reads out signals from two StriPixel sensors and hosts four SVX4 chips. The SRMs are mounted on a common ceramic substrate which are connected to each other by means of short 50-line flat-flex jumpers that form one or two daisy-chains, connected to an FEM. The maximum number of SVX4 chips per daisy chain is 16.

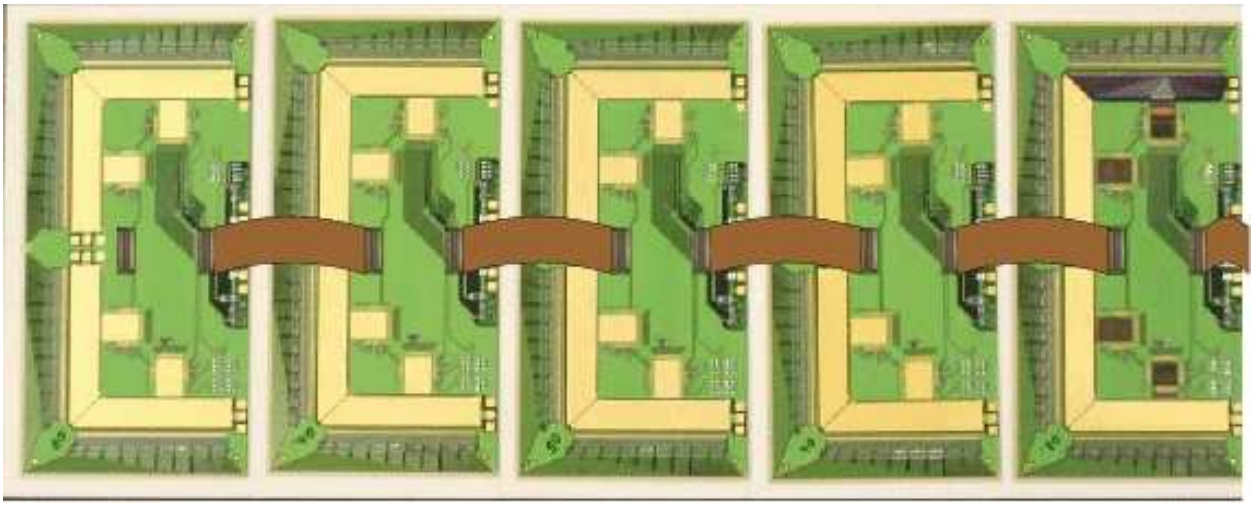

Figure F.4: StriPixel ladder comprising 5 daisy-chained Sensor Readout Modules with two sensor on each. The rightmost SRM is populated with SVX4s and has one pitch adapter out of four installed.

Figure F.5 shows the arrangement of the StriPixel ladder inside the brick. The ladders are inserted between tungsten plates with pad-sensor layers mounted on them.

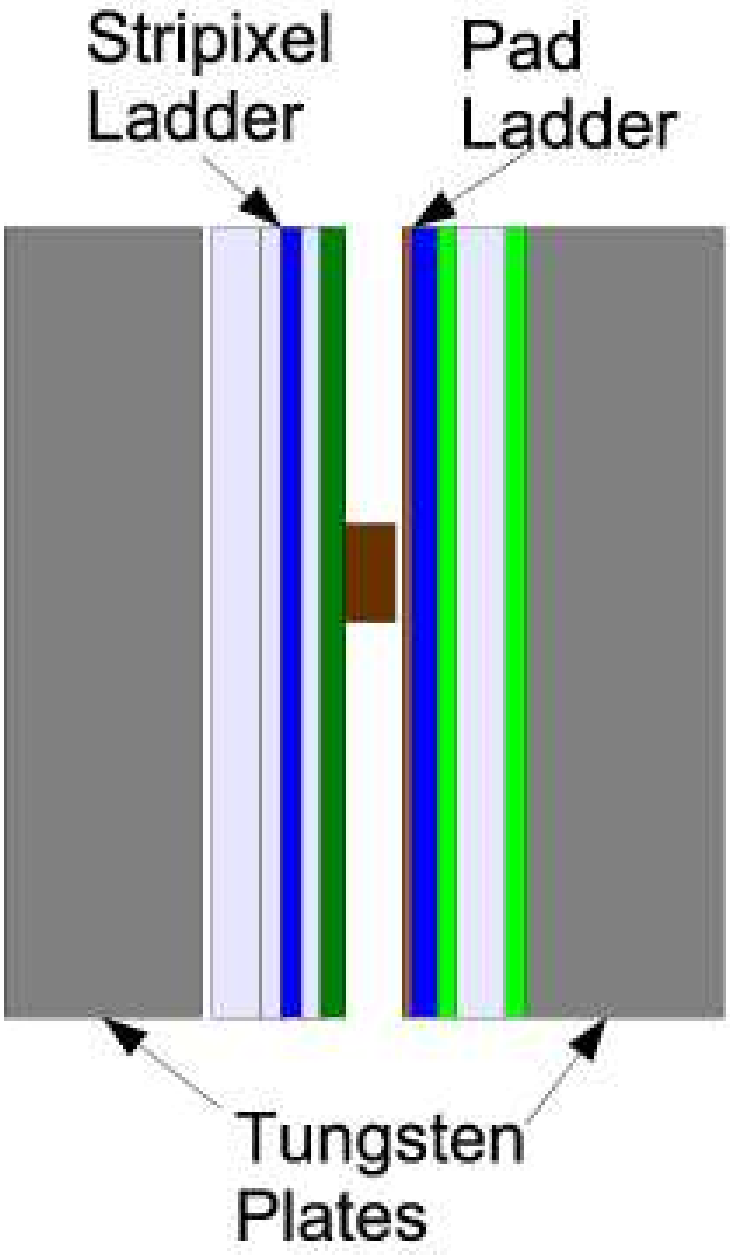

Figure F.5: The arrangement of StriPixel ladders between pad sensor assemblies on tungsten plates

F.3 Sensor Readout Module (SRM)

Figures F.6 and F.7 show the sensor readout module comprising two silicon StriPixel sensors, which are arranged vertically side-by-side, and a Sensors Readout Card (SRC) mounted on top of them. Sensors are wire-bonded to the edges of the SRC. The SRC is a 0.25 mm thick PCB board manufactured with minimal line width of 75 μ and minimal line space of 75 μ. The board hosts 4 of SVX4 chips.

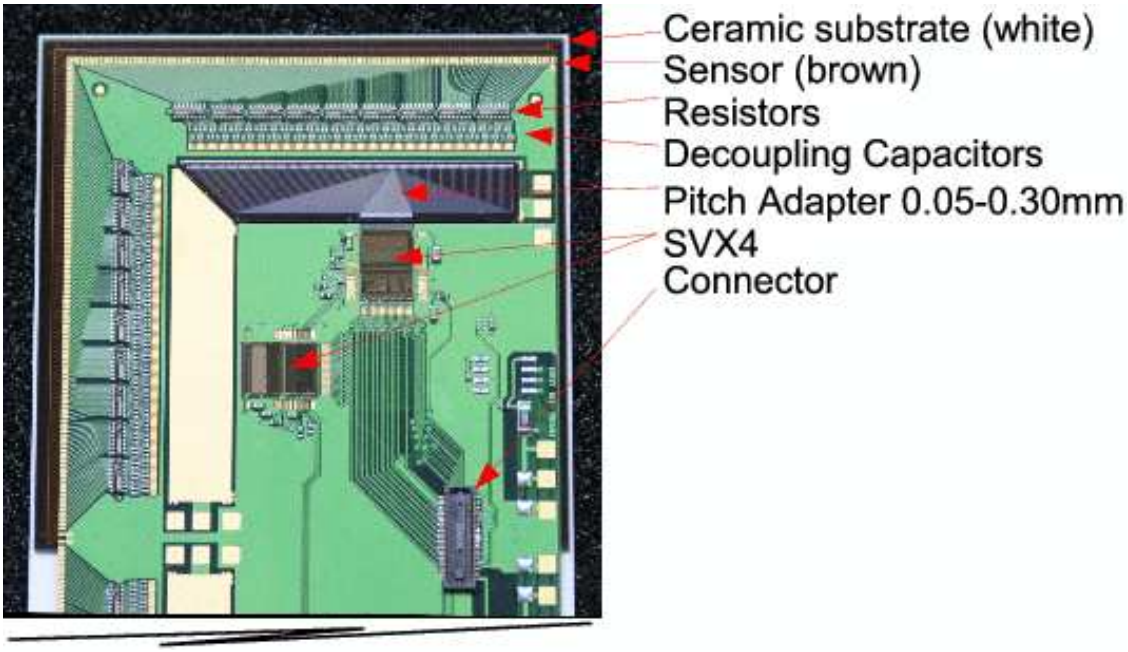

Figure F.6: Sensor Readout Module, the upper half of the module shown. In the final version two connectors will be installed instead of one.

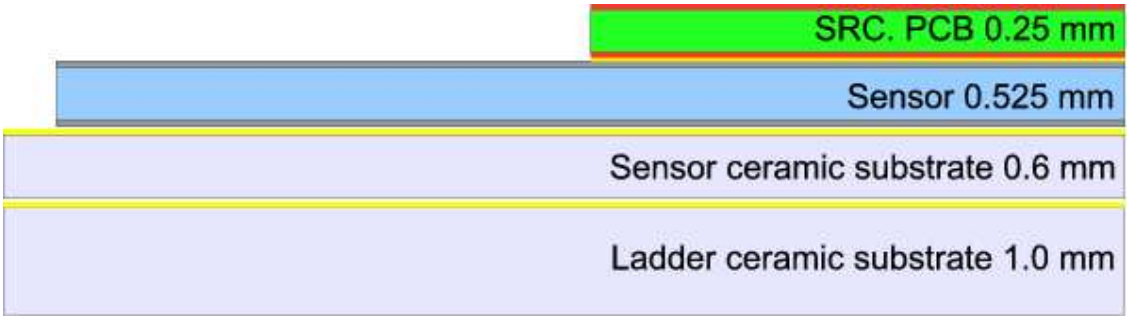

Figure F.7: Stack-up of the Sensor Readout Module.

Connection of DC-coupled sensors to the SVX4 chips requires an AC-decoupling network. This network is build using type 0201 capacitors. The pitch adapter is metal-on-silicon bare die, produced from the same wafers as the sensors. The sensor ceramic substrate is metalized and has vias for bias voltage distribution.

A prototype of the sensor ceramic substrate has been manufactured and allows for multiple methods of providing **bias voltage to the sensor**:

1. Wire-bonding from the bottom of the sensor to the bottom of the sensor ceramic substrate and from there soldering to the ladder ceramic substrate.

2. Conductive gluing of sensor ceramic to ladder ceramic.

3. Soldering conductive foil from the bottom of the sensor ceramic to the top of SRC and distributing the bias voltage as a separate line on the signal daisy-chain.

The SRM modules are daisy-chained using flat-flex cable jumpers.

Several prototype boards have been manufactured and electrically tested.

The sensor readout modules are mounted on a ladder ceramic substrate which provides mechanical stability and transfers heat from the sensor to the outer skin. It has thin film conductors on top to distribute the bias voltage.

The slow control and monitoring of the SRM is done usin 1WIRE devices. The following parameters a monitored:

1. Temperature (it is easy to monitor it in several locations) (DS18B20X chip).

2. Leakage current

3. 3 control voltages (DS2450 chip).

Setup voltages for the SVX4 such as VTH and VCAL are also controlled by 1WIRE devices (DS2890).

F.3.1 Power consumption

The main power consumption sources on the SRM are the SVX4 chips. The average load current per chip is 52 mA from AVDD and 13 mA from DVDD, which correspond to 0.22 W. The AVDD load depends on preamp current setting and can reach 90 mA. The average power dissipation per silicon-strip plane is expected to be of the order of 10 W.

F.4 Front-End Module (FEM)

The FEM has 4 readout chains for the SVX4. The LVDS data buses are independently fed into the FPGA. The FPGA buffers the event, compresses the data stream using Huffman Coding, stores the result in the output buffer and sends it through the optical transceiver to the PHENIX DCM. The PHENIX DAQ requires that all subsystems should be able to buffer at least 5 events. The SVX4 chips on the SRC have internal buffering for 4 events; the FEM provides at least one additional buffer.

The FEM connects to the PHENIX DAQ over a small-form-factor (SSF) optical transceiver. The receiving part is connected to a PHENIX GTM module, while the transmitter part is connect to a PHENIX DCM module.

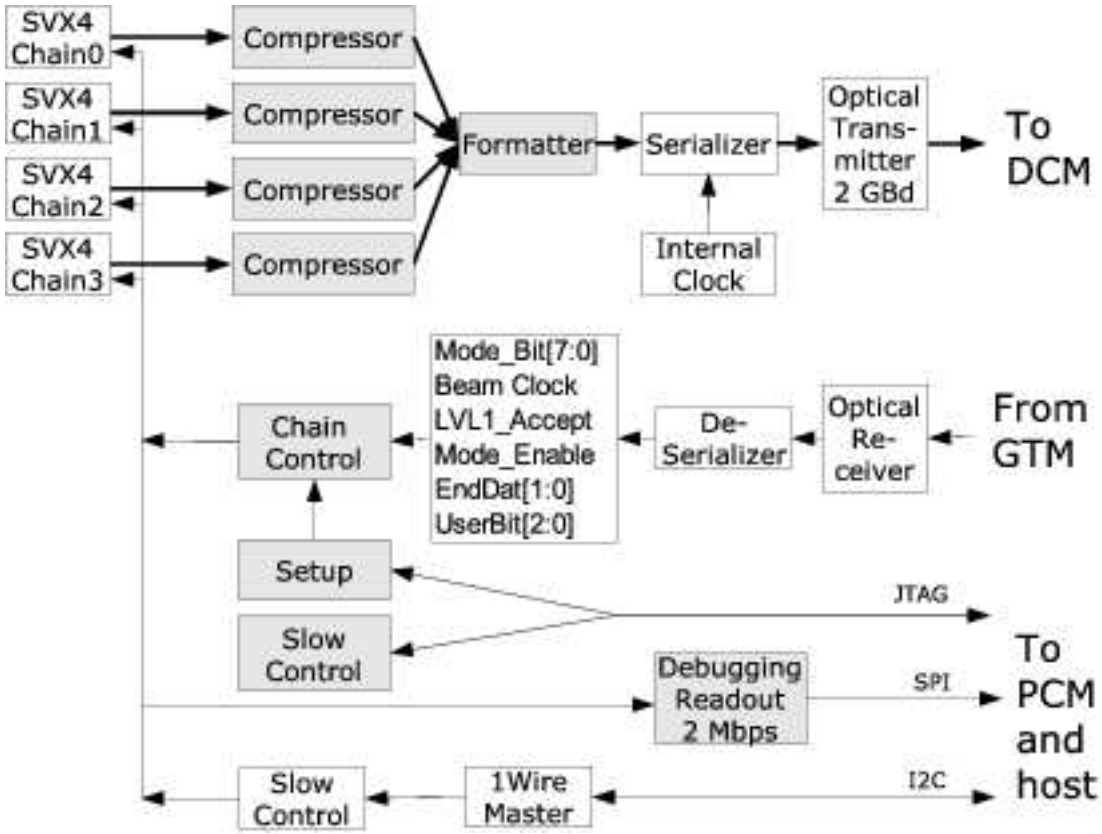

Figure F.8: FEM Block Diagram. Shaded boxes represent the elements implemented in the FPGA.

Figure F.9 shows the signals that the FEM receives from the GTM. These signals are de-serialized using a SerDes chip.

Mode_Bit[7:0]	8
Beam Clock 9.4 Mhz	1
LVL1_Accept	1
Mode_Enable	1
EndDat[1:0]	2
UserBit[2:0]	3
Reserved[3:0]	4
Total	20 Bit

Figure F.9: PHENIX Synchronization Signals.

The clock is defined by the PHENIX Granule Timing Module (GTM); it is clock time us four times the Beam Clock, i.e. 40 MHz. This clock is recovered by the SerDes chip. The clock jitter is guaranteed to be less than 40 ps. The transceiver and SerDes are mounted on a small mezzanine board and will be compatible to the optical protocol of the latest DCM.

Raw event size, no pedestal suppression	14448	Bytes
Raw event size with channel ID removed	**7224**	**Bytes**
FEM readout clock, both edges used	40	Mhz
Collection time from 4 SVX4 chains on FEM	22.58	us
Data transfer rate to DCM	2.0	Gbps
Transfer time of raw event	**36.1**	**us**
Hit occupancy	5%	
Output data size, pedestal suppressed	722	Bytes
Transfer time of zero-suppressed event	**3.6**	**us**
Lossless Compression		
Compression factor for raw data	2.5	
Size of compressed event	2890	Bytes
Data transfer time of compressed event	**14.4**	**us**
Lossy compression		
Compression factor for zero suppressed data	3.0	
Event size, zero-suppressed & compressed	241	Bytes
Transfer time, zero-suppressed & compressed	**1.2**	**us**

Figure F.10: Size and Transfer Time of StriPixel Data from Single Electromagnetic Brick.

The digitization at 40 MHz will be finished in 1.7 μs. It is important to keep this time as short as possible since the SVX4 chip cannot do digitization and readout simultaneously.

The longest chain has 16 SVX4 chips. Assuming 5% occupancy the size of the average chain will be 722 bytes and the average readout time will be **3.6** μs. During this time the SVX4s are open to acquire new triggers.

For normal data taking with pedestal suppression and Huffman compression (we expect that Huffman coding of pedestal suppressed data can achieve compression factor of 3:1) the estimated data size from the whole brick is 241 bytes. This data will be transferred to the DCM in **1.2** μ**s**. This fits safely into the PHENIX DCM data-taking window (ENDAT) of **40** μ**s.**

The optical transmitter will be clocked by an internal clock generator to eliminate uncontrolled jitter of the beam related clocks, which could result in high probability of data losses.

Note: Even for calibration runs when the pedestal suppression is switched off the data size will be reduced from 14.4 Kbytes to 3.0 KB by removing ChannelID bytes from the SVX4 data and applying Huffman compression. The data transfer time in this case will be **14.4** μ**s**, which can be handled by a single DCM by occupying two ENDAT windows of the

DCM.

F.4.1 FPGA Selection

F.4.2 Number of LVDS pairs.

Fig F.11 shows that the FEM should process data from four SVX4 chains in parallel. This will require

1. Data transfer bus 4*9 = 36 LVDS pairs.
2. Common clocks BECLK, FECLK. = 2 LVDS pairs
3. PRIOUT[0] 4*1 = 4 LVDS pairs
4. Optional PIOUT[3:1] 4*3 = 12 LVDS pairs

In total it is 42 obligatory and 12 optional pairs.

Number of ladders in brick	2	
Max Number of SEM in a Ladder	7	
Number of SVX4 in SEM	4	
Max Number of SVX4	56	
Number of channels	7168	
Max data size per SVX4	258	Bytes
Max input data size	14448	Bytes
Number of input buffers	1	
Output data size unsuppressed	7284	Bytes
Compression factor for unsuppressed data	2.5	
Output data compressed	2914	Bytes
Hit occupancy	5%	
Output data size, pedestal suppressed	829	Bytes
Compression factor for suppressed data	3	
Output data size, suppressed & compressed	276	Bytes
Size of the pedestal memory	7168	Bytes
Size of the Huffman coding map	512	Bytes
Total memory requred	**29412**	**Bytes**
	235296	**Bits**

Figure F.11: BEM Memory Requirements.

FPGA	Dist RAM [Kbits]	Block RAM [Kbits]	DCM	IO USER	IO DIFF	Price	Source
XC3S500E	73	360	4	190	77	?	
XC3S1200E	136	504	8	190	77	?	
XC3S400	56	288	4	173	76	$27.76	digikey
XC3S1000	120	432	4	173	76	$47.87	Digikey
XC2V1000	160	720	8		324	$200	

Figure F.12: Comparison of FPGA options.

Of the options in Fig. F.12 the XC3S500E is most attractive and could be less expensive in the near future. Currently the SPARTAN3E FPGA has a very long lead time and is more expensive than SPARTAN3. The FPGA XC3S400 and XC3S1000 both meet all requirements, are not expensive, and are readily available. For prototype boards the XC2V1000 is used.

F.4.3 FEM Ports

SVX4_Chain[3:0] ports These daisy-chains provide all signals, power and ground to the SRCs. Using the prototype we will test an option of sending bias voltage over the daisy-chain. The longest SVX4 chain has 16 SVX4 chips.

JTAG Port The JTAG port is vital for the system. It is used for the configuration of the SVX4 chips, reconfiguration of the FPGA and also to access programmed registers of the FEM module. It also can be used for data transfer for testing and debugging. Essentially all control of the StriPixel readout electronics is done through the JTAG port of the FEMs. The JTAG ports of the 7 FEMs are daisy-chained and connected to the PCM module. The signals on this daisy-chain are LVDS levels and are converted to standard JTAG levels on each FEM. The performance of the JTAG communication link was thoroughly tested on the FEM prototype board. It achieved reliable communication in both direction using 15m cable at the rate of 400Kbits/s.

MONITOR Port The monitor port has an I2C link to read out 1WIRE devices on SRC boards, and a QSPI link to read data from the FEM. The QSPI port will be used for data taking during testing and prototyping when the DCM and GTM are not available. The data transfer over QSPI link was tested on the FEM prototype board and reliable data transfer at 2 MByte/s was achieved.

F.5 Zero Suppression and Data Compression

The SVX4 allows for on-chip zero suppression. However, the PHENIX DAQ is not designed to handle zero-suppression prior to the DCM because the pipelined architecture assumes

a fixed length data packet. However, the use of this feature has significant advantages. Without zero suppression the event size from the brick will be 14448 bytes (Fig. F.11). The compressor will remove the ChannelID bytes reducing size to 7284 bytes. Assuming a 40 MHz 16-bit optical data link, this data will be sent in 92 μs, which does not fit to the 40 μs ENDAT window. To handle this amount of data in time we will need to triple the number of DCM links.

If we allow on-chip zero suppression then assuming 5% occupancy the data size will be reduced to 829 bytes (table 3), which is manageable by a single DCM. We plan to further compress data using Huffman Coding of the zero-suppressed data inside FPGA. Based on our experience at PHOBOS we expect a compression factor of 3. This leads to average data size from one brick of the order of 300 bytes.

F.6 Program and Control Module (PCM)

The Program and Control Module provides a remote JTAG interface to the FPGA over Ethernet, fast configuration of the FPGA and control and readout of programmable resources of the FEM. It also provides 2 modes of slow data readout for testing and monitoring: 1) using JTAG (70 Kbyte/s) and 2) using QSPI (2Mbyte/s). One PCM serves one half-disk of the NCC, i.e. 7 bricks; it is located close to the detector. During the initial stage of the project the PCM will also be used for slow control and monitoring of the front-end electronics as well as for remote configuration of the FPGAs. The module is hosts a M5235BCC which is a credit-card-size CPU board with a ColdFire 64-bit 150 MHz CPU, 32 MB of memory, Ethernet connection and I2C and QSPI ports. It operates under tiny Quadros OS. Another OS – ucLinux was successfully tested but rejected due to excessive complexity. As a prototype module we are using Evaluation Module for the Motorola MCF5235 MCU[114].

F.7 Readout Chain Development

The readout chain was manufactured in February 2007. We have tried to be as close as possible to the final design. For the final design only minor modifications will be necessary:

- on the SRC – change connector type, add a second connector, modify solder masking.
- On the FEM – change connector type, implement communication with DCM.

The readout chain consists of the FEM board (big green board in Fig. F.13), PCM board (ColdFire Evaluation board), JTAG LVDS cable connector between FEM and PCM. It has an Ethernet connection to a host workstation. The setup will be used for testing system integrity and sensor parameters during all stages of assembly.

Figure F.14 shows the data analysis of pedestals and calibration pulses from SVX4 with disconnected inputs.

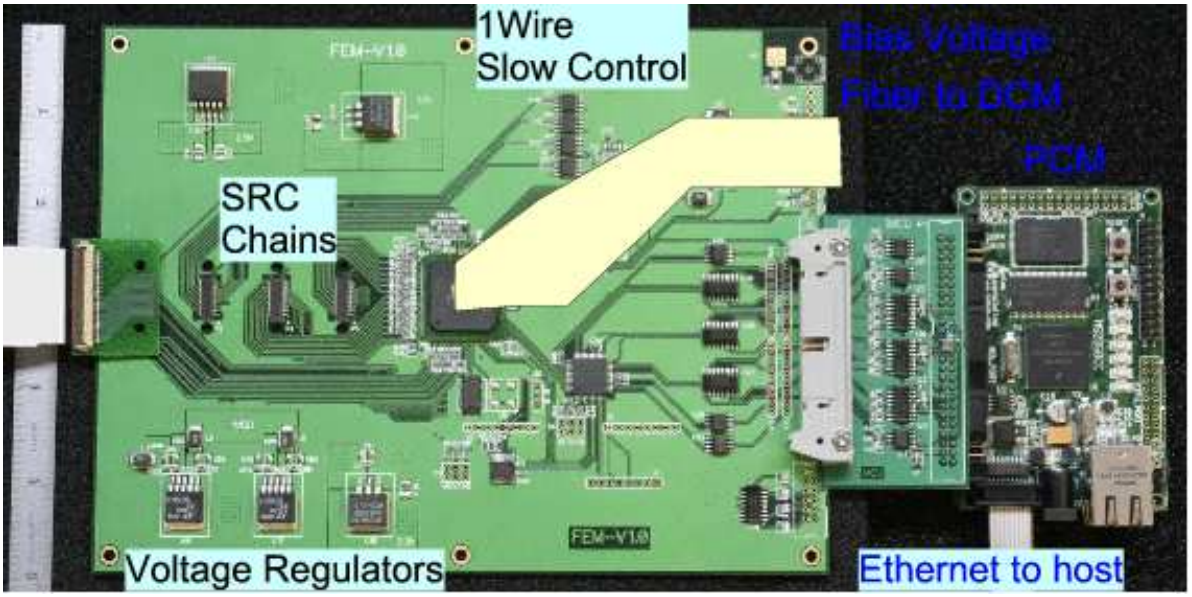

Figure F.13: Photo of the StriPixel readout chain.

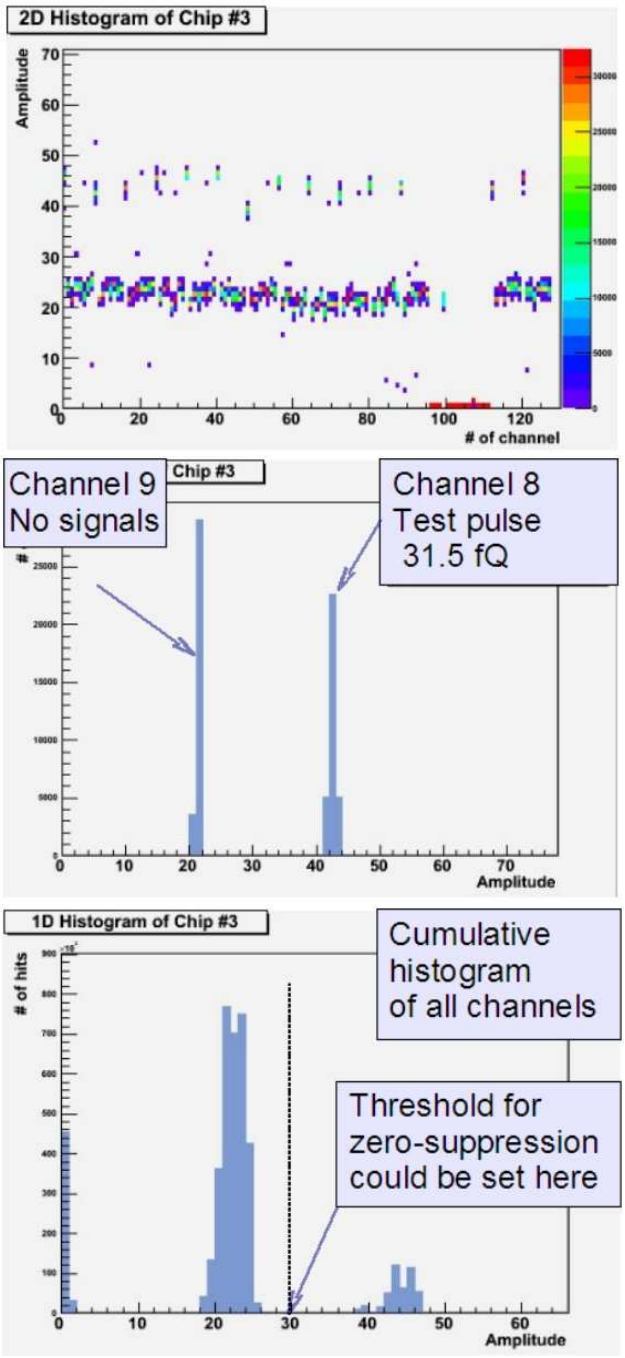

Figure F.14: Data analysis of SVX4 channels when pitch adapter is not connected. Amplitudes from all channels (top), single channels (center) and cumulative histogram of all channels (bottom).

F.8 Production and Assembly of Silicon Readout Layers

The silicon wafers will be manufactured by one or more commercial vendors; at the moment wafers have been manufactured by ELMA(Russia). At the vendor the wafers will undergo resistance and doping tests and then be diced into sensors. Further quality assurance (QA) includes IV and CV curves, and laser pulse tests of each strip and sensor uniformity response. The QA tests will be carried out at BNL and JINR(LPP). The design and layout of all electronics boards is done by JINR(LHE).

Figure F.15: Automatic wire-bonding machine in clean room facility at Helsinki Institute of Physics.

The SRC modules with installed SMT components will be shipped to Helsinki Institute of Physics (HIP) where the SVX4 chips and pitch adapters will be mounted and wire-bonded. On each stages the integrity of the SRC readout chain and parameters of the readout channels will be tested and recorded. This will be done without removing the jig from the wire-bonding machine.

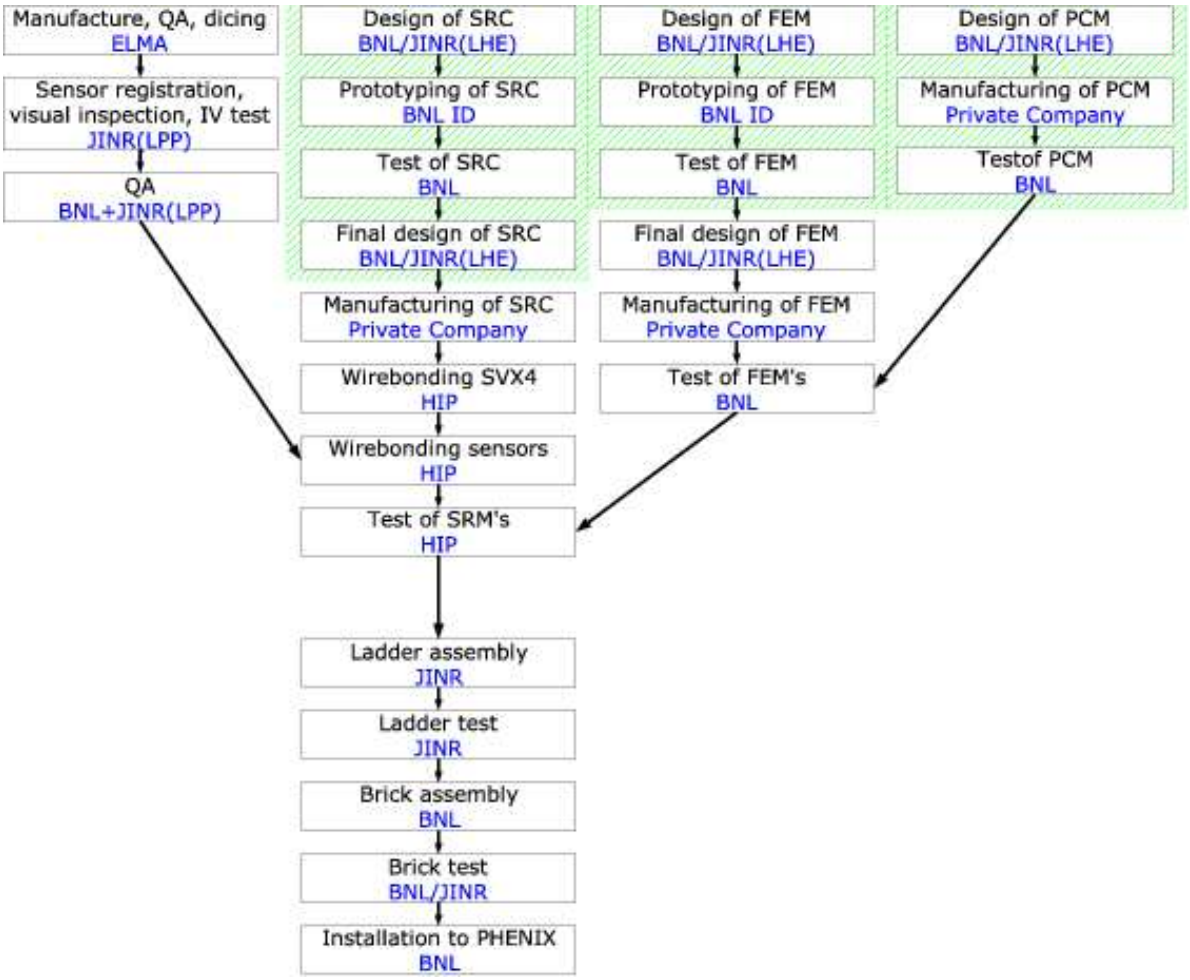

Figure F.16: Strip detector production flow chart. The green area shows accomplished tasks.

F.9 Radiation Tolerance of Front-End Electronics

F.9.1 Inside calorimeter

The components, which are subject to radiation damage inside the calorimeter are the silicon sensors, SVX4 chips and 1WIRE sensors (DS18B20X, DS2890, DS2450).

The estimates based on total energy flow simulation predict the Total Ionization Dose (TID) of 100 kRad (in Si) that correspond to the fluence of $3*10^{12}$ equivalent neutrons per cm^2 over the period of 10 years (assuming p+p interaction at 200 GeV with luminosity $\sim 2*10^{32}cm^{-2}*s^{-1}$). The leakage current for a 300μ sensor after this irradiation will be of the order of 120 μA/sensor. This corresponds to 0.5μA per strip. This current poses no problem provided the strip is AC decoupled from the SVX4 chip.

The SVX4 chip is radiation hardened and should sustain the expected TID. Little is known about radiation tolerance of the 1WIRE devices; The radiation tolerance of the 1WIRE devices will be tested after completing the full prototype of the readout chain.

F.9.2 Outside calorimeter

The components, which are subject to radiation damage outside the calorimeter are the components of the FEM boards: FPGA (Xilinx XC3S1000), optical transceiver and SerDes, clock oscillators and voltage regulators.

The TID estimation for this region for Au+Au collisions is obtained from PHENIX publication[115]: and is summarized in Fig. F.17.

	RHIC I	**RHIC II**
R = 53 cm	0.79 rad $2.4*10^7$ cm^{-2}	7.9 rad $2.4*10^8$ cm^{-2}
R = 250 cm	0.17 rad $5.1*10^6$ cm^{-2}	1.5 rad $4.5*10^7$ cm^{-2}

Figure F.17: Mean total ionizing dose (TID) for RHIC I and RHIC II fills, for two positions: 53 and 259 cm from the interaction region in rads/fill and equivalent neutrons per cm^2 per fill.

Assuming running periods of 30 weeks per year with 3 shifts per day, the expected dose for 10 years of running RHIC II will be of the order of 50 krad or $1.5*10^{12}$ $n*cm^{-2}$(for 53cm).

The ALICE collaboration published the results of radiation tolerance tests of similar components in [116], which are summarized below.

1. Clock Oscillators and Voltage Regulators
   The clock oscillators PL75108A, SDB0149N, CFPIQXO-71C, PLE5144A where tested.
   All the oscillators found to be tolerant to the gamma irradiation up to 100 krad.
   The voltage regulator of the Linear Technology LT1663 family passed all tests.

2. Optical Transceiver and SerDes
   All Small Form Factor (SFF) optical transceivers which have been tested (HFBR5910E, HFBR5921L, HFBR5920E, V23818-K305-L57, V23818-N305-B57) as well as SerDes (TLK2501, VSC7211) all passed the irradiation test with 10^{12} n*cm^{-2}.

3. FPGA

It was found that the cross section of bit flips in application memory is acceptable, but the cross section for errors in configuration memory is too high. Translated to 50 krad TID it corresponds to 12000 of lost configurations for SRAM-based FPGA (Xilinx Virtex II). The flash-based FPGA (ACTEL ProASIC+) did not show any degradation.

Therefore the only unacceptable tolerance we may expect is in the configuration memory of the SRAM-based FPGA. There are two solutions to that:

1. Use the flash-based FPGA (ACTEL ProASIC+), which is somewhat slower than the Xilinx

2. Monitor the configuration error and reconfigure the FPGA when necessary- the expected rate of such reconfigurations is once per store.

The performance of the StriPixel readout electronics in radiation condition will be tested with full-scale prototype of the electromagnetic brick. It will also establish the maximum length of the daisy-chain cable which, according to D0 experience we expect to be about 2 m. If the rate of Single Event Upsets is not acceptable then **we will move the FEM further from the interaction point**.

Appendix G

Power Proposal

G.1 PHENIX NCC Bias Voltage Supply

The PHENIX Nosecone Calorimeter Bias Voltage power supply is to be implemented as four, 12 channel cards for each of the North and South arms. Each card contains a single Emco 400 volt 20 mA bulk supply which feeds 12 computer controlled push-pull bias output voltage channels. An addressable onboard microcontroller provides control and monitoring of the supply card through an RS485 interface to the PHENIX Rack Monitor and Control (RMC) system. The microcontroller controls and monitors the output voltages via isolated 16 bit DACs and 24 bit ADCs. A controller output port line enables / disables the bulk bias supply by controlling its low voltage regulator source. Serial control commands and responses go through an isolation barrier between the controller and the PHENIX Rack Monitor and Control RS-485 LAN.

Each NCC Power Supply card has its own two digit hex address which is set by the Address High and Address Low rotary switches on the board. There are two indicator LEDs on the front panel. The top green LED flashes at 1Hz indicating computer operation and the bottom amber LED flashes when valid commands are executed. Three grounds are used-chassis ground, bias ground and LAN ground. The control section is referenced to the chassis ground plane. The bias ground plane is isolated from the chassis ground but they are joined at a point near the bulk bias converter by a voltage limiting network. After system reset, the bulk bias supply is disabled and therefore starts in a safe condition with output voltages at zero. The user enables the high voltage by issuing a bias Enable command. This causes the output voltages to begin ramping up to the previously set levels at a predetermined rate. The user sets the individual output voltages by entering the values in the SCADA workstation (Iconics Graphworx32 screen).

The voltage setpoint values are automatically stored in EEPROM and are restored as the default levels on the next reset. All circuitry is enclosed in an aluminum NIM module with steel cover plates and is therefore isolated. The output connectors are Tyco 1586037-8, 4.2 mm PE series which are UL94V-2, 600 V AC and 9 amp rated. The pins are deeply embedded and therefore protected from hand contact. In addition, the controller is monitored by a watchdog timer and disables the bulk bias supply on either power up, watchdog or manual

reset. Vertical airflow cooling is required mainly for the bulk bias converter and is achieved by using a fan tray.

G.2 PHENIX NCC LV Supply

The proposed NCC LV is the PHENIX standard low voltage supply system based on Vicor second generation DC-DC converters. The 2^{nd} generation PHENIX Low Voltage Power System (LVPS-2) is implemented as a 6U crate with a set of 8 to 12 340 mm ("C" size) removable power supply cards (LVLP-2). Each card contains from 6 to 8 Vicor 2^{nd} Generation 300 V to 12V converters which provide output of 5V to 14V DC. A Front End crate controller card (LVLPFE-2) provides both backplane power and computer control for 8 to 12 power supply cards. The low voltage outputs then proceed to 160 mm noise filter cards installed in the rear of the crate. The filtered low voltage from the filter boards is connected to terminal blocks on the rear panel. Control and monitoring of the LVPS-2 crate is achieved through an RS485 interface to the PHENIX Rack Monitor and Control (RMC) system.

Appendix H

Contingency Analysis

This section describes how the contingency for a given WBS element was calculated. Risk is a function of the following factors: the sophistication of the technology, the maturity of the design effort, the accuracy of the cost sources and the impact of delays in the schedule. Risk analysis is performed for each WBS element at the lowest level estimated. Results of this analysis are related to a contingency, which is listed for each WBS element. The goal is to make the method of contingency determination uniform for all project WBS elements. The total contingency for the NCC is 25%.

- **Definitions**
  - **Base Cost Estimate** The estimated cost of doing things correctly the first time. Contingency is not included in the base cost.
  - **Cost Contingency** The amount of money, above and beyond the base cost, that is required to ensure the project's success. This money is used only for omissions and unexpected difficulties that may arise. Contingency funds are held by the Project Manager.
- **Risk Factors**
  - **Technical Risk** Based on the technical content or technology required to complete the element, the technical risk indicates how common the technology is that is required to accomplish the task or fabricate the component. If the technology is so common that the element can be bought "off-the-shelf", i.e., there are several vendors that stock and sell the item, it has very low technical risk, therefore a risk factor of 1 is appropriate. On the opposite end of the scale are elements that extend the current "state-of-the-art" in this technology. These are elements that carry technical risk factors of 10 or 15. Between these are: making modifications to existing designs (risk factor 2-3), creating a new design which does not require state-of-the-art technology (risk factor 4 & 6), and creating a design which requires R&D, and advances the state-of-the-art slightly (risk factor 8 & 10).
  - **Cost Risk** Cost risk is based on the data available at the time of the cost estimate. It is subdivided into 4 categories.

  * The first category is for elements for which there is a recent price quote from a vendor or a recent catalog price. If the price of the complete element, or the sum of its parts, can be found in a catalog, the appropriate risk factor to be applied is 1. If there is an engineering drawing or specification for the element, and a reliable vendor has recently quoted a price based on these, the cost risk factor to be applied is 2. Similarly, if a vendor has quoted a price based on a sketch that represents the element, and the element's design will not change prior to its fabrication, the appropriate cost risk factor would be 3.
  * The second category is for elements for which there exists some relevant experience. If the element is similar to something done previously with a known cost, the cost risk factor is 4. If the element is something for which there is no recent experience, but the capability exists, the cost risk is 6. If the element is not necessarily similar to something done before, and is not similar to in-house capabilities, but is something that can be comfortably estimated, the risk factor is 8.
  * The third category is for elements for which there is information that, when scaled, can give insight into the cost of an element or series of elements. The cost risk factor for this category is 10.
  * The fourth category is for elements for which there is an educated guess, using the judgment of engineers or physicists. If there is experience of a similar nature, but not necessarily designing, fabricating or installing another device, and the labor type and quantity necessary to perform this function can be estimated comfortably, a cost risk factor of 15 is appropriate.

- **Schedule Risk** If a delay in the completion of the element could lead to a delay in a critical path or near critical path component, the schedule risk is 8. If a delay in the completion of the element could cause a schedule slip in a subsystem which is not on the critical path, the schedule risk is 4. Only elements where a delay in their completion would not affect the completion of any other item have schedule risks of 2.
- **Design Risk** is directly related to the maturity of the design effort. When the element design is nearly complete, quantity counts and parts lists finished, the risk associated with design is nearly zero; therefore a risk factor of 0 is applied. This is also the case when the element is an "off-the-shelf" item and the parts counts and quantities are finalized. When the element is still just an idea or concept, with crude sketches the only justification for the cost estimate, the risk associated with design state is high or 15. Between these two extremes are the stages of conceptual design and preliminary design. In conceptual design, when layout drawings of the entire element are approaching completion, some preliminary scoping analyses have been completed, and parts counts are preliminary, the design risk factor is 8. During preliminary design, when there are complete layout drawings, some details worked out, complete parts counts, and some analysis for sizing and showing design feasibility, the appropriate design risk is 4.

- **Weighting Factors**
  - The weight applied to the risk factors depends on whether there are multiple or single risks involved in completing an element.
  - The weights applied to technical risk depend upon whether the element requires pushing the current state-of-the-art in design, manufacturing, or both. If the element requires pushing both, the weight to be applied is high, or 4; if either the design or manufacturing are commonplace, the weighting factor is 2.
  - For weights applied to cost risk, the two factors are material costs and labor costs. If either of these are in doubt, but not both, the weight to be applied to cost risk is 1. If they are both in doubt, the weight applied is 2.
  - The weight factor given to schedule risk is always 1.
  - The weight factor given to design risk is always 1 and so is not shown explicitly.
- **Procedure** The following procedure is used for estimating contingency.
  1. The conceptual state of the element is compared with Table H to determine risk factors. A technical risk factor is assigned based on the technology level of the design. A design risk factor is assigned based upon the current state (maturity) of the design. A cost risk factor is assigned based on the estimating methodology used to arrive at a cost estimate for that element. Similarly, a schedule risk factor is identified based on that element's criticality to the overall schedule.
  2. The potential risk within an element is compared with Table H to determine the appropriate weighting factors.
  3. The individual risk factors are multiplied by the appropriate weighting factors and then summed to determine the composite contingency percentage.
  4. This calculation is performed for each element at its lowest level.
  5. The dollar amount of contingency for an element is calculated by multiplying the base cost by the composite contingency percentage.

Risk Factor	**Technical**	**Cost**	**Schedule**	**Design**
0	Not used	Not used	Not used	Detail design > 50% done
1	Existing design and off-the-shelf H/W	Off-the-shelf or catalog item	Not used	Not used
2	Minor modifications to an existing design	Vendor quote from established drawings	No schedule impact on any other item	Not used
3	Extensive modifications to an existing design	Vendor quote with some design sketches	Not used	Not used
4	New design; nothing exotic	In-house estimate based on previous similar experience	Delays completion of non-critical subsystem item	Preliminary design > 50% done; some analysis done
6	New design; different from established designs or existing technology	In-house estimate for item with minimal experience but related to existing capabilities	Not used	Not used
8	New design; requires some R&D but does not advance the state-of-the-art In-house estimate for item with minimal experience and minimal in-house capability	Delays completion of critical path subsystem item	Not used	Conceptual design phase; some drawings; many sketches
10	New design of new technology; advances state-of-the-art	Top-down estimate from analogous programs	Not used	Not used
15	New design; well beyond current state-of-the-art	Engineering judgment	Not used	Not used

Table H.1: Technical, cost and schedule risk factors.

Risk Factor	**Condition**	**Weight**
Technical	Design OR Manufacturing	2
	Design AND Manufacturing	4
Cost	Material Cost OR Labor Rate	1
	Material AND Labor Rate	2
Schedule	Same for all	1
Design	Same for all	1

Table H.2: Technical, cost, schedule and design weighting factors.

		Tech risk	tech weight	Cost risk	cost weight	sched risk	design risk	contingency [%]
1.6.1	**NCC One: Grand Total**							**25**
1.6.1.1	**NCC One: Construction**							**25**
1.6.1.1.1	**Stock components (connectors etc)**	1	2	15	2	1	0	**33**
1.6.1.1.2	**Silicon Sensors**							**29**
1.6.1.1.2.1	Silicon wafers	2	2	4	2	8	0	20
1.6.1.1.2.2	Pad sensor production [each]	2	2	4	2	8	0	20
1.6.1.1.2.3	Certification [each]	1	1	4	1	8	4	17
1.6.1.1.2.4	Strip sensor production [each]	15	4	10	2	8	8	96
1.6.1.1.2.5	Certification [each]	2	1	4	1	4	4	14
1.6.1.1.3	**Pad-structured readout units**							**20**
1.6.1.1.3.1	Ladder carrier boards	2	4	2	2	8	0	20
1.6.1.1.3.2	Stack kits	2	2	2	2	8	4	20
1.6.1.1.3.3	Assembly and testing [stacks]	2	2	2	2	8	4	20
1.6.1.1.3.4	FPC cables	2	2	4	2	4	4	20
1.6.1.1.4	**Pad front-end (preamps)**							**31**
1.6.1.1.4.1	Mather boards	4	4	3	2	8	4	34
1.6.1.1.4.2	Preamp hybrids	3	4	3	2	8	4	30
1.6.1.1.4.3	Crates	3	4	3	2	8	8	34
1.6.1.1.5	**Strip-structured readout units**							**30**
1.6.1.1.5.1	SVX4's	1	1	2	1	4	0	7
1.6.1.1.5.2	Ladder Carrier Boards	4	4	2	2	4	4	28
1.6.1.1.5.3	Sensor Readout Modules (SRM)	4	4	2	2	4	4	28
1.6.1.1.5.4	Dual sensor stack kits	4	4	2	2	4	8	32
1.6.1.1.5.5	Assembly and testing [stacks]	4	4	2	2	4	8	32
1.6.1.1.5.6	Interstack jumpers	4	4	2	2	4	8	32
1.6.1.1.5.7	FEM cables	3	4	2	2	2	8	26
1.6.1.1.6	**Strip front-end (data collection)**							**24**
1.6.1.1.6.1	Front End Modules [FEM]	2	4	4	2	2	4	22
1.6.1.1.6.2	Trigger and timing module	4	4	4	2	4	8	36
1.6.1.1.6.3	Bias Power	4	4	4	2	4	8	36
1.6.1.1.7	**Mechanical Structure**							**20**
1.6.1.1.7.1	W plates for a single NCC	2	4	4	2	4	0	20
1.6.1.1.7.2	Components for brick construction [kit]	4	4	4	2	4	8	36
1.6.1.1.7.3	Bricks-to-crates interface	2	2	4	2	4	8	24
1.6.1.1.7.4	Support structure	4	4	4	2	4	8	36
1.6.1.1.7.5	Cooling system	4	4	4	2	4	15	43
1.6.1.1.8	**Assembly of bricks**							**43**
1.6.1.1.8.1	Assembly of pad sampling cells	4	4	6	4	4	4	48
1.6.1.1.8.2	Assembly of pad ROU's	4	4	6	4	8	4	52
1.6.1.1.8.3	Certification of pad sampling cells	4	2	4	4	8	4	36
1.6.1.1.8.4	Assembly of PreShower layer	4	2	4	4	8	4	36
1.6.1.1.8.5	Assembly of ShowerMax layer	4	4	4	4	8	4	44
1.6.1.1.9	**Digital signal processing [channels]**	2	2	4	2	4	4	**20**
1.6.1.1.10	**HM Cables**	2	2	4	2	4	4	**20**
1.6.1.1.11	**System test**							
1.6.1.2	**NCC One: DAQ**	2	2	4	1	4	4	**16**
1.6.1.3	**NCC One: Integration**	2	2	4	1	4	8	**20**
1.6.1.4	**NCC One: Installation**	2	2	4	1	4	8	**20**
1.7.1	DAQ One							**15**
1.7.1.1	Calorimeter DCM (NCC-I)	2	2	2	1	2	1	9
1.7.1.2	PS and SM DCM (NCC-I)	2	2	2	1	2	1	9
1.7.1.3	Calorimeter trigger (NCC-I)	4	2	4	1	2	4	18
1.8	Auxiliary Systems + Integration							**16**
1.8.1	Support structure	2	2	2	1	2	8	16
1.8.2	Infrastructure	2	2	2	1	2	8	16
1.8.3	Safety	2	2	2	1	2	8	16
1.9.1	Installation (NCC-I)	2	2	2	1	2	8	16
1.9.2	Ready for PHYSICS (NCC-I)							

Figure H.1: Contingency calculation. Contingency is calculated on the base cost which includes spares.

List of Figures

List of Tables

References

[1] **PHENIX** Collaboration, A. Adare *et. al.* arXiv:0705.3238 [nucl-ex].

[2] **STAR** Collaboration, J. Adams *et. al. Phys. Rev. Lett.* **97** (2006) 162301 [nucl-ex/0604018].

[3] G. Baum, M. R. Bergström, P. R. Bolton, J. E. Clendenin, N. R. DeBotton, S. K. Dhawan, Y. N. Guo, V. R. Harsh, V. W. Hughes, K. Kondo, M. S. Lubell, Z. L. Mao, R. H. Miller, S. Miyashita, K. Morimoto, U. F. Moser, I. Nakano, R. F. Oppenheim, D. A. Palmer, L. Panda, W. Raith, N. Sasao, K. P. Schüler, M. L. Seely, P. A. Souder, S. J. S. Lorant and K. Takikawa *Phys. Rev. Lett.* **51** (Sep, 1983) 1135–1138.

[4] **European Muon** Collaboration, J. Ashman *et. al. Nucl. Phys.* **B328** (1989) 1.

[5] **European Muon** Collaboration, J. Ashman *et. al. Phys. Lett.* **B206** (1988) 364.

[6] **PHENIX** Collaboration, 1993. PHENIX Conceptual Design Report(PX20, BNL48922, internal report).

[7] **PHENIX** Collaboration, K. Adcox *et. al. Nucl. Phys.* **A757** (2005) 184–283 [nucl-ex/0410003].

[8] T. Matsui and H. Satz *Phys. Lett.* **B178** (1986) 416.

[9] **BRAHMS** Collaboration, I. G. Bearden *et. al. Phys. Rev. Lett.* **94** (2005) 162301 [nucl-ex/0403050].

[10] **PHENIX** Collaboration, K. Adcox *et. al. Phys. Rev. Lett.* **88** (2002) 022301 [nucl-ex/0109003].

[11] **PHENIX** Collaboration, K. Adcox *et. al. Phys. Lett.* **B561** (2003) 82–92 [nucl-ex/0207009].

[12] **PHENIX** Collaboration, S. S. Adler *et. al. Phys. Rev. Lett.* **91** (2003) 072301 [nucl-ex/0304022].

[13] **PHENIX** Collaboration, S. S. Adler *et. al. Phys. Rev.* **C69** (2004) 034910 [nucl-ex/0308006].

[14] **PHENIX** Collaboration, S. S. e. a. Adler *Phys. Rev. Lett.* **91** (2003) 072303 [nucl-ex/0306021].

[15] **PHENIX** Collaboration, S. S. Adler *et. al. Phys. Rev. Lett.* **91** (2003) 172301 [nucl-ex/0305036].

[16] E. Wang and X.-N. Wang *Phys. Rev. Lett.* **89** (2002) 162301 [hep-ph/0202105].

[17] C. Loizides *Eur. Phys. J.* **C49** (2007) 339–345 [hep-ph/0608133].

[18] R. Baier, Y. L. Dokshitzer, A. H. Mueller and D. Schiff *Nucl. Phys.* **B531** (1998) 403–425 [hep-ph/9804212].

[19] B. Sahlmueller nucl-ex/0701060.

[20] J. Lajoie *To appear in Journal of Physics G: Nuclear and PArticle Physoics* (2007).

[21] J. D. Bjorken, *Energy loss of energetic partons in quark - gluon plasma: Possible extinction of high p(t) jets in hadron - hadron collisions*, 1982. FERMILAB-PUB-82-059-THY.

[22] M. Gyulassy and M. Plumer *Phys. Lett.* **B243** (1990) 432–438.

[23] X.-N. Wang, M. Gyulassy and M. Plumer *Phys. Rev.* **D51** (1995) 3436–3446 [hep-ph/9408344].

[24] X.-N. Wang and M. Gyulassy *Phys. Rev. Lett.* **68** (1992) 1480–1483.

[25] R. Baier, Y. L. Dokshitzer, S. Peigne and D. Schiff *Phys. Lett.* **B345** (1995) 277–286 [hep-ph/9411409].

[26] R. Baier, Y. L. Dokshitzer, A. H. Mueller and D. Schiff *Phys. Rev.* **C58** (1998) 1706–1713 [hep-ph/9803473].

[27] M. Gyulassy, P. Levai and I. Vitev *Phys. Rev. Lett.* **85** (2000) 5535–5538 [nucl-th/0005032].

[28] M. Gyulassy, P. Levai and I. Vitev *Nucl. Phys.* **B594** (2001) 371–419 [nucl-th/0006010].

[29] **PHENIX** Collaboration, A. Adare *et. al. Phys. Rev. Lett.* **98** (2007) 172301 [nucl-ex/0611018].

[30] N. Armesto, M. Cacciari, A. Dainese, C. A. Salgado and U. A. Wiedemann *Phys. Lett.* **B637** (2006) 362–366 [hep-ph/0511257].

[31] H. van Hees, V. Greco and R. Rapp *Phys. Rev.* **C73** (2006) 034913 [nucl-th/0508055].

[32] G. D. Moore and D. Teaney *Phys. Rev.* **C71** (2005) 064904 [hep-ph/0412346].

[33] **PHENIX** Collaboration, S. S. Adler *et. al.* nucl-ex/0507004.

[34] F. Wang *AIP Conf. Proc.* **892** (2007) 417–420 [nucl-ex/0610027].

[35] J. Casalderrey-Solana, E. V. Shuryak and D. Teaney *J. Phys. Conf. Ser.* **27** (2005) 22–31 [hep-ph/0411315].

[36] S. Lin and E. Shuryak hep-ph/0610168.

[37] J. J. Friess, S. S. Gubser, G. Michalogiorgakis and S. S. Pufu hep-th/0611005.

[38] G. Policastro, D. T. Son and A. O. Starinets *Phys. Rev. Lett.* **87** (2001) 081601 [hep-th/0104066].

[39] J. J. Friess, S. S. Gubser, G. Michalogiorgakis and S. S. Pufu hep-th/0607022.

[40] S. S. Gubser *Phys. Rev.* **D74** (2006) 126005 [hep-th/0605182].

[41] F. Antinori and E. V. Shuryak *J. Phys.* **G31** (2005) L19 [nucl-th/0507046].

[42] O. Kaczmarek, F. Karsch, P. Petreczky and F. Zantow *Phys. Lett.* **B543** (2002) 41–47 [hep-lat/0207002].

[43] M. Asakawa and T. Hatsuda *Phys. Rev. Lett.* **92** (2004) 012001 [hep-lat/0308034].

[44] S. Datta, F. Karsch, P. Petreczky and I. Wetzorke *Phys. Rev.* **D69** (2004) 094507 [hep-lat/0312037].

[45] C.-Y. Wong *Phys. Rev.* **C72** (2005) 034906 [hep-ph/0408020].

[46] F. Karsch *Eur. Phys. J.* **C43** (2005) 35–43 [hep-lat/0502014].

[47] **PHENIX** Collaboration, H. Pereira Da Costa nucl-ex/0510051.

[48] **NA50** Collaboration, M. C. Abreu *et. al. Phys. Lett.* **B521** (2001) 195–203.

[49] **NA60** Collaboration, R. Arnaldi *et. al. Eur. Phys. J.* **C43** (2005) 167–172.

[50] Y. V. Kovchegov, *Isotropization and thermalization in heavy ion collisions*, 2005.

[51] S. Mrowczynski *Acta Phys. Polon.* **B37** (2006) 427–454 [hep-ph/0511052].

[52] R. Venugopalan hep-ph/0511117.

[53] D. Kharzeev, E. Levin and K. Tuchin hep-ph/0602063.

[54] B. Kopeliovich, A. Tarasov and J. Hufner *Nucl. Phys.* **A696** (2001) 669–714 [hep-ph/0104256].

[55] L. Frankfurt, V. Guzey and M. Strikman *Phys. Rev.* **D71** (2005) 054001 [hep-ph/0303022].

[56] K. J. Eskola, V. J. Kolhinen and C. A. Salgado *Eur. Phys. J.* **C9** (1999) 61–68 [hep-ph/9807297].

[57] A. Accardi *Acta Phys. Hung.* **A22** (2005) 289–299 [nucl-th/0405046].

[58] L. D. McLerran and R. Venugopalan *Phys. Rev.* **D49** (1994) 2233–2241 [hep-ph/9309289].

[59] L. D. McLerran and R. Venugopalan *Phys. Rev.* **D49** (1994) 3352–3355 [hep-ph/9311205].

[60] L. D. McLerran and R. Venugopalan *Phys. Rev.* **D50** (1994) 2225–2233 [hep-ph/9402335].

[61] H. Kowalski and D. Teaney *Phys. Rev.* **D68** (2003) 114005 [hep-ph/0304189].

[62] L. C. Bland *et. al. Eur. Phys. J.* **C43** (2005) 427–435 [hep-ex/0502040].

[63] D. Kharzeev, E. Levin and L. McLerran *Nucl. Phys.* **A748** (2005) 627–640 [hep-ph/0403271].

[64] N. Borghini and F. Gelis *Phys. Rev.* **D74** (2006) 054025 [hep-ph/0607098].

[65] **BRAHMS** Collaboration, I. Arsene *et. al. Phys. Rev. Lett.* **93** (2004) 242303 [nucl-ex/0403005].

[66] **PHENIX** Collaboration, M. Chiu *AIP Conf. Proc.* **842** (2006) 1091–1093.

[67] **PHENIX** Collaboration, M. Chiu nucl-ex/0701031.

[68] **New Muon** Collaboration, P. Amaudruz *et. al. Nucl. Phys.* **B441** (1995) 3–11 [hep-ph/9503291].

[69] D. F. Geesaman, K. Saito and A. W. Thomas *Ann. Rev. Nucl. Part. Sci.* **45** (1995) 337–390.

[70] D. M. Alde *et. al. Phys. Rev. Lett.* **64** (1990) 2479–2482.

[71] **NuSea** Collaboration, M. A. Vasiliev *et. al. Phys. Rev. Lett.* **83** (1999) 2304–2307.

[72] L. L. Frankfurt, M. I. Strikman and S. Liuti *Phys. Rev. Lett.* **65** (1990) 1725–1728.

[73] B. Z. Kopeliovich, J. Nemchik, I. K. Potashnikova, M. B. Johnson and I. Schmidt *Phys. Rev.* **C72** (2005) 054606 [hep-ph/0501260].

[74] D. Boer and W. Vogelsang *Phys. Rev. D* **69** (2004) 094025.

[75] C. Adloff *et. al. Eur. Phys. J.* **C19** (2001) 289–311.

[76] H. Lai *et. al. Eur. Phys. J.* **C12** (1999) 375–392.

[77] A. Martin, R. Roberts, W. Stirling and R. Thorne *Eur. Phys. J.* **C39** (2005) 155–161.

[78] M. Gluck, E. Reya, M. Stratmann and W. Vogelsang *Phys. Rev.* **D53** (1996) 4775–4786.

[79] Y. Goto *et. al. Phys. Rev. D* **69** (2004) 054021.

[80] E. Laenen, G. Sterman and W. Vogelsang *Phys. Rev. Lett.* **84** (2000) 4296–4299.

[81] E. Laenen, S. G. and W. Vogelsang *Phys. Rev. D* **63** (2001) 114018.

[82] J. Ashman *et. al. Nucl. Phys.* **B328** (1989) 1–35.

[83] G. Baum *et. al. Phys. Rev. Lett.* **51** (1983) 1261–1265.

[84] G. Bunce *et. al. Phys. Rev. Lett.* **36** (1976) 1113–1116.

[85] **STAR** Collaboration, D. Adams *et. al. Phys. Lett. B* **265** (1991) 462–466.

[86] **STAR** Collaboration, J. Adams *et. al. Phys. Rev. Lett.* **92** (2004) 171801.

[87] L. Bland `hep-ex/0602012`.

[88] T. Sjostrand *et. al. Comput. Phys. Commun.* **135** (2001) 238–259 [`hep-ph/0010017`].

[89] D. Sivers *Phys. Rev.* **D41** (1990) 83.

[90] J. Collins *Nucl. Phys.* **B396** (1993) 161.

[91] J. P. Ralston and D. E. Soper *Nucl. Phys.* **B152** (1979) 109.

[92] J. Qiu and G. Sterman *Phys. Rev. D* **59** (1998) 014004.

[93] A. Airapetian *et. al. Phys. Rev. Lett.* **84** (2000) 4047–4051.

[94] A. Airapetian *et. al. Phys. Rev. Lett.* **94** (2005) 012002.

[95] K. Abe *et. al.* `hep-ex/0507063`.

[96] J. Collins, S. Heppelmann and G. Ladinsky *Nucl. Phys.* **B420** (1994) 565.

[97] **HERMES Collaboration** Collaboration `hep-ex/0512019`.

[98] P. Mulders and R. Tangerman *Nucl. Phys.* **B461** (1996) 197–237.

[99] A. Bacchetta, C. Bomhof, P. Mulders and F. Pijlman *Phys. Rev. D* **72** (2005) 034030.

[100] M. Anselmino *et. al. Phys. Rev. D* **73** (2006) 014020.

[101] A. Airapetian *et. al. Phys. Rev. D* **71** (2005) 012003.

[102] C. Bourrely and J. Soffer *Phys. Lett.* **B314** (1993) 132–138.

[103] P. Nadolsky and C.-P. Yuan *Nucl. Phys.* **B666** (2003) 35.

[104] M. Harrison, T. Ludlam and S. Ozaki *Nucl. Instrum. Meth.* **A499** (2003) 235–880.

[105] I. Golutvin *et. al.*, 1992. A Silicon Hadron Calorimeter module operated in a strong magnetic field with VLSI read out for LHC, CERN-DRDC-91-54, CERN-DRDC-P-34.

[106] J. Adams *et. al.*, 2001. The Silicon Matrix as a Charge Detector for the ATIC Experiment, Instrum. Exp. Tech. 44, 455-461, 2001, Prib.Tekh.Eksp. 2001 N4, 38-44, 2001.

[107] V. Bonvicini *et. al. Nucl. Instrum. Meth.* **A518** (2004) 186–187.

[108] R. L. Chase and S. Rescia *IEEE Trans. Nucl. Sci.* **44** (1997) 1028–1032.

[109] H. Spieler. Oxford, UK: Oxford Univ. Pr. (2005) 489 p.

[110] K. Golec-Biernat and M. Wusthoff *Phys. Rev.* **D59** (1999) 014017 [hep-ph/9807513].

[111] H. Spieler. http://www-physics.lbl.gov/∼spieler/Heidelberg_Notes_2005/index.html, 2005. Radiation Detectors and Signal Processing, p.85.

[112] Z. Li *Nucl. Instrum. Meth.* **A518** (2004) 738–753.

[113] L. C. *et al.* http://www-d0.fnal.gov/d0pub/d0_private/4252/m_svx4_user_guide.pdf, 2005. SVX4 User's Manual.

[114] http://www.axman.com/files/CMM5235_man.pdf.

[115] S. Skutnki. http://shepody.physics.iastate.edu/skutnik/thesis.pdf, 2005. A scalable analytic model for single event upsets in radiation-hardened field programmable gate arrays in the PHENIX interaction region.(Thesis).

[116] E. Denes *et. al.* http://lhc-workshop-2004.web.cern.ch/lhc-workshop-2004/5-Posters/74-denes_proceedings.pdf, 2004. ALICE DDL Radiation Tolerance Tests for the FPGA Configuration Loss. (Report).